Francisco de Figueiredo e Silva Cunha Salvado

Licenciatura em Ciências Sociais Militares

Master of Science in Naval Architecture

ESTUDO DO EFEITO SEQUENCIAL DE ONDAS DE CHOQUE EM ESTRUTURAS CONFINADAS E ADJACENTES

STUDY OF SEQUENTIAL EFFECTS OF BLAST WAVES IN CONFINED AND ADJACENT STRUCTURES

Dissertação para obtenção do Grau de Doutor em Engenharia Mecânica

Orientador:	Doutor Filipe Miguel Horta e Vale Teixeira Dias, Senior Lecturer, School of Engineering, University of Edimburgh
Co-Orientador:	Doutor João Mário Burguete Botelho Cardoso, Professor Auxiliar, Faculdade de Ciências e Tecnologia, Universidade Nova de Lisboa

Juri

Presidente:	Doutor Jorge Joaquim Pamies Teixeira, Professor Catedrático, Faculdade de Ciências e Tecnologia, Universidade Nova de Lisboa
Arguentes:	Doutor Corneliu Cismasiu, Professor Associado, Faculdade de Ciências e Tecnologia, Universidade Nova de Lisboa
	Doutor Robert Ângelo Fontes Valente, Professor Associado, Universidade de Aveiro
Vogais:	Doutor Victor José de Almeida e Sousa Lobo, Professor Catedrático, Centro de Investigação Naval, Escola Naval, Marinha
	Doutor Filipe Miguel Horta e Vale Teixeira Dias, Senior Lecturer, School of Engineering, University of Edimburgh, UK

FACULDADE DE CIÊNCIAS E TECNOLOGIA
UNIVERSIDADE NOVA DE LISBOA

Dezembro 2017

Copyright

Estudo do efeito sequencial de ondas de choque em estruturas confinadas e adjacentes

Acknowledgements

My gratitude:

- To my family and my father who regrettably left us too early.

- To Professors Filipe Teixeira Dias and João Burgete Cardoso for their diligent support, guidance and help.

- To Prof. Pamies Teixeira who opened to me the possibility to perform experimental work. His help was priceless.

- I also thank Prof. Victor Lobo who ensured the involvement and support from the Navy. A special thanks to the Submarine Squadron, in the person of its commanding officer Captain Silva Gouveia and to his team of instructors whose professionalism and expertise in the use and handling of explosives was much noticed and appreciated. To Sarg. Lourenço a special recognition for his support, encouragement and precious help.

- A very special reference to Mrs. Maria do Rosário Duarte from the Library and Documentation Division (Divisão de Documentação e Biblioteca) of FCT for her diligent help in the bibliographic research.

- I also thank Arsenal do Alfeite, SA for their support in the manufacturing of the test bench and aluminium alloy plate samples.

- Finally my appreciation to all those that in a way or another participated in this project.

Resumo

O estudo do efeito de ondas de choque explosivas em compartimentos fechados, em particular as condições em que essas ondas se transmitem a compartimentos adjacentes e qual o efeito produzido, afigura-se de grande interesse para a avaliação da vulnerabilidade de edifícios, aeronaves e navios, sendo por isso um tema importante no âmbito da segurança e defesa nacional, dada a natureza permanente e diversificada das ameaças do presente. Em particular pretende-se, através da modelação numérica do fenómeno, estudar a resposta de dois compartimentos adjacentes em que num deles ocorre uma explosão, procurando identificar o efeito do volume e do material dos compartimentos nas condições em que se verifica a perda de estanqueidade à onda de choque e o efeito da onda de choque sequencial na estrutura do compartimento adjacente. Em conjunto com um estudo dos modos de colapso e de rotura de materiais tipicamente utilizados na construção naval militar, neste caso a liga de alumínio AA5083-H111, este trabalho constitui um contributo para uma ferramenta de projeto de navios e embarcações militares, possibilitando análises e previsões da sua vulnerabilidade a diversos tipos de explosivos e projéteis.

Palavras-Chave:
Onda de choque, Onda de choque explosiva, Explosão confinada, Ondas de choque confinadas, Impacto explosivo

Abstract

The study of the effect of explosive blast in confined spaces, particularly the conditions under which blast is transmitted to adjacent compartments and the effects produced, is of relevance for the vulnerability assessment of buildings, aircraft and ships, being of paramount importance in the context of national security and defence due to the permanent and diverse threats of present times. In particular it is aimed, through numerical modelling of the phenomena, to study the response of adjacent compartments, one of them subjected to an internal explosion, to identify the effect of compartment volume and material properties in the conditions that will cause rupture and loss of structural integrity and the effect in neighbouring structures of the sequential wave blast. Together with the study of the modes of collapse and rupture of materials used in naval shipbuilding, in this case the AA5083-H111 aluminium alloy, the present work will be the basis for the setting-up of a tool for the design of naval ships and vessels, providing the means to analyse and predict their vulnerability to several types of military ordnance.

Key-Words:

Shock wave, Blast wave, Confined blast, Confined explosions, Explosive impact

Table of Contents

Table of Contents

Table of Contents

List of Figures

List of Figures

List of Figures

List of Figures

List of Tables

List of Tables

Table of Acronyms

AIREX	Airborne Explosion
ALE	Arbitrary Langrangian-Eulerian
BAZOOKA	Portable grenade launcher (EUA)
CJ	Chapman-Jouguet
Composition B	Hexotol (HE: mixture of TNT and RDX)
Composition C	A family of US plastic explosives (HE: mixture based on RDX). The C4 is a 91% mixture of RDX and a plasticizer plus a binder).
CONWEP	Conventional Weapons Code
EBC	Equivalent Bare Charge
DoD	Department of Defence (USA)
EBW	Enhanced-blast weapon
EOS	Equation of state
FSI	Fluid-structure interaction
HE	High explosive
HMX	Ciclotetrametilene-tetranitramine also known as Octogen (HE)
JWL	Jones-Wilkins - Lee
LAW	Lightweight Anti-tank Weapon (EUA)
LE	Low explosive
OPNAVINST	US NAVY Operations Instruction
PANZERFAUST	*Tank Fist (*in english) Anti-Tank Portable Weapon (ALEMANHA)
PE4	British version of the C4 plastic explosive
PETN	Tetranitrate of pentaeritritol (HE)
PG2	Plastic explosive
PM	Maritime Police

Table of Acronyms

RDX	Ciclotrimetilenotrinitramine also known as Hexogen or Ciclonite (HE)
RPG	Routchnoy Protivotankovy Granatomiot (Anti-Tank grenade launcher) (RUSSIA)
RShG-1	Multipurpose Assault Weapon
RPO-SHMEL	Rocket Assisted Flame Thrower (RUSSIA)
SMAW	Shoulder-Launched Multipurpose Assault Weapon (EUA)
TNT	Trinitrotoluene, Trotil, Dynamite (HE)
TBX	Thermobaric explosive
UNDEX	Underwater Explosion

1. Motivation, objectives and thesis organization

In this chapter the reasons behind the choice of the scope and the objectives that were pursuit during the research work are explained. The organization of the text is also presented so that it's reading may be made easier and clearer allowing a better understanding of the subjects covered in each of the following chapters.

1.1 Motivation

The study of the effect of blast waves in confined spaces and particularly how those waves are transmitted to neighbouring spaces and what will be the resulting effects, is of interest for the vulnerability assessment of buildings, airplanes and vessels, being for this reason an important subject within the field of security and national defence given the diversity and permanent nature of present threats. In the particular case of ships and smaller craft engaged in the enforcement of the authority of the state at maritime areas under its jurisdiction, it is paramount the knowledge of such vessel's vulnerabilities and of the risks involved in such missions, notably in missions of prevention and repression of smuggling, traffic of narcotics, arms or human beings or the prevention of terrorist activity or Force and Harbour Protection.

Not only the terrorist threat should be under consideration but also the possibility that organized crime groups are becoming increasingly better equipped and more audacious. Fire engagements at sea with law enforcement agencies or even the navy, may be possible and probable in a near future.

There is a vast number of past and ongoing research projects relatively to the vulnerability of warships in combat scenarios, i.e. facing highly powerful weapons (torpedoes, missiles, mines and bombs). However, the related information is generally classified and is not available to the public. Similar studies on smaller vessels (police or patrol) are scarce and there are virtually no published work on such type of craft. The

concept of vulnerability is well defined in naval doctrine, for instance as in the OPNAVINST (Department of the Navy, 1988), and relates to the broader concept of survivability. Survivability of a ship is given by her capacity to avoid or resist the damage and to recover the necessary integrity to accomplish her mission. This definition encompasses three components related by:

$$S = 1 - P_h P_{k/h}(1 - P_{r/k}) \tag{1.1}$$

where S is the probability of survival, P_h is the probability of being hit (susceptibility), $P_{k/h}$ is the conditional probability of loss of capacity to accomplish the mission (vulnerability) and $P_{r/k}$ is the conditional probability of recovering from the damaged condition (recoverability). Fig. 1.1 shows how this survivability process evolves with time.

Susceptibility has to do with those means the ship has to avoid being hit, such as sensors, signature control and decoys or the preventive use of her weapons, and is outside of the scope of this work. The same applies to the analysis of recoverability known in all navies as damage control and more recently as internal battle.

The vulnerability of a ship is thus measured by the conditional probability of the occurrence of a given damage when hit by a certain type of weapon. All vessels have a certain capacity to absorb damage due to systems redundancy, structural resistance and suitable internal arrangement and it is obvious that design decisions influence survivability. Therefore, some guidance or data on vulnerability assessment must be available to the naval architect. This work attempts to give a novel contribution to the vulnerability analysis of ships and small craft. The direct relationship between ship design and ship vulnerability constitutes the incentive to a deepening of all aspects that can provide the designer with guidance and criteria for the design of safer and more resilient vessels.

The present study characterizes the effect on a vessel of a high explosive (HE) explosion inside one of her compartments, considering the loading resulting from the blast wave, when it expands sequentially through the first compartment and propagates to neighbouring spaces. The overall effect on structural integrity is assessed with the intent of obtaining useful data for the derivation of future design recommendations for

overall damage risk mitigation and, eventually, the definition of operational doctrine for the crews operating in small coastal light craft for surveillance and patrol.

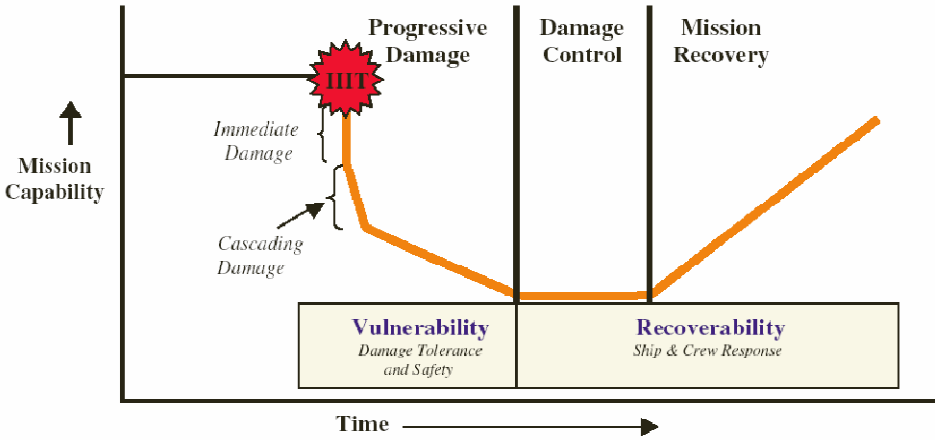

Figure 1. 1- Survivability of a damaged ship as a function of time (Webster, 2007).

The present study is restricted to confined explosions, which limits the number and type of the weapons that may constitute the threat. This means that free air explosions have not been considered nor underwater explosions, which constitute a very specific area of research. Stand-off explosions are also outside the scope of this study as the resulting blast would mainly cause external damage. A confined explosion may result from an explosive device left intentionally inside a compartment. This, although unlikely to happen in a military or police vessel, may happen in a passenger or transport vessel. However, portable grenade launchers may represent a very powerful threat. The ammunition fired by the vast panoply of existing launchers sends to the target a relatively significant HE charge, capable of inflicting a large damage in the light structures of those light craft. There are many manufactures of weapons of this kind originating from dozens of countries (LAW, SMAW, BAZOOKA, RPG, PANZERFAUST, CARL GUSTAV, SHMEL; etc). From all these the most widespread is undoubtedly the RPG[1], thanks to its low cost, robustness and simplicity. However, most of the available ammunition has contact fuses or are armour-piercing. The first detonates outside the target as an airborne explosion and the second projects to the inside a high energy jet of

[1] The RPG 7, worldwide available and regularly owned by terrorist groups, pirates, guerrillas, militia and all sorts of irregular troops costs only about 3000 dollars each.

melted metal that in light structures without armour protection will have only a local penetrating effect, propagating as a straight line through the compartment. Both effects will not fit in the concept of a confined blast. We are thus left with HE ammunitions with time fuses that will delay the detonation to a few milliseconds after impact allowing the projectile to penetrate a light bulkhead and to detonate in the inside. Also hand grenades may be considered as possible origins for confined blast. A hit by one of these weapons will result in an internal detonation causing direct damage in the hit compartment and indirect damage in the neighbouring spaces. The amount of damage may vary with other factors than the mass and nature of explosive, such as compartment dimensions, venting, internal arrangement and strength of bulkheads and decks.

As far as the author is aware there is no work published on the subject of damage inflicted in a compartment due to internal blast loading on the adjacent compartment.

1.2 Work methodology

Such a scope of work implied that the problem had to be subdivided into three major phases, each of them encompassing a wide range of knowledge and ongoing research, such as the mechanics of the explosion, the response of the structure up to failure and the transfer of the remaining energy to a secondary structure which response will also be of interest. The explosive load effects on impacted structures may be addressed with analytical functions but these have limitations in considering different explosive shapes, complex geometries, confinement, etc. Analytical solutions are unavailable for confined explosions for instance. On the other way, experimental work requires facilities and expensive instruments prone to damage after repeated exposure to such high test loadings. The destructive nature of explosive testing makes them inappropriate for extensive real scale experiments or for parametric analysis where a large number of different test arrangements are required. This leaves numerical analysis the most viable research tool for the present study. However the complexity of the phenomena required some means of validation of results which led to the set-up of a series of experiments destined to gain insight on the physics involved and data to compare with the numerical analysis.

Chapter 1

The numerical analysis of high speed and very intense loading of structures and materials employs, in general, a category of software bearing the traditionally designation of hydrocodes. The designation persisted since the first numerical investigations on high speed impact at the Los Alamos laboratory in the 1950's. Because the pressures imparted by such impacts were several orders of magnitude higher than the strength of the materials impacted, calculations assumed pure hydrodynamic behaviour of those materials, ignoring deviatoric stresses. In result, material stress tensors would resemble those of fluids and so such codes were baptised as hydrocodes.

Hydrocodes are programs for the computation of continuum mechanics models involving large transfer of energy in short periods of time (blast and impact) and the behaviour of materials subject to very high loading rates (Zukas, 2004). Hydrocodes deal, *in latu sensu*, with nonlinear problems with time dependence, typically with transient loading and involving large deformations occurring in very small time intervals (Benson, 1990).

They are basically similar to finite element codes developed for structural analysis or solid mechanics but because of the large deformations involved in the analysis, explicit time integration is preferred as well as Arbitrary Lagrangian-Eulerian (ALE) meshes as these will avoid the excessive deformation of a Lagrangian mesh. These options require advection algorithms to transport material between cells as ALE techniques are based on a relative motion between mesh and material. Equations of state (EOS) will also be employed to relate energy, pressure, volume and density. Finally constitutive equations will relate stress, strain, strain rate, internal energy and failure criteria. This will be explained in detail in the following chapters.

All hydrocodes are similar in their structure. They may just resume to a solver but some add pre-processor and post-processing modules for data input and result checking. A flow diagram of a typical hydrocode solver is shown in Fig. 1.2.

LS-DYNA, a commercially available finite element code, multi-purpose and well suited for the solution of dynamic, transient and non-linear analysis, has been used in the present work. It had its origin in DYNA3D, a program developed in 1970's at the Lawrence Livermore National Laboratory. The first commercial version came out in 1976. After several developments, Hallquist, responsible for DYNA3D, decided, in 1989, to leave the laboratory and to open his own software house, the Livermore Software and Technology Corporation (LSTC), distributing LS-DYNA.

Table 1.1 shows a selection of explicit codes used for blast loading or impact analysis. Setting up an experiment of blast loading is time consuming and expensive due to the destructive nature of the experiments and the degree of sophistication of the equipment required to collect data from the explosion and its effects. This recommends the use of numerical tools where parameter variation can be easily performed for any number of combinations desired. However, numerically modelling a physical phenomenon implies a number of approximations and simplifying assumptions to maintain the complexity of the model within practical boundaries. Numerical tools are also prone to error and validation involves considerable effort and analysis but this disadvantage is largely compensated by the richness of the information that can be obtained through computing. In general trends, parameter relations and comparative results will often be as important as absolute results and this is where the real power of computational tools is unfold.

Small light craft are the main purpose of the intended findings. Small light craft are mainly constructed either of composite materials or naval aluminium alloys. In both cases there are a large number of vessels involved in patrol and law enforcement activities. Typical naval grade aluminium alloy has been used in many high-speed light craft, such as patrol boats, ferries and small passenger vessels and was the choice for the present work.

Most of published work on aluminium alloys is dedicated to other than the grades of interest for shipbuilding. There is very little published material on aluminium marine structures subjected to blast although its ballistic performance has been a topic of intense investigation in the last decades. Good reasons exist for such interest: Aluminium shows a very good strength to weight ratio, high specific energy absorption capacity and good thermal conductivity, that indicates that aluminium is less sensitive to adiabatic shear banding and thermoplastic instability than most steels (Borvik, et al., 2004).

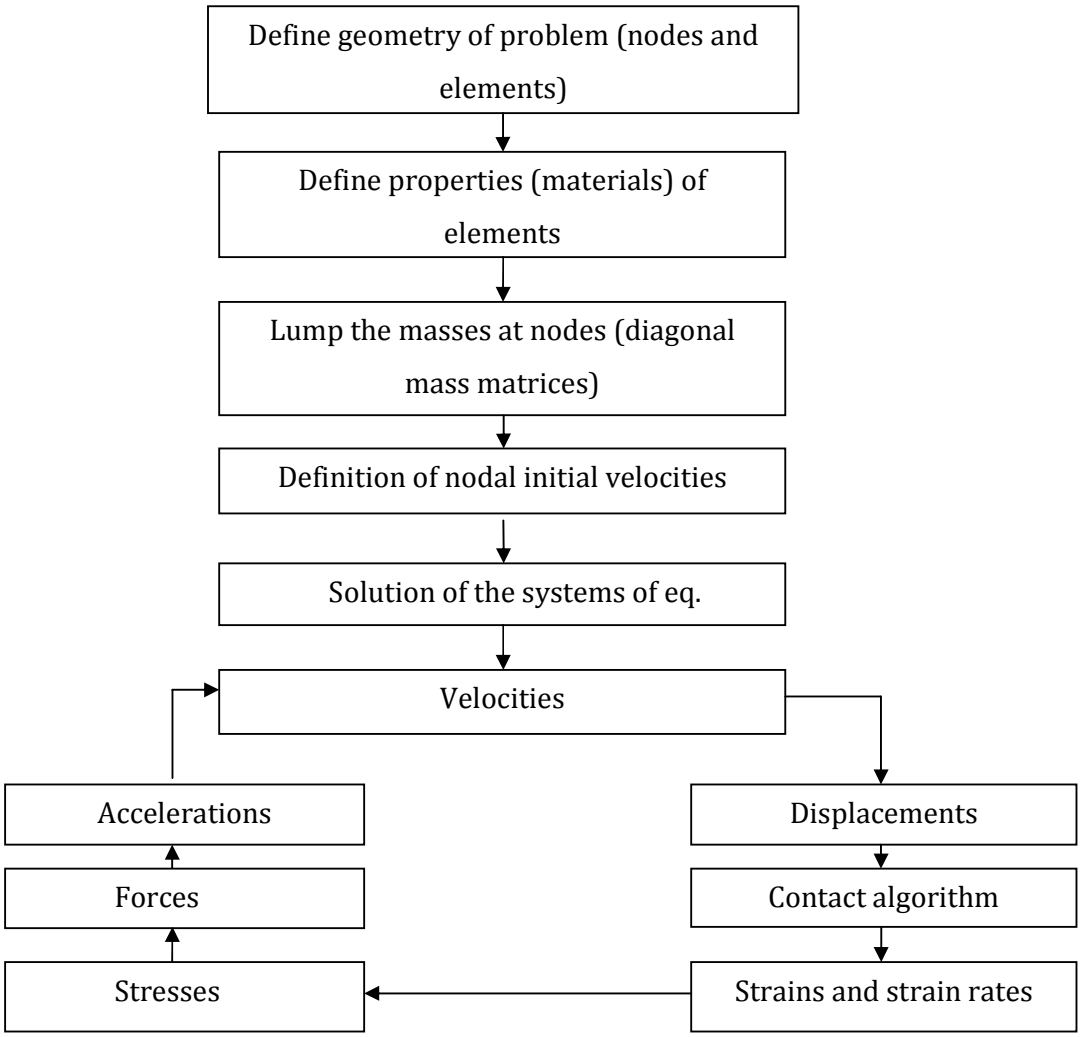

Figure 1. 2 - Diagram of blocks of a typical hydrocode (Zukas, 2004).

Table 1. 1 - Computer programs for the analysis of load blast in structures (Tang, 2009)

Product	Analysis type	Author or owner
BLASTX	Blast loading predictions, CFD, semi-empirical	SAIC
CTH	Blast loading predictions, CFD, *first principles*	SANDIA National Labs
FEFLO	Blast loading predictions, CFD, *first principles*	SAIC
FOIL	Blast loading prediction, CFD, *first principles*	Applied Research Associates, Waterways Experiment Station
HULL	Blast loading prediction, *first principles*	Orlando Technology
SHARC	Blast loading prediction, CFD, *first principles*	Apploied Research Associates, Inc
DYNA3D	Structural analysis, CFD , Coupled analysis, *first principles*	Lawrence Livermore National Laboratory
ALE3D	Coupled analyis, *first principles*	Lawrence Livermore National Laboratory
LS-DYNA	Structural analysis, CFD , Coupled analysis, *first principles*	Livermore Software Technology Corporation
EPSA-II	Structural analysis, *first principles*	Weidlinger Associates
FLEX	Structural analysis, *first principles*	Weidlinger Associates
ALEGRA	Coupled analyis, *first principles*	Sandia National Laboratories
Air3D	Blat loading predictions, CFD, semi-empirical	Royal Military College of Science, Cranfield University
CONWEP	Blast loading predictions, empírical	US Army Waterways Experiment Station
ABAQUS	Structural analysis, CFD , Coupled analysis, *first principles*	ABAQUS Inc

1.3 Materials

Typically aluminium hulls employ magnesium based aluminium alloys AA5083 or AA5086, due to their excellent resistance to corrosion in marine environment. Stiffeners are normally made of alloys of series 6000 as the requirement of corrosion resistance is not critical for the internal structure which is not permanently exposed to sea water. AA5083-H116 is the second strongest commercial aluminium-magnesium

alloy, only exceeded by AA5456. The main mechanical properties of this alloy can easily be obtained from manufacturers but some typical values for tensile strength, yield strength and elongation have been reported to be 347 MPa, 261 MPa and 17%, respectively (Borvik, et al., 2004). The amount of magnesium in AA5083 is relatively high, with about 4.5 wt%. Moreover, AA5083 also contains up to 1% manganese, and minor quantities of elements such as iron, copper, zinc, chromium and titanium to improve strength or other characteristics.

The main stream of published work for utilization of these alloys under very strong and high speed impact loading has been for ballistic applications (Corbett, et al., 1996)(Pekutowski, et al., 1996)(Woodward, et al., 1998)(Piekutowski, 1999)(Forrestal, et al., 2000)(Borvik, et al., 2001)(Roeder, et al., 2001)(Warren, et al., 2001)(Borvik, et al., 2004)(Borvik, et al., 2005)(Gupta, et al., 2006)(Gupta, et al., 2007)(Showalter, et al., 2008)(Sorensen, et al., 2008)(Borvik, et al., 2009) (Borvik, et al., 2011)(Jones, et al., 2012)(Iqbal, et al., 2013) and very little studies are available, until very recently, on blast loading of naval structures.

However, hulls must be welded and the heat from welding will affect the mechanical properties of a tempered or work hardened aluminium alloy. In the heat affected zone the softening effect will significantly reduce the values of such properties and it is common procedure in the design of aluminium boats to use 0 temper aluminium (or close). This will avoid the complexity of having to consider different plate properties in way of weldings. AA5083-H111 aluminium alloy is commonly used for naval construction and it has been chosen in the present work.

1.4 Organization of the thesis

Finally to help the reader to navigate within the many subjects that had to be covered a description of how they were ordered is presented.

The objective of this work has been to obtain a numerical tool that could be used by design engineers in the assessment of the load blast parameters, and hence the degree of damage, that would be observed in a compartment immediately adjacent to another, where an explosion, of sufficient energy to break the frontier between the two compartments, had occurred. With such a tool it should be possible to determine the

lethal radius of the detonation of explosive ordnance inside a given compartment of a ship, for instance.

The focus has been the smaller and lighter craft where, in general, no special shock provisions are considered in their design. It has been necessary to consider a closed space with one of the walls defined with elasto-viscoplastic behaviour and where a HE has been detonated to the point of rupture of that wall. The transfer of energy and blast pressure through the ruptured wall to the adjacent compartment has been modelled and their loading effects measured and compared with those of the first compartment. Experimental results were obtained from field tests with explosives. In a first phase, thin aluminium plates firmly attached to an assumed rigid frame were exposed to free air explosions. The aim was to observe their deformation and calibrate a material constitutive model to be used in the second phase of the experimental program, in which a closed chamber, with two adjacent compartments separated by a thin aluminium alloy plate, was subjected to a confined detonation inside one of the compartments, to cause rupture of the dividing thin plate. Test benches were manufactured specially for the purposes described above and some instrumentation has been used, although budgetary restrictions severely limited the number and type of measuring devices.

The extensive numerical analysis work performed provided a good understanding of the physics of the phenomena involved. Validation has been pursuit by using experimental work published by others, or the direct measured results of the two experimental phases performed under the subject of the thesis.

In all relevant parts of this project a work review has been added, particularly in the part dedicated to constitutive material behaviour where a more thorough review was performed in an attempt to clarify that particular subject, obscured by the profusion of available models.

The organization of the thesis is described as in the following paragraphs:

Chapter 1: Motivation, objectives and thesis organization

This chapter explains and justifies the choice of the subject and states in broad terms the scope of work. The development of a vulnerability assessment tool has been the main objective of the program of work set-up which will be made possible with the understanding of blast loading structural response of ships and smaller craft.

Chapter 2: Explosives and blast waves

An introduction on the mechanics and physics of the explosive phenomena is provided, in the depth considered adequate for the understanding of the modelling options followed in the subsequent Chapters. An essential review of the Rankine-Hugoniot relations and basic thermodynamics of explosions are also presented.

Chapter 3: The effect of blast on structures

The response of materials to blast involves plastic deformation, strain rate, hardening and temperature effects and micro-structural changes, which in itself constitutes a very wide field of research. The complexity of the subject required an extensive review which helped to direct the choice of the material model to be used in this very specific, high velocity, high pressure type of loading. Many constitutive relations exist to describe the elastic visco-plastic and failure behaviour of metals and particularly naval grade aluminium plates were described in this work. The main content of the chapter is a review on constitutive models for metals subjected to high strain rate loading.

Chapter 4: Numerical modelling

An extensive numerical analysis was performed implying the input of a significant number of data and various modelling techniques. Such techniques and input are presented and explained together with a theoretical background of the algorithms that have been used in the analysis. ALE theories, fluid-structure interaction, contact algorithms, advection and explicit time-integration are some of the subjects covered together with fundamental aspects of non-linear continuum mechanics theory.

Chapter 5: Confined explosions – a parametric numerical analysis

This chapter considers the effect of a particular compartment geometry in the parameters of an explosion occurring inside it. This effect was explored varying the dimensions and the position of the explosive in a closed rigid box. A description of the effect of the confinement together with an attempt to predict the peak pressures that result from such a confinement, bearing in mind the effect of wave reflections, is presented in a parametric way.

Chapter 6: The behaviour of AA5083-H111 plates exposed to free air blast

Since the material chosen for the subject of the thesis was the AA5083-H111 aluminium alloy, it was necessary to investigate its properties under blast loading. This Chapter details the experimental work and the analysis performed to characterize the visco-plastic behaviour of the chosen material. The experimental data obtained from a series of free-air blasts has been used to validate a numerical constitutive model, to serve as the basis for the subsequent and last phase of this work.

Chapter 7: Blast wave transmission between two adjacent, confined compartments

This Chapter presents the experimental work on a set of two closed chambers connected by a AA5083-H111 plate diaphragm, where confined explosive charges were detonated in one of the chambers to observe the effect of the blast in the second chamber after rupturing the diaphragm plate. The experimental data is presented and discussed. The numerical simulations attempting to validate the model are also presented although a complete validation was not possible to be obtained.

Chapter 8: Conclusions

The last Chapter presents the relevant conclusions and the major objectives that were reached as well as those who were not. A final synthesis of the project is presented.

As it can be seen the work presented in each chapter leads the reader through a sequence related to the progression of knowledge:

- The theory behind explosive loading (wave blast, pressure curves, the influence of stand-off distance and confinement); Chapter 2.
- The theory behind constitutive material behaviour under blast loading, including a relatively comprehensive review of high strain rate plasticity and failure of metals; Chapter 3.
- The numerical tools, where the most important numerical technologies necessary to address numerically these problems are explained; Chapter 4 and 5.
- The experimental and numerical program of investigations; Chapter 6 and 7.
- The final conclusions; Chapter 8

2. Explosives and blast waves

Some definitions of explosives are presented. The mechanics of explosion and wave blast are presented along with a brief reference to important work published in the field. Explosions in confined spaces are also presented and the published relevant work is reviewed.

2.1 Nomenclature of explosives

An investigation on the effects of blast loads on plated structures requires a basic knowledge of the physics of the explosive phenomena. It is outside the scope of this thesis to describe the state of art of explosion and shock mechanics but some essential knowledge has been collected to provide a more clear understanding of the whole problem in hand. An accurate modelling of the explosive detonation is a very demanding task requiring a deep knowledge of chemistry. For instance, the constant specific heat ratio γ, of air will change its value at high temperatures and afterburning effects will affect the reflected impulse. The chemical composition of an explosive will govern its physical properties. Most of the data and information gathered in this chapter comes from Sherkar (Sherkar, et al., 2010).

High explosives science couples chemistry and fluid mechanics but although the latter is well understood the detailed knowledge of the chemical reactions and thermomechanics that cause the detonation is still not completely understood. It is not possible to obtain a sample of material when it is being reacted to see how the chemistry is progressing. There is no way of studying the chemicals and their reaction at the detonation front with most laboratory apparatus. More sophisticated techniques such laser spectroscopy may solve many of the difficulties to understand such phenomena.

Most explosives appear in a condensed form (as solids) but due to the very high detonation pressures their material strength may be neglected and reactive fluid dynamics is used to study explosions. Also the nature of the phenomenon makes that

motion will be the major driving mechanism for energy transport, rather than heat radiation or conduction or viscosity.

Explosions can be characterized in different ways. The classification criteria adopted here is one of the many possible and starts from a broad division into nuclear, mechanic and chemical explosions. Nuclear and mechanical explosions are outside the scope of the thesis. One example of a mechanical explosion is, for instance, the rupture of an over-pressured vessel when its maximum strength is exceeded causing a sudden and violent expansion of the contained gas.

The usual classification for chemical explosives divides them into low explosives (LE) and high explosives (HE) and this division determined the choice of energetic material to be simulated. We will discard LE which includes powders, rocket and missile fuel and flares as their use is not of interest for this work due to their low reaction speeds. Fig. 2.1 depicts the combination of a primary (HE) explosive used to initiate the detonation of the secondary (HE) explosive.

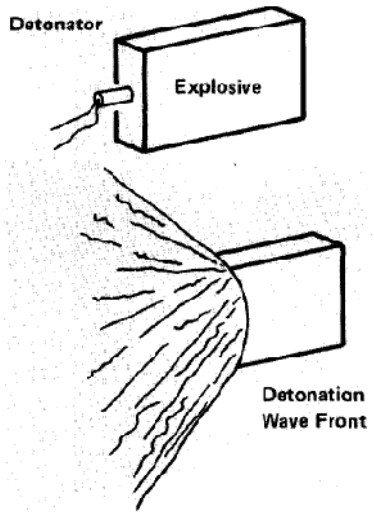

Figure 2. 1- Illustration of the basic mechanism of an explosion: The detonation is initiated by a primary explosive and the reaction wave front will in turn detonate the rest of the explosive material

The classical classification of chemical explosives divides them as shown in Fig. 2.2. Another subdivision can be made in the HE group, into primary and secondary explosives. Primary explosives have reaction speeds of the order of 3500 – 5500 ms^{-1}

and are very sensitive to initiation by shock, friction or heat, which makes them suitable to be used as fuses and detonators as their detonation will activate the reaction of the secondary explosive. Examples are lead azide, lead styphnate (trinitroresorcinate), lead mononitroresorcinate (LMNR), potassium dinitrobenzofuran (KDNBF) and barium styphnate (Sherkar, et al., 2010). Secondary explosives are more energetic, with reaction speeds in the range 5500 – 9000 s^{-1} but are much less sensitive and cannot be easily detonated by heat or shock. This difference in stability between primary and secondary explosives requires certified personnel to handle them in the field and strict safety rules to be followed by the research team.

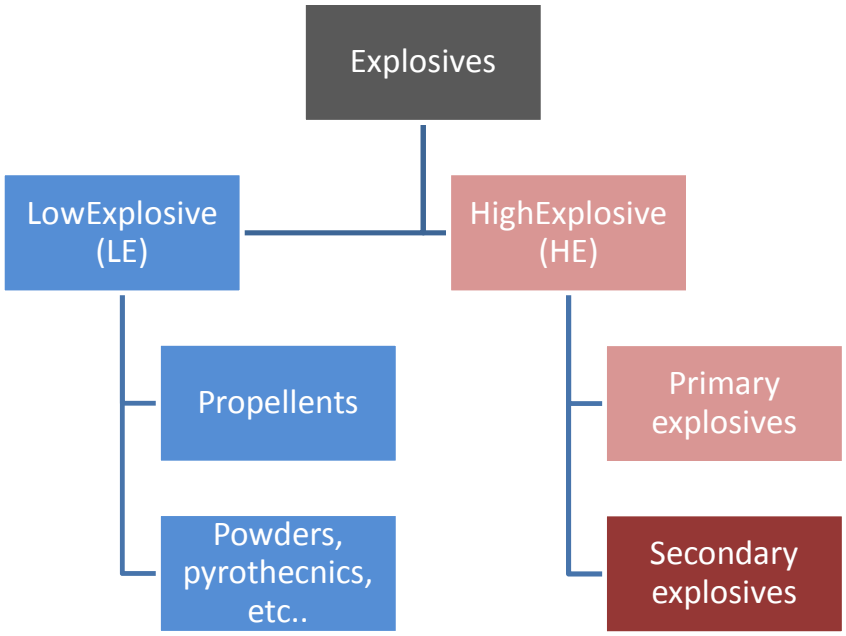

Figure 2. 2- Classification of chemical explosives (Sherkar, et al., 2010).

An explosive is a composition of the type $C_xH_yN_wO_z$ and one explosion is a reaction of oxidation where the oxidizer may be, instead of atmospheric oxygen, an oxidizing salt, such as a nitrate or a perclorate belonging to the composition itself. The presence of these products speeds up the oxidation, allowing a very fast reaction with supersonic speeds up to 9000 ms^{-1}. These high speeds are what make the violent nature of detonations when compared with deflagrations, concepts that will be explained later. This supersonic wave velocity is almost constant for a particular explosive but it varies from one explosive to another, depending on the composition and density of the

explosive. The extraordinary propensity of explosives to react will result in large amounts of energy released during their combustion and being converted to mechanical work in a very strong and damaging loading process. Naturally such reaction is also strongly exothermic and besides its mechanical effect a very hot mixture of gases will also result from the reaction.

Reaction speeds as large as those described above will produce a sudden release of rapidly expanding gaseous products that will compress the surrounding media at such a rate that shock waves will form. These are characterized by a very sharp and high incident pressure that will give the detonation its high destructive power. This release of energy is quite fast as typically 90% of the chemical reaction is complete in no more than one micro-second. During the detonation the explosive will decompose and carbon and hydrogen will react with the available oxygen. The following defines approximately the order of reaction of products (Wilkinson, et al., 2003) :

1. All nitrogen reacts and combines;
2. All hydrogen is used up into the production of water;
3. The available oxygen left after combination with hydrogen reacts with carbon forming CO;
4. The oxygen not reacted in the two processes above reacts with CO to give CO_2;
5. The remaining oxygen combines to form molecules;
6. The remaining carbon stays as solid carbon;
7. Remains of NO_x are formed.

Thus, $C_xH_yN_wO_z \rightarrow xC + yH + wN + zO$ which will recombine to form the final products of the reaction such as described above.

Many explosives are available (Meyer, et al., 2007)(Dobratz, et al., 1985) and research on new formulations continues in specialized laboratories. They may be grouped into molecular groups such as:

1. Nitro compounds;
2. Nitric esters;

3. Nitramines;
4. Derivatives of chloric and perchloric acids;
5. Azides;
6. Compounds capable to produce an explosion, such as fulminates, acetylides, nitrogen-rich compounds such as tetrazene, peroxides and ozonides (Sherkar, et al., 2010).

Some examples of secondary HE used in conventional military ordnance but also found in laboratories are presented below:

7. TNT (Trinitrotoluene $C_7H_5N_3O_6$), perhaps the most common;
8. PETN (Tetranitrate of pentaerytrite $C_5H_8N_4O_{12}$), which combined with TNT gives the well known Pentolite;
9. RDX (US Research Department Explosives - Trimethylenetrinitramine, $C_3H_6N_6O_6$), also known as Hexogen or Cyclonite;
10. HMX (Cyclotetramethylenetetranitramina $C_4H_8N_8O_8$), named also as Octogen (Meyer, et al., 2007).

RDX can be mixed with other compounds to give special purpose compositions. A well known military composition is known as Composition B or Hexotol that is a mixture of RDX e TNT in the proportion 60:40. It is found in grenades and many artillery warheads. Another well known composition is the group of plastic explosives or Compositions C, which can yield very strong detonation rates and show a very high brisance.[2] Composition C uses a mix of hexogen and a plasticizer (which may be an explosive itself). The well known C4, for instance, is a military grade mixture of 90% of RDX and 10% of polyisobutyelene, which is a plasticizer. This explosive has the ability to be moulded into a desired geometry thanks to that plasticizer. A close version of C4, the PG2 has been used in the experimental part of this research which is based on 88% of RDX.

[2] Brisance is a property of explosives characterized by their destructive fragmentation effect (Meyer, et al., 2007) and may be measured as the speed with which the peak pressure is achieved after detonation. It depends on the detonation rate (reaction speed) of the HE material.

ANFO is also a widely used industrial explosive mixture of ammonium nitrate (AN) and fuel oil (FO). PBX (Polymeric Based Explosive) is presently under investigation as it shows a very good stability and produce a smoother wave front than ordinary HE.

Thermobaric explosives or a group of explosives designated by TBX, are a particular case of fuel-air mixtures using aluminium or magnesium cased with the HE.

In some compositions (excepting nitroglycerine and ammonium nitrate) the present oxygen is not sufficient for a complete oxidation and an incomplete reaction will result which imply that an additional energy-release mechanism will contribute to drive the shock front away. The heat generated (heat of detonation) will be lower than the heat of combustion (maximum available energy). The reaction with atmospheric oxygen produces solid oxides and the resulting shock wave is generated by the heat of combustion rather than by the expansion of gaseous oxides that are generated by the combustion of the explosive. This means that the pressures generated will be lower but the reaction will take longer as the unburned products will react with the ambient oxygen producing additional energy, continuing to release heat. This reaction is called afterburning. The available energy in the post-combustion phase is the difference between the heat of combustion and the heat of detonation. For TNT, which has a deficit of oxygen, this difference is about 10.6 MJ kg^{-1}, a lot more than the energy of detonation which is about 4.6 MJ kg^{-1}. But this may show that the energy available for release in the after burn phase is quite considerable although it will depend on the way the products of detonation will expand and mix with ambient oxygen. Adding aluminium powder will allow an after burn (Wilkinson, et al., 2003) and the resulting effect is often designated as an overdriven explosion.

For the present thesis only TNT and C4 or PE4 are considered as their burning properties are easily found in the open literature. Unfortunately, the PG2 characteristics are not available and some conjecture had to be used. It was, therefore, assumed that it should behave as PE4 (the British version of C4). It was observed that this assumption worked relatively well.

2.2 Explosives related phenomena

Explosions can be defined in many ways. Most of these definitions refer to a very rapid combustion of an energetic material causing a large and rapid release of energy in the form of heat and a sudden expansion of the gaseous products of the reaction, which will cause a sharp increase in pressure that will form a blast wave. It is important to explain the difference between detonation and deflagration. Both are types of explosions but in detonations the speed of combustion is higher than the speed of sound in the explosive material. In deflagrations the speed of combustion is subsonic and they propagate by the liberated reaction heat. Changes in momentum and kinetic energy are small. In detonations the phenomena are much more energetic. Detonation waves are supersonic, momentum and kinetic energy changes dominate. A detonation will be self sustained and once initialized the explosive will react to completion.

Only detonations have been considered in the present study and when referring to explosives we mean high explosives (HE). Deflagrations would be applied to gas or fuel explosions and the overpressure that they cause is much lower than that of a detonation. Table 2.1 shows typical values of overpressures and the resulting damage.

The damage mechanism of a detonation is not only based on blast but also on flying fragments out in motion by the passage of the blast wave. A large amount (about 50%) of the released energy during detonation is dissipated in the breaking and fragmentation of the casing that contains the explosive and in the acceleration of the fragments and only the rest is converted into thermal energy and pressure wave. The blast wave produced by a bare charge is stronger that produced by an equivalent charge placed in a casing (Arnold, et al., 2008) (Grady, 2008) (Bishop, et al., 1968). Fisher's equations (Fisher, 1953) defined an equivalent bare charge (EBC), the mass of bare explosive that would cause the same blast of the considered ammunition. Ficher's method gives better results for heavy and thick casings and modifications were introduced for use with light or pre-fragmented casings. These equations are :

$$EBC_{FISHER} = C\left(0.2 + \frac{0.8}{1+\frac{M}{C}}\right) \tag{2.1}$$

$$EBC_{FISHER\ MOD} = \frac{1}{2}\left(C + C\left(0.2 + \frac{0.8}{1+\frac{M}{C}}\right)\right) \quad (2.2)$$

were M is the mass of casing or fragments (kg) and C is the mass of the charge or the mass of the gases prior to the rupture of the casing.

The theoretical work of Gurney is also often addressed for the consideration of splinter and fragments (Hutchinson, 2010).

Table 2. 1 – Reproduced from http://www.globalsecurity.org/wmd/library/report/enviro/eis-0157/eis0157_d4.html (Kinney and Graham, 1985)
***The concept of scaled distance will be explained in section 2.4**

Scaled distance $*Z = R/W^{1/3}$	**Overpressure (kPa)**	**Effects**
125 – 60	0.7 – 1.5	Breakage of glass windows
60-30	1.4 – 2.8	Debris and missile damage
24.5 – 12.5	3.5 – 7.6	Windows shattered. Plaster cracked, minor damage to buildings
13.2 – 9.5	7.6 - 10	Personnel knocked down, sheet metal buckled
8.4 – 6	12.5 - 20	Failure of concrete walls
6-4.8	30-30	Self-framing panelled buildings collapse, oil storage tanks ruptured
4.2 – 3.3	40 - 60	Reinforced concrete structures damaged, trains overturned
2 – 1.35	200 - 500	Lung damage
1.15 – 0.8	700 - 1500	Lethal effects
0.7 – 0.55	2000 - 3000	Crater formation in average soil

Objects in the flow of a blast wave may be displaced but these effects (Bowen, et al., 1961) (Nystrom, et al., 2009) will not be considered in the present work nor the energy dissipation in breaking the explosive casing. This would bring an almost intractable complexity to the simulations and experimental work has been performed with uncased explosives.

In a HE explosion the peak pressure will suffer a quick decay with time, which is affected by ambient temperature, humidity and wind. In an overdriven explosive peak pressure will be lower but the duration of the overpressure period will be longer and will reach a longer distance, resulting into a higher impulse. This will increase the lethal radius and the damage imparted by the explosion blast wave, because it has been observed that the intensity of damage increases with impulse. The peak pressure of a TBX is lower than that of a typical HE but typical duration will be about 200 milliseconds, which is about 200 times larger than the duration for a conventional HE blast. It is common to ear these types of explosives being designated as thermobaric.

There are a number of formulations under study for thermobaric explosives such as mixtures of HMX/aluminium/HTPB(PBXIH-135) which are used in BLU 118-B bombs (Meyer, et al., 2007). Other published formulations are the PAX series, PAX29, PAX30 and PAX 42 which use mixtures of explosive with about 15% of finely graded aluminium powder (Baker, et al., 2010).

Although there is increasingly available information on these formulations, the use of aluminium based thermobaric explosive in numerical simulations is extremely difficult. Recently some tables with data for use in numerical analysis have been made available for PAX (HMX or RDX plus nano-particles of aluminium) (Baker, et al., 2010). To allow the numerical modelling of the combustion of these formulations a special equation of state (EOS) has been developed, the Jones-Wilkins-Lee-Baker (JWLB) (Baker, et al., 2010). Other studies, particularly Russian (Bosrisov, et al., 2009) or Indian (Vadhe, et al., 2008) give a detailed account of aluminized explosives but do not provide data that could be used in simulations. Due to the lack of experimental data and the fact that published data is scarce, validation is quite difficult and this type of explosives has not been considered in the present work, although there are a number of thermobaric ammunitions for portable rocket-propelled grenade launchers capable of being considered a probable threat in the context of the present work.

2.3 The thermomechanics of explosions

2.3.1 Introduction

HE are extremely energetic materials which combustion will be processed very quickly being extremely exothermal and releasing a high amount of energy and a large volume of gases. This sudden release of gases, together with an increase of temperature, will produce a strong increase of pressure that will propagate through the surrounding material at very high speed, outwards and radially from the point of detonation, under the form of a compressive shock wave. This wave is denominated detonation wave. The phenomena will be addressed in two phases. The first, where the explosive reacts, will be designated as the detonation phase. The second phase where the shock wave is travelling through the encircling air and no further chemical reaction is taking place, will be called the blast phase.

A number of simplifying assumptions has to be accepted in order to model the physics of a detonation (Zukas, et al., 1998):

1. The model consists of an uni-axial planar wave front;
2. The wave front is discontinuous and jump conditions applicable to simple non-reactive waves will hold;
3. The gaseous products behind the shock front are in chemical and thermodynamic equilibrium (the reaction is complete) and they expand as an inert flow;
4. The chemical reaction completes itself instantaneously and the reaction zone length is zero;
5. The detonation process is in steady state, that is, the wave velocity is constant and the reaction products remain in the same state regardless the position of the wave in distance and time;

The above assumptions are also known as the ZND model (a fluid-dynamical model after Zeldovitch, von Newmann and Doering). This ZND model is represented by Fig. 2.3.

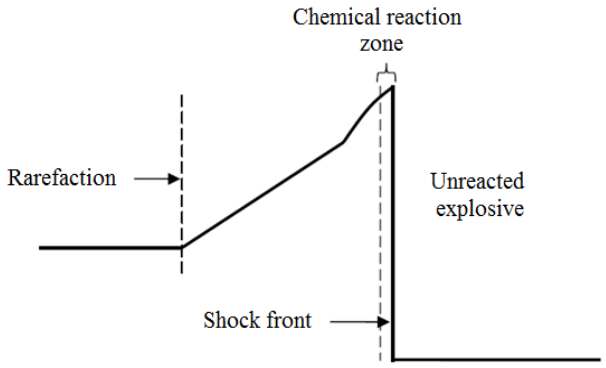

Figure 2. 3 – Physical model of a detonation wave (ZND assumption) (Sherkar, et al., 2010).

As the shock front resulting from a primary detonation moves through the explosive the resulting compression raises the temperature of the adjacent unburned material above the ignition point[3], igniting it and continuing the chemical reaction until all the material has reacted. This chemical reaction takes place within a small region just behind the shock front, known as the reaction zone and the released energy drives the wave forward. The speed of reaction is sufficiently fast such that the system does not looses significantly quantities of heat before the end of the combustion process and it may be assumed as adiabatic. The initial maximum pressures resulting from the hot gases generated by the detonation of a condensed HE will reach 100 to 300 kbar and the temperatures will be around 3000 to 4000 °C (Ngo, et al., 2007). At the same time the gaseous products from the reaction expand and form a rarefaction (or expansion wave) that moves towards the wave front. This wave front can be seen in the photography shown in Fig. 2.15, taken in a full scale test.

It is interesting to note that this detonation wave is supersonic which means that no sound precedes it. Two detonation waves travelling along the same explosive will only affect each other when they collide.

Once the HE has been burnt and the reaction is complete the product gases expand as an inert flow. The detonation wave will propagate to the surrounding mass of air that will suffer a very high pressure increase due to extreme temperature rise and violent expansion of the gases caused by the explosive reaction. This will travel through the mass of air as a shock wave, compressing and heating it and some relation giving the

[3] The ignition point is the minimum temperature at which a substance will spontaneously ignite at normal atmospheric conditions without an external ignition source.

hydrostatic pressure P, depending on density ρ and specific internal energy or, conversely, volume V and temperature T, is necessary. Such relation is an Equation of State (EOS). The kinetic gas theory provides us with a simple one, based on the adoption of the simplifying assumption that the mass of air will obey the ideal gas equation where P is pressure, V is volume, n is number of moles, R^* is the ideal gas constant and T is the temperature. Then

$$PV = nR^*T \tag{2.3}$$

or

$$PV = RT \tag{2.4}$$

in which R is the gas constant for air. From the definition of internal energy

$$T\mathrm{d}s = \mathrm{d}e + P\mathrm{d}V = c_v\mathrm{d}T + P\mathrm{d}V = 0 \tag{2.5}$$

and the definition of enthalpy

$$h = e + PV \tag{2.6}$$

where e is internal specific energy, h is enthalpy and s is entropy, and remembering that in the isentropic process $\mathrm{d}s = 0$, after deriving eq.(2.6) we get,

$$\begin{aligned} &\mathrm{d}h = \mathrm{d}e + P\mathrm{d}V + V\mathrm{dP} \\ &\therefore c_p\mathrm{d}T - V\mathrm{d}P = 0 \end{aligned} \tag{2.7}$$

and equating (2.5) and (2.7) through $\mathrm{d}T$ we obtain:

$$\frac{\mathrm{d}P}{P} = -\frac{c_p}{c_v}\frac{\mathrm{d}V}{V} \tag{2.8}$$

which after integration leads to $PV^{\gamma} = cte$ for an ideal gas. In the equation we make $\gamma = \frac{c_p}{c_v}$. Finally, from this result we arrive at the isentropic version of the ideal gas EOS : (We also need to recall that $R = C_p - C_v$ in the ideal gas law)

$$P = (\gamma - 1)\rho e = \rho(\gamma - 1)c_v T \tag{2.9}$$

This thermodynamic description of the air that encircles the explosive at the instant of detonation shows an obvious relation between pressure and temperature. A large temperature increment at constant volume will imply a large pressure increase.

A shock wave is then a high pressure state moving across a material. The impulse resulting from this shock wave on the surrounding structures will impart them deformations, stresses and, eventually, failure. The characterization of the pressure wave will depend on the chemical composition of the explosive, its mass, the stand-off distance (distance between the centre of the detonation and the target) and the geometry of the area along which the wave is propagating. That characterization is important to quantify the mechanical loading on the exposed structures. This mechanical loading is usually designated as blast loading.

The large release of energy that results from the detonation of a HE will propagate under the form of various shock waves. Normally we will mainly observe longitudinal pressure waves but there are also longitudinal rarefaction waves and some energy will dissipate through shear and surface waves. For large stand-off distances these waves will hit the target at different times and for sequential explosions interferences may occur between them. For close detonations it may be assumed that arrival times will be the same for all those shock waves and interferences may be neglected.

At this point it is important to note that we have two phenomena in the explosion mechanism: the chemical reaction and the propagation of the detonation, which being apparently independent, led many researchers to consider a separate study of (1) the chemical reaction zone where the detonation takes place and (2) the acceleration of the inert products of reaction or even of the fragments or debris.

One of the assumptions used is that the reaction zone is so thin that assuming the reaction as instantaneous will not affect the reaction performance. Thus after an

instantaneous reaction of the explosive at the detonation front the expansion of the reaction products can be calculated as it pushes the surrounding media (atmosphere, casing) outwards. This idealization will result in a small increase of pressure and temperature at the detonation front. Since the interest of the study of an explosion relies on this subsequent phenomenon of the expansion of the shock wave after the chemical reaction of the explosive this will be left behind and the thermomecanics of the detonation will be dealt with more detail. This simple way of treating detonation is sufficient to determine the equation of state of the explosive products and to calculate the subsequent flow and the explosive performance. This requires that the state (pressure and particle velocity) of the materials at the end of the reaction zone and their equation of state (which is a relation between the way pressure varies with the particle velocities of the gaseous products during their adiabatic of free expansion) are known. Since there is no way of measuring directly these quantities, the so denominated CJ (Chapman-Jouguet) theory is used, which is a simple fluid dynamic detonation model that will be detailed below. This theory gives us a generalization of shock wave theory that enables the fluid properties of the flow behind the detonation front to be determined knowing the shock wave velocity (High, 1982).

The shock front is extremely thin and its width varies with shock velocity. For instance, for a Mach 2 wave the shock front in air has a thickness of 0.25 μm. Being so thin the shock wave may be approximated as a discontinuity where a jump in flow properties is observed. Pressure, density, velocity and temperature discontinuities are observed in the ambient air particles that are run by the wave. However, the states just before and after the passage of the wave can be described by the conservation laws for mass, momentum and energy, which are collectively known as the Rankine-Hugoniot relations. This is the approach known as the Chapman-Jouguet (C-J) theory.

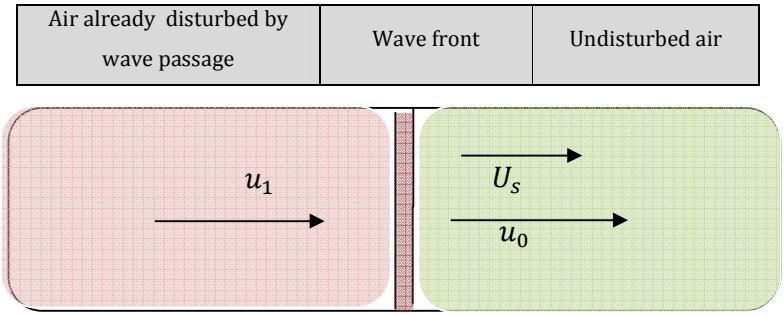

Figure 2. 4- Lab frame cartoon depiction of velocities inside a control volume, forward and after the wave front

In the C-J theory the jump conditions apply but because energy is totally released at the front, making the wave self-propagating, an additional condition is needed to determine the detonation wave velocity U_s. This condition, named after Chapman and Jouguet, the C-J condition, will be discussed below.

Let's consider a shock wave travelling from left to right at a speed U_s as shown in Fig. 2.4. A control volume is defined such that it moves with the wave front, at the same speed. The control volume will include a part of undisturbed flow, shown in green in Fig. 2.4, and another part, in brown, with the flow just after the passage of the wave front. The undisturbed particles of air not reached yet by the shock wave move at a speed u_0 to the right and the particles already disturbed by the passage of the wave are animated with a speed u_1, moving in the same direction of the shock wave. If an observer "stays" with the wave, then will notice the air coming through the wave front at a speed $w_1 = U_s - u_0$ and moving away to the rear of the wave at a speed $w_2 = U_s - u_1$.

The propagation of the shock wave and the characterization of the respective states 1 and 2 can be described with the help of the three main balances[4]. The equations for the mass conservation or equation of continuity, conservation of linear momentum (second Law of Newton) and conservation of energy (first Law of Thermodynamics) can be written as (Henderson, 2001):

$$\rho_1 w_1 = \rho_2 w_2$$

$$P_1 + \rho_1 w_1^2 = P_2 + \rho_2 w_2^2 \qquad (\mathrm{Nm^{-2}}) \qquad ((2.10)\text{a,b,c})$$

$$h_1 + \frac{w_1^2}{2} = h_2 + \frac{w_2^2}{2}$$

The entropies are $s_2 \geq s_1$ and the reaction gases will obey the equation of state (2.3). At the shock front a sudden change of the value of some state variables (temperature T, pressure P, density ρ and velocity w) occurs. This jump obeys certain relations that can be expressed in terms of the shock wave velocity w_1 and the ratio of densities ρ_2/ρ_1 as

[4] The main balances or fundamental laws are in fact four, but conservation of angular momentum will be omitted

$$P_2 = P_1 + \rho_1 w_1^2 \left(1 - \frac{\rho_2}{\rho_1} \frac{w_2^2}{w_1^2} \right) \tag{2.11}$$

However from eq. ((2.10)a) it results that,

$$P_2 = P_1 + \rho_1 w_1^2 \left(1 - \frac{\rho_1}{\rho_2} \right) \tag{2.12}$$

Applying the same method to the enthalpy equation gives

$$h_2 = h_1 + \frac{w_1^2}{2} \left[1 - \left(\frac{\rho_1}{\rho_2} \right)^2 \right] \tag{2.13}$$

These are the jump conditions imposed by the conservation Laws. Usually they are transformed so that they can be expressed in terms of the *PV* thermodynamic coordinates. Then taking eq. (2.12) and replacing the density by the volume *v*, such that: $(\rho_i = {}^1/_{v_i})$, the resulting expression is

$$P_2 = P_1 - \rho_1^2 w_1^2 (v_2 - v_1) \tag{2.14}$$

and this is the equation of a straight line, known as the Rayleigh line:

$$\frac{P_2 - P_1}{v_2 - v_1} = \frac{\Delta P}{\Delta v} = -(w_1 \rho_1)^2 = -\left(\frac{w_1}{v_1} \right)^2 = -\left(\frac{w_2}{v_2} \right)^2 \tag{2.15}$$

If we use eq. (2.13) in (2.15) and noting that the relative density is the inverse of the volume, the energy conservation takes the following form:

$$h_2 - h_1 = \frac{1}{2} (P_2 - P_1)(v_2 + v_1) \tag{2.16}$$

This curve is called the Hugoniot or shock adiabat. It may be written in an alternative form in terms of internal energy. Thus knowing that

$$e_i = h_i - P_i v_i \tag{2.17}$$

the resulting Hugoniot energy equation is then

$$e_2 - e_1 = \frac{1}{2}(P_2 + P_1)(v_1 - v_2) \tag{2.18}$$

A typical Hugoniot curve can be seen in Fig. 2.5. In most cases the particle velocity in the undisturbed region u_0 may be considered zero, P_0 is the atmospheric pressure and may be disregarded when compared with the shock pressure P_1 and the mass and moment balances can be respectively expressed as,

$$\rho_0 (U_s) = \rho_1 (U_s - u_1) \tag{2.19}$$

$$P_1 = \rho_0 U u_1 \tag{2.20}$$

Since there are five unknowns left and only three equations are available, another relations will be necessary. One such relation would be an equation of state but a general one, valid for all materials, does not exist. However, from the equation of state $Pv = RT$, we may combine it with the energy jump equation and eliminate the energy *e,* to obtain a relation of the type $P = f(v)$, the Hugoniot curve. It is also possible to use the mass and momentum jump equations instead, to obtain an alternative Hugoniot where any pair of the four variables could be related in a way that could describe all states of the material. Out the possible six pairs, the most used are the *U-u*, the *P-v* and the *P-u* Hugoniots. Combining the U-u Hugoniot with the two mentioned balances an expression of the type $P = f(v)$ is obtained by eliminating the particle and shock velocities. This is the Hugoniot *P-v* which is represented by Fig. 2.5. It shows the locus of all possible material states behind the shock front but it does not represent a path of equilibrium states. Such a path is represented by the isentrope for the shock relief wave but for

engineering purposes this isentrope can be replaced by the Hugoniot. Since the Hugoniot is a locus of possible material states behind the shock front, plotting the initial and the final status will define a line, named the Rayleigh line, which represents the jump condition. This line is shown in Fig. 2.6.

Eliminating the particle velocity u, and after some manipulation of the mass and momentum balances, the Rayleigh line can be expressed in the form

$$\frac{P_1 - P_0}{v_1 - v_0} = -\frac{U^2}{v_0^2} = -U^2\rho_0^2 \tag{2.21}$$

This result is the slope of the Rayleigh line. If two out of the three following quantities, the initial shock state, the final shock state or the shock velocity are known, the third one can then be found. This equation, which introduces a constraint between the three quantities referred above, allows the fifth variable to be set, as explained below.

For an equilibrium (or frozen) composition in a non-exothermic mixture like air, the Hugoniot curve passes through the initial state. In an exothermic mixture the chemical energy release displaces the Hugoniot curve from the initial state. To determine the state of the gas and to solve the jump conditions it is important to know the chemical composition of the gas and two cases are normally considered: (i) a frozen composition that corresponds to a non-reactive shock wave and an (ii) equilibrium composition that is associated to a complete reaction to an equilibrium state. We will consider frozen compositions as it will be assumed that the shock wave is the result of the expansion of the products of the explosive reaction, i.e, the thickness of the reaction zone will be neglected as explained above, and consequently the composition will not change across the shock.

It is possible to represent both the Rayleigh line for a particular shock velocity and initial density ρ_1 and the Hugoniot curve for a particular material in the same graph. The intersection of the two lines on a P-v plot gives the jump conditions solution at the shock front for a given wave propagation velocity i.e, the state of the material behind the wave front. Fig. 2.6 shows the Rayleigh line of an explosive material intersecting its

Hugoniot in two points so that the final state for the shocked explosive is not uniquely determined by the jump conditions and the equation of state.

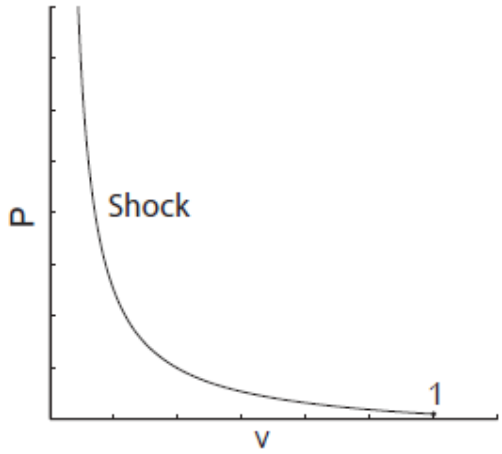

Figure 2. 5 – Hugoniot for a shock wave propagating in a non-exothermic mixture (Browne, et al., 2004).

This ambiguity has been removed by the C-J condition which assumes that an unsupported detonation proceeds at the minimum detonation velocity, which is an unique velocity given by the Rayleigh line tangent to the Hugoniot curve, as is detailed below.

The Rayleigh line passes through initial and final states 1 and 2 and has always a negative slope. The entropy S of state 2 must be greater or equal than the entropy of state 1, then it can be assumed that $S\ (P,\ v,\ Y)$ = constant, where Y is the chemical composition of the gas . The slope of the isentrope can be interpreted in terms of sound speed, as

$$\frac{\partial P}{\partial v}_{S} = -\left(\frac{a}{v}\right)^2 \tag{2.22}$$

Different isentropes can be drawn where it will be admitted that the compositions of upstream and downstream states will be the same .

$$P = P\left(v, S\right)\Big|_{Y} \tag{2.23}$$

Fig. 2.6 and 2.7 show that entropy will increase from the upstream to downstream conditions. Isentrope, s_1, passes through state 1 and isentrope, s_4, passes through state 2 and as can be seen, as $s_4 > s_1$ the entropy increases along the Hugoniot.

A few other interesting conclusions can be drawn from Figs. 2.6 and 2.7. At the upstream state the slope of the Rayleigh line is steeper than the slope of the isentrope and

$$\left.\frac{\partial P}{\partial v}\right|_{s,\gamma} = \frac{\Delta P}{\Delta v} \tag{2.24}$$

From eq. (2.15) and (2.22) comes that $w_1 > a_1$, and the flow upstream of the shock wave is supersonic. At state 2 we have the opposite. The steepness of the Rayleigh line is smaller than that of the isentrope and the flow downstream the shock wave is subsonic (obviously assuming a reference frame where the wave front is fixed). It is also observed that the isentrope and the Hugoniot have the same slope at state 1. This is valid for weak shock waves showing that they are close to acoustic waves.

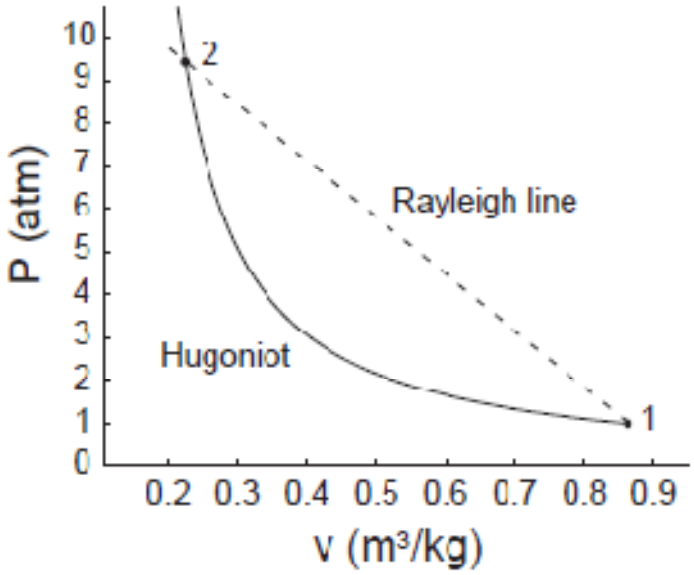

Figure 2.6– The Rayleigh line and Hugoniot for air with initial conditions 1 atm and 300 K considering frozen composition and a shock wave speed of 1000 ms-1 (Browne, et al., 2004)

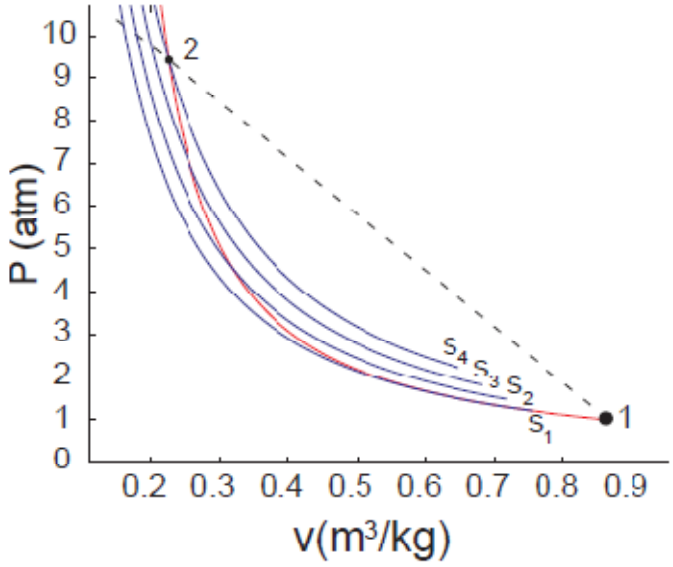

Figure 2. 7– Frozen isentropes, Hugoniot and Rayleigh line for a 1000 m/s shock wave in air (Browne, et al., 2004)

2.3.2 The physics of detonations

As a simplifying assumption let us consider a one dimensional process of pressure and temperature increase in the explosive as it is burned. Three zones can be observed in the explosive (Fig. 2.8). One that corresponds to the material already burned, another where part of the reactant has not yet been consumed by the reaction and a third one will constitute a transition plane between the other two, corresponding to the wave front.

The chemical reaction will occur at this transition zone. It is often seen that to derive the main equations of equilibrium a different approach is normally used: the reaction zone is assumed fixed in space and material will flow from right to left. Whatever the reference frame the underlying physics are the same. The unburned material will flow through the transition zone changing from a stationary state to a turbulent, high pressure and unstable state of gaseous combustion products. At the

reaction front a pronounced peak in the pressure curve will be generally present: the Von Newman spike, which is the shock state that initiates the reaction. After this peak pressure will drop sharply behind it until it reaches a point designated by Chapman-Jouguet (C-J) plane at the rear of the transition or reaction zone. The C-J point represents the state of the detonation products at the end of the transition zone, (Krauthammer, 2008). This state of pressure, density and shock wave velocity is characteristic of the explosive material. Fig. 2.8 illustrates these concepts.

The pressure then decreases gradually past the C-J point, as the shock wave moves away in a rarefaction wave from this state to the fully expanded state at ambient pressure. This rarefaction wave is called the Taylor wave. The Von Newman spike is normally ignored and the thickness of the reaction zone is assumed to be zero in numerical models. In most explosives the width of this reaction zone is around 1 mm.

The shock wave, the rarefaction wave and the reaction zone are all in equilibrium, moving at constant velocity, called the detonation speed. For military ordnance this speed varies between 6700 and 8840 ms^{-1}.

Both the condensed explosive material and the reaction gases have their own Hugoniot curve, which can be derived from the balance of energy and due to very high speed of the reaction it may be assumed that the transition from the first to the second happens instantaneously (See Figs. 2.10 and 2-11).

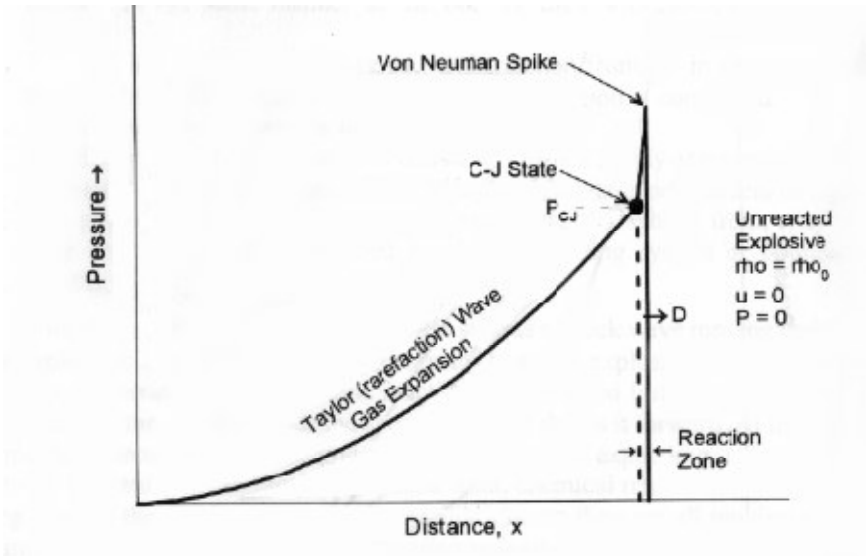

Figure 2. 8 - Relation between pressure and distance travelled by wave (Sherkar, et al., 2010).

The two states of the Hugoniot of the solid explosive presented in Fig. 2.9 show the two limiting states in which the material may be found: the initial state and the total shocked state. The Rayleigh line of the explosive is tangent to the Hugoniot of the reaction products. This point is the Chapman-Jouguet state (CJ). Fig. 2.10 will help to understand the concept behind the CJ point. The slopes of the various Rayleigh lines correspond to different flow velocities, as given by eq. (2.15). Below a minimum wave speed $w_1 < U_{CJ}$ the Hugoniot and the Rayleigh line do not intersect and there are no stable solutions. When $w_1 > U_{CJ}$ the lines intersect in two points, the strong, (S), and the weak, (W), solutions. Then a unique solution exists when $w_1 = U_{CJ}$, where U_{CJ} is the detonation velocity, i.e, *the minimum wave speed for which there exists a solution to the jump conditions from reactants to equilibrium products travelling at supersonic velocity* (Browne, et al., 2004), and it is the only point allowing the existence of an unique state for reaction products (Biss, 2009).

Differentiating eq. (2.18) it can be shown that at the CJ point the entropy has an extreme which implies that the isentrope passing through the CJ point must be tangent to both the Hugoniot and the Rayleigh line.

In practice the CJ model gives accurate results for the detonation velocity under ideal conditions of initiation but do not translate so well the actual thermodynamic state at the CJ point. The tangency conditions mean that the thermodynamic state is very sensitive to small variations in wave speed and detonations in air are unstable.

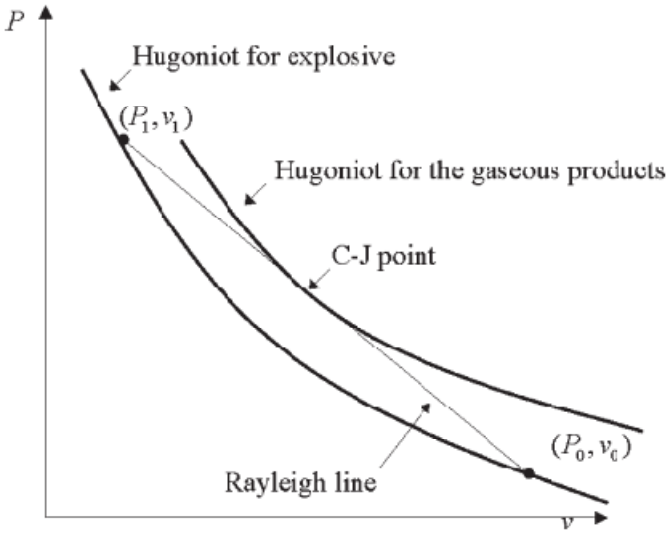

Figure 2. 9- Hugoniot of the solid explosive and of the gases from combustion and the Rayleigh line (Alia, et al., 2006).

In a stationary process the combustion gases are assumed to be produced at an infinite reaction rate to ensure chemical equilibrium. The wave front propagates through the non reacted explosive, compressing particles from the initial state 1 to the final shocked state 2, which corresponds to the von Newmann spike (Fig. 2.8). After the detonation the reaction products will reach vey high temperatures and pressures and will expand, generating a shock wave, that from now on, will be designated by blast wave, and the material will assume the CJ condition. Fig. 2.10 shows the three states of the explosive. The von Newmann spike may be neglected as its energy is small due to the very small duration. Combustion products will be considered as inviscid. The blast wave will move with the interface between the air and combustion gases.

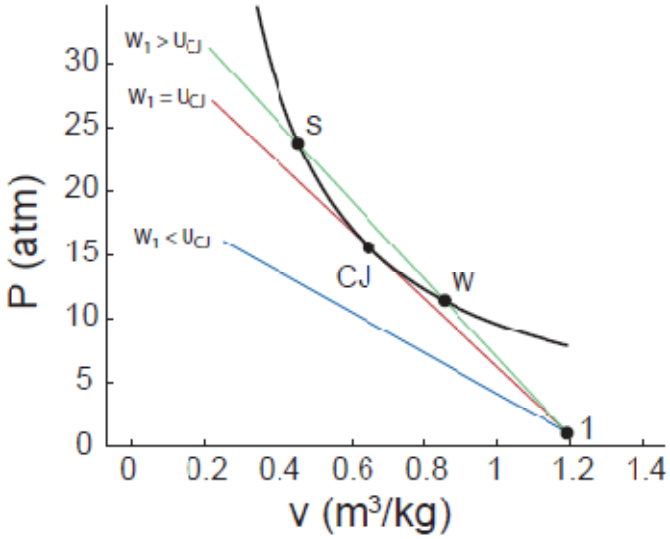

Figure 2.10– Hugoniot and three representative Rayleigh lines for different shock wave velocities, lower, higher and equal to the CJ state velocity (Browne, et al., 2004).

2.3.3 Reflected waves

Waves impinging rigid surfaces will be reflected and it is possible to determine gas properties resulting from the reflection of a blast wave at normal incidence. The jump conditions across both the incident and reflected wave will be applied to find the

corresponding Rayleigh and Hugoniot equations. From Fig. 2.11, we have the following relative velocities

$$w_2 = U_R + u_2$$
$$w_3 = U_R \qquad ((2.25)a,b)$$

Now substituting into the shock jump conditions we obtain:

$$(U_R + u_2)\rho_2 = U_R\rho_3$$
$$P_2 + \rho_2(U_R + u_2)^2 = P_3 + \rho_3 U_R^2 \qquad ((2.26)a,b)$$

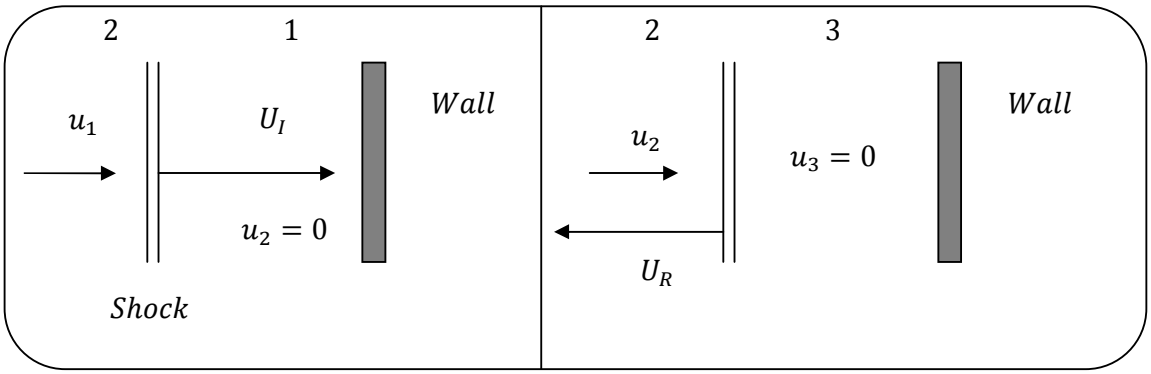

Figure 2. 11– Diagrams showing the incident blast wave before (a) and after (b) reflection with a wall

Combining these relationships we can obtain the pressure behind the reflected shock, that is:

$$P_3 = P_2 + \frac{\rho_3 u_2^2}{\frac{\rho_3}{\rho_2} - 1} \qquad (2.27)$$

Using the perfect gas Hugoniot relations for both the incident and the reflected waves the volume (or densitiy) jumps can be eliminated and the following expression for the pressure ratio across the incident and reflected waves can be found:

$$\frac{P_3}{P_2} = \frac{(3\gamma - 1)\frac{P_2}{P_1} - (\gamma - 1)}{(\gamma - 1)\frac{P_2}{p_1} + (\gamma + 1)} \tag{2.28}$$

For large incident blast waves the ratio (2.28) tends to

$$\frac{P_3}{P_2} = \frac{(3\gamma - 1)}{(\gamma - 1)} \quad \text{as} \quad \frac{P_2}{P_1} \to \infty \tag{2.29}$$

where γ is the ratio of specific heats. This theoretical prediction shows that for air ($\gamma = 1.4$), the ratio of reflected and incident pressures will be around 8. This shows that reflected shock waves may be a significant component of the overall loading, particularly in confined spaces.

2.4 Scaling and other effects

Many authors have been attempting to develop empirical relations to describe the blast pressure, duration and intensity of the impulse and the time interval between detonation and blast wave arrival. There are other variables of interest but these are the most important for the structural engineer facing the problem of designing or assessing blast resistance of buildings, shelters or vehicles. Obviously these parameters depend on the weight and composition of explosive, stand-off distance, environmental conditions (wind, atmospheric pressure, density of air, humidity and geometry of both the explosive, the target and of eventual obstacles in the path of the wave blast and a few others).

Perhaps the most important is pressure and it may be characterized by a peak value and a decay curve which is function of the distance to the detonation point. The energetic characteristics of the explosive will also influence the temperature rise of the reaction products and some kind of reference value has been established to allow comparisons between different explosive formulations. As the character of blast waves from condensed high explosive is nearly similar to those of TNT, all explosives may be characterized by their TNT equivalent (defined as the *free air equivalent mass of an*

explosive), i.e., the mass of TNT necessary to produce a shock parameter of the same value of that obtained with a mass unit of the considered explosive (Krauthammer, 2008). Basically, the energy released in the detonation of an explosive is compared with the energy that would be obtained with the detonation of the same mass of TNT. The detonation of one gram of TNT releases about 4680 J of energy but to account for errors it is generally accepted for comparison purposes the equivalence of 10^6 kcal for 1 ton of TNT, which agrees with average experimental values.

There are two approaches to determine the TNT equivalent. A widely used method is the Chapman – Jouguet theory, described above, where the equivalent TNT mass can be obtained as the ratio of the Chapman –Jouguet supersonic detonation wave velocities of the considered explosive and TNT:

$$M_{TNT} = MD^2/D_{TNT}^2 \tag{2.30}$$

where M_{TNT} and M are the equivalent mass for TNT and the explosive charge, respectively. D and D_{TNT} are the detonation velocities for the explosive charge and for TNT , respectively ($D_{TNT} = 0.693$ cmμs^{-1}).

Alternatively the heat of reaction per unit of mass, Q (kJkg^{-1}) of both explosives can be compared:

$$M_{TNT} = MQ/Q_{TNT} \tag{2.31}$$

This ratio gives the equivalent mass of TNT. For instance the equivalent weight for nitroglycerine is obtained by dividing 6700 kJkg^{-1} by 4520 kJkg^{-1} for TNT, giving 1.48. This means that, based on the heat of reaction, 1 kg of nitroglycerine is equivalent to 1,48 kg of TNT (Krauthammer, 2008).

To consider different stand-off distances a scaling factor must be used, usually based on the cubic root of the mass of explosive (Hopkinson-Cranz scaling law). Using this factor it is possible to obtain all parameters (overpressure, dynamic pressure, particle velocities, etc.) associated to a given stand-off distance and explosive mass, by means of the scaling factor, from known values of those parameters for a given distance or explosive mass. With scaling laws it is possible to transfer the results of a specific explosive test, in terms of blast wave properties, into another test with different

conditions. These laws are based on geometrical similarities and they have the same principles of any other kind of scaling law. The scaled distance is usually defined with the parameter *Z:*

$$Z = R/W^{1/3} \tag{2.32}$$

where, *R,* is the distance (in m) from the centre of the explosive source (Stand-off distance) and, *W,* is the total mass (in kg) of a standard explosive, such as TNT, that can represent the explosive energy. This scaling law was thoroughly verified by many experiments conducted over a large range of explosive charge energies. Limited reflected impulse measurements showed that it may become inapplicable for close-in detonations, e.g. $Z < 0.16$. Generally, the equivalent weight factors found by comparing blast data from different high explosives vary slightly with scaled distance. Using this scaling factor *Z*, with *W* being the unknown explosive TNT equivalent, the expression is,

$$\frac{Z}{Z_1} = \left(\frac{W}{W_1}\right)^{\frac{1}{3}} \tag{2.33}$$

Stand-off distance is scaled with eq. (2.33). A few manuals exist with abacuses based on this idea of equivalent distance (DoD, 2008). Impulse and time of arrival are scaled in the same way, that is

$$i_1 = \frac{i}{W^{\frac{1}{3}}} \quad , \quad t_{a1} = \frac{t_a}{W^{\frac{1}{3}}} \tag{(2.34)a,b}$$

These scaling rules assume that the shape of the charge is the same, that the ambient conditions at the time of the explosion are identical and that the released energy propagates as a spherical expanding shock wave. This assumes that the explosion occurs at a point. For a linear explosive the propagating wave would take a cylindrical shape and the flow will be described by square root rather than cubic root laws. The idea of a scaling law for explosions is illustrated in Fig. 2.12 where it can be

seen how affecting the mass of explosive by a factor λ will alter the overpressure and the length of the loading curve as shown.

If a spherical charge with diameter, *d*, is placed at a distance, Z_1, from a target then the mass of explosive necessary to produce the same overpressure at a location distant from the charge by Z_2 will be obtained by using eq. (2.33).

The scaling law is also very important to define a distinction between a near field from a far field explosion. This is important because some variables will be important in the near field and increasingly negligible with distance. The charge shape and the position of the ignition point inside the explosive are known to affect the overpressure distribution in the near field. For far field explosions the pressure wave tends to be more uniform.

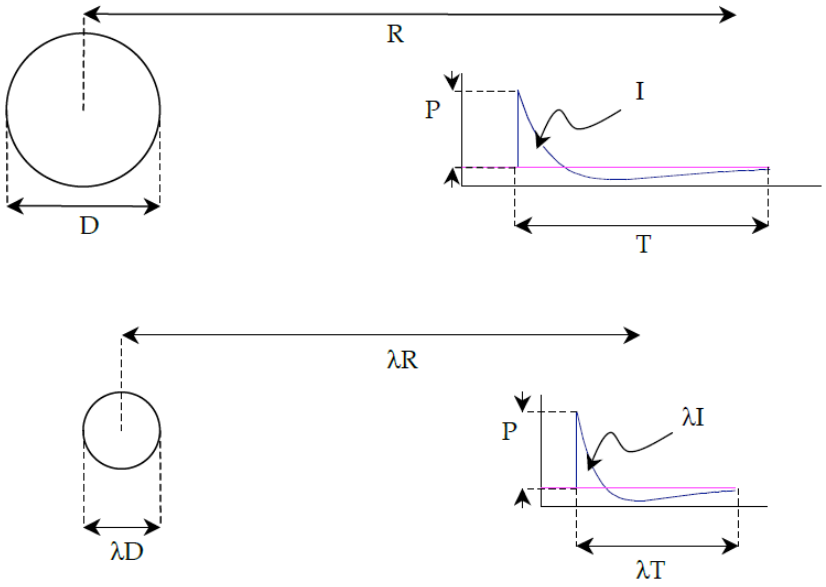

Figure 2. 12– Effect of the scaled stand-off distance on pressure curve

2.5 Modelling detonation, empirical approach

In the past decades many investigators developed methods for engineering predictions of blast loading effects. Early work presents a number of empirical and

semi-empirical approaches and as more complex computing tools became available numerical methods became predominant, together with experimental work since laboratory measuring, registering and analysing equipments are being continuously improved to a level of accuracy and sophistication unattainable shortly ago. State of the art modelling of explosions still uses empirical equations and data such as the Tri-Services manual UFC (DoD, 2008) manual which will be addressed bellow. Alternatively explicit modelling by using CFD or hydrodynamic codes have been used in the present thesis and will be covered in the next chapters.

Empirical methods derive from the analysis of experimental data. The approach is essentially mathematical and statistical and most of the results are limited by the experimental database and their range of validity cannot be extrapolated outside the data sample range. In general, the accuracy of all empirical equations decreases as the scaled distance diminishes.

Semi-empirical methods are based on some approximation of theoretical and analytical solutions attempting to describe the physical processes with simplified phenomenological models. They require an extensive data and their accuracy is generally better than that provided by empirical methods due to the physical foundations of these methods.

Numerical methods are based on mathematical equations that describe the basic laws of physics governing a problem, such as conservation of mass, momentum and energy laws, while the physical behaviour of either structural and fluid materials is described by constitutive relationships. To enable a solution, the domain under analysis is divided into finite sub-domains that allow the setting of systems of differential equations that solved together provides an approximate solution for problems of high complexity (those do not allow closed form solutions or where empirical solutions lack the required degree of accuracy).

Studies on blast effects date mainly from World War II and after. Many of the available theoretical studies from that time come from a small number of laboratories mostly working for governments and armed forces. Therefore it is plausible to admit that a number of reports are classified and not releasable to the open public and so no attempt has been made to present a review of the field but only to mention a few.

In early reports (Bethe, et al., 1947), the extension of damage caused by nuclear weapons was investigated together with some specific effects. A point source solution was used to model the blast wave problem. Most blast waves can be reasonably

modelled as spherical and the point source theory agrees with these assumptions. A point source solution and a spherical isothermal expansion were developed to initiate a numerical integration of the differential gas motion equations in Lagrangian form (Brode, 1955)(Brode, 1958). The experimental evidence confirmed this assumption by means of a series of experiments with cylindrical charges in free-air (Esparza, 1992). However, the orientation of the charge was found to produce non- spherical patterns of pressure distribution (Adamik, et al., 2004). The point–source theory gained many adepts (Chang, 1964) due to its relative simplicity and reasonable results. Blast wave incident pressure and impulse can vary significantly with the angle of incidence and this influence can also be found in early experimental work (Kingery, et al., 1983).

The theory of detonation process for gamma law gas has been established by a number of authors but discrepancies with experimental work remained. Attempts to improve the models led to the consideration of the burning of the condensed explosive. Many tools were published like, for instance the Landau-Stanyukovitch equation of state used by Lutzky to calculate the flow field in the reaction products behind the CJ zone (Lutzky, 1965).

The safety or resistance of structures has always been a concern and the pressure increase in blast reflections challenged many researchers. An extensive investigation on the effect of blast loads on structures can be found in various works. Reviews of methods for predicting blast effects on structures are also available in the literature(Rose, 2001) (Peng, 2009) (Remennikov, 2003)(Ngo, et al., 2007).

The work of Kingery remains as an important reference in the parameterization of the effects of explosions with distance (Kingery, 1966), which was based on a considerable ensemble of experimental data. The data were presented in the form of tables and abacuses but they were later re-compiled and presented as polynomials (Swisdak, 1994). The work of Kingery (1966) was also re-compiled later (Kingery, et al., 1984)(Larcher, 2007)) and a set of abacuses were derived to present the parameters of the wave blast. The report contains data from explosive tests with charge weight ranging from 1 kg to over 400,000 kg. Graphic results were presented in the form of double logarithmic curves with the scaled distance, Z, as the independent variable. As this work was based on a very large database of measurements made on free air explosions, regression analysis was performed on the data and polynomial expressions of those curves were developed based on Kingery's work for implementation in numerical codes.

The resulting code, CONWEP (Conventional Weapons Code), developed for the U.S. Army is the result of that effort and is used to calculate the effect of conventional ammunition blast. These curves can also be found in TM5-855-1[5] (Army, 1986), but only in graphical form.

The diagrams or their numerical implementations are widely used and accepted by researchers as they rely on a very extensive and rich body of experimental data. For engineering calculations involving structures intended to survive exposure to explosive blast the use of such abacuses is common and one of the most comprehensive sources openly available is the manual jointly edited by the three services of U.S. Armed Forces (DoD, 2008) formerly known as TM5-1300. More simplified engineering calculations, using one degree of freedom, are also available (Nebuda, et al., 2005).

It is important to note that the effects of blast differ substantially depending on the detonation point being above or on the ground (Lu, et al., 2006). Computer codes include in their algorithms this different behaviour since between the two types of explosion the effect of ground reflection will be different. Often, an explosion on the ground is better modelled as an hemispherical burst.

2.6 Some empirical curves

Empirical expressions have a very important field of application in engineering calculations and design. They are well established and are a suitable complement to numerical analysis in early stages of design. It is useful to recall some of the most used sources in this field. A more comprehensive compilation of empirical formulae can be found elsewhere (Rose, 2001). Technical manuals and reports such as the TM 5-1300, now superseded by UFC-3-340-02 (DoD, 2008) are the most widely used manuals for designing protection structures against blast load. The design curves presented in these manuals give the blast wave parameters as a function of scaled distance, Z, for the three main types of unconfined explosion: free air burst, air burst and surface burst. A step-by-step procedure is described in the manual for determining blast wave parameters

[5] TM5-855-1 provides procedures for design and analysis of protective structures subjected to the effects of conventional weapons, such as air-blast loads. A methodology is also presented to calculate blast load on multi-stored buildings, but it was not possible to access it because it is protected against dissemination outside the U.S.A.

for a surface blast. They require the charge mass, *W*, as TNT equivalent, and the stand-off distance, *R*, from the charge to the surface of a structure. With this data and the calculated stand-off distance, *Z*; the blast wave parameters can be read from the manual for the corresponding scaled stand-off distance, *Z*.

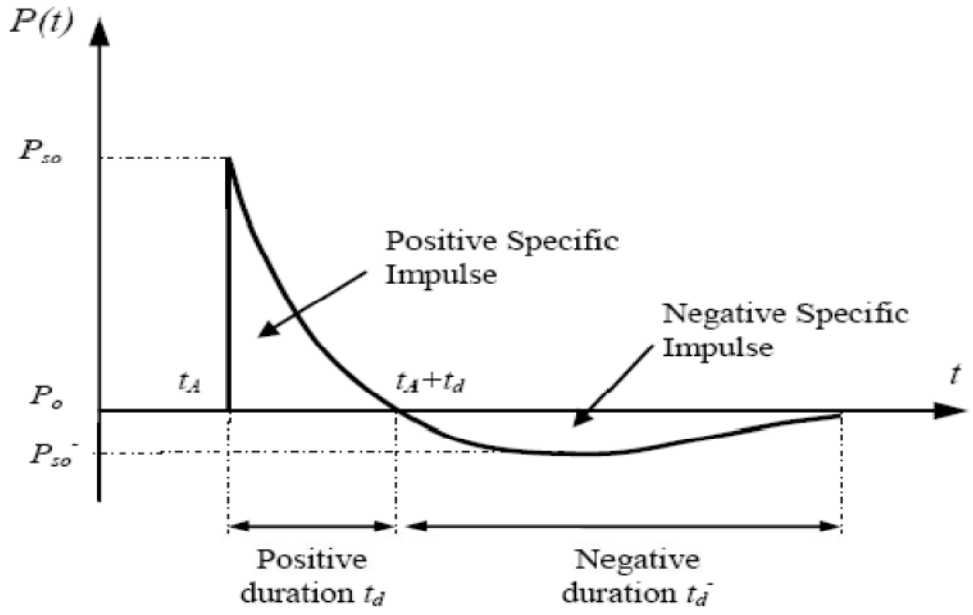

Figure 2. 13– Representation of the Friedlander equation (Adapted from (Krauthammer, 2008)).

One of the most cited empirical curves to describe wave blast pressure vs time (but apparently very seldom used) for the passage of a wave blast in an aerial explosion (AIREX) is called the Friedlander curve and is shown in Fig. 2.13. Although it is of little practical use it gives an insight on the underlying physics of the fluid structure interaction due to a wave blast. Actually CONWEP uses a Friedlander curve.

The wave blast arrives at the measuring point at instant, t_A, and pressure rises abruptly approximately following a vertical line. The incident pressure is applied on the surface facing the propagating wave. The velocity of the propagating wave front, U_s, diminishes with the travelled distance and with time but is, in general, superior to the sound velocity in the considered media (air, in this thesis). Gas particles downstream of the shock wave move at a speed lower than U_s, and are responsible for the wind that is generated by the passage of the blast wave.

As the shock wave moves away from the detonation point, the incident pressure decreases and the pulse duration increases. The instant of the arrival of the shock wave is the time of arrival t_A, and practically coincides with t_r, the instant in which pressure reaches its peak value. An exponential decay follows until $t_o = t_A + t_D$, when the pressure drops to atmospheric pressure and the negative phase is initiated, where pressure is below ambient pressure and the direction of blowing will reverse.

The impulse delivered to an imparted structure will be the area under the $P - t$ curve. During the positive phase the impulse is i_s. Partial vacuum occurring during the negative phase has in general a negligible destructive effect and is in many cases ignored.

The Friedlander equation is given by,

$$P_{inc} = P_s(1 - \tau)e^{-\alpha\tau} \tag{2.35}$$

were α is the decay parameter and the over-pressure P_s is given by:

$$P_s = P_{s0} - P_0 \tag{2.36}$$

The non-dimensional time, τ, is obtained in the following way:

$$\tau = \frac{t - t_a}{D_P} \tag{2.37}$$

where $D_P = t_d - t_a$. The negative phase is normally computed only when the stand-off distance is larger than ten times the charge radius. Larcher suggests a bilinear representation for the negative phase of Friedlander's curve, *r* (Larcher, 2007):

$$P = P_0 - \frac{2P_n}{t_{d^-}}(t - t_d) \qquad \text{for} \quad t > t_d \wedge t < t_d + \frac{t_{d^-}}{2}$$

$$P = P_0 - \frac{2P_n}{t_{d^-}}(t_d + t_{d^-} - t) \qquad \text{for} \quad t > t_d + \frac{t_{d^-}}{2} \wedge t < t_d + t_{d^-} \tag{(2.38)a,b}$$

where P_n is the pressure in the negative phase and t_{d^-} is its duration. The impulse of the loading, as mentioned above, is given by:

$$i_s = \int_{t_a}^{t_a+t_d} F(t)\mathrm{dt} \tag{2.39}$$

where *F(t)* is the load-time curve. If the impulse is divided by the area an equivalent expression can then be obtained and used, where *P(t)* is the overpressure as a function of time and I_s is the specific impulse, given by

$$I_s = \int_{t_a}^{t_a+t_d} P(t)\mathrm{dt} \tag{2.40}$$

When the blast wave hits a rigid surface normal to its movement, the fluid particles will immobilize abruptly and due to air compressibility a new blast wave is formed, moving in the opposite direction of the previous motion. The pressure resulting from the flow stagnation plus the incident pressure will have values 2 to 13 times higher than the incident pressure (see section 2.3.3). This will be the pressure effectively applied to the surface. Friedlander's equation can be applied to the reflected wave as long as an adequate decay parameter is introduced in the equation. When the incident direction is not perpendicular to the surface the following expression is used in numerical codes (Randers-Pehrson, et al., 1997).

$$P_{eff} = P_{inc}\left(1 + \cos\theta - 2\cos^2\theta\right) + P_r\left(\cos^2\theta\right) \tag{2.41}$$

which includes both incident and reflected contributions to the resulting effective pressure. (The subscripts inc and r stand for incident and reflected respectively). From section 2.3.3 the reflected pressure can also be given approximately by

$$P_r = 2P_s + \frac{(\gamma+1)P_S^2}{(\gamma-1)P_s + 2P_0\gamma} \tag{2.42}$$

If $\gamma = 1.4$ the reflected pressure becomes (Kingery, et al., 1983):

$$P_r = 2P_{S0}\left[\frac{7P_o + 4P_{S0}}{7P_o + P_{S0}}\right] \tag{2.43}$$

The reflected pressure, together with the incident pressure and the dynamic pressure (dynamic pressure is that resulting from the action of the blast wind, which is the flow behind the shock front, resulting from the velocity of the particles of air put in motion by the passage of the wave blast) can be seen in Fig. 2.14.

The dynamic pressure times a suitable drag coefficient is used to calculate the blast wind resulting forces on building openings and other obstacles in the path of a blast wave. In this way, two types of loading may be considered: (i) the pressure impact of the blast wave and (ii) the dynamic pressure resulting from the blast wind. Kinney proposed one expression for the overpressure, resulting from an air blast (Kinney, et al., 1985)

$$\frac{P_{S0}}{P_0} = \frac{808\left[1+\left(\frac{Z}{4.5}\right)^2\right]}{\sqrt{1+\left(\frac{Z}{0.048}\right)^2}\sqrt{1+\left(\frac{Z}{0.32}\right)^2}\sqrt{1+\left(\frac{Z}{1.35}\right)^2}} \tag{2.44}$$

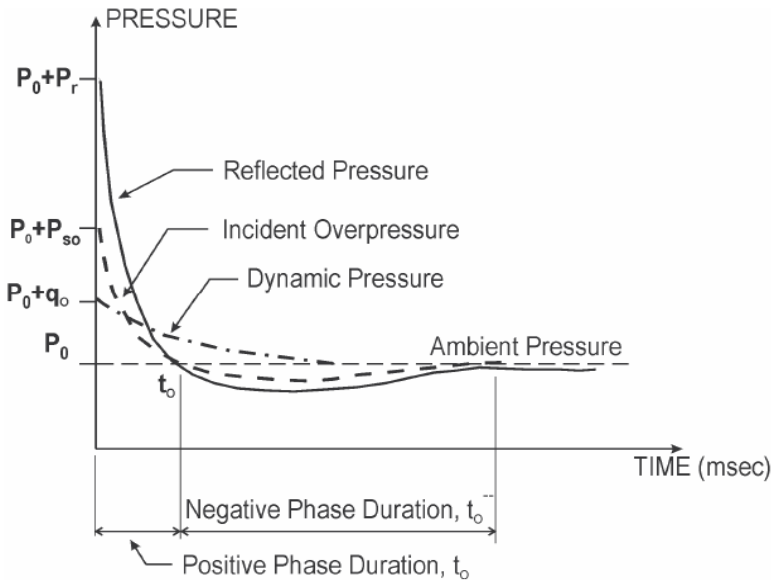

Figure 2.14 – Variation of overpressure, reflected pressure and dynamic pressure with time at a fixed location.

In the same work Kinney also presents one expression for impulse :

$$I = \frac{0.067\sqrt{1+\left(\frac{Z}{0.23}\right)^2}}{Z^3\sqrt{1+\left(\frac{Z}{1.55}\right)}} \quad \text{[Pa.s]} \qquad (2.45)$$

A rather comprehensive review on phenomenological formulae for the analysis of plates subjected to blast loading has been provided by Rajendran (Rajendran, et al., 2009). Because they have been used by the engineering community the equations of Henrych (Henrych, 1979) are shown below:

$$P_0 = \begin{cases} \frac{14.072}{Z} + \frac{5.540}{Z^2} + \frac{0.357}{Z^3} + \frac{0.00625}{Z^4} & 0.05 < Z < 0.3 \\ \frac{6.194}{Z} - \frac{0.326}{Z^2} + \frac{2.132}{Z^3} & 0.3 \le Z < 1 \\ \frac{0.662}{Z} + \frac{4.050}{Z^2} + \frac{3.288}{Z^3} & 1 \le Z < 10 \end{cases} \qquad (2.46)$$

where Z is the scaled distance given by eq. (2.32).

.

Figure 2.15- Detonation of 500 ton of high explosive charge in air (from Operation "Sailor Hat" Explosive tests (February – June 1965) www.history.navy.mil., October 2013. This interesting picture shows the wave front (indicated by the arrows) travelling away from the detonation point, faster than the reacted gases of combustion.

A rather interesting picture can be seen in Fig. 2.15 where a shock front caused by an explosion can actually be seen

2.7 The basic problem of a confined explosion

In a confined space the complexity of the analysis will increase. The early time-blast phenomena will be similar to a free air spherical or hemispherical burst but as soon as the internal surfaces are hit reflected shock waves will be formed from those surfaces. This initial phase, i.e. the shock phase, is very short and afterwards the blast environment will be very complex to describe (See Fig. 2.16). Reflected waves will propagate and interact with the other surfaces generating new reflected waves. The high pressure and temperature gases will expand throughout space in a more lengthy process. This is called the gas pressure phase where pressure will decay to ambient pressure as the gases cool down or leakages occurs (Krauthammer, 2008).

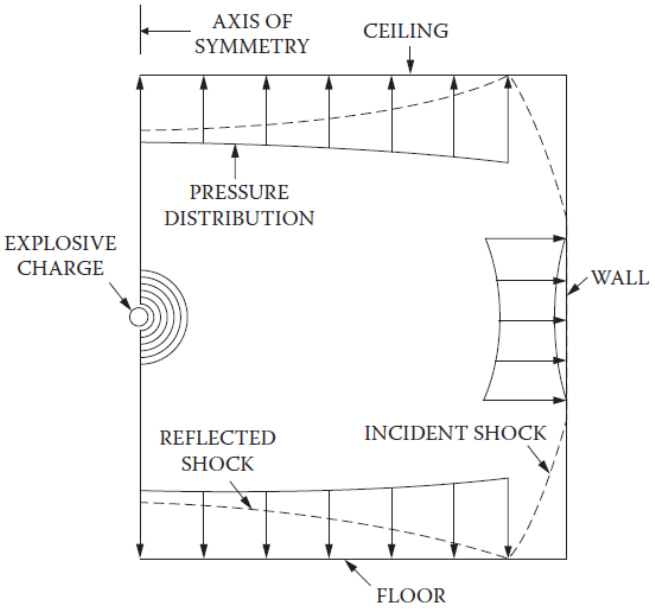

Figure 2. 16- Shock reflection from walls during internal detonation (Krauthammer, 2008).

An initial shock-pressure spike will be followed a series of many lower pressure reflections, forming the gas pressure phase where pressure decays to ambient pressure. The main parameter to be considered in such an analysis will be the equivalent TNT charge mass, the room volume, V_I, the vented area, A_i, the ambient pressure, P_a, and the

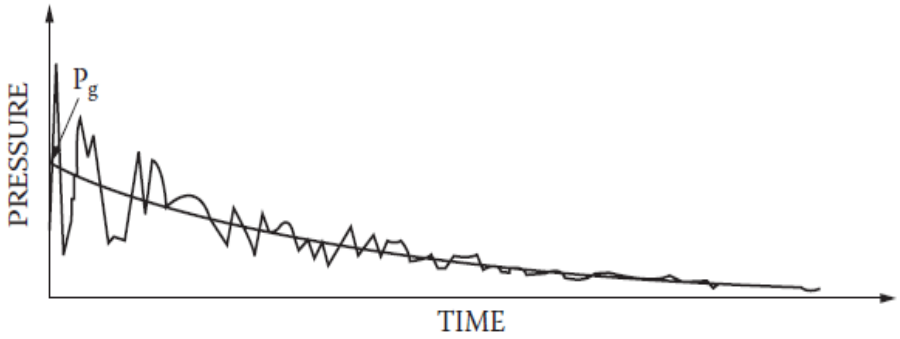

Figure 2. 17- Typical pressure-time history in a confined space blast (Krauthammer, 2008).

total exposed internal area A_w. This decay is represented by the curve shown in Fig. 2.17.

2.8 Confined explosions

The following empirical relation between overpressure , mass W (kg) and confined volume V (m^3), was suggested in 1945 at the Los Alamos Scientific Laboratory (Kinney, et al., 1979):

(2.47)

A refinement of the equation for adiabatic conditions and unvented spaces, but still simplifying the phenomenon, can be given by:

$$\Delta p = 10^{-5}(\gamma - 1)(H/V) \tag{2.48}$$

where H is the heat of combustion (J) and γ is the ideal gas ratio of heat capacities, usually 1.4 for air at room temperature. Both equations provide only rough approximations to real data and improvements were possible through consideration of thermodynamic equilibrium and conservation equations. Pressure and temperature were obtained from the change in energy and enthalpy that result from the reactions of the explosive constituents and the resulting products of combustion, applying the main balances of mass and energy and second law of thermodynamics. The compartment boundaries ensure adiabatic and rigid boundaries that avoid energy and mass dissipation (Strømsøe, 1978) (Kinney, et al., 1979) that could affect peak overpressure calculation.

Other early efforts on the subject were devoted to the analysis and design of suppressive structures in order to increase safety in ammunition or other sites exposed to explosion hazards. Reports on the subject are available giving a number of empirical equations meant to facilitate the design of safe suppressive structures (Baker, et al., 1975a) (Baker, et al., 1975b) (Kingery, et al., 1978). These reports consider empirical relations between overpressure and energy release or derive such relations from experimental data. Empirical formulae were also developed to design frangible covers (Keenan, et al., 1982) and to assess the peak pressure inside exit tunnels in underground ammunition storage facilities (Kingery, 1989). With these empirical formulae it was possible to derive peak pressures and the pressure decay curve for internal explosions as a function of the effective vented area. Numerical analysis and hydrocodes (Tancreto, et al., 1998) were later used to calibrate the empirical equations and new semi-empirical methods were developed that were also used in the tri-service manual (DoD, 2008). Compartment boundaries are assumed to be rigid in these calculations. More recent work (Ferrara, et al., 2006) considered CFD codes to derive the venting effect of relief pipes. The position of the ignition point relatively to the relief pipe was found to have a strong influence on the measured peak pressures inside the chamber. Proctor (1972) was one of the first published computer codes designed to

describe energetic reactions inside closed structures. In 1976, Ward and Lorenz of the Naval surface Weapons Centre introduced in the program the capability to use time-dependent burning of the energetic material (rather than detonation) and new codes were developed (e.g. INBLAST or BLASTINW in the early 1980's (Montanaro, et al., 1990)).

Other authors (Sewell, et al., 1968) proposed criteria for the assessment of the damage potential of an explosive based on a distributed energy concept. Traditionally, overpressure and impulse have been used as damage criteria but Sewell and Kinney (Sewell, et al., 1968) proposed another criterion based on a specified overpressure applied over a determined critical time, to overcome the limitations of both criteria. The critical time was decided to be one quarter of the natural period of oscillation of the structure under analysis and its critical impulse is calculated based on the dynamic yield strength and speed of sound, yield strength and elastic modulus or critical velocity. They also concluded that the effect of a lumped explosive is rather different than that of distributed charge weapons. Theoretically the subdivision of a charge in multiple segments is more effective than the use of a lumped charge but in this thesis only single charges are considered.

It was reported that peak overpressures resulting from explosions in confined spaces are lower than those resulting from free air explosions and the decay is also slower than for a free air burst. The final equilibrium pressure in non-vented spaces is expected to be higher than the initial ambient pressure but it can be lower if reaction products such as aluminium oxides are present as they diminish the mass of gas present in the compartment. Also, the slow pressure decay time increases the overpressure duration resulting in a higher impulse (Kinney, et al., 1979). Theoretically, this higher impulse would result in an increase of damage but the extended time decay may exceed some critical time for the structure and so an internal explosion may not be as effective as expected. These findings were, however, contradicted by recent observations (Geretto, et al., 2014).

No consideration on oxygen usage during the explosion will be made in this thesis as HE is considered to have the necessary oxidant to feed the combustion reaction. Therefore, overpressure depends mainly on the mass of explosive and less on the volume of oxygen available.

Chan (Chan, et al., 1994) used CFD to analyse the wave reflexions phenomena inside an enclosure. An Eulerian mesh has been used and results were compared with experimental results. Fig. 2.18 illustrates the results measured in one of the sensors placed inside the enclosure. The results showed that reflexions can continue for a significant amount of time and geometric symmetry in the enclosure can make multiple shock waves to converge with strength comparable to the initial shock wave. Similar studies used hydrocodes to model the wave blast reflexions inside a closed prismatic box (Hu, et al., 2011) . The overpressure distribution profiles along a section of the box showed an increase at the corners and in general variations of L/D ratios in a cubic chamber were found to have greater effects on reflected overpressure. The impact of cubic chamber volumes on peak reflected overpressure was also found to be significant. In a comparison with results from the UFC-3-340-02 manual (DoD, 2008) blast experiments in a closed chamber revealed results 27% lower (Edri, et al., 2011) and the pressures at the corners were lower than at the centre of the walls which was not expected. Sauvan and co-workers (Sauvan, et al., 2012) considered the influence of the walls of a progressively built almost closed volume around the explosive (the chamber had no ceiling). The individual effects of each wall were then computed in terms of overpressures and pressure history. The interactions and reflexions originated by the walls were recorded by pressure sensors at each wall and it was concluded that in semi-confined explosions the negative phase can be as destructive as the positive which does not agree with the vast majority of other reported results of blast wave experiment and modelling. Confined explosions in a blast chamber are often used to provide data on

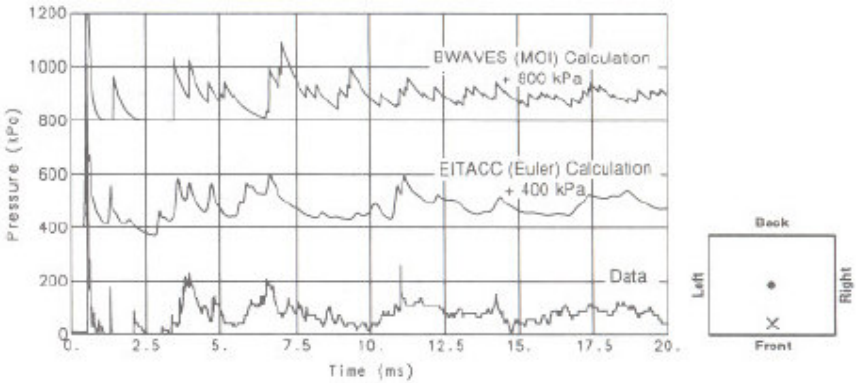

Figure 2. 18– Comparison of predictions with data from the front sensor (Chan, et al., 1994).

different explosive charge shapes. Wu et al. (Wu, et al., 2013) compared results of enclosed explosions within a blast chamber with the UFC-3-340-02 (DoD, 2008). The results obtained from the publication are under-predicted for horizontally oriented cylindrical charges. The effect of the charge shape in free-air explosions had been analized in a previous study by Wu and co-workers (Wu, et al., 2010).

Whenhui et al. (Whenhui, et al., 1997) stated that the coupling effect between the deformation response of a closed structure subjected to an internal blast loading can be assessed in three independent phases: (a) Determination of the blast loading acting on structural members assuming the compartment to be rigid; (b) evaluation of the stress and strain state of the structure and of the corresponding strength criteria, to obtain the limiting load or the maximum weight of the explosive (3) estimation of the fracture probability and the working limits. His work addressed the strain growth phenomena observed in explosive chambers (Duffey, et al., 2000) during loading experiments by using shell theory considering transverse shear and rotatory inertia. Auslender et al. (Auslender, et al., 2000) also presented work on thin spheres subjected to internal blast using a simplified approach that relies on the main hypothesis that inertia effects for radial stress are negligible. An analytical solution has been obtained in the elastic field and a quasi-analytical solution was derived for perfectly plastic or linear work-hardening behaviour. However, the method is limited to thin shells or pipes. Cylindrical vessels are often used as pressure vessels and their response to internal blast has also received attention (Chow, et al., 2000) but their practical interest resides more on the field of deflagrations due to the type of the contents they normally carry which constitutes another field of investigation dealing with explosion hazards in the oil or chemical industry and in any place where fuel vapours and gases can be accidentally ignited initiating a deflagration in a confined space. However there are investigations with HE explosions inside cylindrical vessels (Langdon, et al., 2014)(Ma, et al., 2013). There exist models for simple enclosure geometries but for complex shapes, models will have to be used (Pritchard, et al., 1996). Three types of models may be considered: empirical, phenomenological or numerical. Pritchard (1996) used a CFD model to simulate the deflagration process with reasonable results. Gas deflagrations can be very destructive and venting is often used to protect process material from being destroyed by the explosion. Empirical and semi-empirical methods can be used (Razus, et al.,

2001) (Tamanini, 2001) to design and evaluate vents as the correct area is crucial for its effectiveness. Sets of equations were proposed by Razus and Krause (2001) for mixtures of air and gas. Janovsky (Janovsky, et al., 2003) presented experimental results for the propagation of blast from methane-air explosions in a closed space, were a weaker structure element will be the first to fail with the pressure build-up initiating venting. This is a typical case were an explosion occurs inside a room or compartment with doors or windows which will not withstand the blast pressure and only a temporary confinement will occur.

A rather comprehensive study on venting has been presented by Molkov and co-workers, considering its occurrence by means of translational covers that will be pushed up by the blast pressure (Molkov, et al., 2003) or through rotation around hinges (Molkov, et al., 2004) or even spring-loaded translational covers (Molkov, et al., 2005). The problem of venting is very important as it has a significant effect on the peak pressure inside a closure but Molkov's works were devoted to the analysis of the vent behaviour (displacement transient) with the aim of designing effective vents for hazards prevention in facilities exposed to gaseous deflagrations. More recently experimental and analytical and numerical model were used to compare a closed chamber with a cover and with a free opening (Feldgun, et al., 2011). In both cases the pressure relief is similar but in the first instants the chamber works as a fully confined room before the overpressures drops to zero after a considerable distance has been travelled by the cover. More recently a few studies were published showing a growing interest in confined blast (Geretto, et al., 2014)(Dragos, et al., 2013). In the latter an equivalent idealized load has been derived from experimental pressure curves inside a closed space subjected to a confined explosion. The authors aimed to obtain a simplified load curve that could be incorporated into a structural response analysis tool such as a pressure-impulse (P-I) diagram. Geretto et al. subjected square mild steel plates to blast loadings to compare deflections when the plate is part of a confined, partially vented or fully vented structure. This last work is the one of the first to appear in the literature contemplating the response of plates subjected to confined blast loads.

Another family of investigations was performed on the propagation of blast waves around buildings in complex city geometries. This has some similarities with confined explosions due to me many reflexions and the channelling effects generated between the buildings (Remennikov, et al., 2005). In problems such as an explosion in

an urban area (e.g. at a crossroads in proximity to tall buildings), we may expect overpressure time histories that are similar to an explosion in a confined space with openings. Results showed that the blast effects in buildings can be both enhanced or attenuated by the presence of other buildings. An assumption of uncoupling between wave propagation and reflexion from the buildings was shown to have reasonable accuracy unless the façade has a large glazed area in which case the leakage would decreases the reflected pressures. The problem of blast wave propagation on complex geometries have also been addressed (Sklavounos, et al., 2004) with a CFD code (the CFX) to analyse the propagation of waves with obstacles on the terrain. The model considered three parallel obstacles perpendicular to the wave front. One of the interesting findings was the fact that structures surrounded by others will suffer more than one shock impact which may result in extensive damages. Hydrocodes are also being used to assess damage in other confined structures (He, et al., 2011) due to their ability to model blast in complex geometries. The consideration of barriers between the explosion and the buildings has been investigated as a way to mitigate blast risks. A barrier alters the wave blast pattern and decreases the reflected pressures and arrival times in buildings behind the blast barrier (Zhou, et al., 2008) and a fit of the numerical results was derived in order to obtain a reliable tool to predict the effect of blast barriers on the blast parameters on surfaces behind them.

Rigas and Sklavounos (Rigas, et al., 2005) used the same code to simulate the blast wave propagation inside an L-shaped circular tunnel. An important conclusion was that peak pressures are smaller in a branched tunnel than in a straight one. This study was applied to gas explosions. Gaseous products and dust constitute a potential source of hazard in the industry and an important number of studies are being published on deflagration of these products in confined spaces, attempting to understand the effects of vents, obstacles and the geometry of the chamber (Karnesky, et al., 2007)(Ferrara, et al., 2008)(Park, et al., 2008)(Park, et al., 2008). It was observed that the existence of ducts strongly enhance the vented explosion. The gas dynamic approach addresses variables that can be disregarded in HE detonation (such as turbulence or flame speed, for instance) but the conclusions go in the same direction. Karnesky and co-workers (2007) pointed up that the model gives good results for enclosures with aspect ratios of one.

The propagation of blast waves inside buildings is also under increasing interest due to the threat of terrorist groups planting bombs inside buildings. Needham (Needham, 2007) presented simplified method, based on the energy yield of the explosion, to calculate peak pressures inside rooms connected by doors or windows to the room where the explosion takes place. Benselama and co-workers (Benselama, et al., 2009) considered two three-dimensional simulations: a rigid and closed box configuration inside which an explosive charge detonates; the second performed case is the blast wave simulation inside a tunnel with bifurcation. It was found that in confined domains, the flow remains supersonic a long distance from the blast charge. The bifurcation lead to a reduction in the overpressure inside the main pipe while the overpressure inside the secondary pipe is weaker and the flow is transonic. As expected, the results for the closed chamber showed the increase in the peak pressure value and reflexions from the compartment walls.

Particular uses of blast wave analysis are also available in the literature like the calculation the overpressure distribution resulting from a blast propagating inside a tunnel (Liu, et al., 2008). A law to predict overpressure peak of a blast wave in a tunnel was derived using the Buckingham "Π" theorem and it was compared and successfully calibrated against the numerical data obtained. Silvestrini et al. (Silvestrini, et al., 2009) used the concept of an Energy Concentration Factor to predict blast-wave overpressures in partially confined geometries such as road tunnels.

More recently Zykowsky and co-workers (Zykowski, et al., 2004) simulated an explosion inside a closed rigid box, using AUTODYN, a commercial hydrocode, and compared it with experimental data. Overpressure curves were produced at selected positions of the internal surface of the box which allows parameter and mesh validation in finite element analysis. Price et al. (Price, et al., 2010) predicted the pressure-time history for specified locations within a canopy consisting of a roof deck suspended over a ceiling deck forming an attic space having using a three-dimensional shock wave physics code (CTH). The aim has been the consideration of a blast wave propagating to the interior of the attic through an opening to analyse the interior wave reflexions and propagation. They found that better results are obtained for compartments with height to width ratios close to unity.

2.9 Afterburn

The discussions above assumed that all the energy of the explosion is released upon detonation and used to drive the shock front forward. This may not be entirely valid for under-oxidized explosives as in these cases afterburn will act as an extra source of released energy. Afterburning involves a post-combustion reaction that will cause an increase of temperature that will enhance the effect of detonation. This phenomenon will stand for milliseconds contrarily to the detonation which only lasts for a few microseconds. As long as there is enough oxygen in the surrounding air and the temperature is high enough for the combustion, afterburn will take place.

Table 2.2 shows the combustion reactions and their related heats of reaction for the constituents of TNT. This explosive is heavily deficient in oxygen (about -73.9%) (Salzano, et al., 2012). Its explosion quickly reaches a high pressure resulting in a very directional shock wave but with a relatively low impulse. If conditions for an afterburning are present this secondary reaction will not increase the primary overpressure but will affect the total impulse. The main important conclusion is that if conditions exist that allow the reaction of all the explosive the released afterburn energy (10.01 MJ/kg) is more than twice the detonation energy of 4.52 MJ/kg of TNT (Sherkar, et al., 2010). This has been the value obtained with CHEETAH a thermo-equilibrium code (Fried, et al., 1998) (which release outside the USA is restricted) but slightly different values are also available from other sources (Ornellas, 1982) (Cooper, 1996). As long as there exists oxygen, and a temperature high enough to allow the reaction to occur and a good mixing between air and the gaseous products of reaction, these will burn. Table 2.2 also shows the temperatures necessary for the combustion of each of the main products of the reaction of TNT.

Table 2. 2 – Combustion reactions occurring during afterburning (Sherkar, et al., 2010)

Oxidation reaction	Ignition temp. (°K)	Moles of fuel/moles of TNT	Heat of reaction ΔH_r (kJ/mole of the constituent)	Afterburn energy ΔH_{ab} (kJ/mol-TNT)
$CO + 0.5CO_2 \longmapsto CO_2$	880	2.233	282.80	631.49
$H_2 + 0.5O_2 \longmapsto H_2O$	850	0.3516	241.80	85.02

$C + O_2 \longmapsto CO_2$	975	3.410	393.60	1342.18
$CH_4 + 2O_2 \longmapsto CO_2 + 2H_2O$	850	0-2656	800.00	212.48
Total energy of afterburning combustion				2271.17 kJ/mol-TNT =10.01MJ/kg-TNT

In a free air explosion the reaction products will rapidly cool down behind the shock wave as its effects dissipate and afterburn is not usually taken into account. The same does not happen in a confined explosion, where the wave bouncing in the inner walls of the confinement will promote a good mixing between air and reaction products and will increase their temperature so that their combustion can take place.

Earlier work (Esparza, et al., 1975) (Proctor, et al., 1972) (Strømsøe, 1978) (Kinney, et al., 1979) studied the effect of the ratio between the mass of explosive and the volume of the compartment in confined detonations having concluded that the increase in this ratio leads to an increase in the peak pressure. However it will be shown in Chapter 5 of the present thesis that peak pressures vary considerably with the shape of the compartment, considering a constant volume, and with the positions of both of the detonation point and the point where pressure is measured. Other conclusions presented by these authors refer to an increased residual pressure in the confinement. This residual pressure is directly affected by the afterburning as this will result in more reaction products being generated which will add to the internal residual pressure after the reactions took place.

For decades most simulations did not account for the phenomenon since it is very difficult to perform analytically as it involves chemical reactions and time-dependent release of energy and is difficult to validate. More recently some work is being published where afterburning has been addressed. A brief review can be found in the report by Sherkar and co-workers (Sherkar, et al., 2010). It is expected that more attention will be given to the phenomena as some commercial hydrocodes such as AUTODYN include some means to simulate afterburning and it has been announced that LS-DYNA (Schwer, 2016) will also include that feature in a next release. For the difficulties in the access to simulation tools, afterburning studies have generally been ignored or restricted to a limited number of laboratories.

To include the energy released during the afterburning it is necessary to know the amount of energy released, the time period over which the phenomenon takes place and the rate of energy release over that time period. The heat of reaction can be derived from the molar mass of explosive and available oxygen knowing the heat of reaction of each of the constituents available to react. These can be checked in Table 2.2 above for TNT. The approximate time the afterburning starts can be assumed when a shock wave reflects from a wall and interacts with the unburned reaction products. This reflected wave will cause sufficient mixing of external oxygen with the available reactants. The afterburning ceases when the temperature drops below that needed to sustain the combustion. The rate of release can range from simple to very complex thermodynamic models. A simple engineering model may consists of an afterburn energy Q added to the energy term E of the equation as it will be explained later, in Chapter 4.

This brief review shows the added complexity of a confined explosion, which involves reflexion and interaction of blast waves and possibly the need to consider the effect of afterburning. The published information on internal blast simulation is still scarce although some parametric analysis have been made available (Hu, et al., 2011). There are not many experimental results available and validation is generally attempted by using third party published results.

Chapter 2

3. The effect of blast on structures

The response of structural materials to the impact of a blast wave is discussed. A review is presented of published work on material constitutive models with emphasis on material response under high pressure and high strain rate loading. Previous work on blast loading of rectangular plates is also discussed, particularly that involving AA5083 aluminium alloy.

3.1 Introduction

In Chapter 2 the subject of aerial explosions has been described but the effect of the resulting wave blast was not considered. The concept of TNT equivalence together with stand-off distance makes it possible for the engineer to predict the response of conventional structures to the blast originated by a number of explosives (DoD, 2008) (Remennikov, 2003). However, for the less conventional materials or geometries, Finite Element Analysis (FEA) is by far the most cost effective method of analysis as experiments may become very expensive (Zukas, 2004) and out of reach of the design engineer. The response of a structure to a blast load is related to both its natural period and to the duration of the loading. Normally this duration is small when compared with the time response of the system. The load will dissipate well before the structure undergoes a significant deformation (the exact opposite occurs for quasi-static loading). The load is often defined as a combination of peak overpressure and the impulse delivered to the exposed area of the structure (Needham, 2010). In fact, overpressure itself may not be the major factor determining the amount of damage suffered by the impacted structure. Impulse may be the dominant factor as a lower

pressure applied for a longer time may be more destructive than a very short though intense pressure burst. This is another aspect difficult to characterize analytically and is directly related to the constitutive behaviour of materials under high strain rates, due to the change in its strength properties. The intense research of this topic produced many constitutive models suggesting that new researchers would need to address and compare many of them. It has then been considered advisable to review the better known and most used models and to look at how they have been used by the scientific and engineering community. Thus, this chapter has been divided in two parts: a review on constitutive models for visco-plastic behaviour[6] and the other is a state-of-the-art survey on experimental, theoretical and numerical analysis on plates, particularly of aluminium, subject to blast loadings with emphasis on failure prediction.

The review only considers models that address high strain rate response regimes, as quasi-static constitutive behaviour is less relevant for blast loading problems. It also divides the available constitutive models in two major groups: physically based and phenomenological. This has reduced the universe of interest into a manageable sub-set of constitutive models. Indeed, other possible ways of grouping them could have been considered, such as a division between those using empirical, additive, or multiplicative hardening laws, for instance. The selected set is obviously incomplete and apologies are addressed to all those authors which work has not been referenced, but hopefully it covers a sufficiently wide number of approaches, spanning most materials of engineering interest.

Impact tests revealed that the failure of ductile metals is highly dependent on the stress-state. It occurs at certain points of a failure locus which spatial locations depend on the stress invariants but no single model can successfully cover the whole range of failure locus and predict the failure. A wide variety of models exists and different sets of calibration parameters have been used by different authors in their constitutive models to cover a specific region in the failure loci in order to match particular test results. However, differences in mesh size and pattern may impair the prediction ability of even these fine tuned material models.

[6] 2017. F.Salvado et all, "A review on the strain rate dependency of the dynamic viscoplastic response of FC metals". Progress in Materials Science, Vol.88, pp: 186-231

3.2 Constitutive models – a review

3.2.1 Framework of the review

Considerable effort is being devoted to the investigation of the response of structures and materials subject to ballistic impacts or blast loads, due to public awareness about terrorist threats or the prevention of accidents such as in offshore oil and gas or chemical industries, where unwanted gas or fuel deflagrations may happen.

In general a blast or impact load will manifest itself by means of a sharp pressure wave travelling at ultrasonic speed impinging on the structure surface. The energy will be transmitted so quickly that deformation will develop at very high rates and stress waves may form and travel through the body. High temperature changes may also be present and both the dynamic loading and the temperature increase will affect the mechanical and failure response of the material. This rate dependent behaviour has been very intensely investigated for a number of materials, namely metals and composites. In broad terms, strains due to explosive blast will increase at rates from 10^2 to 10^4 s^{-1}, leading to a regime of elastic and plastic wave propagation, plane stress and deformation heating (Zukas, 2004).

One important aspect of the research effort needed to understand the response of engineering materials to blast loading involves the definition of suitable constitutive models that can be used in numerical analysis. It is important to emphasize the relevance of numerical computations in these analyses since experiments may reveal themselves unpractical or expensive. Under blast loads, deformations will be quite large meaning that the elastic component of strain will be comparatively smaller than the plastic strain. This led many researchers to focus their attention on plastic constitutive expressions. However, many constitutive models for the response of metals in high speed and loading regimes exist and a compilation may be of some help for those involved in the field. Few models consider high strain rate effects but some others that were developed and tested at low strain rate regimes will also be addressed due to their relation with other models. Nonetheless, reference will be made to regimes around

10^4 s^{-1}, where shock waves may be present in the material. For the reader interested in extreme strain rate regimes, reviews are available (Remington, et al., 2006).

The variety of engineering materials of interest (steel, non ferrous alloys, composites, foams, etc.) is too wide to be tractable and since studies on steel and ferrous alloys have been widely reviewed (Chaboche, 2008) the scope of this review will restrict itself to those constitutive models that can be used for the simulation of the dynamic behaviour of non-ferrous alloys (e.g. aluminium alloys) since the use of these materials spans for virtually all fields of industry (aeronautical, automotive, marine and civil) and also protective structures and armour. However, non-ferrous metals may exhibit different behaviour under dynamic loading and a preference will be made to those models that have been tested with aluminium. Aluminium is a widely used material in all sorts of civilian and military crafts and has a polycrystalline face centred cubic (FCC) structure, which is the main reason for its ductility. For plastic deformation at least five independent slip systems are needed, as pointed by von Mises by the first time (Lee, et al., 1995), but although both FCC and BCC (body centred cubic) have those systems, FCC metals have a higher packing efficiency and the slip planes are more closely packed than BCC metals, which makes them more ductile as the energy required to move atoms along denser planes is smaller than for lesser packed planes. Emphasis will be put on those constitutive models that work better for FCC metals and, consequently, this review may ignore models and variants developed for other crystallographic structures such as BCC or hexagonal closed packed (HCP). The main difference is that in BCC metals the yield stress is determined by strain rate hardening and temperature softening and in FCC metals by strain hardening (Armstrong, et al., 2008). The plastic deformation of FCC metals is less sensitive to temperature than BCC metals. Dislocation movement in BCC metals is more thermally activated than in FCC metals, meaning that the latter will maintain ductility at lower temperatures. In BCC metals dislocation motion is increasingly influenced by the periodic lattice potential such as the Peierl's stresses while for the FCC there are short range stresses induced by forest dislocations and solute atoms that mostly affect dislocation motion. BCC metals are also more strain-rate sensitive than FCC metals.

The problem of the simulation of explosively driven deformation of metals and alloys is a complex one, that requires suitable and realistic models of plastic constitutive behaviour (Preston, et al., 2003). The range of variation of mechanical and

thermodynamic state variables can be extremely wide (plastic strain of several hundreds per cent, pressures exceeding 10 GPa and plastic strain rates of millions per second, and temperatures up to melting point). Many models are available, each one emphasizing a few aspects of material response but none being completely satisfactory. For instance, those constitutive equations that were derived from thermally activated dislocation glide theory are known not to work properly for strain rates above 10^5 s^{-1} where a sharp increase in the flow stress is observed. It will be discussed that this increase is due to phonon drag and most constitutive methods do not consider this effect in the equations.

One of the most interesting aspects related to high strain rate loading regimes is the increase of flow stress with strain rate and the strain rate sensitivity. Both phenomena can be observed in Fig. 3.1, which shows how the stress-strain curves move upwards with strain rate but also how a structure alteration due to the change in strain rate will affect the stress-strain curve making it jump from one curve to another. A strain rate insensitive material strained at a certain rate (lower curve of Fig. 3.1a) will start following the upper curve if there occur an increase in strain rate. However if a structure alteration occurs due to the change in strain rate (if the material structure is sensitive to strain rate) the stress-strain curve may follow a different path as shown in Fig. 3.1b) by the dotted line (Meyers, 1994). This aspect will be a main issue in most constitutive model discussions. A basic review of the main theoretical aspects that constitute the basis for most of the constitutive models described is presented below. To help to understand the formulations proposed below the reader is referred to the sources for a more detailed and complete treatment of these matters.

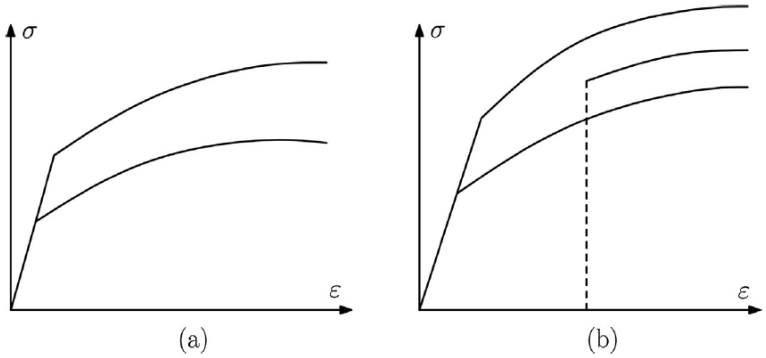

Figure 3. 1 - Stress-strain curves at different strain rates for material in which work hardening rate is (left) insensitive and (right) sensitive to strain rate (adapted from (Meyers, 1994), pp.367)

3.2.2 Constitutive behaviour theory

At the micro-scale level, polycrystalline metals show crystal defects termed dislocations. Under load, dislocations will move along various glide planes resulting in plastic flow. Mobile dislocations will move rapidly until they are arrested by energy barriers lying in their paths. The rate of deformation is controlled by the interaction of dislocations with defects such as grain boundaries, forest dislocations, second phase particles, etc. For FCC metals the dominant short-range obstacles are expected to be other dislocations (forest dislocations). However, for solid solution or dispersion strengthened alloys other effects will come into play. When encountering barriers, dislocations will need to overcome them in order that deformation can proceed and that requires energy. For low strain rates, where dislocation drag is not significant, thermal activation will be the main mechanism for deformation rate control. Thermal activation will be expressed in terms of large and random vibrations that allow the overcoming of the obstacles by the dislocations, which will then accelerate until they are stopped by another obstacle and the same process has to be repeated.

Obstacles vary with temperature. For low temperatures (below 25% of melting temperature) the main rate-controlling mechanism in FCC metals is the intersection of forest dislocations which controls the thermally activated process (Conrad, 1964) cited by Read et al. (Read, et al., 1970)).

The plastic deformation behaviour of metals and alloys depends not only on the instantaneous value of strain rate but also on the strain history (Klepaczko, 1974). This is true for FCC and HCP metals while BCC metals are considered as not path dependent and makes it difficult to establish reliable constitutive relations that account for strain history. Walley (Walley, et al., 2000) investigated a Taylor impact experiment in copper and found a good agreement between measured data and numerical data obtained with the path-dependent constitutive method from Goldthorpe (Gould, et al., 2000). We will observe different dislocation structures for the same level of plastic strain, depending on the rate of deformation imposed on the material. The same happens for plastic deformation at different temperatures. Therefore, flow stress is not a unique function of strain, strain rate and temperature but it is accepted that plastic deformation is the

result of displacement of many dislocations and plastic deformation rates can be described in terms of thermally activated processes.

A few theoretical notes that are presented below following the work of Meyers et al. (Meyers, 1994) (Meyers, et al., 2002) present a more detailed introduction to the mechanism of thermally activated dislocation motion.

It is normally stated in most papers on the subject of plasticity that dislocations or strain rate follow an Arrhenius law. This comes from an observation made by Arrhenius that there are "activation states" in chemical reactions between reactants and products. He suggested that the reaction rate could be expressed by a constant K given by

$$K = A \exp\left(\frac{-\Delta E_a}{KT}\right) \tag{3.1}$$

where A is a frequency factor, ΔE_a is the activation energy for the process and KT are the Boltzmann constant and temperature, respectively. Proof for this equation or a theoretical treatment of these matters are beyond the scope of this work. For the moment it is assumed that dislocations will pass through an activated state. If we consider N dislocations that are arrested at obstacles then, considering the dislocations as oscillators, each one will have its own energy level. These energy levels, e_i are quantised (i.e. they are discrete) and for each energy level we will have a number of dislocations n_i which distribution can be mathematically represented by an exponential function

$$n_i = Ae^{-\beta e_i} \tag{3.2}$$

This is the Boltzmann distribution, where A and β are the distribution parameters. The probability that a dislocation has an energy equal or greater than E is given by

$$P_E = \frac{A\int_E^\infty e^{-\beta e_i} \mathrm{d}e_i}{A\int_0^\infty e^{-\beta e_i} \mathrm{d}e_i} = e^{-\beta E} \tag{3.3}$$

From thermodynamics it can be shown that $\beta = 1/(KT)$, and that the probability of a dislocation having an energy greater than E is

$$P_E = e^{-E/(KT)} \tag{3.4}$$

It is assumed that dislocations will overcome an obstacle when their energy exceeds the height of the obstacle. Also, from basic thermodynamic relations, we can conclude that the internal energy is approximately equal to enthalpy, since the PV term is negligible in condensed solids. Thus,

$$p = \exp\left(-\frac{\Delta H}{KT}\right) = \exp\left(-\frac{\Delta G - T\Delta S}{KT}\right) = \exp\left(-\frac{\Delta G}{KT}\right)\exp\left(-\frac{\Delta S}{K}\right) = A\exp\left(-\frac{\Delta G}{KT}\right) \tag{3.5}$$

The term $\exp(\Delta S/K)$ becomes the coefficient A. Most constitutive models are based on this expression, meaning that given a barrier of height ΔG, the probability that a dislocation will jump over it is p. When temperature rises, this probability increases because the energy of the dislocation will increase due to the thermal contribution. The frequency of successful jumps, v_1, is related to this probability p, by $p = v_1/v_0$, where v_0 is the frequency of vibration of the dislocations. Thus,

$$v_1 = v_0 A\exp(-\Delta G/KT) \tag{3.6}$$

The Orowan equation applied to eq. (3.6) relates the strain to the movement of dislocations:

$$\dot{\gamma} = \frac{1}{M}\rho b\frac{\Delta l}{\Delta t} \tag{3.7}$$

where M is an orientation factor, ρ is the dislocation density, b is the Burgers vector and Δl is the distance between dislocation barriers. The total transit time of a dislocation is the sum of the waiting time to jump over the obstacle and the travel time between obstacles. The travel time may be assumed to be negligible and Δt, the waiting time, is the inverse of the successful jump frequency, v_1. Substituting eq. (3.6) in eq. (3.7) yields

$$\dot{\gamma} = \frac{v_0 \rho b \Delta l}{M} A \exp\left(-\frac{\Delta G}{KT}\right) = \dot{\gamma}_0 \exp\left(-\frac{\Delta G}{KT}\right) \tag{3.8}$$

where all the terms outside the exponential were grouped together and named $\dot{\gamma}_0$. Other authors use similar constitutive relations for thermally activated dislocation mechanism, such as (Klepaczko, 1974)

$$\dot{\gamma} = v(\tau, s_\alpha, T) \exp\left[-\frac{\Delta G(\tau^*, s_\alpha, T)}{KT}\right] \tag{3.9}$$

where v is a reference value, ΔG is the activation free energy, K is the Boltzmann constant, τ and γ are shear stress and shear strain, respectively, and τ^* is the effective shear stress. The s_α family of parameters is intended to account for the history of metal structure change. eq. (3.8) can be solved for, ΔG, leading to

$$\Delta G = KT \ln \frac{\dot{\gamma}_0}{\dot{\gamma}} \tag{3.10}$$

The barriers can have different shapes and may lead to different constitutive equations. Several authors attempted to find suitable barrier shapes and a generalised form has been proposed by Kocks et al. (1975, Kocks UF, Argon AS, Ashby MF, *Thermodynamics and kinetics of slip,* Prog. Mater. Sci. vol. 19, Pergamon Press, Oxford, cited by (Meyers, et al., 2002)) using two parameters to define the shapes, p and q. These authors proposed an equation of the form

$$\Delta G = \Delta G_0 \left[1 - \left(\frac{\tau}{\tau_0}\right)^p\right]^q \tag{3.11}$$

Combining eq. (3.10) and (3.11) a general constitutive equation is obtained relating stress, strain rate and temperature.

It is usual to decompose stress into two components, one dependent on temperature and another independent of thermal effects. Some authors define an effective stress, τ^*, associated to successful thermal activation that is related to the

applied stress by means of a term independent of temperature, called athermal stress τ_a:

$$\tau^* = \tau - \tau_a \tag{3.12}$$

The athermal stress is the stress necessary to overcome long-range obstacles. The other term, called the effective stress, is temperature dependent and is related to the force necessary to overcome short-range obstacles (Perzyna, 1988). At very high strain rates the applied stresses are sufficient to overcome the obstacles without any aid from thermal activation. At these strain rates dislocation drag will be the main damping mechanism for dislocation movement. The thermal stress component decreases with temperature and increases with strain rate. The athermal component increases with the accumulation of dislocations as the elastic field will hinder the motion of mobile dislocations (Nemat-Nasser, et al., 1998b). This elastic field will not depend directly on temperature but will be affected by it in two ways: (i) by means of temperature dependence of elastic moduli and (ii) through the effect of temperature on the density of far-field dislocation forests. At certain temperature levels metals will anneal, which will reduce dislocation density and this may have to be taken into account when high temperature regimes are present. Temperature history is also dependent of strain rate, which will affect the current density of dislocations. A schematic explanation of how thermal energy can help the dislocation to overcome obstacles is shown in Fig. 3.2. The figure shows the energies necessary to overcome a barrier (the areas under the force-distance curve) and as temperatures increases the respective thermal energies will also increase (represented by the hatched areas) decreasing the effective height of the barrier to be overcome. So the stress necessary to move the dislocation past the barrier decreases as temperature increases.

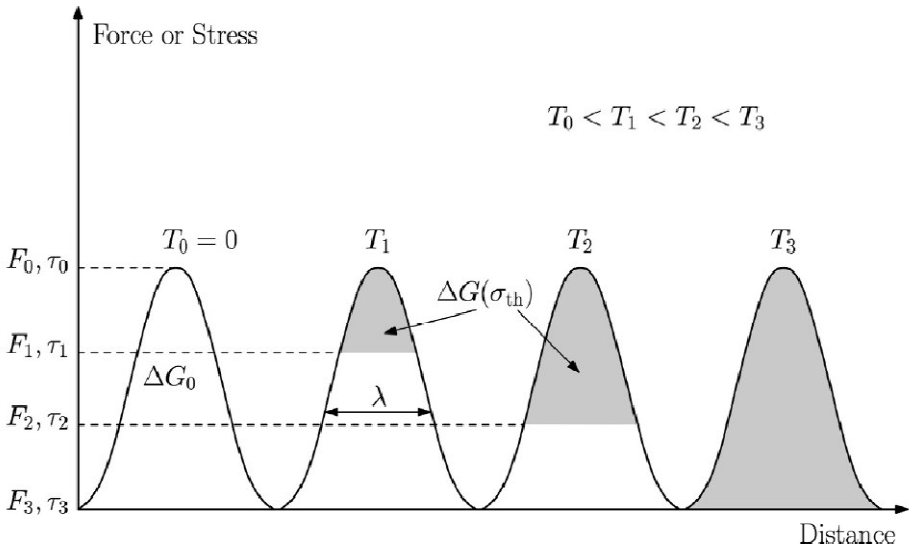

Figure 3. 2 - Schematic of a dislocation overcoming barriers with the assistance of a termal energy (reprinted from (Meyers, et al., 2002) , Copyright 2003, with permission from Elsevier)

3.2.3 Twinning

There are two basic modes of plastic deformation in polycrystalline metals, slip and twinning (Read, et al., 1970). Twinning can be dominant at high strain rates under shock loading and constitutive models for high strain rate loading should consider both twinning and slip. Twinning at low temperatures and high strain rates is responsible for higher predicted yield stress values than experimental results. This has been reported from the findings of Zerilli and Armstrong for instance (Meyers, et al., 2002) and was attributed to the change of the major deformation mechanism from dislocation slip to twinning at high strain rates and low temperature. Other occurrences of twinning are reported for shock-induced deformation (Nemat-Nasser, et al., 1998b). However, twinning is seldom addressed in most widely used constitutive models.

3.2.4 Dynamic recovery and recrystallization (DRV and DRX)

When a metal deforms plastically at high temperatures two softening mechanisms such as dynamic recovery (DRV) and dynamic recrystallisation (DRX) may take place which have a strong effect on the microstructure and mechanical properties of the material. At the microstructure level DRX will begin when strain hardening and recovery can no longer store more immobile dislocations. Strain-hardening plus recovery and DRX are important mechanisms responsible for the stress-strain response of FCC metals although not restricted to these.

Dynamic recovery consists of a re-arrangement, at high temperatures, of crystal defects of a plastically deformed metal. Some restoration of the original structure and properties may occur through annihilation of point defects and dislocations and a spatial re-distribution of dislocations that will soften the metal. As deformation progresses the flow stress increase as dislocations interact and multiply but as the dislocation density increases the rate of recovery also increases and at a certain strain a dynamic equilibrium will be found between the rates of work hardening and recovery. Work hardening rates are therefore counterbalanced by DRV or DRX.

DRX can be characterised by a nucleation rate of low dislocation density grains and a posterior growth rate that can produce a homogeneous grain size at a reached equilibrium status.

Recovery and recrystallisation are competing processes and the temperature regimes where they operate may overlap. Recrystallisation will usually be the first phenomena to occur and once it has occurred no further recovery will take place since the driving force for both mechanisms is the reduction in the stored energy of the deformed material. Conversely recovery will retard recrystallisation. DRX occurs during straining of metals at high temperature and will affect crystallographic texture and thus material anisotropy. As dislocation are eliminated by DRX the hot plasticity of materials is improved. DRV is typical of high stacking-fault energy (SFE) such as Al, where the flow stress saturates after an initial period of work hardening.

Shear stresses and strain rates will determine which dislocation mechanism controls the mechanical response. For shear stresses smaller then the quasi-static yield

stress the response will remain elastic and below the level of τ (see eq. 3.11) the plastic flow will be in the thermally activated regime (Read, et al., 1970). For stresses above τ the strain rate regimes will influence the mechanism that controls dislocation motion. At very small strain rates, rate effects are negligible and the strain hardening characteristics of the material will determine the stress strain response. For small strain rates thermal activation will be the rate-controlling mechanism. At higher strain rates viscous drag will control the plastic flow. When increasing the shear stress even further it is observed that for very high rates relativistic effects will influence the process, setting a limit for dislocation velocity. The transitions between these dislocation motion regimes are not precise and vary with the material and the temperature. Meyers (Meyers, 1994) points that, as a rule, relativistic effects start becoming important for mean dislocation velocities above 0.8 of shear-wave velocity. For titanium the drag-controlled plasticity regime starts at above a strain rate of 10^4 s^{-1}.

It is important to note that the flow stress at a given temperature T is typically proportional to the shear modulus μ, (Murr, et al., 1997) at this temperature. This allows the activation work done by the applied forces to be independent of material properties and so ΔG is proportional to $\mu(T)$. This allows the definition of a normalised activation energy, $g \equiv \frac{\Delta G}{\mu b^3} = g\left(\frac{\tau \mu_0}{\hat{\tau}\mu}\right)$ where μ_o is the shear modulus at 0 K (Kocks, 2001). Inverting the equation and combining with eq. (3.10) gives

$$g = \frac{KT}{\mu b^3} \ln\left(\frac{\dot{\varepsilon}_0}{\dot{\varepsilon}}\right) \tag{3.13}$$

As deformation progresses the material structure changes as the result of a balance between dislocation accumulation and dynamic recovery. The strain hardening θ can be decomposed into components due to dislocation accumulation and dynamic recovery respectively, which can be written as $\theta = \theta_a - \theta_r(T, \dot{\varepsilon}, \hat{\sigma})$ (Follansbee, et al., 1988), where $\hat{\sigma}$ is the mechanical threshold stress. The dynamic recovery term depends strongly on strain rate and temperature. If the strain-hardening rate $(\mathrm{d}\hat{\sigma}/\mathrm{d}\varepsilon)$ is plotted against $\hat{\sigma}$ as a function of strain rate and temperature, a Voce (linear) behaviour is observed for a limited range of strain, as can be seen in Fig. 3.3. A closed-form description for dynamic recovery has been proposed (Kocks, 2001) in the form

$$g = g_0 \left[1 - \left(\frac{\tau\mu_0}{\hat{\tau}\mu}\right)^p\right]^q \tag{3.14}$$

This equation has been used for dynamic recovery with the exponent $q = 2$. It may be concluded (Kocks, 2001) that an expression of the form

$$\Delta G = KT \ln\left(\frac{\dot{\varepsilon}_0}{\varepsilon}\right) = \mu b^3 g_0 \left[1 - \left(\frac{\tau\mu_0}{\hat{\tau}\mu}\right)^p\right]^q \tag{3.15}$$

can describe the mechanism of dislocation and obstacle interaction.

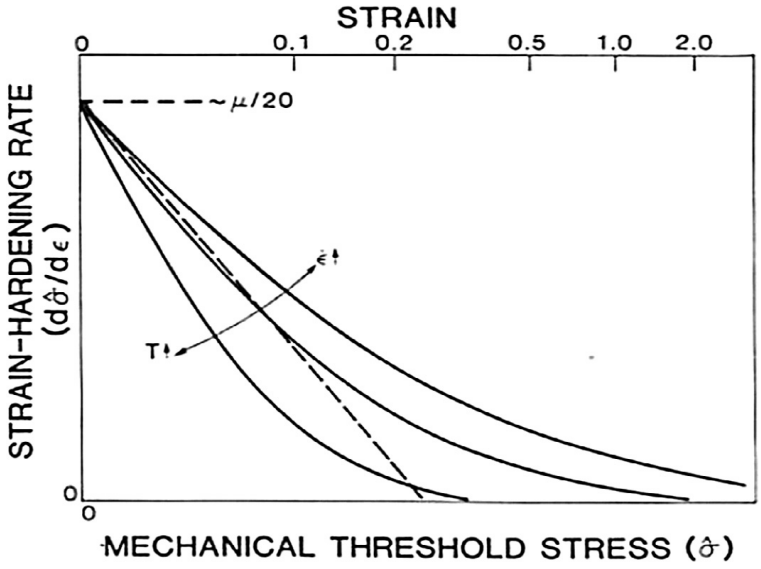

Figure 3. 3 - Schematic illustration of the variation of the strain-hardening rate with $\hat{\sigma}$ as a function of strain rate and temperature. The dashed line shows Voce behaviour (reprinted from (Follansbee, et al., 1988). Copyright 1988, with permission from Elsevier).

The strain hardening representations for a given strain rate and temperature can be grouped into two categories: (i) the Voce type group where a saturation stress is approached at large strain and (ii) the Hollomon or power-law group (Sung, et al., 2010) that are unbounded at large strains. Due to dynamic recovery most metals do not show Voce behaviour, that is strain hardening rate decreasing to zero with increasing stress or strain.

For strain rates up to $10^4\ s^{-1}$ the dominant mechanism of viscoplastic flow is glide kinetics of dislocations overcoming obstacles with the assistance of thermal fluctuations. Above the mechanical threshold this thermally activated dislocation glide is no longer the dominant mechanism that controls viscoplastic flow but, instead, the continuous glide of mobile dislocations that are subject to damping and relativistic effects.

Thermally activated stored deformation energy will control the softening mechanisms. The DRX activation energy will be an important parameter determining the critical conditions for DRX initiation.

The increase in strain rate or the decrease in deformation temperature prevents the occurrence of softening due to DRV and DRX and the material will exhibit a work hardening behaviour. For a given strain rate the work hardening effect will predominate in the first stages of deformation and the flow stress rapidly increases to a critical value. Then DRV and DRX become predominant and the true stress-strain curves of most materials will tend to adopt the shape of a plateau after the flow stress curve may show an inflexion after its peak value. DRX thus occurs after a critical amount of strain, which is dependent on the temperature and strain rate and also on initial grain size. It will become the dominant stress-strain response mechanism in FCC metals after the critical strain is attained. However, normally the effect of DRX has not been included in the constitutive equations although DRX causes significant changes in the thermomechanical response of the material, particularly in the high-strain rate regimes. A procedure exists that incorporates the contribution of DRX into the constitutive equations. Such contribution will be shown in section 6, after a review of relevant constitutive models since its discussion is more appropriate after the relevant constitutive model and their underlying assumptions have been presented.

3.2.5 Constitutive equations

The mechanisms of plastic deformation and their relation with applied loads can be mathematically described by constitutive laws which are basically sets of relations between stresses, stress derivatives, strains, strain derivatives, temperature, microstructure and damage. The deformation and failure responses of engineering

materials require the knowledge of suitable constitutive equations if accurate predictions are to be numerically obtained. A constitutive model is a combination of independent functions of strain, strain rate and temperature which are generally represented as $f(\varepsilon), g(\dot{\varepsilon})$ and $h(T)$. A constitutive model is therefore a relation of the type:

$$\sigma = F(\varepsilon, \dot{\varepsilon}, T, \text{deformation history}) \tag{3.16}$$

where $\varepsilon, \dot{\varepsilon}, T$ are the strain, strain rate and temperature, respectively. Some constitutive models also consider internal variables that characterize the metal structure. The deformation history is required due to the irreversible nature and path dependence of the plastic deformation, particularly for FCC metals. The effects of each of the above three variables can be combined with the other in a multiplicative or additive way (Sung, et al., 2010) allowing many possible different constitutive equations. Many will be modifications of existing ones. The strain rate will have, for instance, hardening or softening effects on certain aluminium alloys, depending on the strain rate range and temperature. That is the main difficulty in identifying a suitable constitutive law, as often they are normally limited to certain classes of materials and limited ranges of strain rates. The many researchers that have addressed this problem have in many cases tried to circumvent this difficulty by introducing modifications to existing models when calibration from experimental data failed to produce good agreement between model and experiments. These efforts result in dozens of constitutive models, for as many materials and loading regimes.

From the many possible regimes of loading we can identify our range of interest of strain rate, from 10^2 s^{-1} upwards. For strain rates higher that 10^3 s^{-1} thermal and wave propagation effects become noticeable and at 10^5 s^{-1} or higher, shock waves will propagate through the material making thermodynamic behaviour important as transition from isothermal to adiabatic behaviour is observed. The thermal behaviour of yield and flow stress of FCC metals is more complex to describe than strain rate. The yield stress follows a curve like the one depicted in Fig. 3.4.

Four regions can be noticed in the curve (Voyiadjis, et al., 2008): (i) a low temperature region in which the pattern of the flow stress depends on the material, (ii) a region where the material is subjected to higher temperatures and the flow stress decreases with increasing temperature, (iii) a region where the temperature has no

effect on flow stress and, finally, (iv) a very high temperature region, where the flow stress decreases again with increasing temperatures. Not all materials exhibit the four regions and some metals can behave in accordance with only one or two parts of the curve. It will be seen that most constitutive models combine strain rate and temperature effects.

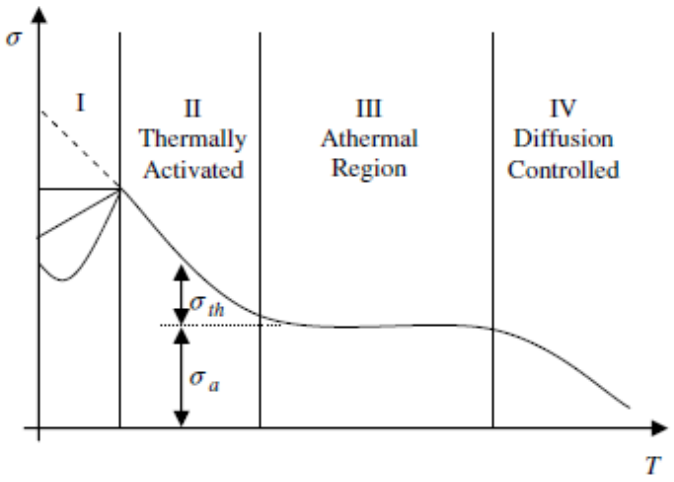

Figure 3. 4 - Schematic behaviour of yield stress versus temperature of pure FCC metal (reprinted from (Voyiadjis, et al., 2008). Copyright 2008, with permission from Elsevier).

Constitutive equations can be broadly classified in two major categories: physically based or phenomenologically based, depending on the assumptions adopted for each of them. The recent trend has increased the focus on physically based models, which extends their application to a wider range of strains (Panov, 2006). However, the empirical approach is often preferred as it produces simpler equations and, although they are not derived from first principles, they are consistent with the laws of physics. Dimensional analysis is one way to obtain phenomenological equations. Physically based models can also be addressed in different ways (Lemaitre, et al., 1990):

- A microscopic approach describing the mechanics of deformation at the molecular or crystalline level, in which macroscopic behaviour results from integrating or averaging microscopic variables over a volume element;

- A thermodynamic approach that assumes a homogeneous continuum equivalent to the real material and represents the microscopic physical phenomena by means of macroscopic internal variables (Rice, 1971).

A considerable number of constitutive models are available, many of them having been implemented in computer codes. It is important to remember that the material dynamic behaviour at high strain rates is affected by the microstructural evolution during deformation, which is not considered in phenomenological models. This is one reason why physically based models are preferred in some situations.

Another way of categorising constitutive equations (Gao, et al., 2012) considers the main loading mechanism: high-pressure loading, where the dominant effect is the shock wave high pressure such as is observed in pressure-shear plate impact tests; or the regular-pressure type which does not include the pressure as a state variable and is observed in one-dimensional-stress experiments like Split Hopkinson Pressure Bar (SHPB) tests. In the second case deviatoric stresses will induce different microstructural responses than those induced by pressure (Meyers, 1994). The available constitutive models for these high-pressure regimes will be referred to in what follows, as reviewed by Remington (Remington, et al., 2006). The regular-pressure models can be reviewed in the works of Chaboche (Chaboche, 2008) and Lin and Chen (Lin, et al., 2011).

Before addressing strain rate dependent models, it is relevant to cite classic constitutive models that describe flow stress changes depending on the deformation conditions, such as temperature and strain rate. These models do not usually consider deformation history but are accurate for cases where strain hardening is the dominant factor. The following well-known equations are part of this group (Gronostajski, 2000):

The Hollomon equation: $\sigma_p = C\varepsilon^n$ (3.17)

The Ludwick equation: $\sigma_p = \sigma_{po} + C\varepsilon^n$ (3.18)

The Voce equations: $\sigma_p = \sigma_{ps} - \left(\sigma_{ps} - \sigma_{po}\right)^{-n\varepsilon}$ (3.19)

There are many other equations but none has proven to be satisfactory for all materials and deformation conditions (Gronostajski, 2000). For higher strain rates the exponential forms such as Voce equation, are more suitable. Other models have been developed such as:

Fields and Backofen equation: $\sigma_p = C\varepsilon^n\dot{\varepsilon}^m$ (3.20)

The Hart equation: $\sigma_p = \sigma_p^* \exp\left[\left(-\frac{\dot{\varepsilon}^*}{\dot{\varepsilon}}\right)^{\lambda}\right] + \sigma_0(\dot{\varepsilon})^{\frac{1}{M}}$ (3.21)

where the first term describes thermally activated plastic flow and the second describes dislocation slip.

The Wagoner equation: $\sigma_p = C(\varepsilon + \varepsilon_0)^n \left(\frac{\dot{\varepsilon}}{\dot{\varepsilon}_0}\right)^m$ (3.22)

Another group of equations that include the effect of temperature may assume the following forms, where the most significant difference is the way temperature depends on strain and strain rate (Gronostajski, 2000)

$$\sigma_p = C\varepsilon^n \exp(n_1\varepsilon)\, \dot{\varepsilon}^m \exp(a_1 T) \quad (3.23)$$

$$\sigma_p = C\varepsilon^n \exp(n_1\varepsilon)\, \dot{\varepsilon}^{(m+bT)} \exp(a_1 T) \quad (3.24)$$

$$\sigma_p = C\varepsilon^{(n+b_2 T)} \exp(n_1\varepsilon)\, \dot{\varepsilon}^{(m+bT)} \exp(a_1 T) \quad (3.25)$$

$$\sigma_p = C\varepsilon^n \exp\left(\frac{n_1\varepsilon}{\varepsilon_m}\right) \dot{\varepsilon}^{(m+b/T)} \exp(a_1 T) \quad (3.26)$$

A few variations on the equations above can also be used, where the forms of the exponents have been slightly modified. In the above equations the indices for the stress symbol σ, are: p for flow stress, p_0 for yield point, p_m for the flow stress at the ultimate tensile strength and p_s for saturation stress. σ_p^* and $\dot{\varepsilon}^*$ are the current states of stress and strain rate, respectively. The indices n and n_1 are the strain hardening coefficients, m is the strain rate sensitivity, ε_o is the pre-strain, ε_m is the critical strain and C, M, λ, a, a_1, b and b_1 are experimentally determined material parameters.

Zener and Hollomon considered a modification for the effect of temperature on the strain rate, proposing the following term:

$$\sigma_p = f\left[\dot{\varepsilon} \exp\left(\frac{Q}{RT}\right)\right] = f(Z) \quad (3.27)$$

where Q is the activation energy and Z is the Zener-Hollomon parameter (Gronostajski, 2000). A number of variations have been developed by several authors, which include Z type parameters, as will be shown below. Classical approaches are good starting points for more recent constitutive models but will not be covered. They normally follow Duvaut, Lion and Perzyna formulations (Perzyna, 1988) (Etse, et al., 1999). As an example (Cheng, et al., 2008) used the Fields – Backhofen equation to investigate the mechanical behaviour of AZ31 magnesium alloy sheets but considered low strain rates, which excludes their work from this review.

3.2.6 Physically based constitutive equations

Early work is well described in a review from Armstrong and Walley (Armstrong, et al., 2008) presenting some pioneering results on attempts to relate strain rate and viscoplastic behaviour. The introduction of the dislocation concept is very well documented. This idea was developed by Taylor (Taylor, 1938) (Taylor, 1934) and other authors in the 1930s. More recent work, particularly from the last three or four decades, has benefited from the rapid increase in the processing capacity of computers that has been translated into more sophistication of the numerical models available.

From this group of more recent work one interesting attempt to obtain a physically based model was published by Read and co-workers (Meyers, 1994) who developed a rate-dependent physically based constitutive model for polycrystalline metals. They assumed that most of the plastic flow at a point was due to slip along planes on which the resolved shear stress has its maximum value. Plastic strain was assumed to depend on the density of mobile dislocations, N_m, by the following expression:

$$\dot{\varepsilon}_p = \frac{4}{3} b N_m v \tag{3.28}$$

where b is the Burgers vector and v is the mean velocity of the mobile dislocations. Expressions were developed for each of the terms of the equations above to construct the constitutive equation (Meyers, 1994) considered that the applied stress could be decomposed into a thermally activated component τ^*, a viscous drag component τ_D, and

an athermal component τ_μ. Combining the expressions for eq. (3.1) and those for the stresses, the constitutive equation they obtained becomes

$$\dot{\varepsilon}_p = \frac{4}{3}\frac{bu_g\left[N_{m\infty}+\left(N_{m0}-N_{m\infty}+M_1\varepsilon_p^2\right)\exp\left(-A_1\varepsilon_p\right)\right]}{1+\beta|u_g|\exp\left(-\frac{v^*\tau^*}{kT}\right)} \tag{3.29}$$

where u_g is the glide velocity (function of the viscous drag stress), N_m is the mobile dislocation density in which subscript "0" refers to its initial value and subscript "∞" refers to the saturation value of the mobile dislocation density. M_1 and A are a coefficient and an annihilation factor, respectively, and k is the Boltzman constant. v^* is an activation volume, T is assumed to be a fixed temperature and β is a function of temperature, activation energy and vibration frequency. It is possible to simplify the equation neglecting the thermally activation stress, which may be adopted for metals in which thermal activation is not a major player at a given temperature. In that case:

$$\dot{\varepsilon}_p = \frac{4}{3}\frac{bu_g\left[N_{m\infty}+\left(N_{m0}-N_{m\infty}+M_1\varepsilon_p^2\right)\exp\left(-A_1\varepsilon_p\right)\right]}{\sqrt{1+\frac{\phi^2}{C_s^2}}} \tag{3.30}$$

where ϕ is a function of the viscous drag stress and C_s is a coefficient to be determined. Read and co-workers (Meyers, 1994) tested the model for 6061-T6 aluminium alloy to assess the effectiveness of the model in considering hardening, thermal activation, Bauschinger effect, viscous drag, dislocation multiplication and annihilation and the limiting dislocation velocity (relativistic effect). Their model is limited to isotropic behaviour and considerable simplifications were introduced due to the lack of knowledge at the time.

Evidence of the importance of the strain rate effect has been studied by many researchers together with the combined effect with temperature history effects (Klepaczko, 1974). The first relationship found was described by a thermally activation process and the second resulted from an evolutionary process, in which the structure changes during plastic deformation.

3.2.6.1 Bodner and Partom (BP)

Bodner and Partom (Bodner, et al., 1975) developed an elastic-viscoplastic equation for large deformation analysis considering the effects of strain hardening and viscosity and has been used with success in many applications. Results published in the original work were obtained for very small strain rates of the order 10^{-3} to 10^{-5} s^{-1} but in a more recent application much higher strain rates were investigated. The model is based on the separation of the total deformation rate into an elastic and a plastic component during the deformation process, that is,

$$d_{ij} = d_{ij}^{e} + d_{ij}^{p} \tag{3.31}$$

where d_{ij} is the symmetric part of the velocity gradient and the elastic component of the deformation rate is related to Cauchy stress rate tensor by Hooke's generalised law (Liang, et al., 1999)

$$d_{ij}^{e} = \frac{\dot{t}_{ij}}{G} - \frac{\lambda \dot{t}_{kk}\delta_{ij}}{2G(3\lambda+2G)} \tag{3.32}$$

in which G is the elastic shear modulus and λ is a Lamé constant. The plastic deformation rate d_{ij}^{p} can be related to the deviatoric part of the Cauchy stress tensor s_{ij}

$$d_{ij}^{p} = \gamma s_{ij} \tag{3.33}$$

where γ is a material parameter. When this equation is squared we obtain $\gamma^2 = D_2^p / J_2$ or $D_2^p = f(J_2)$, where D_2^p is the second invariant of the plastic deformation rate, J_2 is the second invariant of the Cauchy deviatoric tensor and f is a function of J_2. Bodner and Partom (Bodner, et al., 1975) deemed appropriate to consider the particular form of that function

$$D_2^p = D_0^2 \exp\left[-\left(\frac{n+1}{n}\right)\left(\frac{Z^2}{3J_2}\right)^n\right] \tag{3.34}$$

where D_o is the maximum strain rate and Z is an internal variable. The strain rate sensitivity is governed by the parameter n. Z is assumed to be a function of the plastic work

$$Z = Z_1 + (Z_0 - Z_1)\exp\left(-m\frac{W_p}{Z_0}\right) \tag{3.35}$$

The original Bodner and Partom (BP) model for uni-axial stress is

$$\dot{\varepsilon}_x^p = \frac{2D_0}{\sqrt{3}}\frac{\sigma}{|\sigma|}\exp\left[-\frac{1}{2}\left(\frac{3A^2}{\sigma^2}\right)^n\right] \tag{3.36}$$

$$A^2 = \frac{1}{3}(Z^2)\sqrt{\frac{n+1}{n}} \tag{3.37}$$

where $\dot{\varepsilon}_x^p$ and W_p are the plastic strain rate and plastic work, respectively, and D_0, n, m, Z_0 (initial value) and Z_1 (saturation value) are material constants.

The interest of the BP model rests on its solid physical foundation (Chen, et al., 2008) and has been widely used although it is not very sensitive to the strain rate and it does not consider temperature effects. An example of its application to high-speed impact of a projectile was proposed by Song (Song, et al., 2001). Results obtained with this constitutive model are shown in Fig. 3. 5 for aluminium deformed at two values of strain rate of the order of 10^3 s^{-1}.

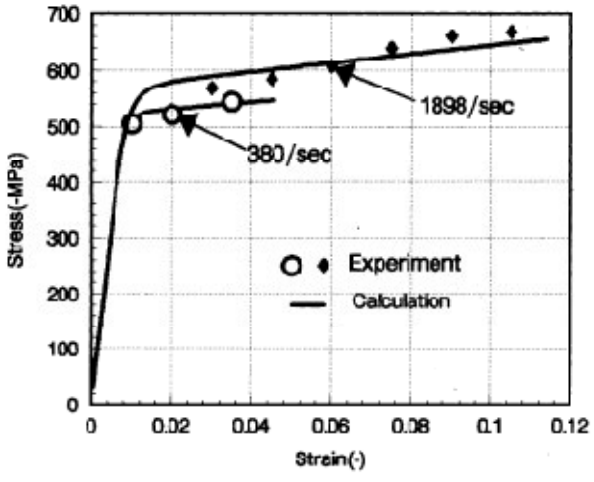

Figure 3. 5 - Experimental and calculated (fitted) stress-strain curves aluminium at constant strain rates (reprinted from (Song, et al., 2001), Copyright 2001, with permission from Elsevier).

A modification to the BP model was later introduced, consisting of an explicit introduction of thermal softening effect (Chen, et al., 2008) to study the behaviour of 30CrMnSiA steel after a high rate heating. The thermal softening effect introduced by Chen consisted in a modification of eq. (3.37):

$$A^2 = \frac{1}{3}\left[Z\exp\left(C_1 T'^{n1}\right)\right]^n \sqrt{\frac{n+1}{n}} \tag{3.38}$$

where C_1 and n_1 are more material constants and the non-dimensional temperature

$$T' = \frac{T - T_0}{T_{\text{melt}} - T_0} \tag{3.39}$$

with T_0 referring to room temperature and T_{melt} being the melting temperature. Z depends on the deformation history of the material and relates to the dislocation density while n relates to dislocation velocity. Results for 30CrMnSiA showing the softening effect of increasing the temperature above 200 K obtained with the BP and other constitutive equations are presented in Fig. 3.6.

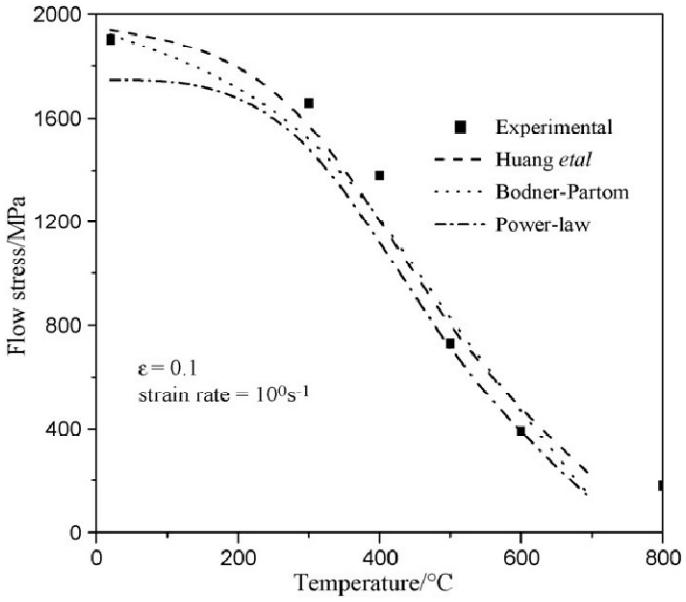

Figure 3. 6 - Comparison of theoretical and experimental values on thermal softening of 30CrMnSiA at a strain rate of 1 s-1 (reprinted from (Chen, et al., 2008). Copyright 2008, with permission from Elsevier).

3.2.6.2 Steinberg-Guinan (SG)

Due to their simplicity, elastic-perfectly plastic constitutive models were implemented early on in most hydrocodes but the need to account for work hardening was soon recognised (Wilkins, et al., 1973) and some modifications that took account of this phenomenon were developed and implemented. Shear modulus G and yield stress Y also increase with increasing pressure and decrease with increasing temperature and a constitutive model has been developed to take account of this (Steinberg, et al., 1980). The authors admitted that an unbounded growth of the flow stress with increasing strain rate was unreasonable and a limit was found for strain rates close to 10^5 s^{-1}. They stated that this was due to the increase in temperature with increasing stress. The temperature effect together with the strain rate effect were combined into the Steinberg-Guinan (SG) constitutive model, relating these state variables to the shear modulus G and yield strength Y. In this equation the yield strength is expressed as a first-order Taylor expansion in pressure and temperature about the ambient state, that is,

$$G = G_0\left[1 + \left(\frac{G'_p}{G_0}\right)\frac{P}{\eta^{\frac{1}{3}}} + \left(\frac{G'_T}{G_0}\right)(T - 300)\right] \tag{3.40}$$

$$Y = Y_0[1 + \beta(\varepsilon + \varepsilon_1)]^n\left[1 + \left(\frac{Y'_p}{Y_0}\right)\frac{P}{\eta^{\frac{1}{3}}} + \left(\frac{G'_T}{G_0}\right)(T - 300)\right] \tag{3.41}$$

subject to the constraint that $Y_0[1 + \beta(\varepsilon + \varepsilon_1)]^n \leq Y_{\max}$. β and n are work-hardening parameters, ε_i is the initial plastic strain (usually zero), the subscript $_0$ refers to the reference state ($T = 300$ K, $P = 0$, $\varepsilon = 0$), primed parameters mean their derivatives at the reference state, with respect to either P or T, shown using appropriate subscripts. Note that the model includes semi-terms such as the work hardening term, $[1 + \beta(\varepsilon + \varepsilon_1)]^n$ which fits data for a wide number of metals at high strain-rates, namely the results of Wilkins and Guinan (Wilkins, et al., 1973), who determined the yield strength of a number of materials through computer simulation of cylinder deceleration experiments at high strain rate regimes (10^5 s^{-1} on average). The effects of the state variables P, T and ε (pressure, temperature and strain) on Y and G has been checked for impact experiments with 6061-T6 Al alloy (results shown in Fig. 3.7), along with the

data that resulted from adding, step-by-step, the effects of those parameters on the constitutive equations. The results for the induced wave profiles show the differences in the arrival times of both the calculated and the measured waves from which the pressure and temperature dependencies of the shear modulus can be examined. The effects of these parameters on yield stress were also shown to be much stronger than work-hardening.

However, the saturation of microstructural processes above a critical strain rate (10^5 s^{-1}) and the rate-independent plastic deformation above this critical strain rate gives a good description of metal plastic response behind the shock front but not at the shock front. The SG model remains one of the few constitutive equations used for strain rates around 10^5 s^{-1}.

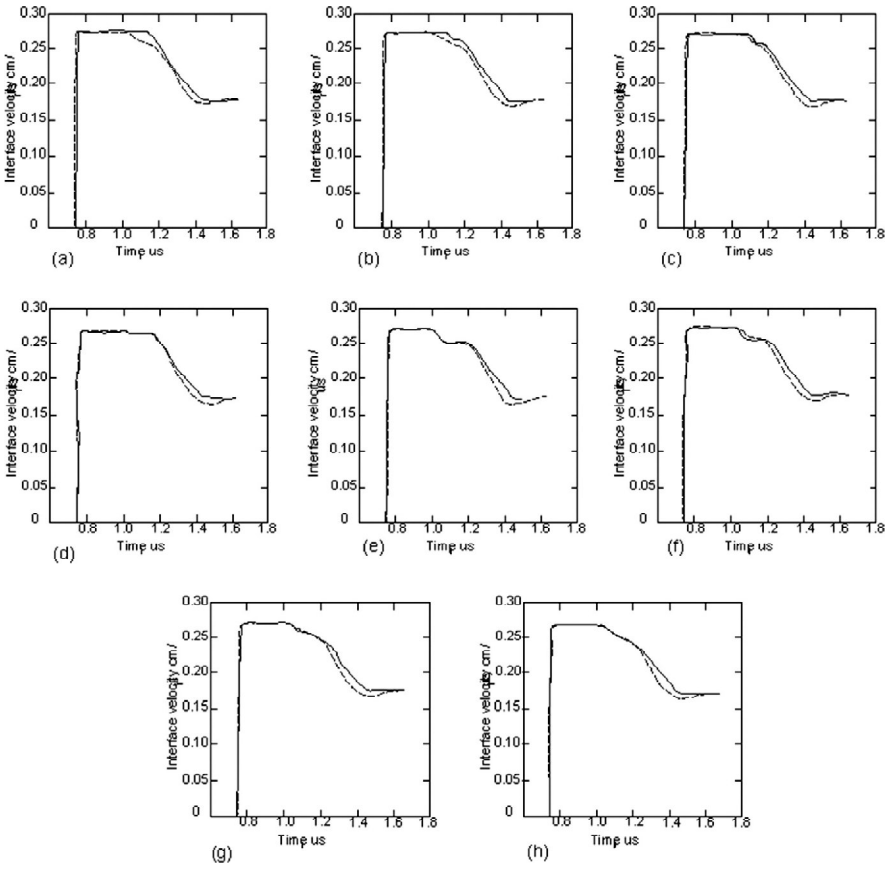

Figure 3. 7 - Experimental (dashed line) and calculated (solid line) shock induced wave profiles showing the motion of aluminium - PMMA interface versus time for various Pressure, Temperature and strain dependencies: (a) pure hydro; (b) constant Y and G; (c) adding work hardening; (d) adding the P dependence of Y; (f) adding T dependence; (g) adding the Bauschinger model with $G_1 = G_0$; (h) the Bauschinger effect with $G_1 = 0.725G_0$ (reproduced with permission from (Steinberg, et al., 1980). Copyright 1980, AIP Publishing LLC).

3.2.6.3 Steinberg and Lund (SL)

This is an extension of the Steinberg-Guinan (Steinberg, et al., 1980) constitutive model to extend its regime of validity to strain rates as low as 10^{-4} s^{-1}. The form used is based on the work of Hoge and Mukherjee (Hoge, et al., 1977) .This modified model is simpler, has fewer coefficients and is more stable when running in hydrocodes. The increase in the range of applicability was achieved by splitting the yield strength into its thermal and athermal components where the former is a function of strain rate and temperature. The equation of Hoge and Mukherjee (Hoge, et al., 1977) was used for the thermal part of the constitutive model but any other expression for plastic strain rate as a function of yield stress and temperature could have been used (Steinberg, et al., 1989). The equation is as follows:

$$\dot{\varepsilon}_p = \frac{1}{C_1}\exp\left[\frac{2U_k}{KT}\left(1-\frac{\sigma_t}{\sigma_p}\right)^2\right]+\frac{C_2}{\sigma_t} \tag{3.42}$$

where σ_p is the Peierls stress, $2U_k$ is the energy necessary to form a pair of kinks in a dislocation segment of length L and K is the Boltzmann constant. $C_2 = D/\rho b^2$ where D is the drag coefficient, ρ is the dislocation density and b is the Burgers vector. Additionally,

$$C_1 = \frac{\rho L a b^2 v}{2} w^2 \tag{3.43}$$

where a is the distance between Peierls valleys, w is the width of a kink loop and v is the Debye frequency. σ_t is the thermally activated component of the yield stress. The method is applied to a wide range of strain rates, from 10^{-4} to 10^{6} s^{-1}, which makes it suitable for shock-induced phenomena representation. Results for a shocked tantalum target are shown in Fig. 3. 8, where excellent agreement between experimental and calculated data is evident although at such a high stress level the model loses sensitivity. The method seems to be applicable to crystalline structures other than BCC, although the only published data corresponds to tantalum, a BCC material.

3.2.6.4 Zerilli and Armstrong (ZA)

Zerilli and Armstrong (Zerilli, et al., 1987) developed a constitutive relation based on dislocation mechanics and incorporating the effect of strain hardening, strain-rate hardening and grain size. They also wanted to include in constitutive models the different behaviour of materials due to their crystalline structures as they observed different dislocation interactions for FCC and BCC metals. The dislocations must overcome barriers of forest dislocations. To overcome those barriers, a certain thermal activation energy is necessary which decreases with plastic strain due to the increase in dislocation density. Therefore, the flow stress is divided into a thermal and an athermal component, $\sigma = \sigma_a + \sigma_{th}$. The thermal flow stress is given as

$$\sigma_{th} = \frac{M\Delta G_0}{Ab} e^{-\beta T} \tag{3.44}$$

$$\beta = -C_3 + C_4 \ln \dot{\varepsilon} \tag{3.45}$$

where M is a direction factor, ΔG_o is the free energy of thermal activation at 0 K, A is the activation area, b is the Burgers vector and β is a parameter associated with strain and strain rate (Lin, et al., 2011).

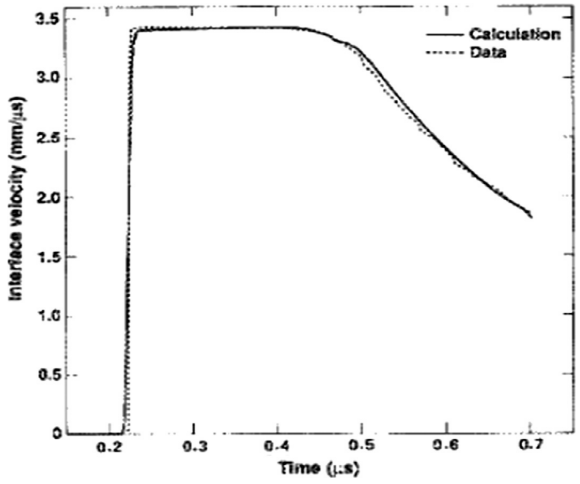

Figure 3. 8 - Comparison of calculation and experiment for a Ta target shocked to a peak stress of 230 GPa (reproduced with permission from (Steinberg, et al., 1989). Copyright 1989, AIP Publishing LLC).

For BCC metals dislocations must overcome Peierls-Nabarro barriers, thermal activation does not depend on strain and A is constant. As mentioned above, yield stress in FCC metals is determined by strain hardening and that of BCC metals is determined by strain rate hardening and thermal softening. Therefore A is not constant but instead proportional to $\varepsilon^{-1/2}$. Based on such considerations, the Zerilli-Armstrong (ZA) model has been developed with two formulations, one for FCC and another for BCC metals. The expression for FCC is within the scope of this review and is

$$\sigma = \sigma_a + C_2\varepsilon^{\frac{1}{2}}\exp(-C_3T + C_4T\ln\dot{\varepsilon}) + kl^{-\frac{1}{2}} \qquad (3.46)$$

where σ is the von Mises equivalent stress, σ_a is an athermal component of stress that considers the contribution of the initial dislocation density for the yield stress. C_i are parameters to be determined experimentally. The last term brings in the effect of grain diameter l and of a micro-structural stress intensity factor k.

The model assumes independency between work-hardening rate, temperature and strain rate increase which is true for most metals but will not accurately model materials that exhibit that type of dependency. It is also observed that the parameters of the model should not be used as constants as this will reduce the accuracy of predictions. Zhang (Zhang, et al., 2009) proposed a modification to the ZA method by considering the integrated effects of the temperature, strain-rate and deformation history on the flow behaviour of alloy IC10. For FCC materials the modified expression is (Zhang, et al., 2009).

$$\sigma = C_0 + C_2\varepsilon^{\frac{1}{2}}\exp\left[\left(-C_3''T + C_4'T\ln\left(\frac{\dot{\varepsilon}}{r(\varepsilon)r(\dot{\varepsilon})}\right)\right)f(T)\right] \qquad (3.47)$$

where the dislocation density $r(\varepsilon) = \rho_o + M\varepsilon$ increases linearly with the plastic strain. In this expression M is a material constant relative to the increasing rate of dislocation density and ρ_o is the initial dislocation density. Parameters C_i, C_3' and C_4'' of the modified ZA equation are material constants. Expressions for $f(T)$ and $r(\dot{\varepsilon})$ were also given (Zhang, et al., 2009). The results from the modified ZA model fit better than those

from the original model. However, the use of these modifications is limited as they are particular to certain materials. Other modified versions of the ZA model were derived to improve the fitting of predictions with data from experiments with materials such as alloy D9 (Samantaray, et al., 2009) a titanium-modified austenitic stainless steel or S15C, S50C and SKS93 carbon steels (Lee, et al., 2006). More general modifications have been derived (Abed, et al., 2005) (Meyer, 2006) (Gao, et al., 2010) to correct some inaccuracies found in results obtained with the method. Reference will be made below to the method of Gao (Gao, et al., 2010) that may be generalized to FCC metals and show good results for strain rates up to 10^4 s^{-1}. The modified expression is

$$\sigma = \hat{\sigma}_a + \hat{Y}\varepsilon^n \exp\left[C_3 T \ln\left(\frac{\dot{\varepsilon}}{\dot{\varepsilon}_{so}}\right)\right]\left\{1 - \left[-C_4 T \ln\left(\frac{\dot{\varepsilon}}{\dot{\varepsilon}_o}\right)\right]^{\frac{1}{q}}\right\}^{\frac{1}{p}} \quad (3.48)$$

where $\hat{Y} = \lambda\hat{\sigma}_{so}$ is the actual reference thermal stress, $\hat{\sigma}_{so}$ is the reference saturated threshold stress, $\hat{\sigma}_a$ is the athermal stress, λ and n are material constants and p and q are parameters representing the shape of potential barriers. $C_3 = k/g_{so}\mu b^3$ and $C_4 = k/g_o\mu b^3$ are also material constants. Fig. 3.9 shows results predicted with the modified equation for OFHC copper.

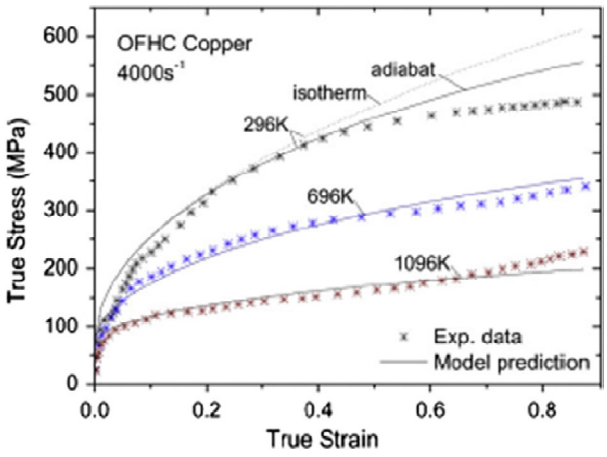

Figure 3. 9 - Comparison of model prediction with the experimental data for annealed OFHC copper at different temperatures with the strain rate of 4000 s-1 (reprinted from (Abed, et al., 2005) Copyright 2010, with permission from Elsevier).

3.2.6.5 Mecking and Kocks (MK)

This is a single internal variable model suitable for high strain rate viscoplastic response of metals (in the range 10^2-10^4 s^{-1}) based on total dislocation density. Mechanical properties (i.e. the flow stress) depend on current metallurgical structure and this structure evolves with strain. Dislocation density is generally used as the parameter that relates the metallurgical structure with strain. The model considers that the flow stress is related to the dislocation density by means of a multiplicative combination of two terms, one being a rate sensitive term dependent on thermal activation and the other a structure sensitive term (Meyer, 2006) representing the flow stress at zero temperature $\hat{\sigma}$:

$$\sigma = s(\dot{\varepsilon}, T)\hat{\alpha}\mu b\sqrt{\rho} \tag{3.49}$$

This relation was shown to be valid for small strains at all temperatures or to apply to a finite range of strain at low temperatures. This behavior breaks down as strain hardening becomes rate sensitive as dynamic recovery increases. To relate the described relation with dynamic recovery the s function has been redefined as

$$s = \left(\frac{\dot{\varepsilon}}{\dot{\varepsilon_0}}\right)^{1/m} \exp\left(-F\frac{\theta_r}{\theta_h}\right) \tag{3.50}$$

and

$$s = \left(\frac{\dot{\varepsilon}}{\dot{\varepsilon_0}}\right)^{\frac{1}{m}} \left(1 - F\frac{\theta_r}{\theta_h}\right) \tag{3.51}$$

where F is an adjustable parameter that decreases from 1 as dynamic recovery increases, θ_r is an athermal hardening rate and θ_h is a normalization factor. Flow stress is then given as the product of a strain only dependent stress $\hat{\sigma}$ and which depends on strain rate and temperature, with the given s function. Above the mentioned strain rate range the dislocation evolution and stress-strain behavior will follow different patterns.

In FCC metals it has been observed that flow stress increases disproportionally when strain rate exceeds the 10^3-10^4 s^{-1} range (Mecking, et al., 1981).

3.2.6.6 Mechanical Threshold Stress (MTS)

The work of Kocks (Mecking, et al., 1981) is very important as it was the precursor of the MTS method. Experimental results have shown that strain rate sensitivity change at constant strain must be due to a change in the structure evolution of the metal (Follansbee, et al., 1988). It was observed that a representative state variable for such an internal microstructure state could be the mechanical threshold stress, i.e. the flow stress measured at 0 K. Follansbee et al. found that this stress is a function of the strain rate at constant strain, meaning that structural evolution is rate dependent. This led to the formulation of a constitutive model based on state variables that describe the current state of the material. This model, the Mechanical Threshold Stress (MTS) model, uses strain, strain rate and temperature to define the yield stress of a material at a specific internal state. The model evolved from previous work (Mecking, et al., 1981) extending their range of application to the high strain rate regime. The equations that describe the model are

$$\sigma = \hat{\sigma}_a + (\hat{\sigma} - \hat{\sigma}_a)\left\{1 - \left[\frac{KT\ln\left(\dot{\varepsilon}_0/\dot{\varepsilon}\right)}{g_0\mu b^3}\right]^{\frac{1}{q}}\right\}^{\frac{1}{p}} \tag{3.52}$$

where σ is the flow stress, which is a function of the mechanical threshold stress $\hat{\sigma}$, the athermal stress $\hat{\sigma}_a$ (a parameter to be found). K is the Boltzmann constant, μ is the shear modulus (temperature dependent), b is the Burgers vector, g_0 is the total activation energy, p and q are constants, as well as $\dot{\varepsilon}_o$ which is a reference strain rate. Voce behaviour has been considered and then the state variable $\hat{\sigma}$ can be determined through a strain-hardening rate

$$\theta = \frac{\mathrm{d}\hat{\sigma}}{\mathrm{d}\varepsilon} = \theta_0\left[1 - \left(\frac{\hat{\sigma}-\hat{\sigma}_a}{\hat{\sigma}_s-\hat{\sigma}_a}\right)\right] \tag{3.53}$$

where $\hat{\sigma}_s$ is the saturation stress or the stress at zero strain hardening rate (temperature and strain rate dependent) and θ_0 is the hardening due to dislocation accumulation. Together with the equation

$$\ln\left(\frac{\dot{\varepsilon}}{\dot{\varepsilon}_{so}}\right) = \frac{\mu b^3 A}{KT}\ln\left(\frac{\hat{\sigma}_s}{\hat{\sigma}_{so}}\right) \tag{3.54}$$

where $\dot{\varepsilon}_{so}$, A and $\dot{\sigma}_{so}$ are constants. $\dot{\sigma}_{so}$ is the saturation threshold stress for deformation at 0 K, these two expressions allow the evolution of the state variable mechanical threshold stress to be determined. The MTS model accounts for the influence on flow stress of the strain, strain rate and temperature histories, but requires a large number of experiments to determine the material parameters necessary to calibrate the equation, rendering it difficult to use. The method attempts to correctly predict the flow stress behaviour in the high strain rate regime (above 10^3-10^4 s^{-1}).

Other authors have attempted to describe strain and strain rate history effects in FCC metals at high strain rates. Klepaczko proposed a model based on dislocation density and considered a strain rate dependence on dislocation accumulation. The model was revised later by Klepaczko and Chiem based on dislocation accumulation and recovery effects (Klepaczko JR, 1975. Mat Science Engng, 18: 121 and Klepaczko JR and Chiem CY, 1986, J. Mech. Phys. Solids, 34: 29 both cited by Follansbee and Kocks (Follansbee, et al., 1988). The citation adds that the Klepaczko-Chiem model has never been used for rates above 10^3 s^{-1}, which makes it less interesting for this review.

Dorward and Hasse reported that flow stresses of aluminium alloys are independent of strain rates below 10^3 s^{-1}. These authors used the following constitutive equation (Dorward, et al., 1995)

$$\sigma = \sigma_0 \varepsilon^n \dot{\varepsilon}^m (1 - \beta \Delta T) \tag{3.55}$$

to perform a number of analysis. However, the range of strain rates was, in general, below 10^3 s^{-1}. Their conclusions are in line with other authors as they report an increase in the flow stress above that value of strain rate.

Zhao and Gary (Zhao, et al., 1995) derived a constitutive model suitable for car crash test simulation. Based on dynamic and quasi-static experiments a phenomenological model has been derived (Zhao, et al., 1995) for strain rates from 10^{-4} to 10^{4} s^{-1}. The authors examined Johnson and Cook (JC) (which will be discussed under section 5), ZA and SG empirical equations but adopted a Ludwig-type expression in which the coefficients depend on strain rate:

$$\sigma = \left[A(\dot{\varepsilon}) + B(\dot{\varepsilon})\varepsilon_p^{n(\dot{\varepsilon})}\right](1 - \mu\Delta T) \tag{3.56}$$

with

$$A = a_1 + a_2 \log\left(\frac{\dot{\varepsilon}}{\dot{\varepsilon}_o}\right) + a_3 \left[\log\left(\frac{\dot{\varepsilon}}{\dot{\varepsilon}_o}\right)\right]^3; \quad B = b_1 - b_2 \log\left(\frac{\dot{\varepsilon}}{\dot{\varepsilon}_o}\right) + b_3 \left[\log\left(\frac{\dot{\varepsilon}}{\dot{\varepsilon}_o}\right)\right]^{0.5} \tag{3.57}$$

and

$$n = n_1 + n_2 \log\left(\frac{\dot{\varepsilon}}{\dot{\varepsilon}_o}\right) + n_3 \left[\log\left(\frac{\dot{\varepsilon}}{\dot{\varepsilon}_o}\right)\right]^3 \tag{3.58}$$

where σ, ε_p and $\dot{\varepsilon}$ are stress, plastic strain and strain rate, respectively, ΔT is the temperature increment in respect to room temperature (23°C) and a_i, b_i, n_i, μ, $\dot{\varepsilon}_o$ are constants to be determined. μ is a thermal softening coefficient to be determined assuming adiabatic conditions during deformation. Good agreement with experimental data was achieved with this model within the range 10^{-4} to 10^{4} s^{-1} for steel sheets.

Banerjee (Banerjee, 2007) compared results from the MTS and JC models for the response of AISI 4340 steel under blast loading. This author concluded that both models give similar results but the JC model is numerically more efficient and is better suited for large numerical simulations. Results for the deformation of copper obtained with the MTS model, eq. (3.4), are presented in Fig. 3. 10.

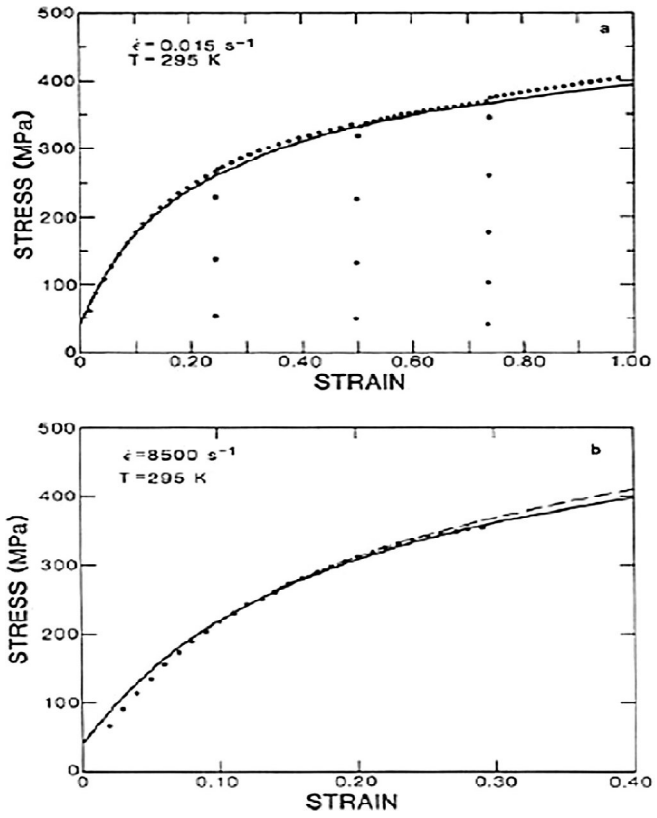

Figure 3. 10 - Predictions of the model and comparison with experimental results for copper at (a) $\dot{\varepsilon} = 0.01$ s-1 and (b) $\dot{\varepsilon} = 8500$ s-1. The calculations for the latter strain rate are for both isothermal ($T = 295$ K dashed line) and adiabatic (solid line) (reprinted from (Follansbee, et al., 1988) Copyright 1988, with permission from Elsevier).

3.2.6.7 Nemat-Nasser and Li (NNL)

A dislocation physically based constitutive model has been proposed by Nemat-Nasser (Nemat-Nasser, et al., 1998b) to calculate finite deformations of FCC polycrystals. These authors had previously derived a phenomenological model (Nemat-Nasser, et al., 1996) for single FCC crystals considering the history of the deformation divided into three regimes depending on the number of active slip systems. The authors followed previous work for BCC and FCC metals (Nemat-Nasser, et al., 1996) (Nemat-Nasser, et al., 1997) (Nemat-Nasser, et al., 1998c).

A computer implementation using a plastic-predictor and an elastic-corrector was used in that formulation. The underlying physical model of inelastic response of metals based on dislocation motion and accumulation considers thermal activation and dislocation drag has a significant degree of complexity and is not easily mathematically modelled for implementation in computer codes. In many cases simplifying assumptions have to be adopted to make models more tractable. Nemat-Nasser and Li (Nemat-Nasser, et al., 1998b) expressed plastic strain rate $\dot{\gamma}$ in the classic way, as a function of the dislocation density, velocity and Burgers vector b, then using a power law to derive the final form of the constitutive equation. An empirical relation was used for the average dislocation spacing and the resulting equation is

$$\tau(\dot{\gamma},\gamma,T)=\tau^{o}\left\{1-\left[-\frac{KT}{G_0}\left(\ln\frac{\dot{\gamma}}{\dot{\gamma}_0}+\ln\left(1+a(T)\gamma^{\frac{1}{2}}\right)\right)\right]^{\frac{1}{2}}\right\}^{\frac{3}{2}}\left[1+a(T)\gamma^{\frac{1}{2}}\right]+\tau_a^{o}\gamma^{n_1} \qquad (3.59)$$

$$\tau^{o}=\frac{G_0}{b\lambda l_0}, \qquad \dot{\gamma}_0=b\rho_m\omega_0 l_0 \qquad a(T)=a_0\left[1-\left({}^{T}/_{T_m}\right)^{2}\right] \qquad ((3.60)\text{a, b, c})$$

where the variables have their usual meaning. $a(T)$ and n_1 are experimentally derived parameters. K is obtained empirically and $G_o=\hat{\tau}b\lambda l$, where $\hat{\tau}$ is the thermal stress for zero absolute temperature and λ, l_o are the average barrier width and the initial dislocation spacing associated with an initial temperature, respectively. The superscripts "o" in the above equations indicate initial values. For instance τ_a^o is the initial value for the athermal part of the resistance to the motion of dislocations. This method differs from others because it is iterative rather than a closed form solution. In Fig. 3.11 material responses (stress-strain) are shown for a number of strain rates and temperatures.

Another physical constitutive model was developed under the same framework suggested by Nemat-Nasser and Li (1998) for 3003 Al-Mn alloy (Guo, et al., 2011). The equation is not of general use as it is calibrated for that particular alloy. It will not be mentioned further because of its very particular application.

Fig. 3.11 shows results obtained with the NNL constitutive model. Fig. 3.12 shows an application of the method to FCC metals comparing results with experimental data gathered in the work of Nemat-Nasser (Nemat-Nasser, et al., 1998b). Fig. 3.12 shows calculated and measured material responses for polycrystalline annealed OFHC

copper at strain rates of 8000, 0.1 and 0.001 s^{-1} A remarkably good correlation with the experimental results has been obtained (Nemat-Nasser, et al., 1998a). The modified model has been successfully used to model the dynamic response of molybdenum (Nemat-Nasser, et al., 1999) and titanium (Nemat-Nasser, et al., 1999). The modified expression is given by

$$\tau = \tau^{o}\left\{1 - \left[-\frac{KT}{G_0}\left(\ln\frac{\dot{\gamma}}{\dot{\gamma}_0} + \ln\left(1 + \alpha(T)\gamma^{\frac{1}{2}}\right)\right)\right]^{\frac{1}{2}}\right\}\left[1 + \alpha(T)\gamma^{\frac{1}{2}}\right] + \tau_a^{o}\gamma^{n_1} \tag{3.61}$$

$$\tau_0 = \frac{G_0}{b\lambda l_0} \tag{3.62}$$

where the parameters have the usual meanings.

3.2.7 Other constitutive models

As we have seen above several approaches have been followed for the prediction of flow stress in the high strain regime. One of such approaches has been the consideration of phonon drag effects (Nemat-Nasser, et al., 2001). Based on experimental uni-axial compression test results on AL-6XN austenitic stainless steel Nemat-Nasser, Guo and Kihil developed a physically based model that considers also the viscous-drag effect. The tests were performed between 10^{-3} and 8000 s^{-1} and at temperatures ranging from 77 to 1000 K. Plastic flow stress of this alloy was shown to

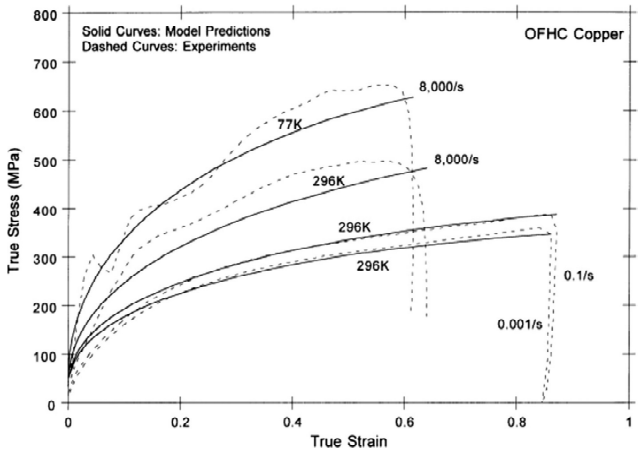

Figure 3.11 - Comparison of model prediction with experimental results for annealed OFHC copper at different strain rates and temperatures using NNL constitutive model (reprinted from (Nemat-Nasser, et al., 1998b) Copyright 1998, with permission from Elsevier)

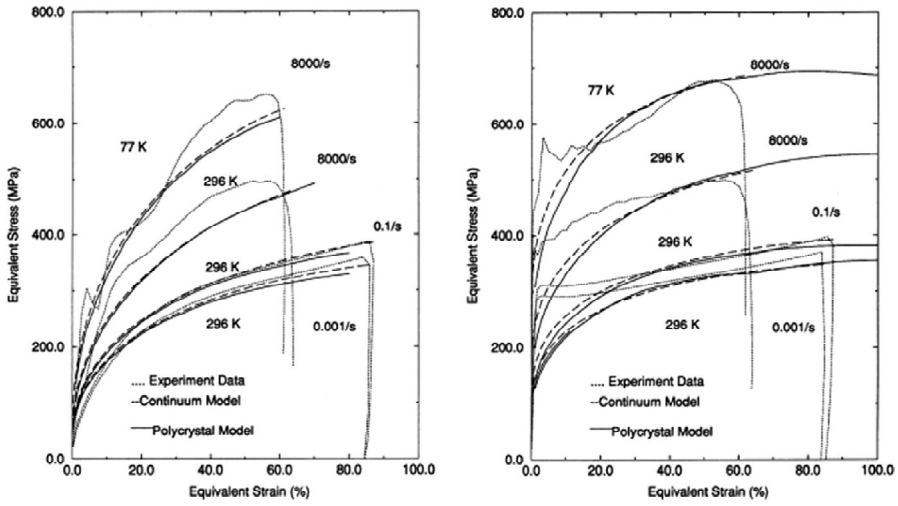

Figure 3.12 - Comparisons between model and experiment for various strain rates and temperatures: experimental data (dotted), continuum model calculations (dashed) and model calculations using the present constitutive model (solid) (reprinted from (Nemat-Nasser, et al., 1998a) Copyright 1998, with permission from Elsevier).

depend on the temperature, the strain-rate and their histories. At low strain rates dynamic strain-aging occurs at the range of temperatures 500 to 1000 K peaking at 800 K. Dislocation motion faced viscous-drag resistance at a range of strain-rates and the microstructure of this material evolved mainly with the temperature history. Thus the constitutive equations were developed to include all these effects following previous work (Nemat-Nasser, et al., 1998b) (Nemat-Nasser, et al., 1997) (Nemat-Nasser, et al.,

1999a) (Nemat-Nasser, et al., 1999b) on several polycrystalline metals. The model assumes a thermal and an athermal part of the resistance to dislocation motion, the main deformation mechanism considered. The flow stress, τ, is considered to be divided into three components: one due to short-range thermally activated effect which may include the Peierls stress and point defects, designated as τ^*; the second part is the athermal component τ_a, due to long-range effects such as the stress field of dislocation forests and grain boundaries; and the third part is the viscous-drag component, τ_d. The flow stress will be a function of strain rate $\dot{\gamma}$, temperature, T, and some microstructural parameters such as the distribution of the density of dislocations, ρ. Then,

$$\tau = \tau_a + \tau_d + \tau^* \tag{3.63}$$

The viscous-drag stress depends on the dislocation motion which average velocity, v is related with the strain rate $\dot{\gamma}$ by $\dot{\gamma} = \rho_m b v / M$, where ρ_m is the mobile dislocation density, and b and M are the magnitude of Burgers vector and the Taylor factor respectively. Using these relations

$$\tau_d = m_0[1 - \exp(-\alpha\dot{\gamma})] \tag{3.64}$$

$$\alpha = \frac{M^2 B}{\rho_m b^2 \tau_y} \tag{3.65}$$

where m_0 is a material constant measured directly measured at a very high-strain rate and α represents an effective damping of the dislocation motion.

The thermally activated component of the flow stress depends on temperature, T, strain rate, $\dot{\gamma}$, and an internal variable characterising the microstructure of the material. The average dislocation density ρ has been considered the dominant microstructural parameter. A relation between τ^*, T and $\dot{\gamma}$ can be obtained using the concept of activation free energy ΔG, eq. (3.11), and a final expression for τ^* has been defined as,

$$\tau^* = \tau^0 \left\{ 1 - \left[-\frac{KT}{G_0} \ln\left(\frac{\dot{\gamma} f(\gamma,T)}{\dot{\gamma}} \right) \right]^{\frac{1}{q}} \right\}^{\frac{1}{p}} f(\gamma,T) \quad \text{for } T \le T_c \quad (3.66)$$

$$\tau^0 = \frac{G_0}{b\lambda l_0} \quad (3.67)$$

$$\dot{\gamma_0} = b\rho_m \omega_0 l_0 \quad (3.68)$$

$$f(\gamma,T) = 1 + a\left[1 - \left(\frac{T}{T_m} \right)^2 \right] \gamma^m \quad (3.69)$$

where

$$T_c = -\frac{G_0}{K} \left[\ln\left(\frac{\dot{\gamma} F(\gamma,T_c)}{\dot{\gamma}_0} \right) \right]^{-1} \quad (3.70)$$

In these equations the parameters p and q define the profile of the short-range energy barrier, T_m is the melting temperature, the index m is a free parameter to be obtained from experimental data, l_0 is an initial average dislocation spacing, K is the Boltzmann constant, λ is the average effective barrier width, a is a free parameter and $\omega_0$is the attempt frequency of barrier overcoming. Results from the use of this constitutive model for the AL-6XN stainless steel are shown below in Fig. 3.13.

Preston et al (Preston, et al., 2003) also developed a physically based model suitable for explosive loading and high-speed impacts. It has been applied to strain rates from 10^{-3} to 10^{12} s^{-1} which makes it one of the few that can cope with hypervelocity phenomena. It is known that for high stresses the Arrhenius form for the strain rate, which is the basis of many constitutive equations, becomes less accurate as thermal activation mechanisms cease to be dominant and dislocation drag predominates. Their model is based on the same mechanisms as for the hybrid SL models, such as thermal activation for shear stresses lower than the dominant dislocation barriers and a viscous drag mechanism for shear stresses greater than the barriers (Remington, et al., 2006). At strain rates of up to 10^4 s^{-1} the model is calibrated using conventional data obtained from Hopkinson bar experiments. For higher strain rates the model includes

formulations that reproduce overdriven shock[7] waves with strain assumed to have a power law dependence on strain rates, represented by an Arrhenius form. Alternatively, data can be extrapolated from strength curves between the two limiting regimes (the low end thermal activation and the high end nonlinear viscous drag). The equations that describe the model are as shown below in their simpler form for the lower strain rate regimes:

$$\hat{\tau} = \hat{\tau}_s + \frac{1}{p}\left(s_0 - \hat{\tau}_y\right)\ln\left\{1 - \left[1 - \exp\left(-p\frac{\hat{\tau}_s - \hat{\tau}_y}{s_0 - \hat{\tau}_y}\right)\right]\exp\left[-p\theta\psi\left[\left(s_0 - \hat{\tau}_y\right)\left[\exp\left(p\frac{\hat{\tau}_s - \hat{\tau}_y}{s_0 - \hat{\tau}_y}\right) - \right.\right.\right.$$

1–1 (3.71)

For shock regimes a function of the type $\hat{\tau} = \hat{\tau}_s G(p,T)$ has to be used, where $\hat{\tau}_s$ is a normalised work-hardening saturation stress. The flow stress normalisation has been performed assuming a proportionality with shear modulus G: $\hat{\tau} = \tau/G(\rho,T)$ where ρ is the mass density and T is the temperature. Temperature was also scaled on the basis of melting temperature T_m, such that $\hat{T} = T/T_m(\rho)$. The work hardening saturation stress and the yield stress in the thermal activation regime are given by

$$\hat{\tau}_s = s_0 - (s_0 - s_\infty)\,\mathrm{erf}\left[K\hat{T}\ln\left(\gamma\dot{\xi}/\psi\right)\right] \tag{3.72}$$

$$\hat{\tau}_y = y_0 - (y_0 - y_\infty)\,\mathrm{erf}\left[K\hat{T}\ln\left(\gamma\dot{\xi}/\psi\right)\right] \tag{3.73}$$

that take the following form of a power law in the overdriven shock regime:

$$\hat{\tau}_s = \hat{\tau}_y = s_0\left(\frac{\psi}{\gamma\dot{\xi}}\right)^{\beta} \tag{3.74}$$

[7] An overdriven shock wave is one in which the plastic wave has overrun the elastic precursor producing a shock wave front steeper than that, which would result from adiabatic elastic compression

It is worth noting that at these high strain rate regimes work hardening may be neglected as it is probably saturated. In the transition gap between the thermally activated regime and the overdriven shock regime the saturation stress is taken as the greater of the two values given by Eqs. (3.72) and (3.73). A similar expression is obtained for the yield stress, to allow for a maximum in the strain-rate sensitivity. It has been shown (Kim, et al., 2009) that a jump in the strain rate sensitivity occurs at about 10^3 s^{-1} exceeding that calculated at strain rates above 10^9 s^{-1}. To allow for such a maximum in the small strain rate sensitivity, Preston and co-workers introduced two additional parameters: y_0 and y_1. The final expression for the yield stress in the transition gap from thermally activated to overdriven shock regimes is then

$$\hat{\tau}_y = \max\left\{y_0 - (y_0 - y_\infty)\,\mathrm{erf}\left[K\hat{T}\ln\left(\frac{\gamma\dot{\xi}}{\dot{\psi}}\right)\right]\min\left[y_1\left(\frac{\dot{\psi}}{\gamma\dot{\xi}}\right)^{y_2}, s_0\left(\frac{\dot{\psi}}{\gamma\dot{\xi}}\right)^{\beta}\right]\right\} \qquad (3.75)$$

where s_o is the value of $\hat{\tau}_s$ at 0 K, s_∞ is the value of $\hat{\tau}_s$ close to the melting temperature, y_o, y_∞ are the values of $\hat{\tau}_y$ at 0 K and close to the melting temperature, respectively. K and γ are material constants. $\dot{\psi} = \dot{\psi}_0 \exp[-\Delta\phi(\tau)/K_B T]$ is the plastic strain rate in an Arrhenius form, where the activation energy $\Delta\phi(\tau)$ is a decreasing function of the applied stress and $K_B T$ is the thermal energy. $\dot{\xi}$ is a scaling factor (the time required for a transverse wave to cross an atom) and is used to obtain a normalised strain rate variable, $\dot{\psi}/\dot{\xi}$, where

$$\dot{\xi} = \frac{1}{2}\left(\frac{4\pi\rho}{3M}\right)^{\frac{1}{3}}\sqrt{\frac{G}{\rho}} \qquad (3.76)$$

where M is the atomic mass.. The model has been employed for wider ranges of strain rates and

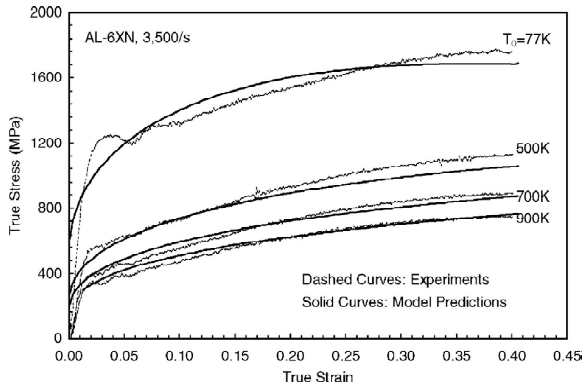

Figure 3. 13 - Comparison of model predictions with experimental results at a strain rate of 3500 s-1 (reprinted from (Nemat-Nasser, et al., 2001) Copyright 2001 with permission from Elsevier).

temperatures and obtained good correlation between predictions and experimental data for wide ranges of strain rates and temperatures by modifying the strain-hardening term in the original PTW model using the Voce equation (Kim, et al., 2009).

A new constitutive equation has evolved from the work of Klepaczko (Klepaczko, 1974) that reported the response of polycrystalline FCC metals within the range of strain rates from 10^{-4} to 10^{3} s^{-1} obtained through experiments. This work was the basis for a further development (Rusinek, et al., 2001) of the model to describe the viscoplastic behaviour of the metal sheet under test. The method considers the addition of an internal stress and an effective stress corresponding to a strain hardening and a thermal activation process, respectively. The thermal stress is given by an Arrhenius relation coupling strain rate and temperature. The corresponding constitutive relation is

$$\sigma = \frac{E(T)}{E_0}\left[B_0\theta_m^{-v}(\varepsilon_0 + \varepsilon^p)^{n_0(1-D_2\theta_n)} + \sigma_0^*(1 - D_1\theta_m)^m\right] \quad (3.77)$$

In the above equations σ is the shear stress,

$$\theta_m = \frac{T}{T_m}\log\left(\frac{\dot{\varepsilon}_{\max}}{\dot{\varepsilon}^p}\right) \quad \text{and} \quad \theta_n = \frac{T}{T_m}\log\left(\frac{\dot{\varepsilon}^p}{\dot{\varepsilon}_{\min}}\right) \quad (3.78)$$

are two homologous temperatures modified by the strain rate. The other parameters are the plasticity modulus B_o, the temperature sensitivity v and the hardening coefficient n_o. The effective stress σ_o^* at T = 0 K and D_1 and D_2 are experimentally derived material constants, ε and $\dot{\varepsilon}$ are strain and strain rate and E and E_o are the Young moduli at current and 0 K temperatures, respectively. An upper bound was set for the strain rate $\dot{\varepsilon}_{\max}$ and the minimum strain rate $\dot{\varepsilon}_{\min}$ is reached at a critical temperature. T_m is the melting temperature. The Young modulus also evolves with temperature in accordance with the following expression

$$E(T) = E_0 \left\{1 - \frac{T}{T_m} \exp\left[\theta^* \left(1 - \frac{T_m}{T}\right)\right]\right\} \tag{3.79}$$

where θ^* is the characteristic homologous temperature.

The method was later modified when it was verified that the RK model could not accurately describe certain aspects relating the thermo-viscoplastic behaviour. To improve the method extensions were produced later (Rusinek, et al., 2009) by adding a third term to the stress σ. The new term, σ_{ns}, is the stress component that accounts for the negative strain rate sensitivity observed in aluminium alloys as the method was improved to study applications of these alloys. A new extension to the RK method has been presented by Rusinek and co-workers (Rusinek, et al., 2010), the modified RK model (MRK) where the von Mises stress is decomposed in the following way

$$\bar{\sigma} = \frac{E(T)}{E_0}\left[\bar{\sigma}_\mu + \bar{\sigma}^*\right] + \bar{\sigma}_{vs} \tag{3.80}$$

The temperature dependent Young modulus ratio $E(T)/E_o$ defines its evolution with temperature. The internal stress component σ_μ is equal to Y, the flow stress of the undeformed material. The effective stress component $\bar{\sigma}^*$ is given as

$$\sigma^* = \sigma_0^* \left[1 - \xi_1 \left(\frac{T}{T_m}\right) \log\left(\frac{\dot{\varepsilon}_{\max}}{\dot{\varepsilon}^p}\right)\right]^{1/\xi_2} \tag{3.81}$$

where ξ_1 and ξ_2 are material constants that describe temperature and rate sensitivity of the material and $\dot{\varepsilon}_{max}$ is the maximum strain-rate for a particular material. The viscous-

drag component $\bar{\sigma}_{vs}$ is given as a function of the Taylor factor M, the drag coefficient B and the mobile dislocation density ρ_m, b is the Burgers vector and an expression based on experimental data has been proposed (Kapoor, et al., 2000)

$$\bar{\sigma}_{vs} = \chi[1 - \exp(-\alpha)\,\dot{\bar{\varepsilon}}^p] \tag{3.82}$$

$$\alpha = \left(\frac{M^2 B}{\rho_m b^2 \tau_y}\right) \tag{3.83}$$

where χ is a material constant, α is an effective damping coefficient affecting the dislocation motion and τ_y is the athermal yield stress. Figs. 3.14a and 3.14b show how this model fits experimental results. The MRK model was also used to obtain the temperature sensitivity description of 2024-T3 aluminium alloy (Rodriguez-Martinez, et al., 2011) in low velocity perforation tests, with good results.

A reference is due to more classical works such as the Hollomon and Voce constitutive models (Sung, et al., 2010) which introduced a multiplicative type phenomenological equation containing three functions

$$\sigma = \sigma(\varepsilon, \dot{\varepsilon}, T) = f(\varepsilon, T) g(\dot{\varepsilon}) h(T) \tag{3.84}$$

Function *f* accounts for the temperature sensitivity of the strain-hardening rate by means of a linear combination of Hollomon and Voce strain hardening equations. This combination showed how the strain-hardening rate varies with temperature, being lower at higher temperatures. This is a behaviour that is not captured by most existing constitutive models. The proposed function was

$$f(\varepsilon, T) = \alpha(T) f_h + [1 - \alpha(T) f_v] \tag{3.85a}$$

$$\alpha(T) = \alpha_1 - \alpha_2 (T - T_0) \tag{3.86b}$$

$$f_h = H \varepsilon^n \tag{3.87c}$$

$$f_v = V(1 - Ae^{B\varepsilon}) \tag{3.88d}$$

where T_o is a reference temperature and $\alpha_1, \alpha_2, H, n, B$ are material constants. Function $\alpha(T)$ can reproduce a Voce type curve at high temperatures and a Hollomon type behaviour at lower temperatures or vice-versa, depending on the sign of α_1.

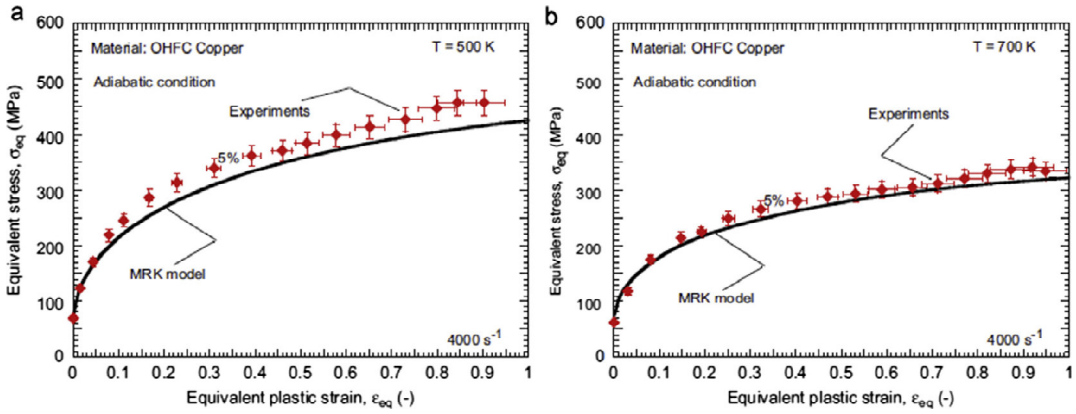

Figure 3. 14 – Description of the flow stress evolution with plastic strain using the MRK model and comparison with experiments at 4000 s-1 (a) $T_a = 500$ K and (b) $T_a = 700$ K (reprinted from (Rusinek, et al., 2010) Copyright 2010, with permission from Elsevier).

Austin and McDowell have also developed a physically based model to include slip in FCC polycrystalline metals subjected to very high strain rates (10^4 to 10^8 s^{-1}) corresponding to loadings in the weak shock loading regime were deviatoric stresses are significant and the shock waves display distinct elastic and plastic wave fronts. For strain rates higher than 10^8 s^{-1}, i.e. strong shock waves (longitudinal stress amplitudes of the order of 50 to 100 GPa) the deviatoric stresses can be neglected due to the high pressures present (Austin, et al., 2011). Other models for shock-induced plasticity considering that the kinetics of viscoplastic deformation are based on thermally-activated dislocations at the shock front (Armstrong, et al., 2007) (Armstrong, et al., 2009) have been considered by Austin and McDowell to model the metal response at higher shock stress amplitudes. However, the model also considers the weak shock loading regime, were slip is the ruling mechanism for plastic deformation and deviatoric stresses and strains have important effects. Volumetric responses using various equations of state are well studied and deviatoric stress-strain models are difficult to tackle. This is mostly due to the complexity of the deformation mechanisms, the

microstructure evolution and the related dependencies on pressure, temperature and rate of deformation (Austin, et al., 2012). This is why most constitutive models for dynamic strength of metals are underdeveloped. The work of Austin and McDowell (Austin, et al., 2011) addresses this and consists of the following set of differential equations:

$$\frac{d\lambda_1^p}{d\zeta} = \frac{2}{3}\frac{\lambda_1^p}{D}\Phi \tag{3.89}$$

$$\frac{d}{dx}(\Delta\theta^p) = \frac{4}{3}\frac{\beta\lambda\_1\tau}{\rho_0 C_\eta D}\Phi \tag{3.90}$$

$$\frac{dN_m}{d\zeta} = -\frac{\dot{N}_m}{D} \tag{3.91}$$

$$\frac{dN_{im}}{d\zeta} = -\frac{\dot{N}_m}{D} \tag{3.92}$$

In the above equations C_η is the specific heat (per unit mass) at constant elastic configuration, β is the fraction of plastic work that is converted to heat, D is the shock wave velocity defined by an empirical equation of state, ρ_0 is the initial mass density, $\Delta\theta^p$ is the temperature change produced by plastic work, λ_1^p and λ_1 are the plastic and elastic stretch ratios components in the longitudinal direction, N_m and N_{im} are the mobile and immobile dislocation densities, respectively, and τ is the shear stress. The dots represent rates of change of these quantities. An expression for Φ is provided by the Orowan equation,

$$\Phi = bN_m\bar{v} \tag{3.93}$$

where b is as usual the Burgers vector and $\bar{v}$ is the mean dislocation velocity. The independent variable in the differential equations is

$$\zeta = \frac{B_0 c_s}{2\tau_{eff} b} \tag{3.94}$$

where B_0 is the nominal value of the damping coefficient, c_s is the shear wave speed and τ_{eff} is the effective stress. Fig. 3.15 shows comparative results for 6061-T6 AA.

The same authors refined their own model based on previous works (Austin, et al., 2012) (Molinari, et al., 2005) for higher shock stresses by considering homogeneous dislocation nucleation. As in their previous work, this model is unique in the sense that it separates the mobile and immobile dislocation populations, making it possible to distinguish the dislocation segments that cause plastic deformation from those which contribute only to material strength. The model also considers homogeneous and heterogeneous dislocation nucleation. These will be considered in accordance with a microstructure-sensitive criterion depending on the stress wave amplitude ranges in which heterogeneous or homogeneous dislocation nucleation are expected to dominate. The later model extended the range of validity to higher shock stresses by developing a treatment of homogeneous dislocation nucleation. The model has a significant number of parameters to be determined from experiments and proved to be difficult to calibrate. However, it was the first approach that resolved the structure of the shock front. Results were considered to be reasonable for shock-wave induced viscoplastic deformation in polycrystalline Cu, Ni and Al. The constitutive model is also suitable for shockless high-strain-rate loading, e.g. quasi-isentropic compression waves. In these regimes the high strength of the loaded materials observed have been attributed to dislocation drag (Armstrong, et al., 2008) and this feature is already incorporated in the model.

Zhang and co-workers have developed a constitutive model (Clausen, et al., 2004) that although not being referenced very often has been considered to be promising since aluminium alloys containing magnesium show a discontinuous yielding behaviour known as the Portevin Le Chatelier (PLC) effect. It is relevant as it is one of the few constitutive models that take account of this behaviour. PLC effects are believed to be a consequence of dynamic strain ageing (DSA). An increase in strain rate within certain ranges of temperature and strain rate will change the local time dependent concentration of solute atoms at temporarily arrested dislocations (Zhang, et al., 2001). The resulting reduction of the solute concentration will justify negative strain sensitivity of the flow stress in the DSA regime. The resulting instability of the plastic flow will give rise to strain localisation and a repeating phenomenon of initiation and

propagation of deformation bands will manifest by means of a serrated yielding. The associated equivalent plastic strain $\dot{\varepsilon}^p$ is given by

$$\dot{\varepsilon}^p = \dot{\varepsilon}_0 \exp\left(\frac{\sigma_v - \sigma_d}{S} - P_1 C_s'\right) \tag{3.95}$$

The stress σ_d introduces the strain hardening effect associated with the dislocation density

$$\sigma_d = d_1 + d_2\left[1 - \exp\left(-\frac{\varepsilon^p}{d_3}\right)\right] \tag{3.96}$$

S is the strain rate sensitivity and is given by $S = s_1 + s_2\sqrt{\varepsilon^p}$ Coefficients $\dot{\varepsilon}_o, P_1, d_1, d_2, d_3, s_1, s_2$ are experimentally derived constants. The non-dimensional solute concentration is

$$C_s = \{1 - \exp[-P_2(\varepsilon^p)^\alpha (t_a^n)]\} C_m \tag{3.97}$$

where C_m is a saturation value to which the solute concentration will tend as the effective ageing time t_a approaches infinity. P_2, α and n are constants. The method has been used to simulate the deformation behaviour of an Al-Mg-Si alloy and it reproduced the conic morphology of the deformation band associated with the PLC effect as shown in Fig. 3.16. The arrows point the direction of propagation of a localized deformation zone. However results are only available for low strain rate regimes.

Voyadjis and Abed (Voyiadjis, et al., 2005) investigated the Zerilli and Armstrong (Zerilli, et al., 1987) model proposing some modifications such as the evolution of mobile dislocation density. In FCC metals the long-range dislocations intersection controls the mechanism of thermal activation and thermal activation is strongly dependent on the plastic strain. This implies that the distance d, between dislocations and consequently the activation volume is determinant for a formulation that introduces the effect of plastic strain on the thermal component of the material flow stress. Their work presents two models for each type of crystalline structure (BCC or FCC). The following constitutive equation for FCC metals has been proposed for the first model:

$$\sigma = B\varepsilon_p^n \left[1 - \left(\beta_1 T - \beta_2 T \ln \dot{\varepsilon}_p\right)^{1/q}\right]^{1/p} + Y_a \qquad (3.98)$$

where Y_a is the initial temperature independent yield stress, p and q are constants and B and n are plastic hardening constants. At the onset of plastic deformation $\sigma = Y_a$ which is not in total agreement with FCC metal behaviour and led to the introduction of a slight strain and temperature dependence of the initial yield stress. The parameters β_1 and β_2 are related to the material behaviour in accordance with the respective expressions:

$$\beta_2 = \frac{K}{G_0} \qquad (3.99)$$

$$\beta_1 = \frac{K}{G_0}\left(\frac{\tilde{m}b\rho_m v_0}{1-\frac{\tilde{m}l\lambda_1}{b}+\tilde{m}bl\lambda_2\rho_m+\tilde{m}l\lambda_3\sqrt{\rho_f}}\right) \qquad (3.100)$$

where v_0 is the reference dislocation velocity, G is the shear stress-dependent free energy of activation, K is the Boltzmann's constant , b is the Burgers vector, λ_i are constants related, respectively, to the multiplication of mobile dislocations λ_1, their mutual annihilation λ_2 , and their immobilization through intersection with forest dislocations λ_3 , and the remaining variables were previously defined before.

The second model, was based on a different formulation for the activation volume, based on experimental results from Hoge and Mukherjee (Hoge, et al., 1977), and yielded the following equation:

$$\sigma = \left(Y_0 + B\varepsilon_p^n\right)\left(1 + \beta_0 T^m - \beta_1 T + \beta_2 T \ln \dot{\varepsilon}_p\right) + Y_a \qquad (3.101)$$

where β_0 is a function of strain rate. Another form of the above constitutive eq. (3.102) was developed later (Voyiadjis, et al., 2008) considering a power variation for the temperature dependence

$$\sigma = B\varepsilon_p^n \left[1 + B_1 T\left(\dot{\varepsilon}_p\right)^{1/m} - B_2 T \exp\left[A\left(1 - \frac{\tau}{\tau_1}\right)\right]\right] + Y_a \qquad (3.102)$$

The temperature independent stress Y_a is independent of the plastic strain or strain rate and A, B, B_1, B_2, m and n are determined from experimental data. This constitutive model relates stress with strain rate by means of a power term. The power law appears to be more suitable to describe the strain rate dependence for a wider range of rates. The model has been compared with experimental results from other sources for OFHC copper. In Fig. 3.17 results have been compared with experimental data from Nemat-Nassser and Li (Nemat-Nasser, et al., 1998b). The constitutive models eq. (3.102) is similar to the Zerilli-Armstrong (Zerilli, et al., 1987) for the stress-strain behavior of a carbon-steel under different strain rate loading.

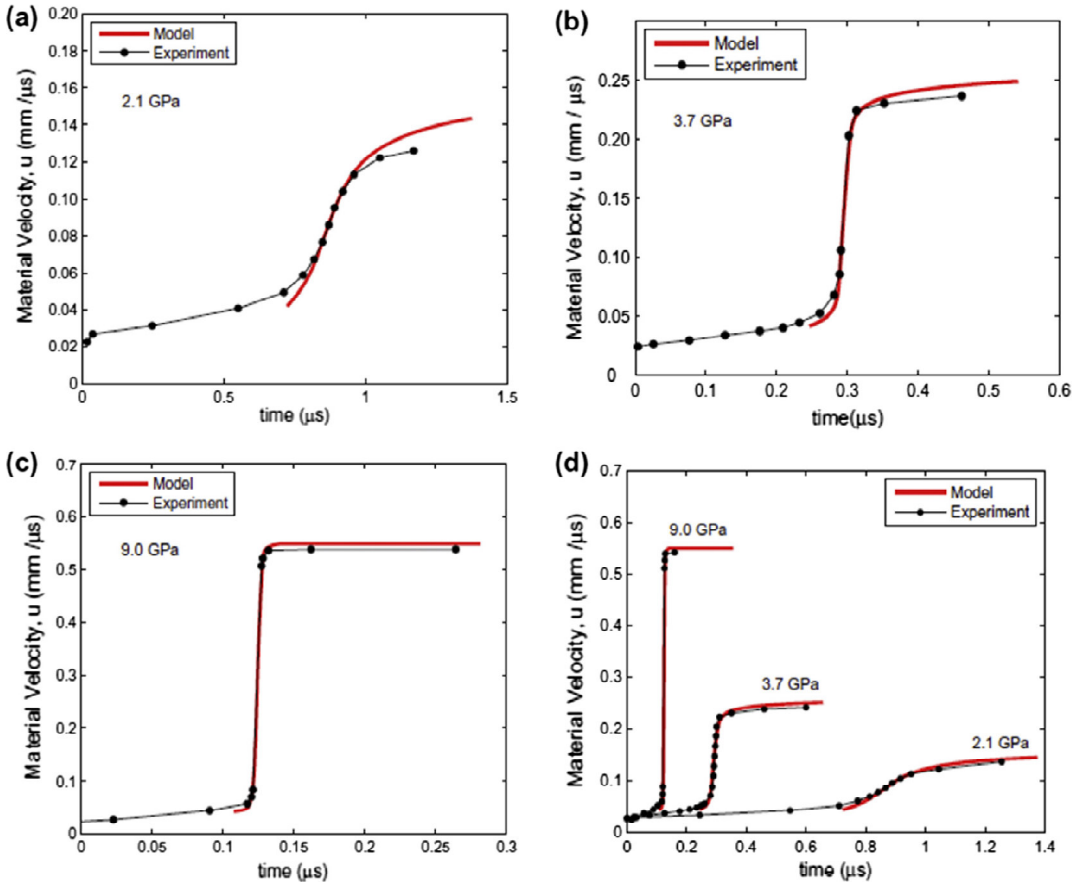

Figure 3. 15 - Fixed-point material velocity profiles for 6071-AA computed using steady wave analysis are compared to experimental measurements for shock stress amplitudes of (a) 2.1 GPa; (b) 3.7 GPa; (c) 9.0 GPa; and (d) material velocities profiles plotted on common axes (reprinted from (Forde, et al., 2009) Copyright 2011, with permission from Elsevier).

Holmedal based his model on the well-known MTS constitutive equation (Follansbee, et al., 1988) whose applicability is limited due to predictions of negative stresses outside of a limited range of strain rates. Consequently, Holmedal considered the use of an algebraic expression for the activation energy term (Kocks, et al., 2003) which made the formulation more general with the equations

$$\dot{\gamma} = \dot{\gamma}_0 \exp\left(-\frac{\Delta G}{KT}\right) - \dot{\gamma}_{\min} \tag{3.103}$$

$$\tau_t = \frac{\mu}{\mu_0}\left\{1 - \left(\frac{KT}{\frac{g_0}{p\mu b^3}}\right)^{\frac{1}{q}} \ln\left(\frac{\dot{\gamma}_0}{\dot{\gamma}+\dot{\gamma}_{\min}}\right)\left|\ln\left(\frac{\dot{\gamma}_0}{\dot{\gamma}+\dot{\gamma}_{\min}}\right)\right|^{\frac{1-q}{q}}\right\}^{1/p} \hat{\tau}_t \tag{3.104}$$

where g is a function of the ratio of the stress and the threshold stress, the meaning of the remaining coefficients was described earlier. Eq. (3.104) provides a value for the thermal stress component of the flow stress (Holmedal, 2007). The new mathematically derived elastoplastic formulation has been applied to OFE copper and compared with the original MTS model.

Another physically based constitutive model for FCC metals that considers temperature and strain-rate effects on the material response has been proposed by Voyadjis and Almasri (Voyiadjis, et al., 2008). It considers the dependence of activation energy on temperature, strain-rate and stress. This is an approach similar to the one of Voyiadjis and Abed (Voyiadjis, et al., 2005) but now a power term relates stress and strain rate while Voyiadjis and Abed (2005) used the logarithm of the strain rate for the stress dependence.

Comparisons were presented for OFHC copper between NNL and the presented method (VA). The VA method gave better predictions at low strains than at higher strains although the NNL model gives a slightly better approximation (see Fig. 3.18).

The Gao and Zhang constitutive model describes the dynamic plasticity of FCC metals using the thermal activation mechanism of dislocation motion under the coupled effect of high strain rate (within the range 10^{-3} to 10^{4} s^{-1}). The equations were successfully applied to the plasticity response of OFHC (Dorward, et al., 1995). This is a physical one-dimensional model based on the idea of thermally activated dislocation motion for moderate strain rates (10^{4} s^{-1}) and dislocation drag deformation mechanism for higher strain rates. The model showed better results than either the JC or the ZA

models when applied to OFHC copper over a broad range of temperatures (from 77 to 1096 K) and strain rates (from 10^{-3} to 10^{4} s^{-1}). The limit of validity for the strain rate in the GZ model was found to be 10^{4} s^{-1}. A new constitutive model was established by the

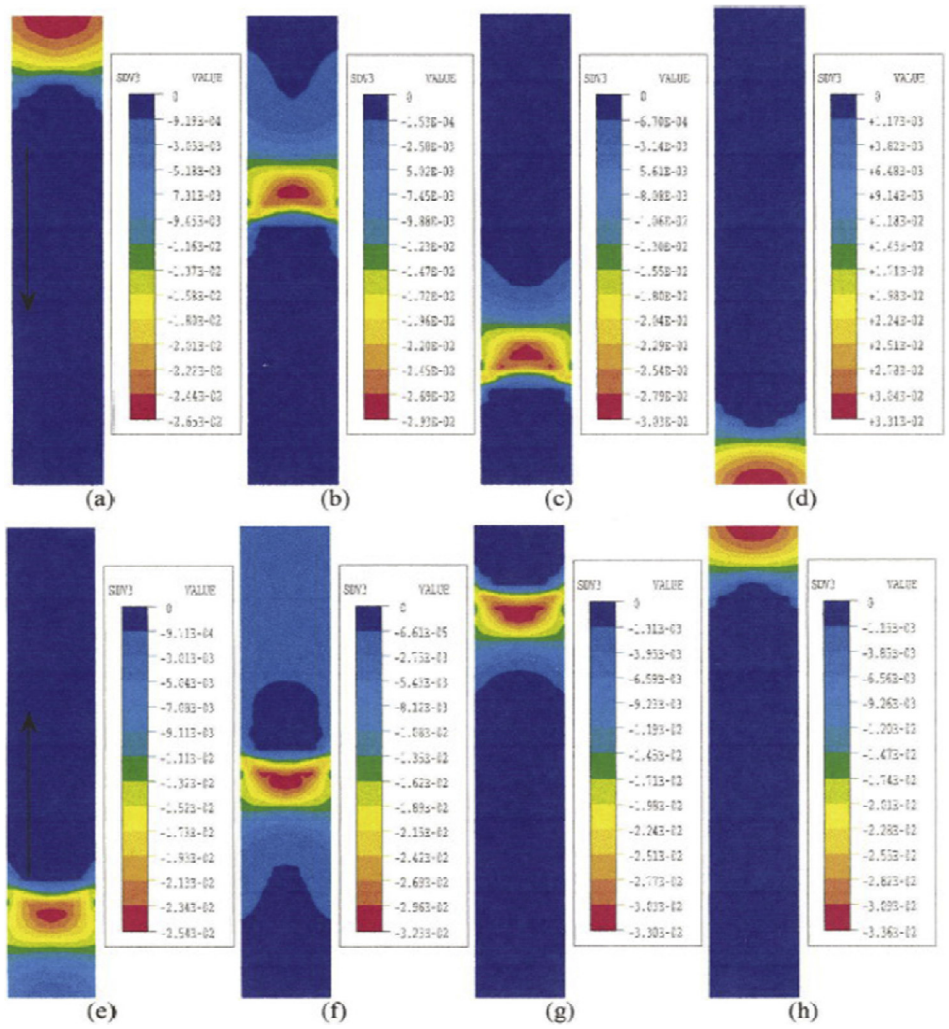

Figure 3.16 - Localised strain-rate pattern in a tensile round bar specimen for an imposed strain rate of 0.002 s-1 (reprinted from [(Zhang, et al., 2001)] Copyright 2001, with permission from Elsevier).

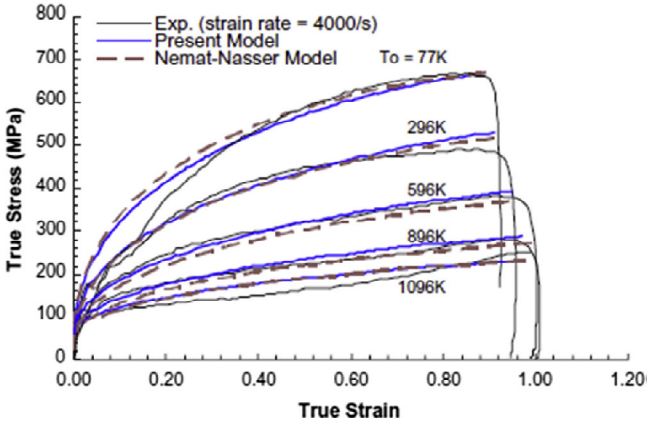

Figure 3. 17 - Adiabatic stress-strain curves for OFHC copper, compared with experimental results at 4000 s-1 strain rates at different initial temperatures (reprinted from (Voyiadjis, et al., 2005) Copyright 2005, with permission from Elsevier).

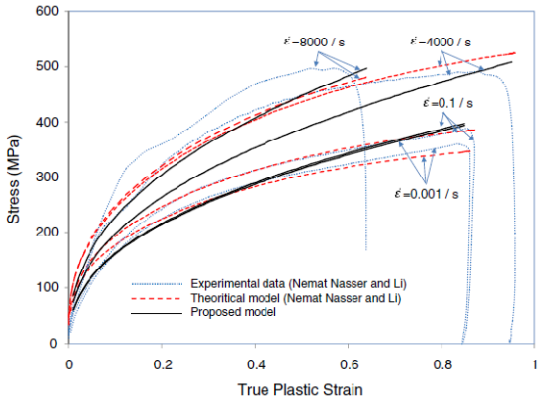

Figure 3.18 - Comparison of VA model for the stress-strain curve at different strain rates with experimental data and the NNL model (Nemat-Nasser, et al., 1998b) (reprinted from (Voyiadjis, et al., 2008) Copyright 2008, with permission from Elsevier).

authors to extend that limit to higher strain rates (Gao, et al., 2012). It is generally not possible to develop a single equation applicable to both the conventional strain rate (10^{-4} to 10^{4} s^{-1}) and the high strain rate ranges (10^{4} to 10^{6} s^{-1}). Most models do not cope with both regimes of strain rate and even the PTW model has a piecewise constitutive form to patch together the low-rate and the extremely high-rate regimes. Therefore, a new unified model was developed considering the athermal and thermal stresses:

$$\sigma_f = \sigma_{ath} + \sigma_{th} =$$
$$\sigma_G + B[1 - \exp(-k_{a0}\varepsilon)]^{1/2} +$$
$$\hat{C}\sqrt{1 - \exp\left[-k_0\left(\frac{\dot{\varepsilon}}{\dot{\varepsilon}_{s0}}\right)^{-C_1 T}\varepsilon\right]}\sqrt{\left\{1 + \tanh\left[C_0 \log\left(\frac{\dot{\varepsilon}}{\dot{\varepsilon}_{s0}}\right)\right]\right\}\left(\frac{\dot{\varepsilon}}{\dot{\varepsilon}_{s0}}\right)^{C_1 T}}\left\{1 -$$
$$-C27\ln\varepsilon\varepsilon s01/q1/p \qquad (3.105)$$

where σ_G is the stress due to initial defects, $\hat{C}$ is the reference thermal stress, C_1 is the absolute rate sensitivity due to defect annihilation, $C_2 = K/(g_o \mu b^3)$ and $B, k_{a0}, \dot{\varepsilon}_{s0}, p, q, n$ are constants to be determined. The above equation is applicable to very high strain rates.

Results from this model for OFHC copper for a high strain rate can be seen in Figs. 3.19 and 3.20 where a comparison with other constitutive models is also presented.

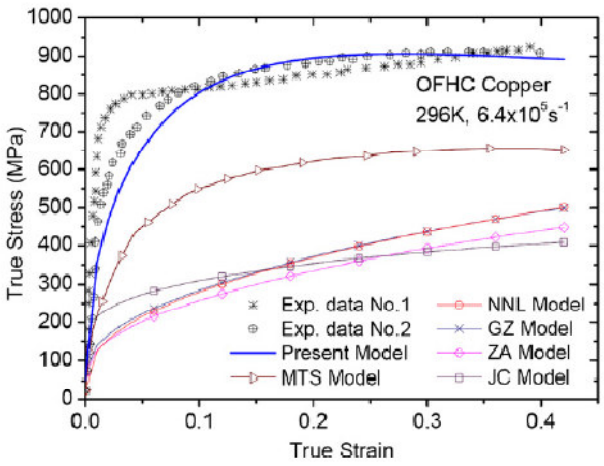

Figure 3. 19 - Comparison of different models' predictions with Clifton's experimental data (Follansbee, et al., 1988)] for the relation of flow stress versus strain in annealed OFHC copper at 6.4×10^5 s^{-1} and room temperature (reprinted from (Gao, et al., 2012) Copyright 2012, with permission from Elsevier).

Goldthorpe has developed a path-dependent constitutive method (Gould, et al., 2000) for gilding copper. The method is said to work well with FCC metals, which depend upon their prior deformation history through the evolution of the structure of

dislocations at different strain rates and temperatures. These two variables will influence dislocation generation and annihilation. The resulting effects of these changing deformation conditions can only be reproduced if the load-path history is considered. The method is a modification of the work of Follansbee and Kock [(Follansbee, et al., 1988) and makes comparisons with results obtained with the Zerilli-Armstrong method (Forde, et al., 2009) (Forde, et al., 2009).

3.2.8 Critical analysis of the selected physically based models

Though far from complete the extents of the list of cited models makes an overall understanding of their differences rather difficult. Some may have result from small changes to other existing models but others resulted from novel approaches and different assumptions. Such understanding requires a systematization of the described models in a way that permits their main features to be pointed. In Table 3.1 such a comparison has been presented and a compilation of the respective proposed constitutive equations is given in Table 3.2.

In the preceding sections some comments on the limitations and capacities of each of the considered models were presented. Most of the methods presented were able to consider strain rates in the high velocity regime ($>10^3$). A few could be used for the specific treatment of materials under shock (such as (Steinberg, et al., 1980), (Steinberg, et al., 1989) (Preston, et al., 2003) and (Austin, et al., 2011)). Theoretical treatment of shock response has normally been addressed by considering the spherical components of stress. The consideration of deviatoric stress-strain models has been much more complex as it involves micro-structure evolution, deformation mechanism and the described dependencies on temperature and rate of deformation. Most authors based their work on dislocation mechanics as shown above and in Table 3.1, below and

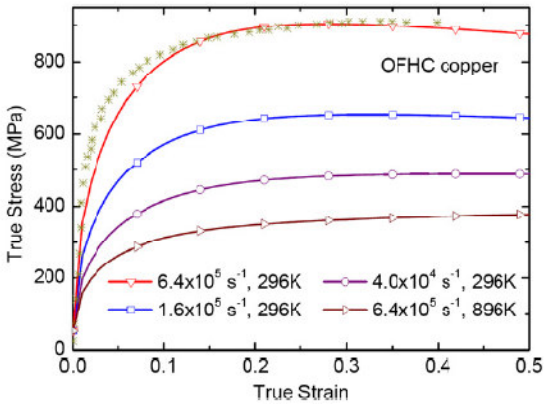

Figure 3. 20 - Model prediction for the relations of flow stress versus strain for OHFC copper under very high strain rates at room and elevated temperatures (reprinted from (Gao, et al., 2012) Copyright 2012, with permission from Elsevier).

although the equations obtained are not the same their physical foundations have a lot in common. Zerilli-Armstrong (Zerilli, et al., 1987) proposed the thermal activation analysis of dislocation motion in which they had many followers. An exception is the MTS (Follansbee, et al., 1988) method in which structural evolution has been based on the flow stress value at 0 K. However, this method has many parameters that are hard to obtain and therefore its calibration is difficult and makes the method far from tractable. Voyadjis-Abed (Voyiadjis, et al., 2005) method came to correct a limitation of the Zerilli-Armstrong model where it was not capable of handling the deformation of metals under high temperature. The Nemat-Nasser-Li method used a varying reference strain rate (Gao, et al., 2010). The Khan–Huang–Liang (Khan, et al., 1992) and Holomon-Voce (Sung, et al., 2010) cannot properly describe the dynamic behaviour of a metal at high strain rates (Gao, et al., 2010).

In general, the more recent work follows previous principles (dislocation mechanics, decomposition of stress in thermal and athermal components, thermal activation, etc..) using other models as starting points. In many cases modification are introduced to obtain better agreement with results of a particular material under test (Gould, et al., 2000).

Table 3. 1- Comparison of the major characteristics of physically based constitutive models.

Year	Model	Strain rate	Main features
1975	Bodner and Parton (Bodner, et al., 1975)	10^{-5} to 10^{-4} s^{-1} (10^{-3} s^{-1} to 1 modified by (Chen, 2008)	• Based upon separation of the total deformation rate into elastic and plastic components • Incorporates strain hardening effects through a plastic work term • Assumes a dependency on J2 invariant • No temperature effects;
1980	Steinberg and Guinan (Steinberg, et al., 1980)	10^{5} s^{-1}	• Incorporates temperature effects, • Considers the effect of shock pressure • Based on equivalent plastic strain
1987	Zerilli-Armstrong (Zerilli, et al., 1987)	$4x10^{3}$ s^{-1}	• Considers temperature effects • Considers grain size. • Based on dislocation mechanics • Considers thermal activation
1988	Mechanical threshold stress (Follansbee, et al., 1988)	10^{-4} to 10^{4} s^{-1}	• Incorporates temperature effects • Based on thermal activation • Uses the flow stress at 0 K (MTS) • Based on dislocation density as state variable
1989	Steinberg and Lund (Banerjee, 2007)	10^{-4} to 10^{6} s^{-1}	• Considers thermal activation • Includes the effect of temperature • Extends the Steinberg and Guinan model • Based on equivalent plastic strain • Considers the pressure
1998	Nemat-Nasser and Li (Nemat-Nasser, et al., 1998b)	10^{-3} to 10^{4} s^{-1}	• Considers dislocation mechanics • Considers thermal activation • Considers temperature
2001	Nemat-Nasser, Guo and Kihl (Armstrong, et al., 2009)	10^{-2} to $\approx 10^{4}$ s^{-1}	• Based on dislocation motion mechanics • Includes viscous drag effects on dislocation motion
2003	Preston, Tonks and Wallace (Preston, et al., 2003)	10^{-3} to 10^{9} s^{-1}	• Uses an Arrhenius form for plastic strain rate but with an activation energy • Suitable for explosive loading
2001	Rusinek and Klepaczko (Clausen, et al., 2004)	10^{-4} to 10^{3} s^{-1}	• Includes temperature effects • Based on two components of stress: effective and internal • Uses an Arrehnius type eq. for the effective component of stress
2011	Austin and McDowell (Forde, et al., 2009)	10^{4} to 10^{8} s^{-1}	• Based on dislocation densities as state variables • Uses J2 flow theory • First plastic-wave analysis using dislocation mechanics in the weak shock regime
2001	Zhang, McCormick and Estrin (Rule, et al., 1998)	10^{-3}	• Models the Portevin-Le Chatelier effect • Based upon separation of the total deformation rate into elastic and plastic components
1982	Anand (Zhang, et al., 2009)	10^{-2}	• Considers temperature • Activation energy • Considers dynamic recovery
2005	Voyadjis and Abed (Vural, et al., 2009)	10^{-3} to 10^{4} s^{-1}	• Modified ZA model • Based on dislocation mechanics • Considers thermal activation
2007	Holmedal (Lin, et al., 2010)	10^{-4} to 10^{9}	• Modification of MTS method
2008	Voyadjis and Almasri (Voyiadjis, et al., 2008)	10^{-4} to 10^{4}	• Based on VA model • Based on dislocation density • Considers temperature effects • Considers activation energy
	Gao and Zhang (Gao, et al.,	10^{-3} to 10^{4}	• Based on dislocation motion • Considers thermal activation

2012	2012)		• Considers dislocation drag for high strain rates
2009	Huang et al. (Shin, et al., 2010)	10^{-5} to 10^{6} s^{-1}	• Dislocation mechanics • Thermal activation • Temperature
2000	Gould and Goldthorpe (Gould, et al., 2000)	Not indicated	• Based on Follansbee and Kocks [17] model • Temperature effect • Dislocation motion • Thermal activation

Table 3.1 (Continuation)

Table 3. 2– Constitutive equations of the indicated models

Bodner and Partom (Bodner, et al., 1975) $\varepsilon_x^p = \frac{2D_0}{\sqrt{3}}\frac{\sigma}{|\sigma|}\exp\left[-\frac{1}{2}\left(\frac{3A^2}{\sigma^2}\right)^n\right]$

Steinberg and Guinan (Steinberg, et al., 1980)

$$Y = Y_0[1+\beta(\varepsilon+\varepsilon_1)]^n\left[1+\left(\frac{Y_p'}{Y_0}\right)\frac{P}{\eta^{\frac{1}{3}}}+\left(\frac{G_T'}{G_0}\right)(T-300)\right]$$

Zerilli and Armstrong (Zerilli, et al., 1987) $\sigma = \sigma_a + C_2\varepsilon^{\frac{1}{2}}\exp(-C_3T + C_4T\ln\dot{\varepsilon}) + kl^{-\frac{1}{2}}$

MTS (Follansbee, et al., 1988) $\sigma = \hat{\sigma}_a + (\hat{\sigma}-\hat{\sigma}_a)\left\{1-\left[\frac{KT\ln\left(\dot{\varepsilon}_0/\dot{\varepsilon}\right)}{g_0\mu b^3}\right]^{\frac{1}{q}}\right\}^{\frac{1}{p}}$

Steinberg and Lund (Banerjee, 2007) $\dot{\varepsilon}_p = \frac{1}{C_1}\exp\left[\frac{2U_k}{KT}\left(1-\frac{\sigma_t}{\sigma_p}\right)^2\right]+\frac{C_2}{\sigma_t}$

Nemat-Nasser and Li (Nemat-Nasser, et al., 1998b)

$$\tau(\dot{\gamma},\gamma,T) = \tau^o\left\{1-\left[-\frac{KT}{G_0}\left(\ln\frac{\dot{\gamma}}{\dot{\gamma}_0}+\ln\left(1+a(T)\gamma^{\frac{1}{2}}\right)\right)\right]^{\frac{1}{2}}\right\}^{\frac{3}{2}}\left[1+a(T)\gamma^{\frac{1}{2}}\right]+\tau_a^o\gamma^{n_1}$$

Nemat-Nasser, Guo and Kihil (Armstrong, et al., 2009)

$$\tau^* = \tau^0\left\{1-\left[-\frac{KT}{G_0}\ln\left(\frac{\dot{\gamma}f(\gamma,T)}{\dot{\gamma}}\right)\right]^{\frac{1}{q}}\right\}^{\frac{1}{p}}f(\gamma,T) \quad \text{for } T \le T_c$$

Preston-Tonks-Wallace (Preston, et al., 2003)

$$\hat{\tau} = \hat{\tau}_s + \frac{1}{p}(s_0 - \hat{\tau}_y)\ln\left\{1 - \left[1 - \exp\left(-p\frac{\hat{\tau}_s - \hat{\tau}_y}{s_0 - \hat{\tau}_y}\right)\right]\exp\left[-p\theta\psi\left[(s_0 - \hat{\tau}_y)\left[\exp\left(p\frac{\hat{\tau}_s - \hat{\tau}_y}{s_0 - \hat{\tau}_y}\right) - 1\right]\right]^{-1}\right]\right\}$$

Rusineck-Klepcazko (Clausen, et al., 2004)

$$\sigma = \frac{E(T)}{E_0}\left[B_0\theta_m^{-v}(\varepsilon_0 + \varepsilon^p)^{n_0(1-D_2\theta_n)} + \sigma_0^*(1 - D_1\theta_m)^m + \sigma_{ns}\right]$$

Voyadjis-Abed (Vural, et al., 2009) $$\sigma = B\varepsilon_p^n\left[1 - \left(\beta_1 T - \beta_2 T\ln\dot{\varepsilon}_p\right)^{1/q}\right]^{1/p} + Y_a$$

Voyadjid-Almasri (Voyiadjis, et al., 2008)

$$\sigma = B\varepsilon_p^n\left[1 + B_1 T\left(\dot{\varepsilon}_p\right)^{1/m} - B_2 T\exp\left[A\left(1 - \frac{T}{T_t}\right)\right]\right] + Y_a$$

Gao-Zhang (Gao, et al., 2012)

$$\sigma = \hat{\sigma}_a + \hat{Y}\varepsilon^n\exp\left[C_3 T\ln\left(\frac{\dot{\varepsilon}}{\dot{\varepsilon}_{s0}}\right)\right]\left\{1 - \left[-C_4 T\ln\left(\frac{\dot{\varepsilon}}{\dot{\varepsilon}_0}\right)\right]^{1/q}\right\}^{1/p}$$

Huang (Shin, et al., 2010) $$\tau = \alpha\mu b\sqrt{\rho} + \left[B_{wind}^0 + \frac{B_{flutter}^0}{1 - \left(\frac{\dot{\gamma}}{b\rho_m C_t}\right)^2}\right]\frac{T}{\theta_D}\frac{\dot{\gamma}}{b^2\rho_m}$$

Gould and Goldthorpe (Gould, et al., 2000) $$\bar{\sigma} = \sigma_a + \phi\eta\left\{1 - \left[\alpha - \theta\frac{\varepsilon}{\eta} + 1\right]^{\frac{1}{1-\alpha}}\right\}$$

Table 3.2 (Continuation)

3.2.9 Phenomenological constitutive equations

Phenomenological constitutive relations are equations normally derived from experimental data rather than from physical principles. However, they are widely used because they are simple to implement and the parameters are often easier to obtain. Although they are not derived from first principles they have physical meaning and can

provide accurate results. The main phenomenological constitutive relations will be presented in the next sections.

3.2.9.1 Molinari-Ravichandran (MR)

This is a single internal variable phenomenological model based on a characteristic length scale of the microstructure that develops in the metal during deformation. A scaling law was considered for the evolution of this characteristic or effective length δ during experimental observations as this variable mimics the cell size δ_c, which is an important structure parameter. The evolution of δ can be described by

$$\frac{d\delta}{d\varepsilon} = -\frac{\delta_r}{\delta_s}[\delta^2 - \delta_s\delta] \tag{3.106}$$

where the expressions for the microstructure refinement rate δ_r, and the saturation value of the microstructure length δ_s at large strains, are empirical or may be derived from the theory of thermally activated processes, and are functions of temperature and strain rate. Using the second approach, the following expressions were derived:

$$\frac{\delta_r}{\delta_{r0}} = \left\{1 - \left[k_r\left(\frac{T}{T_{r0}}\right)\log\left(\frac{\dot{\varepsilon}_{r0}}{\dot{\varepsilon}}\right)\right]^{p_r}\right\}^{q_r} \tag{3.107}$$

$$\frac{\delta_s}{\delta_{s0}} = \frac{1}{\left\{1-\left[k_r\left(\frac{T}{T_{r0}}\right)\log\left(\frac{\dot{\varepsilon}_{r0}}{\dot{\varepsilon}}\right)\right]^{p_s}\right\}^{q_s}} \tag{3.108}$$

where δ_{ro} and δ_{so} are the reference values of δ_r and δ_s, respectively, and $k_r, p_r, q_r, k_s, p_s,$ and q_s are constants that describe the dependence of micro-structural refinement and steady state characteristic length on strain rate and temperature. $T_{ro}, T_{so}, \dot{\varepsilon}_{ro}$ and $\dot{\varepsilon}_{so}$ are reference temperatures and strain rates for modelling the observed behaviours in micro-structure refinement and steady state characteristic length. The flow stress is a function of the intrinsic resistance of the material and the strain-rate and it is expressed as (Clausen, et al., 2004):

$$\sigma = \sigma_0 \left(\frac{\dot{\varepsilon}}{\dot{\varepsilon}_0}\right)^{1/m} \quad ((3.109)a)$$

$$\sigma_0 = \hat{\sigma}(d)\left(\frac{\delta}{\delta_0}\right) \quad ((3.109)b)$$

where $\dot{\varepsilon}_o$ is the reference strain-rate and m is the instantaneous material strain rate sensitivity which is a function of the temperature. It accounts for part of the thermal softening of the material due to the change in ambient temperature and the rise of temperature during adiabatic deformation. The other part of the thermal softening is controlled by the temperature dependence of δ_{ro} and δ_{so}. d is the grain size and is the internal characteristic length which reduces when the plastic strain ε increases in accordance with a phenomenological evolution equation. This internal variable, governed by an evolution law with temperature and rate-dependent coefficients, expresses the response of the material in a simple way, adequate for engineering applications. Other authors used the same approach based on a single internal parameter as micro-scale models demand too much computational time for applications to high-speed dynamics (Durrenberger, et al., 2008). Their work used part of the MR model (Molinari, et al., 2005). It reproduced strain-rate history effects for various materials at a range of strain rates from $8\text{x}10^{-3}$ to 10^3 s^{-1}. Fig. 3.21 shows results for copper at a strain rate of 5000 s^{-1}.

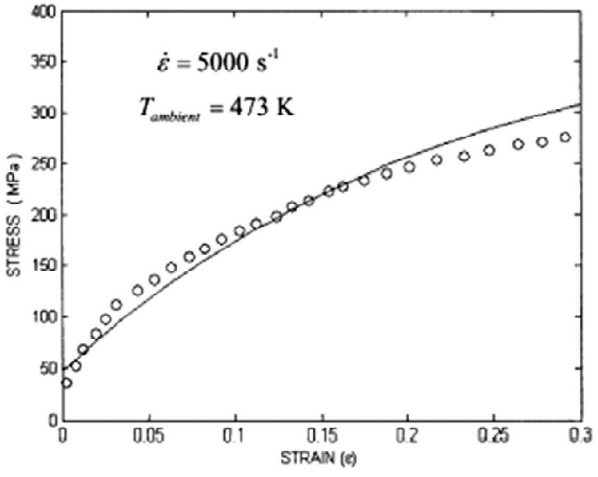

Figure 3. 21 - Model prediction (solid line) compared with experimental results (circles) for a compression test for annealed copper (Follansbee, et al., 1988) (reprinted from (Molinari, et al., 2005) Copyright 2005, with permission from Elsevier).

3.2.9.2 Johnson and Cook (JC)

Perhaps the most widely used constitutive model for high strain rate applications is the Johnson-Cook (JC) (Johnson, et al., 1983) empirical equation. One of the reasons for this preference resides in its simplicity as it only requires calibration of five parameters and has been successfully used for a wide range of materials at different temperatures and strain-rates. It has also been the object of many modifications, which demonstrates the generalised interest that it raises throughout the scientific and engineering community. This model assumes that the material is isotropic and its constitutive relation is

$$\sigma_{eq} = (A + B\varepsilon^n)(1 + C \ln \dot{\varepsilon}^*)(1 - T^{*m}) \tag{3.110}$$

where σ_{eq} is the von Mises equivalent flow stress, ε is the equivalent plastic strain, $\dot{\varepsilon}^* = \dot{\varepsilon}/\dot{\varepsilon}_o$ is a dimensionless plastic strain rate ($\dot{\varepsilon}_o$ is a reference strain-rate, set to 1 s^{-1}) and $T^* = (T - T_o)/(T_m - T_o)$ is a dimensionless temperature where T_m is the melting temperature and T_o is room temperature. A is the yield stress at a reference temperature and a reference strain-rate, B is a strain-hardening coefficient and n is the strain-hardening exponent. C and m are material constants that represent the coefficient of strain-rate hardening and a thermal softening coefficient, respectively.

The equivalent flow stress is then the product of three factors taken independently without concern about strain-rate or temperature history effects, strain hardening, strain rate and the softening effect temperature. The constants are parameters to be obtained from experiments (e.g. Split Hopkinson Tension Bar) although originally they were obtained from Taylor impact. When the loading approaches static conditions (low plastic strain rate, $\dot{\varepsilon}^*$) the $\ln \dot{\varepsilon}^*$ term tends to infinity and so a modification to the JC equation has been suggested by Borvik (Borvik, et al., 2001a)]. The modified equation is:

$$\sigma_{eq} = \left(a + B\varepsilon_{eq}^n\right)\left(1 + \dot{\varepsilon}_{eq}^*\right)^C (1 - T^{*m}) \tag{3.111}$$

Another modification to the J-C model was proposed to account for the strengthening exhibited by many ductile metals at strain rates above 10^4 s^{-1} (Rule, et al., 1998). To better reproduce that high strain rate sensitivity, Rule and Jones proposed the following revised Johnson-Cook equation (RJC):

$$\sigma = (C_1 + C_2\varepsilon^n)\left[1 + C_3 \ln \dot{\varepsilon}^* + C_4\left(\frac{\dot{1}}{C_5 - \ln \dot{\varepsilon}^*} - \frac{1}{C_5}\right)\right](1 - T^{*m}) \qquad (3.112)$$

where C_1 to C_5 are material constants. The term $1/(C_5 - \ln \dot{\varepsilon}^*)$ increases the strain rate sensitivity at higher rates and parameter C_4 controls how much the RJC model deviates from the original. To solve the problem of the yield stress being unbounded and tending to infinity as $(C_5 - \ln \dot{\varepsilon}^*)$ approaches zero these authors defined an extra non-dimensional parameter, C_6, defined as

$$\left[1 + C_3 \ln \dot{\varepsilon}^* + C_4\left(\frac{\dot{1}}{C_5 - \ln \dot{\varepsilon}^*} - \frac{1}{C_5}\right)\right] \leq C_6 \qquad (3.113)$$

This way the strain rate sensitivity term will be limited to a maximum value. A number of other authors have been experimenting with other modifications to the JC model. Rule and Jones (Rule, et al., 1998) cite two modifications (Holmquist TJ, Johnson GR, *J. Phys. France*, 1, C3-853, 1991 and Kang WJ, Cho SS, Huh H and Chung DT, *Int. J. Vehicle Design*, Vol 21, Nos. 4/5, 1999, pp.424-435). The first has not been widely used due to the fact that the modified version did not produce a significant enhancement over that provided by the original formulation. The second modification introduced a quadratic form for the strain rate sensitivity such that

$$\sigma_{eq} = (A + B\varepsilon^n)(1 + C_1 \ln \dot{\varepsilon}^* + C_2(\ln \dot{\varepsilon}^*)^2)(1 - T^{*m}) \qquad (3.114)$$

Another modification (Zhang, et al., 2009) considered the effect of temperature on the strain rate-hardening behaviour of IC10, and can be expressed as:

$$\sigma = [A(1 - T^m) + BT^*\varepsilon^n](1 + C \ln \dot{\varepsilon}^*) \qquad (3.115)$$

where the coefficients maintain their original meanings and the following additional function $B(T^*)$ is introduced:

$$B(T^*) = \frac{\sigma_{br}(1-T^{m_1})-\sigma_{0.2r}(1-T^{*m})}{\left[\varepsilon_{br}(1-P_1T^*-P_2T^{*P_3})\right]^n} \quad (3.116)$$

where m_1, P_1, P_2 and P_3 are material constants, σ_{br} is designated by the author as *broken stress* at room temperature and reference strain rate and ε_{br} is the corresponding strain at room temperature and reference strain-rate. Finally $\sigma_{0.2r}$ is the yield stress at $\varepsilon = 0$.

Vural and Cairo (Vural, et al., 2009) derived another modified version of the JC equation noting that experiments show that strain-hardening decreases faster than predicted by the thermal softening rate term in the original JC model. To provide a direct coupling between temperature and strain-hardening they introduced the modification $B = B_o(1 - T^{*P})$ (Khan, et al., 2004) where P is a material constant. They also noted that the original JC model does not provide an enhanced strain rate effect at high rates and gives a too small and unrealistic strain rate dependence at high temperatures, and introduced a temperature dependence in the strain-rate sensitivity parameter C. The MJC equation has the following final form:

$$\sigma = \left\{\sigma_0 + B_0\left[1 - \left(\frac{T-T_0}{T_m-rmT_0}\right)^P\right]\varepsilon_p^n\right\}\left[1 + (C_1T_r^{*P} + C_2H)\ln\left(\frac{\dot{\varepsilon}}{\dot{\varepsilon}_0}\right)\right]\left[1 - \left(\frac{T-T_0}{T_r-T_0}\right)^P\right] \quad (3.117)$$

where $H(\dot{\varepsilon}, \dot{\varepsilon}_t, k) = \frac{1}{2} + \frac{1}{2}\tanh\left[k\ln\left(\frac{\dot{\varepsilon}}{\dot{\varepsilon}_r}\right)\right]$ and C_1 and C_2 are the rate sensitivity in the quasi-static strain rate regime ($\dot{\varepsilon} < \dot{\varepsilon}_t$) and the enhancement in rate sensitivity in the dynamic strain-rate regime ($\dot{\varepsilon} > \dot{\varepsilon}_t$), respectively. H is a smooth approximation of the Heaviside step function. The transition interval between quasi-static and dynamic regimes can be made to vary thanks to the scaling factor k. Examples of results obtained with the MJC are shown in Fig. 3.22 where comparison is made with experimental data for a 2139-T8 aluminium alloy subject to uni-axial compression and tension experiments over a range of strain rates up to 10^4 s^{-1}.

Lin and co-workers (Lin, et al., 2010) proposed another modified JC equation considering the coupled effects of temperature and strain rate, giving the following expression (Lin, et al., 2010):

$$\sigma = (A_1 + B_1\varepsilon + B_2\varepsilon^2)(1 + C_1 \ln \dot{\varepsilon}^*) \exp[(\lambda_1 + \lambda_2 \ln \dot{\varepsilon}^*)(T - T_r)] \qquad (3.118)$$

where $A_1, B_1, B_2, C_1, \lambda_1, \lambda_2$ are material constants and all the other parameters keep their original meanings.

Other modifications of the JC model are available in the literature but most of them were developed for specific materials (Shin, et al., 2010) (Wang, et al., 2004) (Hou, et al., 2010). However, it is important to refer to a hybrid model resulting from the Johnson-Cook and Zerilli-Armstrong constitutive models, namely a physically based model developed to describe the response of 42CrMo alloy steel to hot compression (Lin, et al., 2010). Another JC equation for use with aluminium alloys, in particular an Al-Cu-Mg alloy under hot forming loads has been published-(Lin, et al., 2012). The authors tried to use the JC model but it failed to provide accurate results for the high temperature flow stress of the alloy studied. Modifications were introduced based on the Zener-Hollomon parameter but as only low strain rates were considered, the model will not be described here. The method is an extension of the JC constitutive model. This method has been widely used by the research and engineering community and a large amount of data has been and still continuous to be published based on its use.

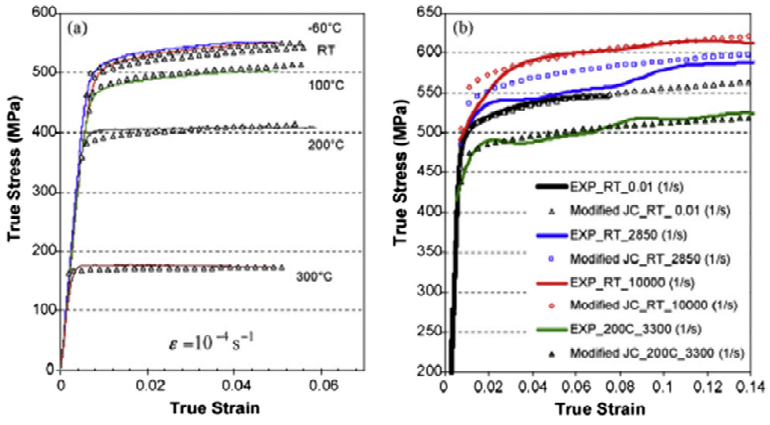

Figure 3. 22 - Comparison of experimental stress-strain curves (solid lines) with MJC model predictions: (a) temperature dependence of flow stress at a reference strain rate of 10-4 s-1; and (b) effect of strain rate and temperature (reprinted from (Vural, et al., 2009) Copyright 2009, with permission from Elsevier).

3.2.9.3 Khan-Huang (KH) and Khan-Huang-Liang (KHL)

Khan and Huang (Khan, et al., 1992) introduced a viscoplastic constitutive model (KH model) to simulate the response of alloy AA 1100 to a wide range of strain rates. They proposed a relation between the second invariant of the deviatoric stress J_2, and functions of the equivalent strain and the second invariants of the plastic deformation rate:

$$J_2 = f_1(\varepsilon) f_2\left(D_2^p\right) \tag{3.119}$$

This expression can be simplified for a one-dimensional case giving $\sigma = g_1(\varepsilon) g_2(\dot{\varepsilon})$ where g_1 describes the correlation of the stress with the plastic strain at the reference strain-rate and g_2 represents the dependence on the strain-rate, that is,

$$g_1(\varepsilon) = \left[3 f_1\left(\frac{3}{4}\varepsilon^2\right)\right]^{\frac{1}{2}} \tag{3.120}$$

$$g_2(\dot{\varepsilon}) = \left[f_2\left(\frac{3}{4}\dot{\varepsilon}^2\right)\right]^{\frac{1}{2}} \tag{3.121}$$

Particular forms for the above functions were presented as

$$g_1(\varepsilon^p) = \sigma_0 + E_\infty \varepsilon^p - a e^{-\alpha \varepsilon^p} \tag{3.122)a}$$

$$g_2(\dot{\varepsilon}^p) = 1 \Big/ \left[1 - \frac{\ln(\dot{\varepsilon}^p)}{\ln(D_0^p)}\right] \tag{3.123)b}$$

where the five constants necessary to calibrate the model are n, E_∞, σ_o, a and α. D_2^p has been chosen to be 10^6 s^{-1} by Khan and co-workers. The model is capable of predicting the strong work-hardening behaviour at larger strain rate regimes than those of the BP model. However, it is worth noticing that no temperature effects have been included in these constitutive equations. The lack of temperature effects led to further

modifications. Meanwhile, a constitutive model has been proposed based on BP model assumptions (Liang, et al., 1999). A modification to that model was proposed by Khan and Liang (Khan, et al., 1999) to introduce the coupled work hardening dependence of flow stress on strain, strain rate and the temperature dependency that was lacking in the previous model. Basically, a temperature multiplicative factor similar to that of JC equation was introduced to improve correlation with experiments. Khan and Liang (1999) started with a new relation between D_2^p and J_2,

$$J_2 = f_1\left(\varepsilon_2, D_2^p\right) f_2(T) \tag{3.124}$$

where ε_2 is the equivalent strain, f_1 describes the coupled strain and strain rate effects on the work-hardening behaviour. The resulting constitutive equation is known as the KHL model,

$$\sigma = \left[A + B\left(1 - \frac{\ln(\dot{\varepsilon}^p)}{\ln(D_0^p)}\right)^{n_1} \varepsilon^{n_0}\right](1 - T^{*m}) e^{C \ln(\dot{\varepsilon})} \tag{3.125a}$$

$$T^* = \frac{T - T_r}{T_m - T_r} \tag{3.125b}$$

where σ, ε, $\dot{\varepsilon}$ are the von Mises equivalent stress, strain and strain-hardening, respectively, and T, T_m and T_r are absolute temperature, melting temperature and reference temperature, respectively. The other parameters A, B, n_o, n_1, C and m are empirical constants. As in other constitutive models the number of parameters to be determined is within tractable limits. Better agreement with experimental data has been obtained but only BCC metals were tested. Later work on tantalum alloy and AerMet 100 steel tested the suitability of the new model to predict complex loading paths of current experimental results (Khan, et al., 2000 a). The model successfully predicted non-proportional experimental results.

In a later study Khan and co-workers adopted the Hall-Petch relation $\sigma_y = a + k/\sqrt{d}$ in the KHL equation, where σ_y is the yield stress, d is the polycrystal average grain size and a and k are material constants) obtaining a model for coarse-grained polycrystalline materials (Khan, et al., 2000 b). The KHL model was further

modified to account for grain size dependence, work hardening, rate sensitivity and temperature effect, as deemed necessary to reproduce the behaviour of fully compacted nanocrystalline iron. Results have shown that the modified KHL model correlates reasonably with both isothermal and adiabatic experimental results. The modified equation is

$$\sigma = \left[\left(a + \frac{k}{\sqrt{d}}\right) + B\left(1 - \frac{\ln(\dot{\varepsilon}^p)}{\ln(D_0^p)}\right)^{n_1} \varepsilon^{n_0}\right](1 - T^m)\dot{\varepsilon}^C \qquad (3.126)$$

A modified version of the KHL model (Khan, et al., 2004) was used for the Ti-6Al-4V alloy to compare with the JC model and experimental results. The KHL model, as given by the following equation, led to much better predictions than the JC model,

$$\sigma = \left[A + B\left(1 - \frac{\ln(\dot{\varepsilon}^p)}{\ln(D_0^p)}\right)^{n_1} \varepsilon^{n_0}\right]\left(\frac{T_m - T}{T_m - T_r}\right)^m \left(\frac{\dot{\varepsilon}^p}{\dot{\varepsilon}^{p*}}\right)^C \qquad (3.127)$$

where σ is the stress and ε^p is the plastic strain, T_m, T and T_r are melting, current and reference temperatures, respectively, $D_o^p = 10^6$ s^{-1}, which is an arbitrary value chosen as an upper bound strain rate, $\dot{\varepsilon}^* = 1$ s^{-1} is a reference strain rate at which some material constants are determined, $\dot{\varepsilon}$ is the current strain rate and A, B, n_1, n_0, C and m are material constants. This model can reproduce the decreasing work-hardening behaviour observed with increasing strain rate through the material constant n_1. The KHL model has a simple temperature dependent term in a multiplicative form. Because of this, the temperature dependence of different metals may not be easy to describe and many attempts led to modified versions of the model, with more constants to be determined.

In 2006, the analysis of the mechanical properties of nanocrystalline aluminium and iron led to another modification to the method (Khan, et al., 2006), including the following bilinear Hall-Petch type relation:

$$\sigma = \left(a + \frac{k}{\sqrt{d}}\right)\left[1 + \frac{B}{a}\left(1 - \frac{\ln(\dot{\varepsilon}^p)}{\ln(D_0^p)}\right)^{n_1} \varepsilon^{n_0}\right]\left(\frac{T_m - T}{T_m - T_r}\right)^m \left(\frac{\dot{\varepsilon}^p}{\dot{\varepsilon}^{p*}}\right)^C \qquad (3.128)$$

The KHL model was also applied to the microscopic stress and strain rate of a nanocrystalline iron and copper mixture (80% Fe and 20% Cu) (Khan, et al., 2000c) assuming the equivalence between macroscopic and microscopic properties:

$$\sigma_M = \left[\sigma_0 + B\left(1 - \frac{\ln(\dot{\varepsilon}_M)}{\ln(D_0^p)}\right)^{n_1} \varepsilon_M^{n_0}\right](1 - T^{*m})\dot{\varepsilon}_M^C \qquad (3.129)a$$

$$T^* = \frac{T - T_r}{T_m - T_r} \qquad (3.129)b$$

where σ_M, ε_M and $\dot{\varepsilon}_M$ are microscopic von Mises equivalent stress, strain and strain rate, respectively, in the matrix material. T is the absolute temperature, T_m is the melting temperature of the material and T_r is a reference temperature. The remaining parameters are material constants as described before.

Yu and co-workers also used the KH model to analyse data from impact experiments in a dual phase 600 steel (DP600) at strain rates ranging from 10^{-4} to 1.6×10^3 s^{-1}. However, the results show a gap between experimental and model predictions at higher strains. This led the authors to propose a new modified KH plastic constitutive model (Yu, et al., 2009) expressed as follows:

$$\sigma = f(\varepsilon^p, \dot{\varepsilon}^p) = \sigma_0 \hat{f}_2(\dot{\varepsilon}^p) + E_\infty \varepsilon^p - a e^{-\alpha \varepsilon^p} \qquad (3.130a)$$

with

$$f_2(\dot{\varepsilon}^p) = 1 + D\left(\ln \frac{\dot{\varepsilon}^p}{\dot{\varepsilon}_0^p}\right)^m \qquad (3.130b)$$

where D and m are material constants. As in the former constitutive model KH, temperature effects were ignored in this new model. In Fig. 3.23 results for the modified KHL model are presented for the stress strain curves at various strain rates, together with measured results. A new grain size and temperature dependent viscoplastic model (Farrokh, et al., 2009) was derived from the KHL (Khan – Huang – Liang) constitutive equation (Khan, et al., 2000 b) (Khan, et al., 2004) (Khan, et al., 2006) to account for

different polycrystalline plastic behaviour as a result of grain refinement. This new constitutive model (see Fig. 3.24), can be described by the following relation:

$$\sigma = \left[\left(a + \frac{k}{d^{n*}}\right) + B\left(\frac{d}{d_0}\right)^{n_2}\left[\left(1 - \frac{\ln(\dot{\varepsilon}^p)}{\ln(D_0^p)}\right)\left(\frac{T_m}{T}\right)\right]^{n_1}(\varepsilon^p)^{n_0}\right]\left(\frac{T_m - T}{T_m - T_{ref}}\right)^m\left(\frac{\dot{\varepsilon}^p}{\dot{\varepsilon}^{p*}}\right)^C \qquad (3.131)$$

where $\dot{\varepsilon}^p$, ε^p are plastic strain and current strain rate, σ is the flow stress, T_m, T and T_{ref} are melting, current and reference temperatures, respectively. D_o^p is an arbitrarily chosen upper bound strain rate, $\dot{\varepsilon}^{p*} = 1$ is a reference strain rate at which certain material constants are obtained and $n^* = 0.5$ (while material follows the Hall-Petch relationship). Coefficients d and d_0 are the average grain size of the material under test and its corresponding coarse-grained counterpart respectively ($d_0 \approx 50\ \mu m$). a, k, $n1$, n_2, c, m and B are material constants.

The proposed model adds a few extra terms to simulate the change in work hardening behaviour as the result of grain refinement and different temperatures. Good correlations were obtained for mechanically milled Cu and Al and it can capture the change in yield stress and work-hardening behaviour with variation in the grain size. The model also captures well the strain-rate sensitivity of nanocrystalline Cu and Al at wide ranges of strain rate.

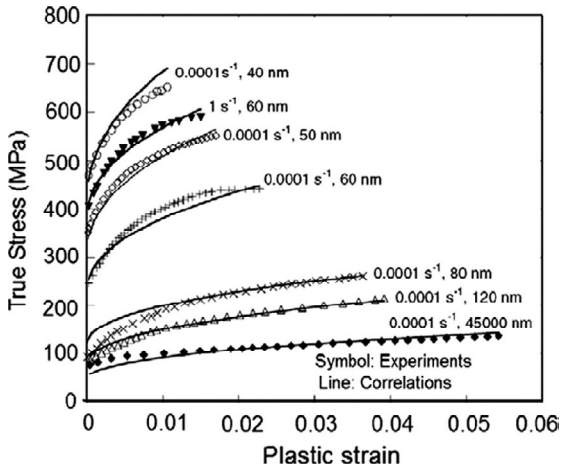

Figure 3. 23 - Observed and calculated responses for nanocrystalline aluminium at different strain rates by using KHL model for various grain sizes (reprinted from (Khan, et al., 2006) Copyright 2006, with permission from Elsevier).

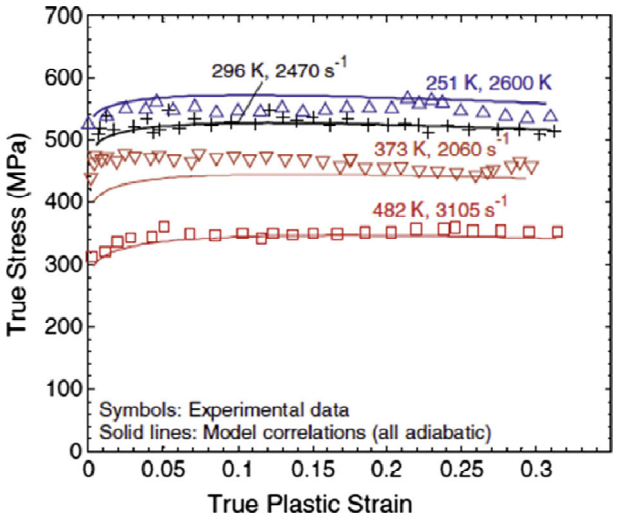

Figure 3. 24 - The KLF model correlation of the compressive viscoplastic response of 10 h milled (d = 82mm) bulk Al at different temperatures and dynamic strain rates (Farrokh, et al., 2009) Copyright 2009, with permission from Elsevier).

3.2.10 Other phenomenological models

Voce and Kocks based a model on the fact that true stress-strain curves of FCC metals are adequately represented by an exponential law to a saturation stress. The exponential law was first proposed by Voce (Voce, 1948) and later expanded by a number of authors. One of these developments (Molinari, et al., 2005) expanded Voce's work to describe the temperature and strain-rate dependence and to give it a physical foundation. Voce's equation, presented in 1948 as cited by Lin (Lin, et al., 2011) was

$$\sigma = \sigma_s + \left[(\sigma_0 - \sigma_s)\exp\left(-\frac{\varepsilon}{\varepsilon_r}\right)\right] \tag{3.132}$$

where σ_s is the saturation stress and σ_o is the initial yield stress and ε_r is the relaxation strain. Kocks (Kocks, 1976) developed a description of the saturation stress σ_s as a function of temperature and stain-rate:

$$\sigma_s = \sigma_{s0}\left(\frac{\dot{\varepsilon}}{\dot{\varepsilon_0}}\right)^{KT/A} \tag{3.133}$$

where K is the Boltzmann constant, b is the Burgers vector, σ_{so} is the saturation threshold stress at zero Kelvin and A and $\dot{\varepsilon}_o$ are material parameters. The initial yield stress is can be obtained as (Naderi, et al., 2008)

$$\sigma_0 = \sigma_{k0}\left(\frac{\dot{\varepsilon}}{\dot{\varepsilon_{k0}}}\right)^{KT/A_0} \tag{3.134}$$

where $A_o = A\mu(T)b^3$ and μ is the elastic modulus and A , $\dot{\varepsilon}_{ko}$ are material parameters. An expression for the relaxation strain ε_r is also given as

$$\varepsilon_r(\dot{\varepsilon}, T) = \frac{\sigma_s(\dot{\varepsilon},T) - \sigma_0(\dot{\varepsilon},T)}{\theta_0} \tag{3.135}$$

where θ_o is the initial work-hardening rate. Naderi (2008) combined MR and VK models to obtain results for 22MnB5 boron steel. However, only fairly low strain-rates were considered (up to 10 s^{-1}). The results, shown in Fig. 3.25, although slightly better than the MR model showed that in spite of this, the constitutive model has more flexibility since history effects (e.g. rapid changes in strain rate or temperature history) can be taken into account via the evolution law of the internal parameter. Lin et al. developed equations to obtain the flow stress of metals and alloys under hot deformation from the Arrhenius equation, using a Zener-Hollomon parameter to describe the stress-strain curve (Lin, et al., 2008). These authors investigated very high temperature deformation of 42CrMo steel at strain rates up to 50 s^{-1}. The modifications introduced were applied to a 2124-T851 aluminium alloy (Lin, et al., 2010). The effect of temperature and strain rate behaviour can be represented by a Zener-Hollomon parameter in an exponent-type equation. The Arrhenius type equation is chosen as it provides a better approximation between the Zener-Hollomon parameter and the flow stress:

$$\dot{\varepsilon} = AF(\sigma)\exp\left(-\frac{Q}{RT}\right) \tag{3.136}$$

$$Z = \dot{\varepsilon} \exp\left(\frac{QR}{T}\right) \tag{3.137}$$

$$F(\sigma) = \begin{cases} \sigma_n \Leftarrow \alpha\sigma < 0.8 \\ \exp(\beta\sigma) \Leftarrow \alpha\sigma > 1.2 \\ [\sinh(\alpha\sigma)]^n \Leftarrow \text{all } \sigma \end{cases} \tag{3.138}$$

in which σ is the flow stress, R is the universal gas constant, T is the absolute temperature, $\dot{\varepsilon}$ is the strain-rate, Q is the hot deformation activation energy, and A, α and n are material constants ($\alpha = \beta/n$). The method has been used to predict the flow stress of a 42CrMo steel at strain rates up to 50 s^{-1}.

A more recent and comprehensive constitutive model has been developed from the previous approach to predict the stress-strain curve of 42 CrMo steel (see Fig. 3.26). Again the authors had in mind hot forming processes at relatively low strain rates (up to 10 s^{-1}) which makes this method depart from the object of this review. Further details on this model are available in the literature (Lin, et al., 2010),

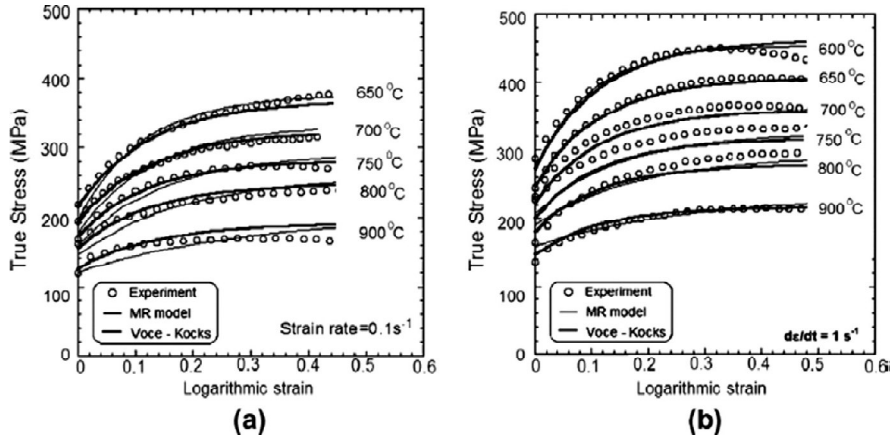

Figure 3. 25 - Stress-Strain correlations between experimental data and constitutive models (a) strain rate 0.1 s-1; (b) strain rate 1 s-1 (reprinted from (Naderi, et al., 2008) Copyright 2008, with permission from Elsevier)

3.2.11 Comparison between the presented phenomenological models

Tables 3.3 and 3.4 compare those constitutive models described in section 5 and compares the main parameters selected by the authors to base the development of their equations. Mecking –Kocks (Mecking, et al., 1981), Molinari-Ravichandran (Molinari, et al., 2005) and Johnson-Cook (Johnson, et al., 1983) are the most cited and from these the Johnson-Cook is by far the most popular due to the simplicity of implementation in hydrocodes.

Table 3. 3- Comparison of the major characteristics of some empirical constitutive models.

Year	Model	Strain rate	Main features
2003	Kocks and Mecking (Kocks, et al., 2003)	10^2 to 10^4 s^{-1}	• Based on dislocation density • Considers thermal activation • Considers flow stress at 0 K
2005	Molinari & Ravichandran (Molinari, et al., 2005)	10^{-3} to $8.5x10^4$ s^{-1}	• Based on a characteristic length scale of the microstructure • Considers temperature effects • Considers grain size
1983	Johnson and Cook (Johnson, et al., 1983)	Up to 10^4 s^{-1}	• Purely empirical model • Considers the effect of temperature • Considers strain rate effects
1976	Voce and Kocks (Voce, 1948)	10 s^{-1}	• Uses the concept of saturation stress as a function of temperature and strain rate
2008	Lin, Chen and Zhong (Lin, et al., 2008)	5x10 s^{-1}	• Defines flow stress in terms of the Zener-Hollomon parameter
1992	Khan and Huang (Khan, et al., 1992)	10^{-5} to 10^4 s^{-1}	• Does not includes temperature effects • Based upon separation of the total deformation rate into elastic and plastic components • Assumes a dependency on J2 invariant
1992	Khan, Huang and Liang (Khan, et al., 1999)	10^{-6} to 10^4 s^{-1}	• Adds temperature effects to the KH model
2009	Khan, Liang and Farrokh (Farrokh, et al., 2009)	10^{-4} to 10^3 s^{-1}	• Derived from KHL method • Includes temperature effects • Considers grain size

Table 3. 4 - Constitutive equations of the indicated phenomenological models

Kocks and Mecking (Kocks, et al., 2003)

$$s = \left(\frac{\dot{\varepsilon}}{\dot{\varepsilon}_0}\right)^{1/m} \exp\left(-F\frac{\theta_r}{\theta_h}\right) \quad \text{and} \quad s = \left(\frac{\dot{\varepsilon}}{\dot{\varepsilon}_0}\right)^{\frac{1}{m}} \left(1 - F\frac{\theta_r}{\theta_h}\right)$$

Molinari and Ravichandran (Molinari, et al., 2005)

$$\frac{\delta_r}{\delta_{r0}} = \left\{1 - \left[k_r\left(\frac{T}{T_{r0}}\right)\log\left(\frac{\dot{\varepsilon}_{r0}}{\dot{\varepsilon}}\right)\right]^{p_r}\right\}^{q_r} \text{ and } \frac{\delta_s}{\delta_{s0}} = \frac{1}{\left\{1-\left[k_r\left(\frac{T}{T_{r0}}\right)\log\left(\frac{\dot{\varepsilon}_{r0}}{\dot{\varepsilon}}\right)\right]^{p_S}\right\}^{q_S}}$$

Jonhson and Cook (Johnson, et al., 1983) $\sigma_{eq} = (A + B\varepsilon^n)(1 + C\ln\dot{\varepsilon}^*)(1 - T^{*m})$

Voce and Kocks (Voce, 1948) $\sigma = \sigma_s + \left[(\sigma_0 - \sigma_s)\exp\left(-\frac{\varepsilon}{\varepsilon_r}\right)\right]$

Lin, Chen and Zhong (Lin, et al., 2008)] $\dot{\varepsilon} = AF(\sigma)\exp\left(-\frac{Q}{RT}\right)$

Khan-Huang-Liang (Khan, et al., 1999) $\sigma = \left[A + B\left(1 - \frac{\ln(\dot{\varepsilon}^p)}{\ln(D_0^p)}\right)^{n_1}\varepsilon^{n_0}\right](1 - T^{*m})e^{c\ln(\dot{\varepsilon})}$

Khan-Liang-Farrokh (Farrokh, et al., 2009)

$$\sigma = \left[\left(a + \frac{k}{d^{n*}}\right) + B\left(\frac{d}{d_0}\right)^{n_2}\left[\left(1 - \frac{\ln(\dot{\varepsilon}^p)}{\ln(D_0^p)}\right)\left(\frac{T_m}{T}\right)\right]^{n_1}(\varepsilon^p)^{n_0}\right]\left(\frac{T_m - T}{T_m - T_{ref}}\right)^m\left(\frac{\dot{\varepsilon}^p}{\dot{\varepsilon}^{p*}}\right)^C$$

.

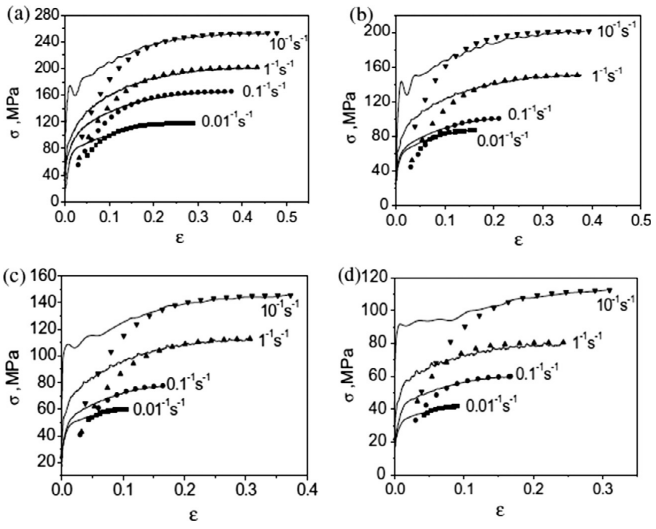

Figure 3. 26 - Predicted and measured flow stress for 42CrMo steel under different strain rates and different forming temperatures: (a) 850˚C; (b) 950˚C; (c) 1050˚C; and (d) 1150˚C (Lin, et al., 2010) Copyright 2010, with permission from Elsevier).

3.2.12 Dynamic recrystallization (DXR)

A brief explanation of this phenomenon has been presented in section 2.2 and in fact DXR has relevance in the case of work-hardened metals undergoing deformations at temperatures in the range of 40 to 50 percent of melting temperature. It has been shown in the preceding sections that this effect has been ignored in most constitutive equations although in high-strain-rate regimes, particularly in adiabatic strain rate regimes the influence of DXR, as Andrade (1994) has shown to be important [(Andrade, et al., 1994). Andrade (1994) used the JC model due to its popularity and simplicity. In its original version JC equation considers a gradual thermal softening and cannot accommodate sudden flow stress changes due to DXR. This reduction was achieved by incorporating a reduction function $H(T)$ which is based on a unit step function of temperature $u(T)$ that takes the zero value when the temperature is below a critical DXR temperature Tc (temperature at which the DXR phenomena or phase transformation occurs) or unity when the temperature is larger than Tc , The reducer function is then:

$$H(T) = \frac{1}{1-(1-\bar{H})u(T)} \tag{3.139}$$

where $\bar{H}$ is a reducer constant. It is expressed by the ratio of the flow stresses just prior to and after the respective reductions and gives the fractional change in flow stress at the temperature of the critical phenomenon. The flow stress of the recrystallized material has to be experimentally obtained to be included into the reducer constant. A plot showing that the sudden drop if flow stress due to DXR can be adequately numerically predicted using this method has been presented in Fig. 3.27 (a). It represents cold- hardened OFHC copper response as a function of temperature for a given strain-rate. Recrystallization occurred at 700 ºC and at a plastic strain of 0.3 (the value of the strain-rate has not been reported). Fig. 3.27 (b) represents the same experiment but this time presenting the results as a function of strain and temperature. The remarkable agreement obtained between experiment and numerically obtained results show that the DXR effects can be incorporated with good accuracy in constitutive models.

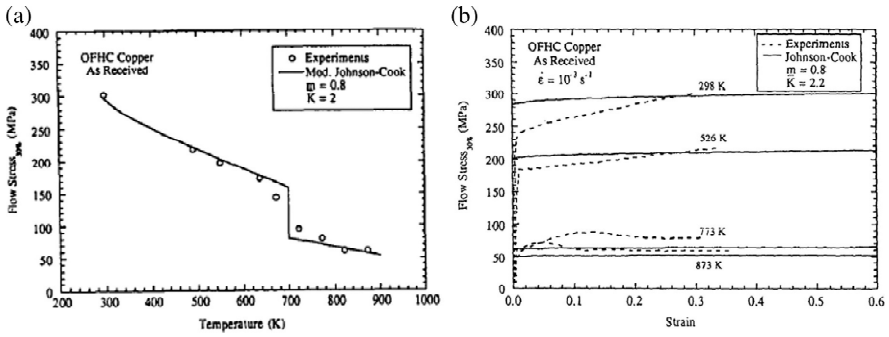

Figure 3. 27 - (a) Predicted and measured values of flow stress at a plastic strain of 0.3 for cold-worked copper as a function of temperature (b) Predicted and measured stress-strain curves for cold-worked copper as a function of temperature. (Andrade, et al., 1994) Copyright 1994, with permission from Elsevier

3.2.13 Dynamic strength and fracture

It has been shown above that a large number of constitutive models have been developed to simulate the viscoplastic response of metals subject to very high speed impact and intense loading regimes. Most of them do not accurately describe viscoplastic behaviour for strain rates above 10^4 s^{-1} and so some authors developed

equations to extend the range of validity of their models to the very high strain rate regime. In the high strain rate regime, single-parameter internal state variable models based on dislocation density are often used. Composite models using two internal variables (Nes, 1998) have also been developed. As explained above, these models are based on glide kinetics that describes the mechanisms of dislocations overcoming obstacles with the assistance of thermal fluctuations. This is valid for applied stresses below the mechanical threshold, corresponding to strain rates not exceeding 10^5 s^{-1}. Above the mechanical threshold the thermally activated dislocation glide no longer controls viscoplastic flow. The production and continuous glide of mobile dislocations that are subject to damping and relativistic effects will be the dominant mechanism. A few constitutive models were proposed, as reviewed above, for the shock loading regime, (Preston, et al., 2003) (Steinberg, et al., 1980) (Steinberg, et al., 1989). Further discussion of these models is available in the literature (Remington, et al., 2006) (Rodriguez-Martinez, et al., 2011).

Large plastic deformation, large strain rates and temperature softening are generally well described by most constitutive models but a complete treatment of nonlinear response to dynamic loads will have to consider the accumulation of damage and material failure. Two approaches are possible in order to account for damage. In the coupled approach the material damage affects the stress response. Constitutive models including damage can be formulated based on continuum thermodynamics (Lemaitre, 1992) or micro-mechanics of voided materials (Gurson, 1977). Uncoupled methods assume that the stress and strain fields will remain unaffected by damage. It is clear that damage will introduce some softening in the material and it will be necessary to take into account this softening to be able to capture strain localisation prior to fracture. However, in impact analysis, high strain rates may lead to adiabatic conditions and temperature softening of the material. It follows that it is possible, at least approximately, to describe strain localisation, for instance in adiabatic shear bands, without using a coupled approach if the constitutive equation takes thermal softening into account (Borvik, et al., 2003). The use of coupled models of viscoplasticity to account for damage softening (Borvik, et al., 1999) (Borvik, et al., 2001) although they provided the best results when compared with experimental data, were found to

provide close results to those obtained from uncoupled models (Borvik, et al., 2001b). So uncoupled models are often used (Borvik, et al., 2003).

A number of models will be capable of predicting the onset of ductile failure when necking appears in the numerical solution. However, in most cases, some form of element deletion will simulate with more realism material rupture under very high loadings. The modelling of failure is rather complex and few models are of practical use but in general there will be a combination of a description of dynamic strain, damage accumulation and failure. So far, various failure criteria have been explored, such as the maximum strain criterion, rupture strain, equivalent plastic work, damage models and energy density models (Yuen, et al., 2005).

Impact loading implies large deformations and large strain rates. Each of these poses different demands on the material models used: large deformations require precise descriptions of the yield locus as plastic flow strongly depends on the effects of anisotropy and work hardening. Barlat's models (Barlat, et al., 1989) are an example of a set of widely used models for forming applications, where plastic deformations are often large. However, for impact simulations, the dynamic response combined with failure prediction will have to be present in material models. For low strain rates the isotropic von Mises constitutive model or the Gurson model (which proposes a porosity based model in which the yield function is modified by the presence of voids and also describes failure) are often used (Neukamm, et al., 2008) (Lesuer, et al., 2001) (Lesuer, et al., 2001). Gurson's model (modified by Tvergaard and Needleman) is based on a micromechanical description of growth and nucleation of voids in a rigid-perfectly plastic material. Gurson's model consists of a yield function dependent on hydrostatic pressure and the effective void volume fraction f:

$$\Phi = \frac{q^2}{\sigma_M^2} + 2q_1 f \cosh\left(-\frac{3q_2 p}{2\sigma_M}\right) - 1 - (q_1 f)^2 = 0 \qquad (3.140)$$

where σ_M is the actual flow stress in the material, p is the hydrostatic pressure, q is the equivalent von Mises stress and f is the effective void volume fraction which is defined in a cumulative way. The damage evolution consists of void growth due to volumetric plastic straining and nucleation of voids due to deviatoric plastic straining. Void growth is normally the dominant effect in material deterioration under tensile loading. The

Gurson method exhibits several problems: it violates the principle of isochoric plastic flow, shows variable values of the plastic Poisson's ratio and cannot describe failure for mean stresses that are near zero or negative. Modifications to the method solved this limitation but made it more difficult to calibrate. These difficulties are avoided by using phenomenological damage models. Of these the Johnson-Cook (JC) is frequently used by researchers. Borvik (Borvik, et al., 1999) (Borvik, et al., 2001) (Borvik, et al., 2001b) (Bovirk, et al., 2008) (Spranghers, et al., 2013) used the JC coupled constitutive model of viscoplasticity and ductile damage, implemented in the LS-DYNA FEM code. This model assumes that damage accumulates in the material element during straining and that the material breaks when the damage reaches a critical value. In this approach the two equations are coupled, leading to the following unified model:

$$\sigma_{eq} = (1 - D)(A + Br^n)(1 + C \ln \dot{r}^*)(1 - T^{*m}) \tag{3.141}$$

where D is the damage variable and $r = (1 - D)p$ is the damage-accumulated plastic strain. The model was complemented with an element deletion algorithm that removes elements in which the damage variable reaches a critical value D_c. This approach is perhaps the most widely found in ballistic penetration, blast loading and other high velocity impact problems.

The concept of the damage variable D derives from Continuum Damage Mechanics (CDM) (Lemaitre, et al., 1990) (Bonora, 1997) in which it is defined as

$$D = 1 - \frac{A_{eff}}{A_0} \tag{3.142}$$

where A_0 is the nominal intersection area (the area of a section of a reference volume element isolated in a damaged solid) and A_{eff} is the effective area of resistance (the nominal area reduced by the presence of microdefects such as cracks and cavities). These three variables are referred to a plane (defined by its normal n) and a tensor description is often used. Failure occurs when $D = 1$.

The phenomenological JC model was developed during the 1980s to address impact, ballistic penetration and blast loading problems, and has been extensively used

by national and military laboratories or private industry to study large strain, high strain rate problems. Its popularity derives from its simplicity and the availability of constants to be used in the equations for a significant number of engineering materials (Neukamm, et al., 2008) (Lesuer, et al., 2001). Physical models very often require constants that are not available and which require complex experimental apparatus to measure them.

The JC model, often known as a viscoplastic constitutive model (Khan, et al., 2000 b) was also developed as a ductile fracture model (Johnson, et al., 1985) that includes the effects of stress triaxiality, temperature, strain rate and strain path on the failure strain. It is also a cumulative model in which the material will break when damage reaches a critical value. The expression for the JC fracture strain is

$$p_f = (D_1 + D_2 \exp(D_3 \sigma^*))(1 + D_4 \ln \dot{p}^*)(1 + D_5 T^*) \qquad (3.143)$$

where D_1 to D_5 are material constants, $\sigma^* = \sigma_m/\sigma_{eq}$ is the stress triaxiality ratio and σ_m is the mean stress. Failure occurs when a damage variable defined as $D = \sum \Delta p/p_f$ reaches unity, where Δp is the increment of effective plastic strain during a load increment. Some drawbacks exist, however: Lesuer (Lesuer, et al., 2001) noted that the JC constitutive model was unable to predict the correct variations of flow stress with strain rate. The model predicted for titanium, in compression, a significantly higher ductility than experimentally observed and the numerically obtained tensile failure strain was also significantly higher than the experimentally observed values. For a 6061-T6 alloy significant deviations were noted for the strength increase when the strain rate changes to values above 10^3 s^{-1}, where the experimental values show a pronounced increase (see Fig. 3.28). These results form two different deformation mechanisms for low and high deformation rates. Different deformation rate equations were developed to represent the two phenomena (Lesuer, et al., 2001). Spranghers (Spranghers, et al., 2013) also reported that generally, the plastic strain is incorrect due to the incorrect hardening parameters obtained from the literature, leading to incorrect modelling of the yielding behaviour. Since the analysis is transient and plastic deformation occurs first, errors are cumulative, resulting in an incorrect amount of plastic deformation.

All this research in constitutive modelling and failure models is often applied to plates as impulsive loading of plated structures (vehicles or facilities) is an actual concern for engineers and a brief note on the subject follows.

A significant research effort on impulsive loading on plates and beams has been reported in recent decades (Nurick, et al., 1989a) (Nurick, et al., 1989b) attempting to model the large inelastic responses observed. In the 1990s investigations began to include other effects such as boundary conditions, plate stiffening and loading conditions to predict not only deformation but also tearing (Teeling-Smith, et al., 1991) (Nurick, et al., 1996a) (Olson, et al., 1993) (Nurick, et al., 1996b).

It is important to refer the seminal work of Menkes and Opat (Menkes, et al., 1973) on beams subjected to blast loads. It was one of the first studies that considered loading up to rupture or tearing at the support points of the structure. Three different failure modes were identified for beams:

a. Mode I – Large inelastic deformation;
b. Mode II – Tearing in the outer fibres at supports;
c. Mode III – Transverse shear failure at the supports.

These modes of failure have been found to also apply to plates (Nurick, et al., 1989b) (Nurick, et al., 1995) but for the square plates' case it was found that mode II failure occurs first in the centre of the sides and then progresses to the corners with increasing impulse (Olson, et al., 1993) (Nurick, et al., 1995). This finding led to some additions to Mode II failure (Nurick, et al., 1996b):

d. Mode II* – Partial tearing at the boundary;
e. Mode IIa – Complete tearing with increasing mid-point displacement;
f. Mode IIb – Complete tearing with decreasing mid-point displacement.

Other subdivisions were identified for localised loading conditions such as those proposed by Nurick and co-workers (Nurick, et al., 1996a) and these modes of failure can be identified in many published experimental results, e.g. (Kazemahvazi, et al., 2007). Failure in plates subjected to blast or impact loading is not limited to Modes II or III ductile fracture because some other forms of tearing (e.g. petalling or dishing) may also occur. Tearing was predicted using the CTOD[8] criterion (Wierzbicki, 1999) or considering the equivalent plastic strain times the average stress triaxiality (Lee, et al., 2005b)(Lee, et al., 2005a). Based on the critical damage value, calculated distributions and histories of stress and strain, these authors (Lee, et al., 2005b)(Lee, et al., 2005a) observed that crack length and final deformed shapes of plates are strongly influenced by the spatial distribution and intensity of impulsive loading.

Many experimental results for stiffened plates have been reported in the last few decades (Schubak, et al., 1993a) (Schubak, et al., 1993b) (Pan, et al., 1999) (Schleyer, et al., 2003). Some of these researchers did not include strain rate or temperature effects in their numerical models. Instead they used (a) an energy balance equation to assess plate or beam inelastic response and tearing (Yu, et al., 1989), (b) the deflecton theory of von Karman and the von Mises yield criterion (Koko, et al., 1991) or (c) use rigid-plastic methods (Yuen, et al., 2005) (Nurick, et al., 1995) (Schubak, et al., 1993a) (Schubak, et al., 1993b) (Balden, et al., 2005) (Langdon, et al., 2005a) (Langdon, et al., 2006). These methods were shown to give good agreement when the ratio of initial kinetic energy to elastic strain energy is larger than 10 and the load duration is sufficiently short with respect to the natural period of the structure (Jones, et al., 1970).

Another field of interest for ductile failure models (and also under intense investigation) is plate penetration and plugging in ballistic problems (Borvik, et al., 2001) (Iqbal, et al., 2013). Most work on terminal ballistics has been based on the Johnson-Cook fracture criterion (Borvik, et al., 2001b) (Iqbal, et al., 2013) (Abdulhamid, et al., 2013) (Borvik, et al., 2011) (Borvik, et al., 2010) (Borvik, et al., 2009) (Gupta, et al., 2006) (Sorensen, et al., 2008) (Borvik, et al., 2005). Sorensen (Sorensen, et al., 2008) used the Johnson-Cook damage-accumulation fracture model in conjunction with a threshold maximum tensile stress criterion and a Weibull statistical distribution for the

[8] CTOD means Crack Tip Opening Displacement

initial failure strain for a 7039 aluminium alloy target material. This allowed the representation of a non-uniform, stochastic failure of the aluminium plate.

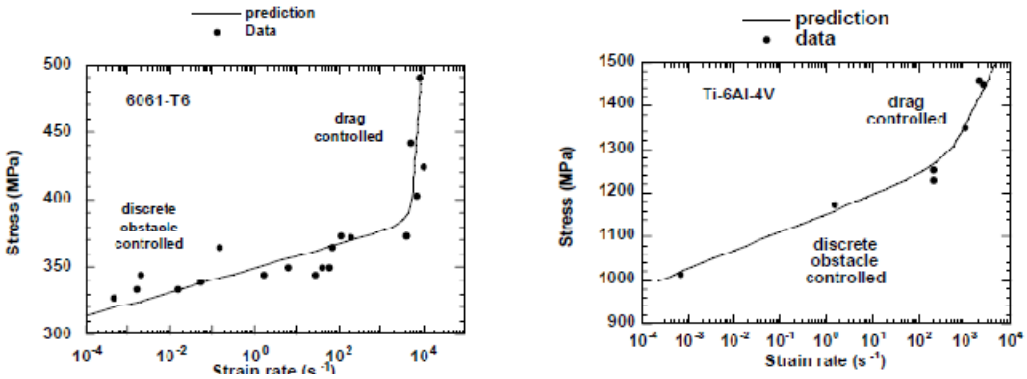

Figure 3. 28 - (a) Comparison between the stress-strain rate behaviour predicted by the mechanism-based material model and experimental data for 6061-T6, with regions of the stress-strain rate curve that are dominated by discrete obstacle plasticity and drag controlled plasticity. (b) Similar comparison for Ti-6Al-4V alloy (reproduced from (Lesuer, et al., 2001) Copyright 2001; with permission of Lawrence Livermore National Laboratory).

When damage of a material occurs, the stress-strain relationship does not accurately represent its behaviour. The use of a true stress-strain relation during material damage introduces strong mesh dependency in results based on strain localisation such that the energy dissipated decreases as the mesh is refined. A fracture energy approach reduces mesh dependency by creating a stress-displacement response after the damage is initiated. The energy required to open a unit area of crack, G_f, may be defined as

$$G_f = \frac{\sigma_{y0}\bar{u}_f^{pl}}{2} \tag{3.144}$$

where σ_{y0} is the ultimate stress and $\bar{u}_f^{pl}$ is the equivalent plastic displacement failure. With this approach the softening response after damage initiation will be characterised by a stress-displacement response rather than a stress-strain response. However, in the majority of published work, the use of constitutive models and fracture strain models has been frequently preferred. Due to its simplicity the Johnson-Cook constitutive model and fracture strain model (Rule, et al., 1998) (Johnson, et al., 1985) combined with ductile damage mechanics (Lemaitre, 1992) to include material degradation due to

damage into the model is the mostly widely present in the available published work involving impact loads. This constitutive equation can be used uncoupled or coupled with different physical phenomena such as damage, temperature and strain-rate. The full model includes linear thermoelasticity, von Mises yield criteria, an associated flow rule, isotropic strain hardening, strain-rate hardening, softening due to adiabatic heating, softening due to isotropic damage evolution and a fracture criterion. Coupling the model with an element-kill algorithm that removes damaged elements from the mesh when the damage variable reaches a critical value may also be adopted to speed up calculations (Borvik, et al., 2001b).

Other authors, particularly in investigations concerning blast-loaded plates, followed a different approach to add strain rate effects by adjusting the yield stress σ_y, in the finite element analysis, with a Cowper-Symonds relation (Yuen, et al., 2005) (Teeling-Smith, et al., 1991) (Nurick, et al., 1996a) (Olson, et al., 1993) (Jones, 1989) (Ramajeyathilagam, et al., 2000) (Yuan, et al., 2013):

$$\sigma_y = \sigma_0\left[1 + \dot{\varepsilon}/D^{1/n}\right] \tag{3.145}$$

where D and n are material parameters. These methods are either based on von Mises plasticity with isotropic hardening/softening behaviour (Balden, et al., 2005) or on plastic work criteria, as rigid-plastic methods are shown to give design level accurate estimates for the response of structures subjected to blast loads (Rudrapatna, et al., 1999). Another approach using fictitious stiff springs at the plate boundary (Rudrapatna, et al., 1999) to simulate the variation of the transverse shear stress along that boundary was used to predict Modes II and III failure. Elastic analysis of blast loaded square plates assuming large deflections has also been addressed (Jacinto, et al., 2001). It is evident that the range of approaches used to tackle blast-loaded plates is quite wide.

Rigid-plastic methods can predict the maximum loads which cause failure due to excessive transverse shear forces on the material. These shear forces play an important role in the process of failure but they add complexity to the analysis (Olson, et al., 1993). It has been reported (Teeling-Smith, et al., 1991) that boundary conditions may determine the tearing mechanism at the plate boundaries. This was investigated for

clamped circular plates (Nurick, et al., 1996a) and for rectangular plates (Bonorchis, et al., 2009) showing that thinning and rupture are highly dependent on the boundary fixation conditions. Mode I predictions were in good agreement with experimental results but for other modes of failure, variations were observed.

For engineering purposes more straightforward solutions can be obtained by means of equivalent single-degree-of-freedom (SDOF) systems, also known as spring-mass systems or modal approximations methods (Schleyer, et al., 2003) but these are outside the scope of this review.

3.2.14 Constitutive models – Some practical aspects

A review of constitutive models highlighting their main assumptions and features as been presented, together with a brief summary of available methodologies for the analysis of ductile failure. Application to plates was also highlighted which gave some indication on the constitutive modelling methods that are being preferred for these analysis. Theoretical derivations have been developed but at present numerical modelling is used most of times to predict material response. The empirical models are simpler and do not call for an understanding of the physical foundation of the phenomena being simulated. Regression analysis is used to determine the parameters necessary to run the models. The study of a particular material led many users to introduce modification to improve the correlation between experimental data and numerical results. This had resulted in many variations of the models, in particular of the JC equation, one of the most widely cited and used. Typically regression models tend to be accurate only within the range of the data used to calibrate the model, which limits the generality of such models. Also the coupling effects between the influencing factors that affect flow stress (e.g. temperature, strain and strain-rate) must be considered in future models or refinements of existing ones. Obviously future models may become more difficult to implement and might need much more testing to obtain the required data to run them, and this will challenge researchers as industry will maintain a need for simple and more straightforward techniques to use in engineering work.

Physically-based models take into account the thermal deformation mechanism of the material under deformation. Work hardening due to dislocations and their interactions and dynamic softening resulting from temperature increase will result in opposing effects special in hot deformation processes, which remains a field of intense investigation in pursuit of constitutive equations that can adequately models both effects. The solid physical foundation of these models makes them more suitable for certain loading regimes but many of them include parameters that require specialized laboratory equipment to determine them. Their implementation in hydrocodes is therefore difficult.

The prediction of ductile fracture and the development of criteria to predict the fracture processes associated with large plastic deformation and high strain rates are essential for the analysis of structures subject to blast load. Macroscopic quantities, such as the strain-energy density, have been proposed but in general it is difficult to base predictions on single parameter models.

Future work will resort more often to technology. For instance shock pressure driven by Laser are being used to study the dynamic yield strength of metals using in-situ X-Ray diffraction (Wehrenberg, et al., 2014) (Hawreliak, et al., 2007). This shows that on-going research is increasingly sophisticated and continuously in pursuit of the most accurate knowledge on dynamic viscoplasticity and strength.

3.3 Strength of plates subjected to blast loads

Investigations on the vulnerability of real structures are unpractical to be carried out experimentally due to the destructive nature of blast load testing but the nature of such research requires engineering accurate modelling of the mechanism of deformation and failure of ship type structures. However, a real structure has stiffeners, imperfections, weld defects, residual stresses and, in the heat affected zone of the welds, material properties and structure have undergone changes. The characterization of these variables is outside the scope of this work and solely unstiffened plates have been considered, to avoid all those sources of error and uncertainty. A review of previous

work on material response under blast loading with emphasis on plates, and in particular aluminium plates is presented below[9].

Investigations on plate response under blast loading have been evolving for decades, at least since WWII. Until the mid-1980s the work reported was mainly concerned with simple plates and beams, which resulted in large inelastic deformations. However, in the 1990s research began to include the effect of boundary conditions, plate stiffeners and loading conditions attempting to improve the methods for predicting deformation and tearing. Analytical and numerical analyses were developed and validated against experimental results.

The modes of failure of beams subjected to blast loads were characterized for the first time by Menkes and Opat (Menkes, et al., 1973). This was one of the first studies that considered loading up to rupture or tearing at the support points of the structure. Similar modes of failure have been found to also apply to fully clamped circular plates (Teeling-Smith, et al., 1991) and for square plates (Olson, et al., 1993) (Nurick, et al., 1995) where plates experimental findings led to some additions in mode II failure for plates (Nurick, et al., 1996b). The interested reader may consult a review from Nurick and Martin (Nurick, et al., 1989a) where the evolution of theoretical work on the influence of dynamic loads on the behaviour of thin plate is referred. This early work on thin disks and circular plates assumed bending action only. The review reported that recorded dynamic load carrying capacities were greater than the corresponding static values and that at higher loading rates the plates tend to deform transversally resulting in smaller circumferential strains than those from static tests. In their review Nurick and Martin (1989) presented a compilation of analytic formulae for predictions of the mid-point deflection and deflection-thickness ratio, available at the time.

An experimental review (Nurick, et al., 1989b) discussed a dimensionless damage number to compare experimental results of the deformed shape and the deflection-time history of the structural elements tested. The expression is

$$\alpha = \frac{I_0}{\rho t^2 \sigma_d} \tag{3.146}$$

[9] This part will complement part 3.2 and some material may be repeated for the sake of clarity.

where ρ is the material density, σ_d is the damage stress, I_0 is the impulse per area, and the t. is the plate thickness. This damage number has been used to assess the behaviour of metals in impact situations, as it correlates with the order of magnitude of deformation. Rewriting the damage number in terms of the impulse a geometrical damage number has been derived by Nurick (1989b), such that:

$$\psi = \left[\beta\alpha \left(\frac{A_0}{A} \right)^2 \right]^{1/2} \tag{3.147}$$

where the damage number is affected by the length/width ratio of the plate, β and the relation between the area of the plate imparted by the impulsive load, A_0, and its total area A. Other formulations for damage number were discussed, some derived from eq. (3.146) or having been presented by other authors and a least squares fit to predict plate deflection has been proposed;

$$\frac{\delta}{t} = 0.471\phi_q + 0.001 \tag{3.148}$$

with

$$\phi_q = \frac{I}{2t^2 \left(BL\rho\sigma_0 \right)^{1/2}} \tag{3.149}$$

where I is the total impulse and B and L are the breadth and length of the plate respectively. The pursuit of dimensionless relations to predict plate response under blast loads has been continued by other researchers. Teeling-Smith (Teeling-Smith, et al., 1991) also used the concept of damage number to examine the failure of circular mild steel plates subjected to impulsive loads. They correlated the impulsive energy and the damage number, and obtained threshold values for the onset of failure in Modes II and III. Li and Jones, (Li, et al., 2000) presented a dimensional analysis extending the use of dimensionless numbers to include strain rate, strain hardening and temperature effects. Jacinto, (Jacinto, et al., 2001) tested full scale plates using modal superposition methods to derive the peak accelerations. Olson (Olson, et al., 1993) examined square

mild steel plates in a set of similar experiments but, as in the previous experiments, the authors admitted that strain rate effects had not been considered. Schubak and co-workers (Schubak, et al., 1993a) studied stiffened plates subjected to blast loading using rigid-plastic analysis. A uniform load distribution was considered and the plate was modelled as a beam with associated plating, and the method adopted provided closed-form and semi-analytical solutions for one way stiffened plates with fully clamped edges. In a second paper the method was extended to cover the cases of partial end fixity, material strain rate sensitivity and two-way stiffening (Schubak, et al., 1993b). Other authors obtained solutions using rigid-plastic analysis as they have been shown to provide design level accurate estimates for the response of structures subjected to blast loads (Jones, 1993)(Yu, et al., 1992).

Nurick (Nurick, et al., 1995) obtained experimental and numerical results for built-in stiffened square plates blast-loaded over a range of impulses sufficient to initiate tearing of the plate. The results showed that for Mode I the permanent deformation would increase with increasing impulse, like as with unstiffened plates. For Mode II failure cases, tearing would start on the middle of the sides then progressing towards the corners as the impulse increases. A simple rupture strain criterion has been adopted for Mode II prediction as the authors aimed to obtain an engineering design-analysis tool. Louca (Louca, et al., 1998) used a simplified large displacement elastic analysis based on Lagrange's equation to study the response of stiffened plates and compared with a finite element analysis of stiffened plates subjected to blast loading.

Nurick (Nurick, et al., 1996b) presented experimental results for clamped mild steel square plates subjected to impulsive loads, exhibiting all three modes of failure. Comparison with circular plates has also been presented. Although the square plates exhibited all three modes of failure, several phases were present in the Mode II failure region, as in the circular plates. The failure modes were observed to be dependent on the boundary conditions. Zhu (Zhu, 1996) reported having been the first to investigate the transient deformation modes of square plates subjected to blast loading.

Rudrapatna (Rudrapatna, et al., 1999) used transverse springs at the plate boundary to obtain a direct estimate of transverse shear forces for Mode III analysis and for Mode II and III interaction. The authors used an interaction failure criterion

comprising bending, tension and transverse shear, and developed an algorithm that successively releases elements to simulate the progression of rupture. All these analysis considered uniformly loaded plates but different failure mechanisms occur when a localized explosion is considered, and Wierzbicki (Wierzbicki, 1999) proposed an analytical model to describe plate damage in the petalling mode. In these cases plate deformation is similar to that resulting from the impact from a cylindro-conical projectile. Wierzbicki (Wierzbicki, et al., 1996) attempted to analytically solve the problem of clamped plates subjected to an impulse load imparted over a central circular region using eigen-functions and wave form solutions or using simple velocity and displacement fields. Jones (Jones, 1989) discussed analytically the response of plates subjected to impact loading using dimensionless numbers. Hu (Hu, 2000) used a concept similar to a dimensionless number, termed response number (Zhao, 1998), to be applied to the dynamic plastic response of plates. They reviewed the expressions of a number of other authors, for the displacement/thickness ratio of plates subjected to impact loading showing that those expressions can be written in terms of the response number, R_n. For quadrilateral plates subjected to uniform impulsive loading the response number, R_n, has the following form:

$$R_n = \frac{I_0^2}{\rho \sigma_0 t^2}\left(\frac{l}{t}\right)^2 \tag{3.150}$$

where l is the half-length of the quadrilateral plate, σ_0 is the yield stress of the material, ρ its density and t is the plate thickness. Jacob (Jacob, et al., 2004) reviewed a collection of displacement/plate thickness ratio expressions published by other authors. They reported experimental results for square and rectangular plates exposed to blast loads to identify the influence of particular parameters such as varying charge height, varying charge diameter, varying length/width ratio of the plate. Based on this results, a new version of the dimensionless damage number reported by Nurick and Martin (Nurick, et al., 1989b) has been proposed. Jacob (Jacob, et al., 2007) considered the effects of the stand-off distance, mass of explosive and plate radius and incorporated them into theoretical and empirical dimensionless numbers and other predictions. They used a pipe to convey the blast wave and therefore obtain an approximately planar wave front. A relation between stand-off distance and the maximum deformation of circular plates

has been investigated and he reported that for stand-off distances lower than the plate radius the blast load is considered localized and for stand-off distances above the plate radius the loading is considered uniformly distributed over the entire plate area. For smaller stand-off distances, Jacobs (Jacob, et al., 2007) also observed that the deformed plate profile resembled a small inner dome superimposed atop a larger global dome. The problem of scaling kept the attention of researchers and similarity has been obtained using replica scaling for all geometrical parameters while blast effects were scaled using Hopkinson's scaling law (Neuberger, et al., 2007). The author has also investigated the overall effect of the strain rate and variability of mild steel properties with plate thickness on the response of the scaled model. Material has been modelled by a Johnson-Cook equation (Johnson, et al., 1985) and it was reported that strain rate had a negligible effect on the scalability of the problem. However, highly strain rate sensitive materials may show significant deviations between model and full scale experiment. Investigation of real scale experiments where mild steel plates were exposed to the explosion of ordnance stacked in different configurations have also been reported (Yuen, et al., 2008). Maximum mid-point plate deflections were plotted against dimensionless damage numbers (Zhao, 1998) with a reasonable agreement. Centrally supported circular plates peripherally clamped were also tested to blast loading showing all three distinct failure modes. Approximate energy analysis using a dimensionless impulse has been reported to correlate well with experiments (Cloete, et al., 2005).

Other phenomena related to blast loading of plates have also been investigated.. Balden (Balden, et al., 2005) reported experiments in uniformly and localized blast loaded plates attempting to characterize their post-failure motion. Fragment velocity was found to be significantly different for the uniform and localized loaded plates. Localized impulsive loading was found to cause dishing (Lee, et al., 2005a) in a transient phase followed by failure by petalling (Lee, et al., 2005b).

The numerical simulations that have been reported for the large deformations of symmetrical structural components and subsequent tearing required the selection of suitable failure criteria, particularly for the onset of tearing and mode transitions. Various criteria have been used such as maximum strain, rupture strain, equivalent plastic work, damage models and energy density models. The effect of temperature on

material properties due to high strain rates has become important within this investigation topic. Li and Jones and later Longère (Li, et al., 2000)(Li, et al., 2000) (Longère, et al., 2005) discuss this matter reporting the formation of a shear hinge in ductile structural elements under transverse high load rate and intensity. Strain rate effects have been thoroughly described in the previous part of this Chapter but most researchers have decided, for the sake of simplicity, to use a Cowper-Symonds relation for strain rate together with simple material-temperature relationships. Only recently more complex constitutive models are being systematically adopted for numerical simulations of dynamic plate failure.

Yuen (Yuen, et al., 2005) studied experimentally Modes I and II of failure of a combinations of stiffened plates (single, double-stiffened, crossed and double-crossed stiffened plates). The plates were uniformly loaded to a pressure P in accordance with the experimentally measured impulses. Strain rate was also considered by means of a Cowper-Symonds relation,

$$\frac{\sigma_y}{\sigma_0} = 1 + \left(\frac{\dot{\varepsilon}}{D}\right)^{1/q} \tag{3.151}$$

where D and q are material constants (it is widely accepted that for mild steel the values for the constants are $D = 40\ s^{-1}$ and $q = -5$) and σ_0 is the static yield stress. A temperature effect was added to the Young modulus, E and the yield stress, σ_y. It was observed that in the region of tearing the temperatures formed a band of very severe temperatures resulting from adiabatic heating due to increased strain rates. This localized temperature increase resulted in a region of unrealistically high elongation and consequently temperature was used to categorize the various modes of failure. Yuen (Yuen, et al., 2005) also observed that the presence of stiffeners will not prevent or reduce tearing and that it may even be initiated earlier. A second part of this study, considering localized loading (Langdon, et al., 2005b) revealed that Mode I peak displacement depended on the location of the stiffeners and tearing was observed to be a combination of both tensile tearing and shear failure. Comparing with uniformly loaded plates the presence of stiffeners had more influence in the localized blast case. The Cowper-Symonds model has been used by a number of researchers due to his simplicity (only two parameters) and works well for steel (Jones, 1989) (Olson, et al.,

1993)(Yuen, et al., 2005)(Teeling-Smith, et al., 1991)(Nurick, et al., 1996a) (Ramajeyathilagam, et al., 2000) (Yuan, et al., 2013).

Corrugated panels were also investigated (Langdon, et al., 2005b) (Langdon, et al., 2005c)(Langdon, et al., 2006) as an alternative to stiffened panels to be applied as blast walls. It was found that results were strongly affected by the way connections are modelled. Bonorchis (Bonorchis, et al., 2009) investigated the influence of boundary conditions on the impulse imparted to a plate, resulting from localised blast loading. Bonorchis (2009) reported that the impulse measured experimentally by the ballistic pendulum increases as the height of numerically the impulse that causes plate deformation, which must be smaller than the total impulse imparted to the ballistic pendulum. Bonorchis and co-workers (Bonorchis, et al., 2010) have also analysed welded stiffened plates subjected to localised blast loading. Numerical analysis of stiffened plates under blast loading were also reported to produce lower displacement than equivalently thickened unstiffened plates (Goel, et al., 2011). Practically most of the available experimental data in the literature applies to square plates, with few exceptions (Ramajeyathilagam, et al., 2000) (Ramajeyathilagam, et al., 2004)(Yuan, et al., 2013). Yuan (2013) explored the effect of the aspect ratio in the deformation of rectangular plates as well as the effect of fixing conditions in their tearing mechanism. They reported some simplified expressions for rectangular plate deformation such as:

$$\frac{w_0}{h} = \frac{w_0}{h}\left[\lambda\left(=\frac{\rho V_0^2 a^2}{M_0}\right), \gamma\left(=\frac{a}{b}\right)\right]. \quad \gamma \geq 1 \tag{3.152}$$

In this equation h is the plate thickness, $M_0 = \sigma_y h^2/4$, is the fully-plastic bending moment per unit length, σ_y is the static yield strength, V_0 is the instantaneous velocity acquired by the plate, ρ is the density and a and b are the half-length and width of the plate, respectively. This expression gives the maximum central displacement for Mode I, assuming that V_0 is lower than the critical velocity corresponding to the transition between Modes I and II*. These and other idealizations are valid since the duration of the blast pulse is much shorter compared to the structural response time needed to reach a permanent set. A factor was also added to the equation to account for strain rate sensitive materials and a conventional J_2 plasticity constitutive behaviour with isotropic

hardening has been considered. Numerical models produced a good agreement with theoretical and experimental results for maximum deflection in Mode I and the critical impulses corresponding to mode transitions.

To summarize the review presented above we may say that:

1. Investigations have considered mostly circular and squared plates, usually with clamped boundaries and in some cases stiffened;
2. Some results exist for rectangular plates and simply supported plate boundaries;
3. Idealized loads have been used such as with triangular or rectangular pressure pulses. In many cases uniform pressures were considered but results for localized loads have also been investigated;
4. Many equations were derived on the basis of dimensionless analysis, particularly on a dimensionless damage or response number;
5. Experiments and analysis attempted to describe the threshold of mode transitions which required failure criteria;
6. The failure criteria used varied considerably, from admissible strains, eleongations, stresses or temperatures. Some authors used combined criteria (say shear and tensile srtresses);
7. Strain rate has been accounted for by using the Cowper-Symonds relation and Johnson-Cook flow stress equation;
8. Most experiments and simulations refer to free air (or underwater) explosions, or to fully vented enclosed spaces;
9. To the knowledge of the author there is no published work on the rupture or tearing of plates, in response to an unvented enclosed explosion. Neither simulations other than lagrangian have been used so far to describe the response of plates deformed up to tearing, when subjected to a blast load.

3.4 Aluminium alloy plates subject to blast loads

Having gone through the major investigations on metal plates under blast loading some emphasis on aluminium alloys is required to set the framework for the experiments described in the present study. Johnson-Cook (JC) (Johnson, et al., 1983) constitutive model coupled with a suitable failure and erosion model has been widely used amongst the research and engineering community as a tool to include in the numerical analysis of aluminium alloy structures under high velocity and impulsive loadings e.g. ballistic impact (Borvik, et al., 2004) (Abdulhamid, et al., 2013). However, the method suffers from limitations specially for complex types of loading along a wide spectra of triaxiality and Lode angles. Gupta (Gupta, et al., 2006) shows results for AA5083-H116 aluminium alloy under the impact of blunt projectiles with the JC model. The constitutive and fracture model have been calibrated from experimental results of tensile tests but the author reports that information on AA5083-H116 is limited in the literature. However, they state that this material is strain rate insensitive. In another set of experiments a similar study has been conducted on AA6005-T6 aluminium alloy. A modified version of JC constitutive and fracture models (material 107 from LS-DYNA) have been used in the study (Borvik, et al., 2005). The model has been developed for isotropic materials but was shown to work well with a moderately anisotropic material such as AA6005-T6. AA5083-H116 was shown to exhibit serrated or jerky flow in certain ranges of temperature and strain rate (Clausen, et al., 2004) (Benallal, et al., 2006) (Benallal, et al., 2008). This phenomenon, also known as the Portevin-Le-Chatelier (PLC) effect, is due to a negative strain-rate dependence observed in the material at certain ranges of strain rate. This negative strain-rate sensitivity is attributed to dynamic strain aging (DSA), resulting from a diffusion of solute atoms or other point defects towards temporarily arrested dislocations at obstacles in the slip path. The same occurrence was also observed in AA5086 alloy (Wagenhofer, et al., 1999). Constitutive equations have been specifically derived to predict the PLC effect, such as those developed by McCormick (Zhang, et al., 2001) or Benallal (Benallal, et al., 2006). As reported by these authors strain rates of the order of 10^{-2} constitute an upper area of the negative strain rate sensitivity regime and the strain rates resulting from the impact of a blast wave are significant higher than that, which justifies that PLC

effects may be neglected in the present study. In fact for lower strain rates the DSA significantly affects the results as reported in low velocity impact investigations (Grytten, et al., 2009a) (Grytten, et al., 2009b). The authors also stated that no significant effects of anisotropy were found (Grytten, et al., 2009a). This subject has been investigated in more detail using a Barlat constitutive model but a recommendation for further refined models has been reported (Grytten, 2008).

Borvik (Borvik, et al., 2009) indicated a wider range of occurrence of both the PLC effect and the negative strain rate sensitivity, between 10^{-5} and 10^{-1} s^{-1} and reported that serrated yielding disappeared at temperatures above 100ºC (Borvik, et al., 2009). Like with other metals, J2 plasticity theories are not sufficient for an accurate characterization of ductile failure of AA5083 aluminium alloy (Gao, et al., 2009). Hydrostatic stress and the third invariant of the stress deviator (which is related to the Lode angle) should be included in the constitutive model.

Another issue related to the dynamic response of aluminium alloys has to do with their response in shear. Strain hardening in high purity FCC metals is due to interactions between dislocations and as strain increases, the volume available to accommodate additional strain decreases due to the increase in the dislocation density (Zerilli, et al., 1987). In cases where damage is predominantly due to shear, it is influenced by the initial microstructure, including dislocation density, as the propensity for shear localization is increased due to the hindrance of dislocation motion (Pérez-Bergquist, et al., 2011). Because of this dependence on dislocation interaction with the microstructure, the shear response of FCC metals is sensitive to alloying, microstructure, and processing. Alloying can increase the work hardening capacity (Kocks, et al., 2003) in some materials by delaying the onset of instability in the microstructure and contribute to shear band broadening when the localization does occur. Shear localization can be an important factor in a dynamic failure process. Bai and Dodd (Bai, et al., 2002) studied the phenomena of adiabatic shear localization, which is typically an unstable deformation and failure mode in metallic materials subjected to dynamic loading. This occurs in regions of very high shear gradient and this occurrence is normally a concern as these are precursors of fracture. A standard definition has been provided by Zener and Hollomon (Zener, et al., 1944), stating that when a material deforms plastically the flow stress increases due to the high strain rate hardening and heat is released upon the production of plastic work. This heat will

increase the temperature of the material causing a softening effect. The two effects, hardening and softening, will compete but when thermal softening prevails the material becomes unstable, plastic deformation increases, more heat is generated drastically affecting its shear strength, and shear bands are developed (Wright, 2002). When the rate of generation of heat is very fast it will not have time to dissipate and the plastic deformation will not be homogeneous but will give place of localized bands, which are called adiabatic shear bands (ASB). The phenomenon is better understood looking at Fig. 3.29 were a shear band is shown together with a local temperature rise and a progressive hardening followed by softening after a certain temperature or critical strain is reached. However, other authors present different views on the formation of ASB (Rittel, et al., 2010) and sustained that their formation is triggered by dynamic recrystallization instead of being the result of a thermal softening. In fact, a variety of characteristic microstructures has been reported whose common point is that the material inside the band almost always undergoes dynamic recrystallization (Meyers, et al., 2000)(Andrade, et al., 1994). From a mechanical point of view characteristic experiments are not so widely available. Prediction of ASB is very complex but some analytical models have been proposed, based on the classical work of Zener and Hollomon (1944) based on the competition between strain-hardening and thermal softening.

The analysis of ASB is computationally very demanding and the range of engineering use of this phenomenon is still limited. In the recent years it is being considered that thermal softening is a minor player in the formation of ASB, while proposing that the dynamically stored energy of cold work is the driving force for strain localization (Rittel, 2009) (Dolinski, et al., 2010). In the present study these effects have been ignored as in similar tests a negligible adiabatic heating has been reported (Spranghers, et al., 2014).

Spranghers (Spranghers, et al., 2013) (Spranghers, et al., 2014) and Aune (Aune, et al., 2016) used optical measurements to capture the dynamic response of commercial code aluminium EN AW1050 (H24 and H14 respectively). They have used successfully the Digital Image Correlation (DIC) technique to measure the in-plane and out-of-plane plate displacement fields in order to validate the Lagrangian finite element analysis used to simulate the experiments. The same optical technique has bee used by Louar

(Louar, et al., 2015) to study the effect of blast loads on EN AW 1050-H14 plates subject to blast loading from an explosive driven shock tube (EDST) which were compared to free air blast from C4 explosions. The EDST tests were reported to show better reproducibility.

More recently Cerik (Cerik, 2017)investigated the effect of blast loads on AA5083-H116 aluminium alloy, particularly in the Heat-Affected Zones of welding. Formulae to predict the permanent set of stiffened plates were presented.

The variety of constitutive models and phenomena associated with the high strain rate loading of naval grade aluminium plates makes their analysis complex and computationally demanding but many researchers have been nonetheless successfully using simple phenomenological models, such as JC (Johnson, et al., 1983), to model these phenomena. A comparison between a few of these (Chaboche, 2008) shows that the JC model predicts quasi-static and dynamic ranges relatively well even for lower and higher strain rates and a good account of its limitations can be found in the work of Xue (Xue, 2007).

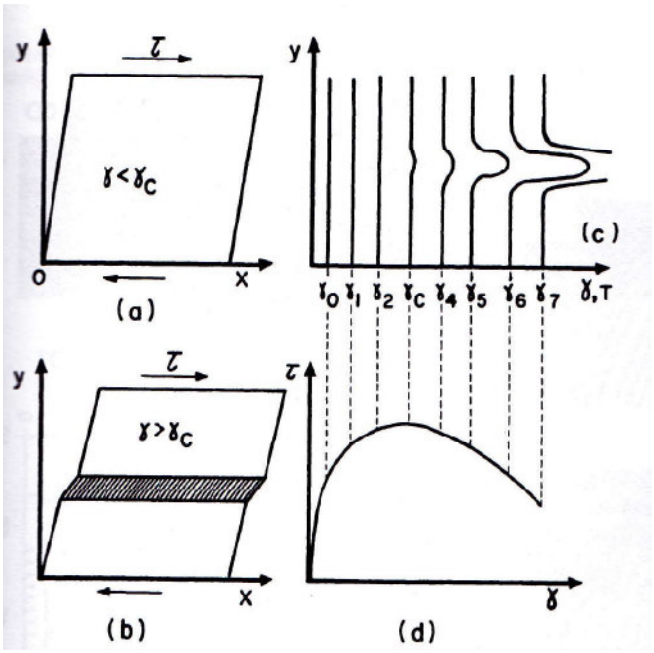

Figure 3. 29- Formation of an adiabatic shear band in a prismatic body subjected to shear . (a) Homogenoeus shear strain (b) A shear band is formed (c) Temperarture profiles are shown were a temperature increase is noticed at the region of the shear band (d) Stress-strain adiabatic curve showing the softening process after a critical shear strain is reached. (Meyers, 1994)

Dynamic recrystallization can be driven by the stored energy of cold work and can develop gradually during the stable plastic phase so that the approach of instability (Zener, et al., 1944) would not be needed in that case. This approach greatly simplifies the numerical treatment of the problem of initiation and propagation of an ASB, although the mesh-sensitivity still persists.

The variety of constitutive models and phenomena associated with the high strain rate loading of naval type grade aluminium plates makes their analysis complex and computationally demanding. However, as has been shown, many researchers have been successfully using simple phenomenological models such as the JC (Johnson, et al., 1983). This model was presented and explained in Chapter 3 together with its failure equation. Fig. 3.30 (Chaboche, 2008) presents a comparison between suggested constitutive models showing the dependence of the visco-plastic stress σ_v vs plastic strain-rate, combined in a logarithmic scale. The curves show that the JC model predicts quasi-static and dynamic ranges relatively well even for lower and higher strain rates. This also adds to the arguments in favour of the choice of this constitutive and failure model. The curves show that the JC model predicts quasi-static and dynamic ranges relatively well even for lower and higher strain rates. It may also be noticed that the original model of Bodner-Parton deviates considerably from the others for strain-rates above 10^{-2}, which questions its suitability for high strain rate regimes. However as explained above in Section 3.3.6.1, the model was later modified with noticeable improvement for higher strain rates (Chen, et al., 2008) (Song, et al., 2001). However Fig. 3.30 did use the original model wich did not not account for thermal effects, which may justify the observed deviations.

A more detailed description of the model has been written earlier in this Chapter and a good account of its limitations can be found in the work of Xue (Xue, 2007):

$$\sigma_{eq} = \left[A + B\varepsilon_p^n\right]\left[1 + C\ln\left(\frac{\dot{\varepsilon}_p}{\dot{\varepsilon}_0}\right)\right]\left[1 - \left(\frac{T - T_0}{T_{melt} - T_0}\right)^q\right] \qquad (3.152)$$

The first term on this equation represents the quasi-static stress-strain relation with strain hardening, at room temperature; the second term is the strain-hardening function and the third term introduces the temperature dependence in the stress-strain

relation. $\dot{\varepsilon}_0$ is a reference strain rate, T_0 and T_{melt} are the room temperature and the material melting temperature respectively. All remaining parameters were described in part 3.2.

3.5 Ductile fracture – Failure models

At this point it may be usefull to clarify the difference between failure and damage: the former relates to the loss of the capacity to carry load resulting from the accumulation of microdefects which is defined as the damage. Ductil failure is of utter importance to the study of the load carrying capacity of most metals and will be dealt with below.

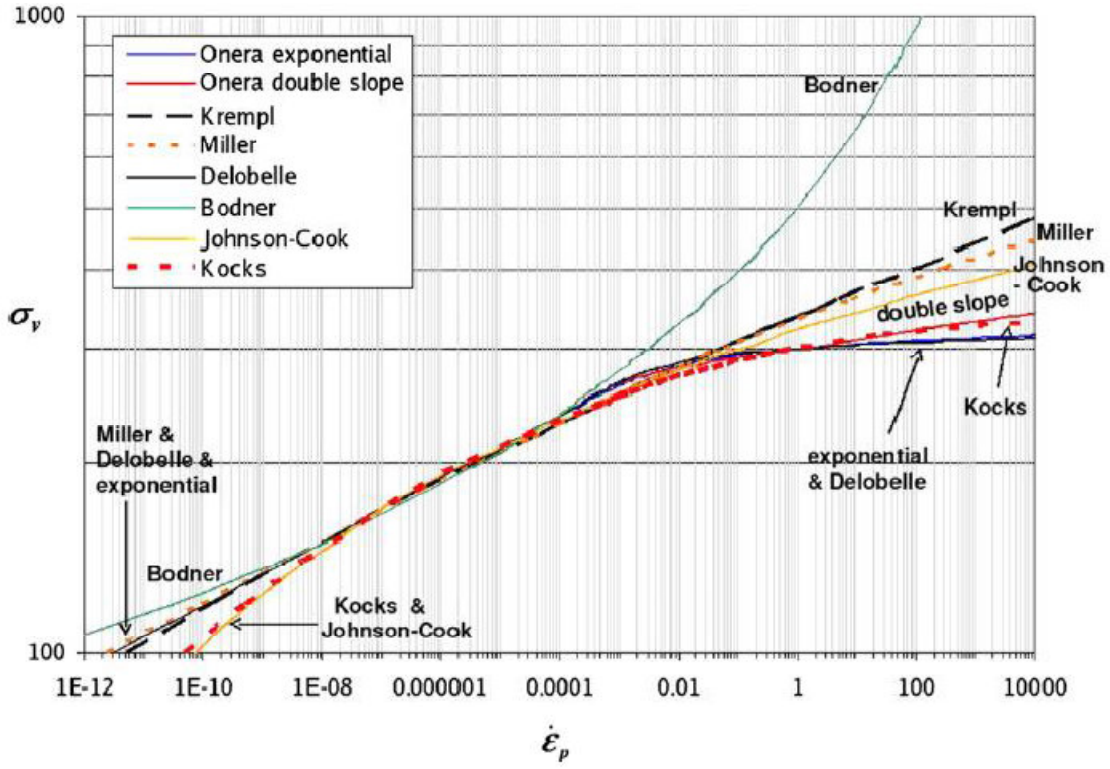

Figure 3. 30- Comparison of viscoplastic flow functions. Adapted from (Chaboche, 2008)

When a metal solidifies a crystalline structure is formed where the cristals are called the grains, each one showing a defined crystallographic orientation. Grain

boundaries separate grains and are important sources of stress concentration. The mechanical properties of a polycrystalline metal are an average of the mechanical properties of each grain and the structure taken as a whole is normally taken as isotropic even if individually the grains are anisotropic.

Defects commonly found on polycrystalline metals are dislocations. Plasticity is due to the motion and accumulation of dislocations due to shear stresses and occurs along crystallographic surfaces, the slip planes. The strain hardening of a material is due to the accumulation of dislocations.

Modeling of some sort of failure mechanism of the aluminium structures under blast load will be neded and some comments on the subject have been added below. Considering the solid material as a continuum (this is true at the macro scale level), up to moderate plastic deformation[10] the microstructure of materials can be assumed to stay unchanged. Thus, for many practical engineering applications, classical plasticity theory is sufficient in dealing with this. Beyond moderate plasticity the changes in microstructure are no longer negligible in the prediction of the ultimate fracture. This phenomenon can be addressed at different scales and a large number of approaches exist to predict material failure under loading. Many different categorizations are possible such as a division in three groups (Jeunechamps, 2008): Criteria of sudden failure; Plasticity models based on micro-voids and Continuous Damage Models. Another categorization more often found considers microscopic versus macroscopic failure. Generally, such categorizations are related to the approach followed in the treatment of the fracture phenomenon and a number of well documented methods are available, such as fracture mechanics, void growth theories, plasticity models of porous materials, damage mechanics and also some empirical methods. Fracture mechanics deals with the propagation of cracks and will not be addressed in this work. However, we will refer to cracks as the result of void growth and coalescence in the sense of damage and not fracture.

Perhaps a better categorization of the theories associated with the phenomena is that associated with the localized nature of fracture. These local models can be classified into coupled or uncoupled. The first group includes the porous plasticity models in

[10] Moderate plastic deformation is a deformation state where plastic strain is much greater than elastic strain but lower that the fracture strain at the current pressure and azimuth angle.

which the internal damage will interact with the flow behaviour of the material by a porous yield function. This model was first addressed by Gurson (Gurson, 1977) and later extended by Tvergaard and Needleman (Tvergaard, et al., 1984) both cited by Lee (Lee, 2005).

The uncoupled theory assumes that damage does not change the constitutive equation and is usually expressed in terms of accumulated plastic strain with various triaxiality weighing functions Mc Clintock (Mc Clintock, 1968) and Rice (Rice, et al., 1969) cited by Freund (Freund, 1990) .

Ductile failure of structures usually evolves through three phases: (a) accumulation of damage, (b) initiation of fracture and (c) crack propagation. Initiation of fracture can be seen as the result of accumulation of the ductile plastic damage. Microscopically, such damage is associated with the formation of shear bands, voids and micro-cracks. Those voids nucleate, grow and coalesce into larger voids, and cracks will develop, shear bands move and micro-cracks propagate. Macroscopically, this material degradation will result in a decrease of the material stiffness and strength and in a reduction of the remaining ductility (Xue, 2007). Such reduction in the load carrying capacity of the material will result in failure if the loading continues to increase. At a micro scale approach, the well known Gurson model (Gurson, 1977) is based on the concept of nucleation and growth of micro-voids during plastic deformation until they will coalesce to produce failure. Earlier models considered the accumulation of micro-defects in the material as the main cause for ductile failure. McClintock (1968) and Rice and Tracey (1969) pioneered this line of research and stated that the increase in volume of voids when the material was subjected to load had more effect than changes in their shape, therefore concluding that failure should be a function of triaxiality. The model of Rice and Tracey (1969) was later modified to include the interaction between voids and their nucleation and plasticity was considered to be coupled to the accumulated damage of the material (Gurson (1977), cited by Xue (Xue, 2007).

The Gurson model introduces a yield function which links plasticity to the accumulation of damage. The material is assumed to be porous and failure is controlled by an internal variable such as the volumetric fraction of voids. This volumetric fraction increases with the coalescence of voids and failure occurs when it reaches unity. The model maintains several limitations such as its inability to consider void shearing, or any “damage” that does not involve void volume increase. This led to several

modifications of Gurson's model where the work of Tvergaard and Needleman (1984) is often cited (Xue, 2007). However Gurson's model remains difficult to calibrate due to the large number of parameters involved.

The other type of coupled failure model has been proposed by Lemaitre (Lemaitre, 1985). The Continuous Damage Mechanics (CDM) theory is based upon an internal "damage" variable that describes the degradation of strength of the material. It differs from the micro-mechanical models in the sense that the micro-mechanism of individual void growth and their interactions are smeared and considered in a phenomenological aggregative way. Damage is assumed to be a scalar quantity (otherwise the anisotropy of plastic strain would imply the use of tensors greatly increasing the complexity of the model). It is an internal quantity meaning that it cannot be measured directly and some relationship with respect to measurable quantities has to be established to allow cumulative damage to be used as a criterion to predict the onset of failure. This set of variables whose evolution is controlled by thermo mechanical phenomena measurable at the current length scale will be assumed to capture the irreversible processes that occur at the micro-scale. Development of the theory is associated to the names of Lemaitre and Chaboche, although they were not their creators.

An aggregate response for the material is considerably more tractable and amenable to calibration than the study of the evolution of the microstructure of the material. However, the same comments applies as previously to the advantages versus accuracy of physically more soundly based models when compared to phenomenological or semi-empirical models.

In addition to the inherent complexity of these phenomena fracture under dynamic loading will introduce different responses. In dynamic fracture the role of material inertia cannot be ignored (Williams, et al., 2010). When loads are applied at high rates to a solid body with an existing crack it may propagate instantaneously. The stress field around the crack will not be in equilibrium, inertial loads effects will be present and the classical fracture mechanics where fracture can be predicted once the stress level reaches a critical value will not provide satisfactory results. However, this field is still not well understood. It is accepted that dynamic failure of materials is a

local, discontinuous change in the behaviour of the material through the creation of new crack surfaces which makes this difficult to observe and predict.

Computational methods for simulating dynamic failure are categorized as either continuum or discrete methodologies. Continuum methods are implemented like a constitutive model and failure (loss of deviatoric or total strength) is obtained at integration points of a finite element. Some numerical methods attempt to denote the formation of new surfaces either through mesh re-mapping or using additional kinematics that accounts for the formation of such surfaces (Williams, et al., 2010). The latter will not be further considered in this work.

CDM has the additional advantage that it can accommodate progressive damage. However, as the stiffness of the element is reduced and approaches zero, distortions can become unacceptably large and a secondary damage method is required (e.g. element deletion, which has been widely used). The loss of material strength is often exaggerated by material weakening induced localizations. Therefore, damage and plasticity are coupled in the plastic loading path and such coupled effect should be captured by the constitutive model used to predict the ductile failure of the material.

One group of widely used models are those based on fits of experimental data. A well known phenomenological model of this group is the Johnson and Cook (JC) (Johnson, et al., 1985) which is a dynamic failure model widely used in simulations and has been inspired in CDM methods (Williams, et al., 2010). It has been used in situations of high strain rate such as the perforation of plates by projectiles (Borvik, et al., 2002)(Borvik, et al., 2004)(Borvik, et al., 2005)(Gupta, et al., 2006) . This constitutive equation can be used uncoupled or coupled with different physical phenomena such as damage, temperature and strain rate. The full model includes linear thermo-elasticity, von Mises yield criteria, an associated flow rule, isotropic strain hardening, strain-rate hardening, softening due to adiabatic heating, softening due to isotropic damage evolution and a fracture criterion. Coupling the model with an element-kill algorithm that removes damaged elements from the mesh when the damage variable reaches a critical value may also be adopted to speed up calculations (Borvik, et al., 2001b). The advantage of the JC model is that the damage evolution and the plastic evolution are uncoupled in the stress integration procedure. One disadvantage is that the fracture is modelled as a sudden drop at the stress-strain curve which over simplifies the mechanical response of the material (Xue, 2007). However, the CDM approach explicitly

models the material degradation and a complete loss of the load carrying capacity occurs at the onset of fracture. The JC model also carries other limitation such as its inability to model the full range of stress triaxiality (Lee, 2005).

From above it emerges that a method where the damage does not change the constitutive model and where the strains and stresses at failure can be formulated in terms of an accumulated plastic strain has been deemed to be the most adequate for simulation purposes. Such accumulated strain must be weighted in terms of the stress triaxiality as fracture predominantly occurs for certain values of the stress state and the corresponding stress space can be described in terms of certain limiting particular stress states that correspond to certain values of triaxiality.

Experimental results have also shown that the fracture initiation of uncracked solids is sensitive to the hydrostatic pressure and is dependent on the Lode angle (Bao, et al., 2004)(Bai, et al., 2008). Hydrostatic tension or compression has a direct influence on void nucleation and growth-coalescence mechanisms and the shear band movement mechanism, either speeding or slowing the process, respectively. The Lode angle characterizes the deviatoric loading.

The Lode angle, θ, is an invariant that together with other two invariants (the hydrostatic component of the stress state and the stress measure of the deviatoric stress) defines a point in the stress space defining the actual 3D tress state. But before continuing, perhaps a brief explanation about the relation between the principal stresses and these invariants, accepting the risk of some repetition, may provide a better understanding of the subject. The reader may also refer to the doctoral thesis by Xue (Xue, 2007) which provides a simple and readable explanation on this subject.

From Fig. 3.31 we notice that the state of the principal stresses can be geometrically represented either by a vector in the three-dimensional space where the principal stresses are taken as Cartesian coordinates, or by a cylindrical coordinate system, Ozθ, aligned with the hydrostatic axis of the same origin. The azimuth angle θ in this cylindrical system is defined on the octahedral plane starting from a deviatoric axis. Along the Oz axis all the three principal stresses are equal.

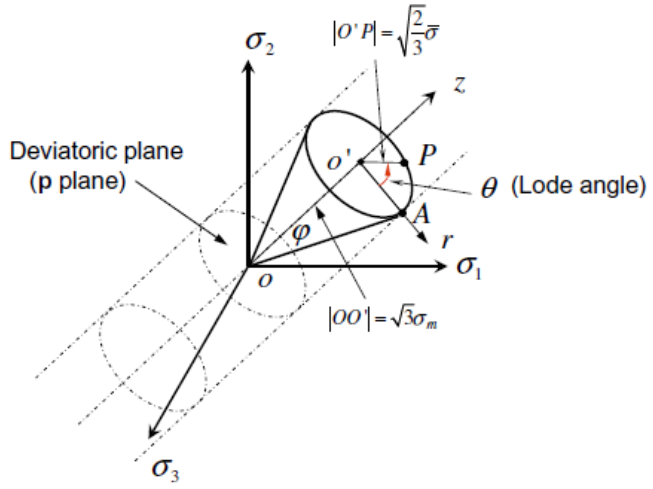

Figure 3. 31- The different coordinate systems in the space of principal stresses

The principal stress vector which represents the stress state is shown in Fig. 3.31 as . This stress state can be represented in three coordinate systems: a Cartesian system, based on the three principal axis; a cylindrical system, based on the hydrostatic axis coordinate, a radial coordinate given by the deviatoric stress and an azimutal angle , the Lode angle; and finally a spherical system given by the distance and the two angles and . At this point we have opted to choose a cylindrical coordinate system where the stress state vector can be decomposed in two components vectors, one perpendicular to the octahedral plane, and other in the octahedral plane, . The first represents the hydrostatic pressure and the second represents the deviatoric term. The magnitudes of both vectors is linearly related to the hydrostatic pressure *p* and the von Mises equivalent stress, :

$$\begin{aligned} \left|\overline{OO'}\right| &= -\sqrt{3}p \\ \left|\overline{O'A}\right| &= \sqrt{\frac{2}{3}}\bar{\sigma} \end{aligned} \tag{3.153}$$

The elevation angle , i.e. the angle to the octahedral plane, is related to the stress triaxiality and the azimuth angle can be characterized by the Lode angle, which is defined as:

$$\theta_L = \tan^{-1}\left\{\frac{1}{\sqrt{3}}\left[2\left(\frac{s_2 - s_3}{s_1 - s_3}\right) - 1\right]\right\} \tag{3.154}$$

The Lode angle is not defined on the hydrostatic axis, where $s_1 = s_3$. It is widely used and its form varies from author to author. Gao (Gao, et al., 2009) considers an invariant θ that is given by

$$\cos(3\theta) = \frac{3\sqrt{3}}{2}\frac{J_3}{J_2^{3/2}} = \frac{27}{2}\frac{J_3}{\bar{\sigma}^3} \tag{3.155}$$

where the *J*'s are the deviatoric invariants. It should be noted that

$$\theta = \theta_L - \frac{\pi}{6} \tag{3.156}$$

θ is controlled by the relationship of the intermediate principal stress to the major and minor principal stresses. When the intermediate principal stress, σ_2, equals the major principal stress σ_1, the Lode angle becomes 0º and when $\sigma_2 = \sigma_3$ it becomes 60º. Thus, the Lode angle varies between 0 and 60º and its value indicates the magnitude of the intermediate principal stress in relation to the other two principal stresses. The other major parameter that affects failure is stress triaxiality which is directly related to the hydrostatic stress tensor. Gao (2009) reported that stress triaxiality has little effect on plasticity but significant effect on ductile failure strain and the Lode angle has a negligible effect on ductile fracture but its effect on plasticity is significant. However, the inclusion of the Lode angle dependence has been ignored in most analysis relating to high strain rate plasticity. Different forms of presenting triaxiality and Lode angle have been used by different authors where they are expressed in terms of the stress invariants (Bai, et al., 2008), such as,

$$p = -\sigma_m = -\frac{1}{2}\mathrm{tr}(\sigma) = -\frac{1}{3}(\sigma_1 + \sigma_2 + \sigma_3),$$
$$q = \bar{\sigma} = \sqrt{\frac{3}{2}[S] : [S]} = \sqrt{\frac{1}{2}\left[(\sigma_1 - \sigma_2)^2 + (\sigma_2 - \sigma_3)^2 + (\sigma_1 - \sigma_3)^2\right]}, \quad (3.157)$$
$$r = \left(\frac{9}{2}[S].[S] : [S]\right)^{\frac{1}{3}} = \left[\frac{27}{2}\det([S])\right]^{\frac{1}{3}} = \left[\frac{27}{2}(\sigma_1 - \sigma_m)(\sigma_2 - \sigma_m)(\sigma_3 - \sigma_m)\right]^{\frac{1}{3}}$$

where $[S]$ is the deviatoric stress tensor, $[I]$ is the identity tensor and the indexes 1, 2 and 3 denote principal stresses. Also,

$$[S] = [\sigma] + p[I] \quad (3.158)$$

The triaxiality parameter can now be defined as:

$$\eta = \frac{-p}{q} = \frac{\sigma_m}{\bar{\sigma}} \quad (3.159)$$

and the Lode angle θ is related to the normalized third deviatoric stress invariant through

$$\xi = \left(\frac{r}{q}\right)^3 = \cos(3\theta) \quad (3.160)$$

The failure surface obtained by means of the Lode angle has the form of a phenomenological decaying function that has symmetry around the $\theta = 0$ meridian, which corresponds to a state of plane-strain (Xue, 2007). Three-dimensional failure loci are usually constructed by surface fitting around test results for stress-triaxiality and Lode angle parameters. This symmetry around the $\theta = 0$ meridian was later found to be not true and a higher order surface fitting is necessary to represent the failure surface more accurately (Bai, 2008) (Bai, et al., 2008).

Bai (2009) also proposed a normalization of the Lode angle defining a Lode angle parameter $\bar{\theta}$, varying between -1 and 1:

$$\bar{\theta} = 1 - \frac{60}{\pi} = 1 - \frac{2}{\pi}\text{acos}(\xi) \tag{3.161}$$

These definitions allow that a stress state can be uniquely characterized by the above defined set of parameters $(\eta, \bar{\theta})$, which incorporates all three stress invariants. The model is however, complex and with many constants to calibrate (Bai, et al., 2008). Failure dependency on stress triaxiality and on the third deviatoric invariant (Lode parameter) is further explained in the section below.

3.6 Damage model

Cumulative strain damage models assume that the damage towards fracture of the material is due to its plastic deformation history and it is assumed failed when the accumulated damage variable D exceeds a critical value, D_c. The damage variable is obtained from an accumulated plastic strain with an appropriate weighting function, which in general is considered to be a function of stress rate, strain, strain rate and temperature, as in

$$D = \int_0^{\varepsilon_c} f(\sigma, \varepsilon, T, \dot{\varepsilon}) \mathrm{d}e_p \tag{3.162}$$

where σ and ε are the stress and strain tensor, T is the temperature and $\dot{\varepsilon}$ is the strain rate.

The JC model may be coupled with an accumulated damage model using a weighted integral with respect to the effective strain, as a fracture criterion,

$$D = \int_0^{\varepsilon_c} \frac{\mathrm{d}\varepsilon_p}{\varepsilon_f\left(\frac{\sigma_m}{\sigma_{eq}}, \dot{\varepsilon}_p, T\right)} \tag{3.163}$$

where the stress triaxiality represents the pressure dependence. The general form of the weighing function considers also the strain rate and the temperature dependencies as in

$$\varepsilon_f = \left[D_1 + D_2 \exp\left(D_3 \frac{\sigma_m}{\sigma_{eq}} \right) \right] \left[1 + D_4 \log \frac{\dot{\varepsilon}_p}{\dot{\varepsilon}_0} \right] \left[1 + D_5 \frac{T - T_0}{T_{\text{melt}} - T_0} \right] \tag{3.164}$$

where D_i are material constants. If the strain rate effects and the thermal dependence are ignored, and knowing that the mean stress σ_m is the negative value of the pressure p. Eq. (3.164) can be expanded using the Taylor series around zero triaxiality. Retaining the first term of the series, and considering that for most metals D_2 is positive and D_3 is negative (Johnson, et al., 1985), gives,

$$\varepsilon_f = D_1 + D_2 - D_2 D_3 \frac{p}{\sigma_{eq}} \tag{3.165}$$

This implies that an increase in the compressive hydrostatic pressure will cause an increase in the value of the failure strain of the material.

The weakening of the material has also been introduced in the JC strength model (Borvik, et al., 2001a), where D has the same meaning as in the original work (Johnson, et al., 1985):

$$\sigma_{eq} = (1 - D)\left[A + B\varepsilon_p^n \right] \left[1 + C \ln\left(\frac{\dot{\varepsilon}_p}{\dot{\varepsilon}_0} \right) \right] \left[1 - \left(\frac{T - T_0}{T_{\text{melt}} - T_0} \right)^q \right] \tag{3.166}$$

The damage variable D, in the JC model has the form

$$D = \int \frac{1}{\left[D_1 + D_2 \exp(D_3 \zeta) \right] \left[1 + \left(\frac{\dot{\varepsilon}}{\dot{\varepsilon}_0} \right) \right]^{D_4} \left[1 + D_5 T^* \right]} \mathrm{d}\varepsilon_p \tag{3.167}$$

where the meanings of the parameters were presented above. This is a stress triaxiality model and it does not consider the azimuth angle to the octahedral plane (Lode angle).

According to Xue (2007) the joint effects of hydrostatic pressure and the effective stress are not sufficient to quantify the equivalent fracture strain. For stress triaxiality models, the fracture loci in the octahedral plane are circles, which are the same as the von Mises yield locus. As mentioned above the Lode angle dependence which may have a strong effect on fracture strain for many materials is not present in the JC model. The damage accumulation along the load path is a three-dimensional problem in that the pressure, the Lode angle and the equivalent stress influence the damage rate. The two effects, pressure and Lode angle may be considered independent of each other as the material become more ductile when exposed to high compressive pressure but flow strength increases much more slowly. The hydrostatic pressure may be considered to have little effect on the flow strength of material but it delays the onset of fracture and there will be no further plastic strain beyond a cut-off value and the fracture locus shrinks to single point at the stress space.

Even thought the JC model does not consider the Lode angle dependence it has a number of important advantages. One of these is the uncoupling between plasticity and damage evolutions in the stress integration procedure. Normally these methods incorrectly predict the fracture modes due the lack of damage induced weakening and unrealistic strengthening in the later stage of deformation (Xue, 2007).

The exponential form of the triaxiality function also limits the ability of the model to predict the whole range of the failure locus. The importance of this triaxiality extended range on failure has been shown by some authors (Bao, et al., 2004). Three distinct failure modes were identified as shown in Fig. 3.32 (Buyuk, 2013) for the Al2024_T351 Aluminium alloy. The various JC models available in the literature are only covering the failure space by single monotonic functions (identified in Fig. 3.32 as Set-1 to Set-4) whereas Bao's work shows the three distinct branches of failure modes (Bao, 2003). The figure shows that failure characteristics do not exhibit a monotonic trend. However, in many problems of interest the loading path is limited to a narrow range of the stress triaxiality and it will increase monotonically as a function of the equivalent strain. This is the case of the loading of flat plates exposed to a lateral pressure distribution. In this case eq.(3.162) is reduced to

$$D_c = \int_0^{\varepsilon_f} \left(\frac{\sigma_m}{\sigma_{eff}} \right) \mathrm{d}\bar{\varepsilon} \tag{3.168}$$

In general the stress triaxiality varies during the deformation process and it is necessary to consider an average triaxiality, defined by

$$\left(\frac{\sigma_m}{\sigma_{eff}} \right)_{ave} = \frac{1}{\bar{\varepsilon}_f} \int_0^{\bar{\varepsilon}_f} \left(\frac{\sigma_m}{\sigma_{eff}} \right) \mathrm{d}\bar{\varepsilon} \tag{3.169}$$

The equations above describe the fracture envelope and in Fig. 3.32 it can be noticed how the locus is related to a set of quasi-static tests and numerical simulations of different types of specimens of Al2024-T351 (Bao, et al., 2004). The authors determined the weighing function in the range of triaxiality (-1/3 to 1.0). It is interesting to note that a triaxiality greater than 1/3 corresponds to fracture associated to void nucleation, growth and coalescence (Zone I). This implied the use of tensile tests on smooth and notched specimens to obtain different values of triaxiality. Zone III was assessed by means of compression tests on short cylinders where the failure mechanism was shear fracture under negative triaxiality. Finally in Zone II combinations of these two failure modes and pure shearing were involved. Eq. (3.169) can be used for Zone I rewritten as

$$\left(\frac{\sigma_m}{\sigma_{eff}} \right) \bar{\varepsilon}_f = D_c \tag{3.170}$$

which turns the fracture criterion of Zone I in a linear relation. Bao (Bao, et al., 2004) made further simplifications by representing the fracture envelope by the parameters *a* and *b* (see Fig. 3.34), respectively the intersection point (0,a) of Zones II and III where *a* is the critical fracture strain in pure shear and the average stress triaxiality and critical fracture strain in uni-axial tension, can fully define the fracture envelope in Bao's formulation. Note that in Fig. 3.33 the sign of triaxiality and the numbering of the Zones are reversed relatively to Fig. 3.32.

Bao (Bao, 2003) and the JC model (Johnson, et al., 1985) do not consider the Lode angle dependence as referred above. This can be better understood in Fig. 3.33, were the failure surfaces proposed by each of the models mentioned (Bao, JC and Xue) can be compared. In Fig. 3.33 a) the JC method shows a monotonic smooth exponential increase. Fig. 3.33 b) represents the surface of the three Zones shown in Fig. 3.32 but still independent of the Lode angle. Fig. 3.33c) represents a Lode angle parameter dependence of the failure surface, constructed from Bao's data (Bao, 2003). It can be seen that although Fig. 3.33 b) and c) were constructed from the same set of data, the failure surfaces obtained can be quite different. The branched nature of the failure locus cannot be represented by a monotonic exponential curve such as the JC model. The JC curve, when properly scaled can be close to the branch curve in the range between plane strain $\left({}^{\sigma_m}/_{\bar{\sigma}} = 0\right)$ and equi-biaxial tension $\left({}^{\sigma_m}/_{\bar{\sigma}} = 1\right)$.

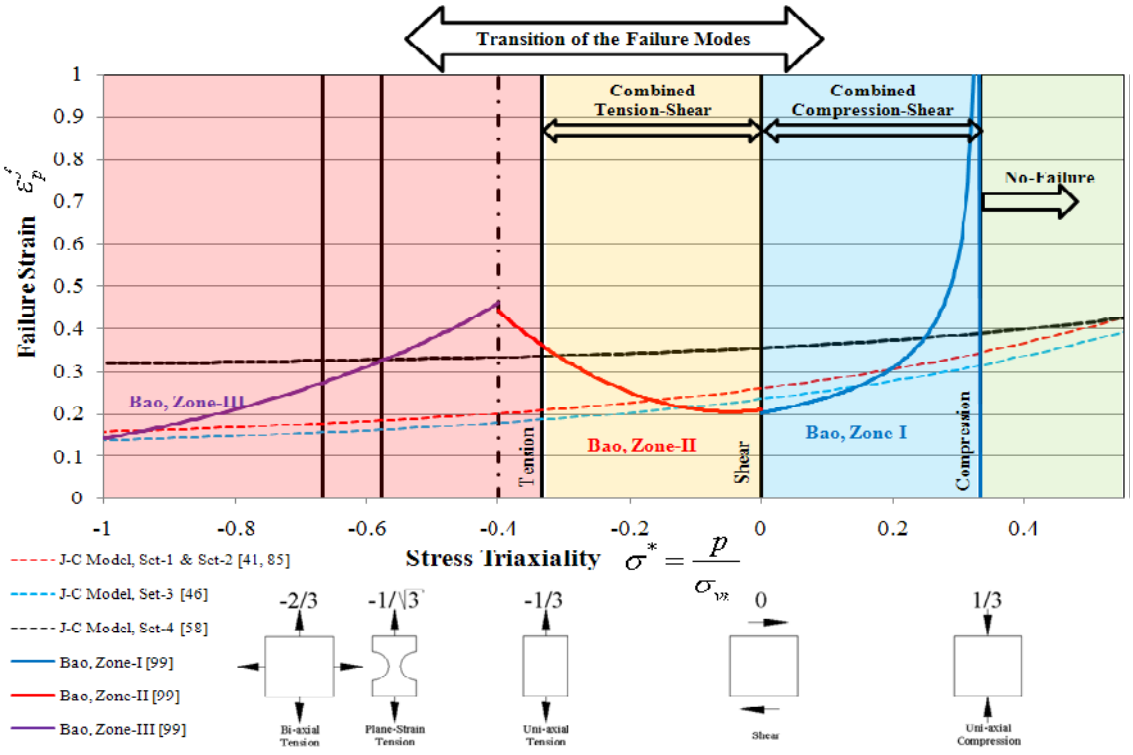

Figure 3. 32- Transition of the failure modes and comparison of the failure loci for AL2024-T351. Reproduced from (Buyuk, 2013). [11]

[11] Note: In Fig. 3-32 ref. [99] corresponds to (Bao, 2003); Ref. [41] to (Lesuer, 2000); Ref: [85] to (Johnson, et al., 1985); Ref. [58] to (Kay, et al., 2007) and Ref.[46] to (Kay, 2003).

This explains the reported success of those using the the JC criteria. However, the prediction of JC rapidly deteriorates as one moves away from plane strain into the negative values of traxiality (Lee, 2005)(Bao, et al., 2004).

Nevertheless the JC model has been preferred by many researchers. It has been used in ballistics and tearing of blast loaded plates where the mechanisms of failure are mostly due to shear localization. Simplicity and the lower number of parameters needing calibration overcomes the disadvantages associated with the shortcoming of the physical emulation of the failure phenomena. It may be thus said that, if properly calibrated it can give a good approximation of the failure locus in the region of high triaxiality or in the region of low triaxiality albeit not both at the same time.

As with other phenomenological models, the JC model is often tuned for a specific test (such as uni-axial tension, shear or compression) in accordance with the expected loading at failure of the component under analysis. Thus, the particular test conditions will be matched by utilizing single monotonic functions and it will be assumed that the model will adequately predict the conditions of the problem under investigation. This may not be a problem as long as the conditions at failure are reasonably anticipated and the experimental data set that the model was calibrated

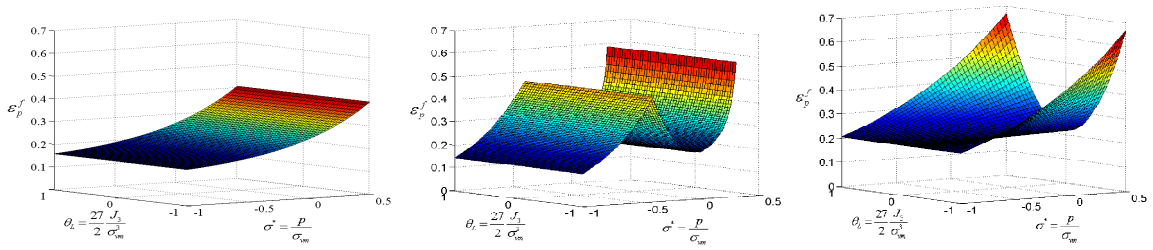

(a) (b) (c)

Figure 3. 33 – Failures models on the space described by stress-triaxiality and Lode-angle-parameter for Al2024-T351: (a) JC model (Johnson, et al., 1985), (b) model by Bao (Bao, 2003), (c) model by Xue with Lode-angle-parameter (Xue, 2007). Adapted from (Buyuk, 2013)

with is identified as being adequate to the investigation of those conditions. Plate thickness, for instance, can yield different calibration parameters for the JC model. In Fig. 3.33 all the JC sets of material parameters were derived for the same material,

AL2024-T351, albeit at different test conditions. This will give different flow stresses and failure surfaces as the conditions of the experiment vary. There is no other way to circumvent this problem dependency of high speed, high strain rate, transient, impact loading than to have test data that allow calibration of the constitutive model.

3.7 Numerical difficulties and conclusions

In non-linear FE analysis simply refining the mesh does not necessarily improve the accuracy of results (Belytschko, 2006)(Zukas, et al., 2000) and no clear theoretical guidelines on mesh refinement requirements are available in the literature. Zukas (2000) presents an interesting review of current FE modelling difficulties, but the major factor to bear in mind is mesh dependency of the range of phenomena that is the object of this dissertation. The JC method has the advantage of showing no mesh dependency on stress triaxiality and it calculates the same plastic strain for failure initiation irrespective of the mesh size (Buyuk, 2013). From all the above it is clear that solely the complexity of the phenomena associated with fracture and failure encompasses many approaches, many models and theories and is far from being fully understood. The most general and mathematically sound methods are hard to calibrate and to implement and the simplest methods are still being used thought those who use them recognize their limitations. However, in the scope of the present investigation propagation of shock waves through a failed bulkhead is the main purpose that only requires engineering approximation for the correct simulation of the failure of a plate under blast. From the review and analysis above it may be concluded that a JC model shall be the most cost effective in terms of computational effort given the expected results. The pursue of an elaborated and rigorous model would imply a disproportionate effort bearing in mind the aim of the work. Besides in itself the setting up of such a model would indeed justify a whole dissertation on the subject. JC model has thus been used in the next sections.

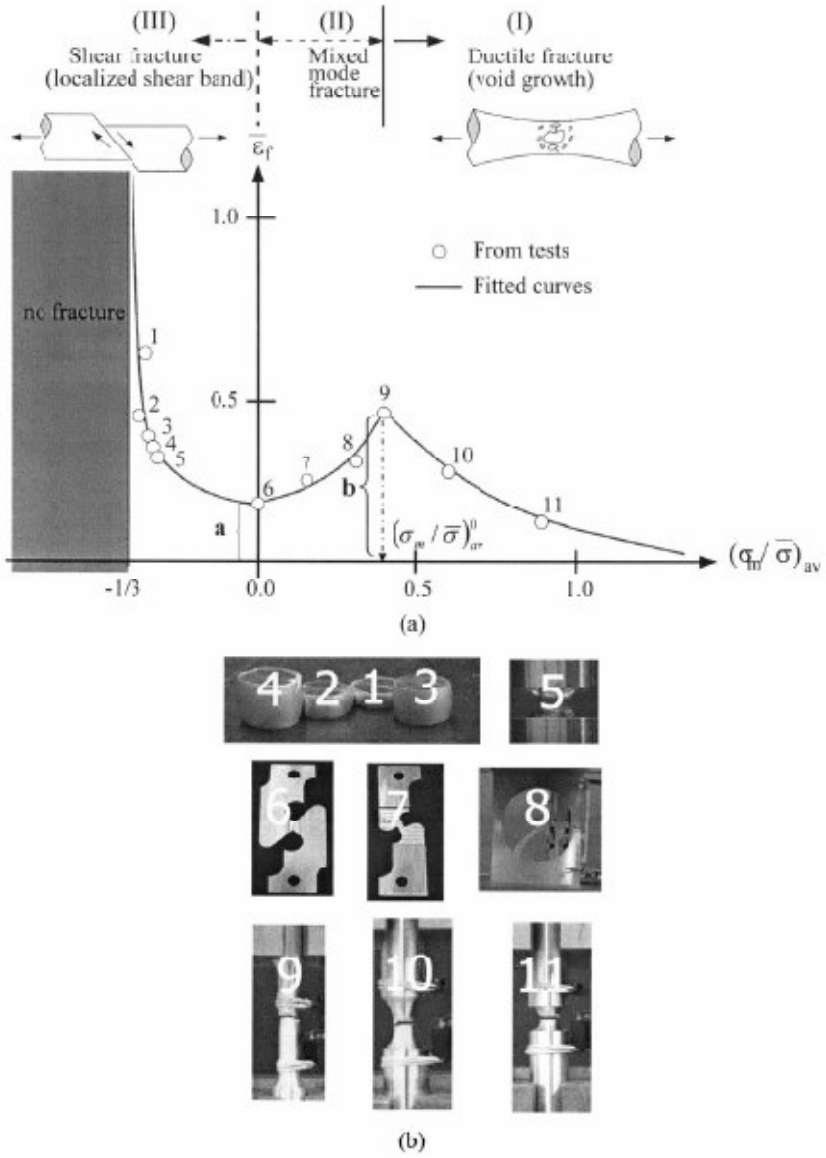

Figure 3. 34 – (a) Bao-Wirzbicki fracture envelope for AL2024-T351 expressed in terms of equivalent plastic strain to fracture $\bar{\varepsilon}_f$ and average stress triaxiality $\left(\sigma_m/\sigma_{eff}\right)$; (b) The different types of specimens used for the determination of the fracture envelope (Bao, et al., 2004)

4. Numerical modeling

The modeling techniques used are explained along with the ALE foundation and the numerical algorithms related to its implementation. Other important functions and techniques that have been used in this work are also described whenever considered relevant

4.1 Introduction

Explosions are very complex phenomena as the incident peak pressures may be affected by the ambient temperature, pressure, relative humidity, density, stand-off distance, mass of explosive and, obviously, its composition, as explained in Chapter 2. For free air explosions the existence of wind can also perturb the results. The ground or the stand can also introduce shock wave reflections. All these aspects hamper the creation of numerical models and validation of numerical results. The evaluation of structural response arising from blast loading is another difficult job as the simulation of dynamic, transient phenomena, at very high speeds, involving shock waves presents many difficulties. The explosion itself generates a complex flow which is associated to a complex phenomenon (combustion and heat transfer). The charge shape may also influence the shape of the wave front and its pressure distribution (Adamik, et al., 2004). Most real ammunition uses conical or cylindrical charges and the vast majority of experimental data is based on spherical charges. For this reason spherical charges were adopted in the present work.

These are some of the problems that arise in the explosion simulation which is the computational fluid dynamic part of the problem. Anther problem is the fluid structure interaction as the blast wave will impact a target surface, which material response at high strain rates (typically in the range of 10^2 to 10^4 s^{-1} as shown in Fig. 4.1) (Ngo, et al., 2007) will also have to be suitably modeled. Many constitutive equations exist for that, almost all of them claiming better results for that specific loading regimes

and materials. The choice of a constitutive model also requires careful analysis of published work. As soon as the material cracks the constitutive equation ceases to be valid and a damage model has to be added to the simulation. This will pose a compromise between accuracy and complexity. The most detailed models provide the more realistic results but at the cost of requiring very finely meshed models. This is the only way of detecting shear band development for instance. However, this means that a complete decoupling of the previous part of the problem would be required because running a blast wave propagation with an extremely refined mesh would not be feasible at least with most commonly available desktop computers.

Hydrocodes incorporate simplified models that may provide acceptable solutions within reasonable computation times and due mention will be made in the present Chapter to the techniques available for these simulations. The next sections describe how to simulate blast and the constitutive behavior of metals exposed to the loading imparted by blast waves.

The tri-services manual (DoD, 2008) or CONWEP can provide approximations to real data and many authors use them as references as they have the advantage of being based on a very large wealth of experimental data. The scaling laws presented in Chapter 2 are well established and work acceptably well at least for engineering purposes. This means that in the absence of measured data from full scale experiments it is possible to find reference values for comparison and analysis purposes. However it will been shown in Chapter 5 that the tri-services manual abacuses and tables yield average rather than peak overpressures which make comparison with wave blast simulations more difficult.

LS-DYNA has been the numerical tool used in this investigation. The modelling options and functions used in the simulations are shown and some of them discussed in this Chapter to allow a better understanding of physical foundations of the methodologies that have been adopted. The phenomena to be investigated encompass many disciplines of science: thermodynamics, fluid mechanics, solid mechanics, material behaviour, and more. A fully detailed simulation of all aspects involved would be unpractical and many simplifying assumptions have been taken. The chemical reactions of the explosive have been ignored and only the conversion of its burning energy into pressure waves was considered, by means of a simple burning model and an equation of state. The next section addresses the modelling tools that were used.

The necessity of using explicit time integrations is discussed below as well as the shortcomings of using an explicit solver. Other techniques necessary to the full analysis of the problem are also presented such as the Arbitrary Lagrangian-Eulerian approach. In alternative to the ALE techniques and whenever possible a Lagrangian approach has been used to simulate the blast waves resulting from the detonation of an HE.

The following fundamental modelling techniques have been used:

a. A Lagrangian or the ALE techniques was necessary to solve the blast resulting from the energetic flow of air and products of the explosive reaction.
b. An algorithm of Fluid-Solid Interaction was necessary to solve the problem of transfer of momentum from the explosive shock wave to the structure;
c. A suitable material model had to be chosen to properly describe material response under blast loading. As it has been shown in Chapter 3 the number of available models is overwhelming and a contribution has been given to help the reader to understand the differences between them.

Some material models include failure, which has the advantage of a physical meaning of the failure criteria but the option exists to use a suitable failure numerical mechanism that has to be added to the model. Both options are being discussed. An element kill routine has been used to simulate a crack or a hole in the failed structure to allow the reacted gases to flow through it and propagate to the adjacent compartment. The ALE analysis was identified as the only that could effectively reproduce the bouncing of shock waves in the interior walls of a confinement subject to an internal blast. All the subjects described in the present Chapter will be used in Chapters 5, 6 and 7.

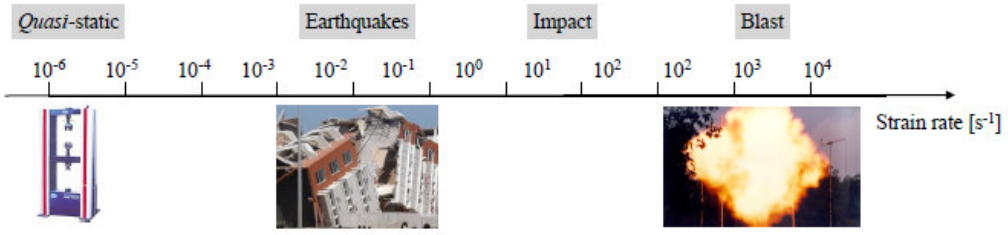

Figure 4. 1- Typical values of strain rates ((Ngo, et al., 2007)

4.2 Implicit and explicit integration

Most of the theoretical background presented is based on the textbook from Belytschko (Belytschko, 2006) and the works of Linder (Linder, 2003), Donea (Donea, et al., 2004) and Benson (Benson, 1992),(Kuhl, et al., 2003).

One major factor in the numerical analysis of transient dynamic problem is the computing time and two numerical schemes exist to solve a nonlinear time varying problem: explicit or implicit integration schemes. Basically a dynamic problem requires the solution of a system of second order differential equations of the type,

$$m\ddot{x}^n + c\dot{x}^n + kx^n = f^n \tag{4.1}$$

where n is the time step and kx terms are usually designated as internal forces. The basic problem resides in finding the displacement x^{n+1}, at time t^{n+1}. Explicit and implicit dynamic solutions can be written as:

Explicit: $$x^{n+1} = f\left(x^n, \dot{x}^n, \ddot{x}^n, x^{n-1}, \dot{x}^{n-1}, \ldots\right) \tag{4.2}$$

Implicit: $$x^{n+1} = f\left(\dot{x}^{n+1}, \ddot{x}^{n+1}, x^n, \dot{x}^n, \ldots\right) \tag{4.3}$$

In explicit schemes all the terms are known at time t^n and t^{n-1} time and the explicit equations can be solved directly. Implicit solutions depend on nodal velocities and accelerations at time t^{n+1} which are unknown quantities. An explicit solution will sum internal and external forces at each node and compute nodal accelerations by dividing by the nodal masses. The solution will advance by integrating these accelerations in time to obtain the velocity and displacement at each node. An implicit solution will compute a global stiffness matrix that is applied to the nodal out-of-balance force to obtain a displacement increment.

The task of implicitly solving a system of dynamic equations of motion is much more computational intensive than the use of explicit integration which means that in problems involving large deformations where time steps are substantially reduced due to element flattening, solution with implicit solvers would be unpractical. An implicit time integration requires equilibrium at time t^{n+1} implying that a relatively large system of equations will have to be iteratively solved at every time step. The scheme has the advantage of being always numerically stable and convergent but usually with a higher CPU cost than the explicit method. In an explicit time integration scheme equilibrium is required at time t^n and no large systems of equations have to be solved.

For high-speed dynamic problems, the solution time is comparable to the time required for a wave to propagate through the structure. This class of problems covers most wave propagation problems, explosives problems, and high-speed impact problems. It may be arguable that in structural dynamics the stability requirement of an explicit scheme will require very small time steps to account for mesh distortion, meaning thousands of iterations whilst with an implicit scheme a few hundred would be sufficient as a larger Δt would be acceptable. However in blast wave problems involving very high strain rates, in order to capture the details of the phenomena, a very small Δt will be required and this favors explicit schemes, due to their speed. Hence, regarding the nature of the problem, the explicit integration scheme is normally the optimal choice in these cases. However, explicit solvers, although much quicker in dynamic problems even with very small time steps, have the inherent problem of being conditionally stable and its stability depends on the time-step size. Numerical errors are proportional to the time step and the square of the space step.

The central difference method is the method used in LS-DYNA to advance the mesh in time. The acceleration at time *n+1* is computed from eq. (4.1) using

$$\ddot{x}^n = m^{-1}(f^n - kx^n) \tag{4.3}$$

where the damping term has been omitted for clarity. Now the nodal velocities and displacements are computed from the obtained nodal accelerations using the central differences scheme,

$$\begin{aligned} \dot{x}^{n+1/2} &= \dot{x}^{n-1/2} + \ddot{x}^n \Delta t^n \\ x^{n+1} &= x^n + \dot{x}^{n+1/2} \Delta t^{n+1/2} \end{aligned} \tag{4.4}$$

where

$$\Delta t^{n+1/2} = \frac{\Delta t^n + \Delta t^{n+1}}{2} \tag{4.5}$$

The solution is advanced from time t^n to time t^{n+1} without iterations and the geometry is updated by adding the displacement increments to the initial geometry:

$$x^{n+1} = x^0 + u^{n+1} \tag{4.6}$$

This method has the advantage of being much less sensitive to round-off error.

Explicit methods are quick and simple to run as all quantities to derive depend on known quantities as they are computed in the preceding step. However, this simplicity has a cost. To have a stable solution that converges, the time-step Δt must satisfy the condition of Courant (Hallquist, 2006). Considering the larger frequency of vibration of the mesh the Courant condition states thus,

$$\Delta t \leq 2/\omega \tag{4.7}$$

The computation of this frequency amongst all elements of the mesh is computationally difficult and LS-DYNA uses a different approach considering instead the local speed of sound c:

$$\Delta t = \frac{L_e}{c} \tag{4.8}$$

where L_e is the characteristic length of the element and c is the local sound speed of the material. The software calculates the value of Δt for all elements and chooses the smaller, multiplying it by a safety factor that reduces it to ensure a better stability of the solution. This reduction factor has a default value of 0.9 but may be modified by the user. For simulations with high explosives this default is lowered to 0.67 as explained in the LS-DYNA Keyword User's Manual Vol I, and this was the value used in all simulations.

However, the process of adjusting the time-step in terms of the smallest element of the mesh is not computationally efficient and LS-DYNA may use, by user option, a sub-cycling algorithm that calculates Δt for all elements, ordering and grouping them by their value so that the time-step of each group is multiple of the smallest Δt found in the mesh. This way the numerical efficiency is increased.

It has been mentioned that the time interval is determined from the smallest element of the mesh and this requires that meshes are as regular as possible. The degree of refinement is determined by the compromise between speed of solution and accuracy of results. However non-linear parameters such as plastic strain, are not as mesh sensitive as linear elastic stresses and coarser meshes may be used in non linear explicit analysis. That is to say that unlike in FE linear analysis, mesh refinement not always results in improved accuracy for explicit analysis (Buyuk, 2013).

However this ceases to be true whenever failure and element deletion are involved. In such cases the mechanism of detecting the conditions of failure has a strong numerical dependence on the mesh refinement which brings another difficulty that will be addressed later.

4.3. The Arbitrary Lagrangian Eulerian (ALE) approach

4.3.1. Lagrangian, Eulerian and ALE descriptions

Lagrangian meshes are the most commonly used in solid mechanics problems because they follow the motion of the body by deforming with it, and result in the straightforward determination of deformations, stresses and the definition of boundary conditions. They also are, generally, the most accurate. However when deformations are very large, element angular distortion will introduce numerical errors and since the explicit time step Δt, depends on the smallest dimension of the elements of the mesh, when they become crushed the iteration time interval will diminish to a point where a solution will not be attainable. Eulerian meshes, though they do not suffer from this problem as they remain fixed in space, will encounter computational difficulties and accuracy problems due the independent motion of the material in respect to the mesh. Non linear transport terms will be introduced due to the motion of material through the element grid. When going through the element boundaries more than one material will share the same cell. It becomes difficult to follow material boundaries or to define contact between different materials. That's where the ALE algorithms come into play, particularly those capable of handling multi-materials and fluid structure interaction. In a Finite Element problem normally two domains are considered: a material and a spatial domain. The Arbitrary Lagrangian Eulerian approach introduces a third domain, which has an arbitrary motion and is associated to a reference mesh, moving independently of the other two domains. It is in this reference mesh that the problem is formulated. This arbitrary motion enables us to deal in a convenient manner, with moving boundaries, free surfaces, large deformations and interface contact problems. So in the ALE formulation three domains are used (Belytschko, 2006)(Hughes, et al., 1981):

1. The initial configuration of the material
2. The current configuration of the material
3. The referential or ALE domain

The material motion is referred to the reference mesh (an arbitrary mesh) which in turn may also move respectively to a fixed referential. This way the material distortion will be smaller as it is referred to a moving referential. These three approaches are illustrated in Fig. 4.2.

The ALE algorithm is basically a re-meshing tool. When the deformations are so large that time-step becomes too small to allow the continuation of the calculations, it is necessary to stop the simulation and make a new mesh and then map the previous results on to the new mesh. The ALE algorithm avoids this need and its results are generally more accurate than those obtained from a rezoning calculation (theoretically this is true as long as a second order advection algorithm is used but it has been shown in Chapter 5 that first-order advection algorithms may, sometimes, yield better results).

An ALE formulation contains both pure Lagrangian and pure Eulerian formulations. In the pure Lagrangian description the mesh moves with the material (the motion of the reference mesh coincides with the motion of the material mesh i.e., the velocity of the reference mesh is the same of the material mesh or, which means the same, the second and third domains coincide). In the pure Eulerian approach the reference mesh remains fixed in space (its velocity is zero) and the material is transported (advected) through it. This is the same as saying that the first and third domains are the same. Therefore mesh distortion is avoided. In an ALE description, the third arbitrary referential domain is introduced in addition to the other domains and its velocity may be arbitrarily defined by the user. The second and third domains will be different and the mesh motion will be independent from material motion. The ALE equations are derived by substituting the relationship between the material time derivative and the reference configuration time derivative for a given state variable *f*:

$$\frac{\partial f\left(X_i,t\right)}{\partial t}=\frac{\partial f\left(x_i,t\right)}{\partial t}+c_i\frac{\partial f\left(x_i,t\right)}{\partial x_i} \tag{4.9}$$

where X_i and x_i are the Lagrangian and Eulerian coordinates, respectively and c_i is the relative velocity ($\boldsymbol{c}=\boldsymbol{v}-\hat{\boldsymbol{v}}$), with $\boldsymbol{v}$ being the velocity of the material and $\hat{\boldsymbol{v}}$ the velocity of the reference mesh. In the Lagrangian case, as stated above, the material moves at the

same velocity as the ALE mesh and the relative velocity is zero. In the pure Eulerian case the mesh velocity is zero and the relative velocity is

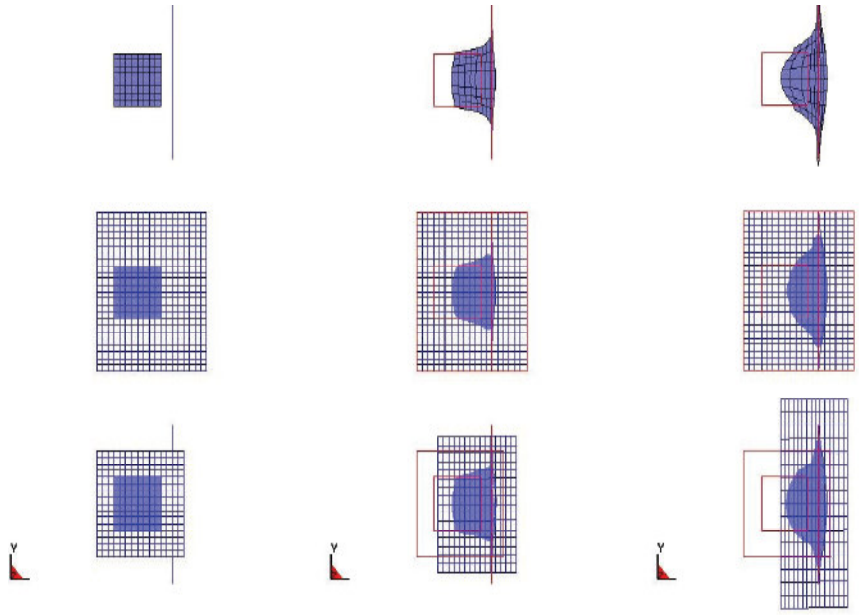

Figure 4. 2 - Examples of Lagrangian, Eulerian and ALE approaches. Three sequences are shown where an initial squared block of material impacts a plate and flattens: In the upper sequence (Lagrangian approach) the mesh follows the material and distorts severely; in the second sequence, Eulerian approach, the material flows through a fixed mesh which remains undistorted and in the third sequence (the ALE approach) the reference mesh also moves as the material mesh moves to the right. Some element distortion is observed but material advection is smaller

4.3.2. Conservation laws in ALE description

Using the notion of relative velocity and the definition of time derivative presented in eq. (4.9) the governing equations can be presented as follows:

The conservation of mass equation in ALE form:

$$\left.\frac{\partial \rho}{\partial t}\right|_{\chi} + \boldsymbol{c} \cdot \nabla \rho + \rho \nabla \cdot v = 0 \tag{4.10}$$

The momentum equation in ALE form:

$$\rho\left(\frac{\partial \boldsymbol{v}}{\partial t}[\boldsymbol{\chi}]+\boldsymbol{c}\cdot\nabla\boldsymbol{v}\right)-\nabla\cdot\boldsymbol{\sigma}-\rho\boldsymbol{b}=0 \tag{4.11}$$

The energy conservation equation in ALE form:

$$\rho\left(\left.\frac{\partial \boldsymbol{E}}{\partial t}\right|_{\chi}+c\cdot\nabla\boldsymbol{E}\right)-\boldsymbol{D}:\boldsymbol{\sigma}=0 \tag{4.12}$$

A derivation of equations (4.10), (4.11) and (4.12) can be found in many textbooks (Belytschko, 2006). If the Eulerian approach is used $\boldsymbol{c}$ = 0 then the above equations can be reduced to their conservative form (Aquelet, et al., 2008):

$$\frac{\partial\rho}{\partial t}+\nabla\cdot(\rho\boldsymbol{v})=0 \tag{4.13}$$

$$\frac{\partial\rho\boldsymbol{v}}{\partial t}+\nabla\cdot(\rho\boldsymbol{v}\otimes\boldsymbol{v})=\nabla\cdot\boldsymbol{\sigma}+\boldsymbol{f} \tag{4.14}$$

$$\frac{\partial\rho E}{\partial t}+\nabla\cdot(E\boldsymbol{v})=\boldsymbol{\sigma}:\nabla\boldsymbol{v} \tag{4.15}$$

These equations can be presented in the general form:

$$\frac{\partial\phi}{\partial t}+\nabla\cdot\Phi=S \tag{4.16}$$

where

$$\phi = \begin{bmatrix} \rho \\ \rho \boldsymbol{v} \\ \rho E \end{bmatrix}, \quad \Phi = \begin{bmatrix} \rho \boldsymbol{v} \\ \rho \boldsymbol{v} \otimes \boldsymbol{v} \\ E \boldsymbol{v} \end{bmatrix}, \text{ and } \quad S = \begin{bmatrix} 0 \\ \nabla \cdot \boldsymbol{\sigma} + \boldsymbol{f} \\ \boldsymbol{\sigma} : \nabla \boldsymbol{v} \end{bmatrix} \tag{4.17}$$

4.3.3. The operator split

Equation (4.17) can be solved in a fully coupled way (Bayoumi, et al., 2004) but this method can only handle a single material in an element. The approach followed in most hydrocodes and in LS-DYNA, is designated by operator split in the literature (Benson, 1992)(Hughes, et al., 1981) (Linder, 2003), (Vitalli, 2007) and divides each time step into two phases. Operator splitting separates the Eulerian conservation equations (4.16) into source and convective equations such as,

$$\frac{\partial \phi}{\partial t} = S \tag{4.18}$$

$$\frac{\partial \phi}{\partial t} + \nabla \cdot \Phi = 0 \tag{4.19}$$

where the abbreviations shown in equation (4.17) have been used.

During the Lagrangian step a finite element problem is solved while in the Eulerian step a finite volume problem is solved (Mahmadi, et al., 2014). The source equations correspond to the Lagrangian conservation equations, therefore, they are referred to as the Lagrangian step. The convective equations correspond to the transport through space and are referred to as the Eulerian step. The two steps are solved independently and sequentially to calculate velocity and internal energy due to the internal and external forces.

The solution is advanced from t^n to t^{n+1} with the second order accurate central difference scheme. The mass is assumed to be lumped at the nodes, which leads to a

diagonal matrix which simplifies the calculation of acceleration. Velocities are calculated at $t^{n+1/2}$ and accelerations and coordinates at t^{n+1} as explained below.

Acceleration $\boldsymbol{a}^n$ is computed from the known nodal masses and nodal forces acting on them, from the equilibrium equation, $\boldsymbol{m\ddot{a}} = \boldsymbol{p} - \boldsymbol{f} + \boldsymbol{h}$ where $\boldsymbol{\ddot{a}}$ is acceleration, $\boldsymbol{m}$ is the diagonal mass matrix, $\boldsymbol{p}$ represents external and mass loads, $\boldsymbol{f}$ is the internal forces vector, $\boldsymbol{f} = \int \boldsymbol{B}^T \boldsymbol{\sigma}^n d\,V$ (where $\boldsymbol{B}$ is the matrix containing the derivatives of shape functions and $\boldsymbol{\sigma}$ is the Cauchy stress tensor) and $\boldsymbol{h}$ is the resistance to hourglass. Then acceleration is given by,

$$\boldsymbol{\ddot{a}} = \boldsymbol{m}^{-1}(\boldsymbol{p} - \boldsymbol{f} + \boldsymbol{h}) \tag{4.20}$$

by means of equation (4.21),

$$\boldsymbol{a}^n = \frac{\boldsymbol{f}^n}{\boldsymbol{m}^n} \tag{4.21}$$

Then the material velocity is updated by equation (4.22)

$$\boldsymbol{v}^{n+1/2} = \boldsymbol{v}^{n-1/2} + \frac{\boldsymbol{a}^n}{2}\left(\Delta t^n + \Delta t^{n+1}\right) \tag{4.22}$$

and the Lagrangian node coordinate at t^{n+1} is finally obtained by equation (4.23)

$$\boldsymbol{x}^{n+1} = \boldsymbol{x}_r^n + \boldsymbol{v}^{n+1/2}\Delta t^{n+1} \tag{4.23}$$

with

$$\Delta t^{n+1/2} = \frac{\Delta t^n + \Delta t^{n+1}}{2} \tag{4.24}$$

where $\boldsymbol{x}^{n+1}$ is the updated Lagrangian nodal coordinate and x_r^n is the remapped node coordinate after the advection phase at t^n. In an Eulerian description $\boldsymbol{x}_r^n = \boldsymbol{x}^n$, i.e., the nodes remain in fixed positions (Aquelet, 2007).

The strain rates are also computed,

$$\dot{\epsilon}^{n+1/2} = B v^{n+1/2} \tag{4.25}$$

and the stresses are updated as functions of the constitutive model, the strain rate, the time increment and so on,(Vitalli, 2007)

$$\sigma^{n+1} = Constitutive\ equation\ (\sigma^n, \dot{\epsilon}^{n+\frac{1}{2}}\Delta t, etc..) \tag{4.26}$$

Next, during the advection cycle, where transport of mass, internal energy and momentum across element boundaries are computed, the mesh is moved to its initial position. This phase may be thought of as a remapping of the mesh displaced at the first phase back to its original or arbitrary positions. The volume differences between the Lagrangian and the rezoned meshes are the fluxes that will be computed in the advection phase. A significant advantage of this split approach is its ability to handle more than one material in each element.

The Lagrangian solution is mapped on the new position of the mesh by solving equation (4.19). The procedure is illustrated in Fig. 4.3.

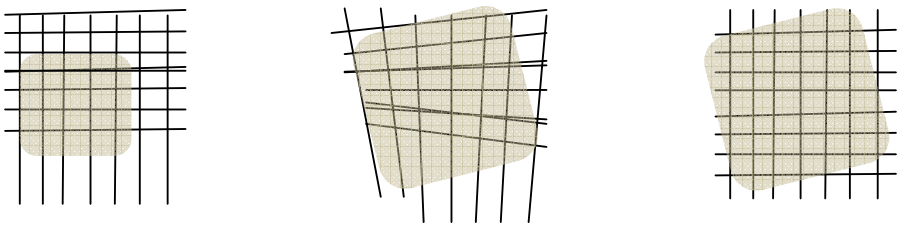

Figure 4. 3–Exemplification of ALE procedure: On the left the initial configuration of the material is shown; on the centre the result of a Lagrangian step is shown: material deformation has occurred and the mesh has been distorted; on the right the Eulerian step is illustrated: the new material configuration has been mapped on the mesh to original position.

In reality this is not a true operator split. The solution is only advanced in time in the Lagrangian step and there is no time increment associated with the Eulerian step. The Eulerian step only maps the solution from the Lagrangian mesh onto the new position of the ALE mesh (or onto de Eulerian fixed mesh if the calculation is Eulerian). The element centred solutions use advection algorithms to be remapped. The transport of volume calculation is essentially geometrical since it is not associated with the physics of the problem (Benson, 1992). Since the mesh moves with the material in the Lagrangian step mass is conserved, the mesh velocities and displacements are computed and the nodal characteristics are updated. A mapping step will follow and an undeformed mesh is obtained again.

4.3.4. Advection and interface tracking algorithms

As the material moves from one element to another it is difficult to track accurately the variation of material properties, interfaces and free surfaces with time. Advection solvers will be needed to solve this flow through a mesh which is either fixed in space or animated with an arbitrary motion not coincident with that of the material.

Eulerian solvers assume that all variables are cell centred in the mesh and uses control volume methods to solve the governing conservative main balances.

When the mesh is moved to the position defined by the rezoning algorithm (the initial position for Eulerian meshes) some elements (the donors) will lose material to its neighbours (the acceptors). The difference between the Lagrangian and final element volumes is the flux. The fluxes of mass, momentum, energy and material volumes are obtained by a finite volume integration of eq. (4.19). The fluxes through the element boundaries are computed at each iteration. Benson (Benson, 1992) described this computation considering two advection methods: The Donor cell (first order accurate) and Van Leer (second order accurate). The numerical implementation details are available in the literature (Souli, et al., 2000) (Fressmann, et al., 2007) (Stoker, 1999) (Armero, et al., 2003). Second-order methods eliminate the numerical diffusion but they originate non-physical oscillations near areas of large gradients (e.g. a shock wave). A

possible way to minimize these oscillations utilizes an hybrid scheme that uses the second order numerical flux in smooth regions and the first order scheme (which is a monotonic upwind method (Belytschko, 2006)) in the vicinity of discontinuities. Other approach is the introduction of artificial viscosity to damp the oscillations.

The discrete form of equation (4.19) in one dimension is (Benson, 1997):

$$\phi^{+}_{j+1/2} = \frac{\phi^{-}_{j+1/2} V^{-}_{j+1/2} + \phi^{-}_{j} V_{j} - \phi^{-}_{j+1} V_{j+1}}{V^{-}_{j+1/2} + V_{j} - V_{j+1}} \tag{4.27}$$

where element *j+1/2* is defined by nodes *j* and *j+1*. The minus and plus superscripts refer to values before and after the transport. The transport volumes V_j and V_{j+1} are defined by the positions of nodes *n* and *n+1*. The transport volumes are calculated by the interface reconstruction algorithm mentioned below. The values centred in the transport volumes, $\phi^{-}_{j+1/2\pm1/2}$ are calculated by the transport algorithm (Benson, 1997).

Since several materials may share the same cell the tracking of material interfaces within the cell is required. There are several methods to perform this interface tracking but Young's method is often cited as one of the most used interface tracking algorithms (Young, 1987) (Young, 1982).

The number of interfaces in a multi-material element corresponds to the number of materials present in the element minus one. The interfaces define two regions and in each of them one or more materials may be contained. The slope of the interface depends on the volume fractions of materials inside the element being considered and its neighbours. Initially a straight line is drawn parallel to the element faces to give a first approximation of the interface in the element (Aquelet, et al., 2003). Then nodal volume fractions are computed at the nodes based on the volume fractions of an element and those that share the same node, and these will determine the slope of material interfaces in the element. The position of the line is then adjusted to divide the element volume into two volumes that correctly match the material volume fractions. That slope is given by the gradient of the nodal volume fraction. More details can be found in the original work (Aquelet, et al., 2005).

4.3.5. Artificial viscosity

The study of blast waves implies that the code being used will have to deal with shock calculations and the treatment of the associated jump discontinuities. A standard approach is the addition of a viscous term into the equilibrium equations. This viscous term can be assumed to have a physical meaning such as the effect of the thermodynamic irreversibility of the shock phenomena (Benson, 1992). A bulk viscosity is used in hydrocodes to treat shock waves. The technique consists of the addition of a viscous term q to the pressure to smear the shock discontinuities into a continuous transition region, keeping the Hugoniot jump conditions valid across that transition (Hallquist, 2006). We have seen in Chapter 2, that for weak shock waves, Hugoniot and adiabatic curves agree to the first order as their slopes are equal at state 1, and can be ignored in numerical calculations. For strong shock waves the bulk viscosity is introduced. LS-DYNA uses the viscosity proposed by (Von Newmann, et al., 1950):

$$q = C_0 \rho \left(\Delta x\right)^2 \left(\frac{\partial \dot{x}}{\partial x}\right)^2 \qquad \text{if } \left(\frac{\partial \dot{x}}{\partial x}\right) < 0$$

$$q = 0 \qquad \text{if } \left(\frac{\partial \dot{x}}{\partial x}\right) > 0 \qquad (4.28)$$

where C_0 is a dimensionless constant and q is added to the pressure in both the momentum and energy equations. This approach satisfies the jump conditions, the equations hold for all shocks, q is negligible outside the shock layer and the shock thickness is independent of shock strength (Newmann and Richtmeyer demonstrated that shock phenomena can be described effectively using a six elements wide shock front and most of the jump occurs over three to four elements in practice).

LS-DYNA uses a slight modification of eq. (4.28) and a control card allows the user to change the default parameters of bulk viscosity used by the program. Two coefficients are used, one quadratic *Q1* and the other linear *Q2*, that default to 1.5 and 0.06 respectively and will define the value of the additive pressure term q which is given by $q = \rho l \left(Q_1 l \dot{\varepsilon}_{kk}^2 - Q_2 a \dot{\varepsilon}_{kk}\right)$. In this equation l is the characteristic length in a 2D

element or a characteristic area in a 3D element, and *a* is the local speed of sound. In the present work the standard bulk viscosity formulation has been maintained.

4.4. Numerical modelling of a blast wave propagation

LS-DYNA has several ways of modeling the effect of blast waves in structures of which two have been used in the present work. One of them is based on algorithms similar to CONWEP and it consists basically of applying a Friedlander curve to the structure, calculated by the program given the stand–off distance, angle of incidence and the weigh and type of explosive. The algorithm will calculate the equivalent TNT charge and the load curve will be applied to the nodes of a Lagrangian structure that will deform accordingly. This is done by a special function named *LOAD_BLAST (Randers-Pehrson, et al., 1997). The modeling process is purely Lagrangian but it does not consider wave reflections, nor the propagation of blast waves around corners and obstacles. With this Lagrangian approach it is not possible to model blast propagation to a neighbor compartment after rupture of one of the boundaries of the initially blasted compartment.

The second approach considers the complete model of both the explosive charge and encircling mass of air. It requires the computation of pressures at all nodes of the mesh which is provided by the equations of state of both media. The flow of expanding products of combustion is described by considering a multi-material ALE formulation for each cell of the mesh in which material is advected between cells. ALE description has been given above. An Eulerian mesh, as a particular case of the multi-material ALE formulation has been used to model the air and explosive domains, from now-on called the ALE domains.

A Lagrangian structure standing inside the mass of air and exposed to the blast will be loaded by means of a FSI (Fluid Structure Interface) algorithm. Descriptions of how to use this function of LS-DYNA are available in the literature (Alia, et al., 2006), (Slavik, 2009), (Mespoulet, et al., 2011),(Chafi, et al., 2009),(Schwer, 2010).

Explosive and air, plus Lagrangian meshes are all identified by a Part number to which the element type, the material constitutive properties plus an equation of state (if required) and hourglassing parameters, are added. This deck of command cards is then completed with suitable boundary conditions, constraints, contact definitions, running controls and output parameters.

4.5. Consistent units

LS-DYNA do not ask for the input of specific unit. It is up to the user to ensure that units are consistent in terms of the input values. For instance if mass is input in kg, lengths in meters and time in seconds then the forces given by the program are expected to be given in Newtons and stresses in Pascal.

In the numerical investigations performed the system of units of Table 4.1 has been used:

Table 4. 1– System of units used in LS-DYNA

Mass	Length	Time	Force	Stress	Energy	Gravity
g	cm	μs	10^7 N	Mbar	10^7 Ncm	9.806×10^{-10}

We may remember that 1 Mbar equals 10^{11} Pa or 100 GPa. Using this system of units the typical densities of steel and aluminum are input as 7.83 and 2.7 g/cm^3 and their Young modulli are approximately 2.07 and 0.7 Mbar, respectively.

4.6. Equations of state

For low pressure loading, the pressure is not significantly affected by temperature and within elastic linear deformations a linear bulk modulus is sufficient to relate pressure changes to volume changes. In these cases an EOS is not needed. The constitutive relation between the stress tensor and the strain tensor is sufficient to

evaluate the state of stress of the material. However. when pressures are large, the hydrostatic components of the stress tensor are larger than the deviatoric stresses and the volumetric deformations are significant. Then a relation of the type $P = f(\mu, e_{v0})$ is necessary and this is the definition of an equation of state. ($\mu = \frac{\rho}{\rho_0} - 1$ is the volumetric parameter, $-\Delta V/V$, and e_{v0} is the internal energy per unit reference volume).

4.6.1. EOS for HE (*EOS_JWL card)

The explosion is initiated at the input detonation point and the pressures in the condensed explosive are calculated by means of an appropriate equation of state. At least two equations of state relating energy, pressure and density, must be included in the simulation, one to describe the reaction of the explosive and the expansion of the reaction products and the other to simulate the behaviour of the air environment where the wave will propagate.

For the explosive detonation a very widely applied equation is the Jones-Wilkins-Lee (JWL) used in different forms (two or three terms) (Baudin, et al., 2010)(van Thiel, et al., 1983). The equation is obtained from the release of internal energy near the isentrope of the detonation products (Grys, et al., 2010) . It is generally presented as a pure empirical EOS with a non physical Gruneisen coefficient taken as a constant. A number of reports are available with parameters for the different explosives (Lee, et al., 1973). The equation models reasonably well HE phenomena. Its isentropic form is (Alia, et al., 2006) :

$$P_S = Ae^{-R_1 V} + Be^{-R_2 V} + CV^{-(\omega+1)} \tag{4.29}$$

where R_1, R_2, A, B, C and ω are empirical constants obtained by calibration of test data. V is the ratio between the condensed explosive density in its initial state and the actual density of the reacted material, and the subscript s refers to the isentrope. P is the pressure.

Considering that the internal energy per unit volume (in Pa) is the product of the solid explosive density ρ_o, by the actual internal energy per unit of mass, e (in J/g)

$$E = \rho_o e \tag{4.30}$$

and integrating the following thermodynamic identity

$$\left(\frac{\partial E}{\partial V}\right)_S = -P \tag{4.31}$$

we obtain the equation for the energy in the isentrope,

$$E_S = \frac{A}{R_1} e^{-R_1 V} + \frac{B}{R_2} e^{-R_2 V} + \frac{C}{\omega} V^{-\omega} \tag{4.32}$$

Considering other thermodynamic identity such as,

$$\left(\frac{\partial E}{\partial P}\right)_V = \frac{V}{\Gamma} \tag{4.33}$$

where Γ is the Grüneisen gamma and using a Taylor expansion, an equation identical to the Mie-Grüneisen equation of state is obtained. The Grüneisen gamma must be held constant and is specified as $\Gamma = \omega$.

$$P = P_S(V) + \frac{\Gamma}{V}\left[E - E_S(V)\right] + \ldots \tag{4.34}$$

Now we can replace equations (4.30) and (4.32) into equation (4.34) to obtain the usual $P = P(E, V)$ form of the JWL equation of state:

$$P = A\left(1 - \frac{\omega}{R_1 V}\right) e^{-R_1 V} + B\left(1 - \frac{\omega}{R_2 V}\right) e^{-R_2 V} + \omega \frac{E}{V} \tag{4.35}$$

The input values for JWL are given in Tables 4.2 and 4.3, for TNT and C4 / PE2 respectively. Many authors assume that PE4 is the same as C4. In fact they are both plastic explosives manufactured respectively in the UK and USA and their input EOS parameters are very close.

Table 4. 2- TNT parameters for use in *EOS_JWL card

EOS data for TNT	A Mbar	B Mbar	R_1	R_2	ω	E_0 Mbar	Vo
Ref A	3.712	0.03231	4.15	0.95	0.30	0.07	1
AUTODYN Manual	3.737	0.03747	4.15	0.95	0.30	0.0694	1

Ref A: (Adamik, et al., 2004)

Table 4. 3– Plastic explosives parameters for use in *EOS_JWL card

EOS data for C4 and PE4	A Mbar	B Mbar	R_1	R_2	ω	E_0 Mbar	Vo
C4-Ref B	5.98155	0.13750	4.5	1.5	0.32	0.087	1
PE4-Ref.C	6.098	0.1295	4.5	1.4	0.25	0.09	1

Ref. B : (Alia, et al., 2006)
Ref.C: (Rigby, et al., 2014)

For reacted products the value of R_1 is usually larger than R_2 and so this term dominates at high pressures when V is around unity. The second term will dominate at intermediate pressures, for values of V approaching two and in an advanced expansion state, where $V \rightarrow \infty$, the equation will be reduced to the third term. This last term of the

equation corresponds to the politropic equation for air where $\omega = \gamma - 1$ and γ is the adiabatic expansion coefficient:

$$P = (\gamma - 1)\frac{\rho}{\rho_o}E \tag{4.36}$$

Then it is seen that the JWL equation follow the perfect gases curve for large volumes.

In Table 4.2 some values available for TNT are reproduced from two different sources. Further discussions on the use of JWL equation of state are available and comparative results for a number of HE are available in the literature (Lee, et al., 1968). The results show that the equation correctly reproduces the CJ adiabat.

4.6.2. EOS for Air (*EOS_LINEAR_POLYNOMIAL card)

The mass of ambient air that will be traversed by the blast wave also needs an equation of state to describe its thermodynamic state as it is being compressed by the passage of the wave front. The gamma law can be modelled by a linear polynomial equation, linear in the internal energy E:

$$P = C_0 + C_1\mu + C_2\mu^2 + C_3\mu^3 + E(C_4 + C_5\mu + C_6\mu^2) \tag{4.37}$$

Coefficients $C_2\mu^2$ and $C_6\mu^2$ are set to zero if μ <0 , where $\mu = \frac{\rho}{\rho_0} - 1$, and $\frac{\rho}{\rho_0}$ is the ratio of current to initial (reference) density defined in the material properties card, *MAT_NULL card.

For an ideal gas the expression is reduced to

$$P = (\gamma - 1)\frac{\rho}{\rho_0}E_0 \tag{4.38}$$

as all coefficients will be made equal to zero except $C_4 = C_5 = \gamma - 1$ and $\gamma = \frac{C_p}{C_v}$ is the ratio of specific heats. E_0 has units of pressure (J/m^3) and means internal energy per unit reference volume,

$$E_0 = \rho_0 C_v T\big|_{t=0} \tag{4.39}$$

For ambient air, $\gamma = 1.4$, $E_0 = 2.533\, x\, 10^{-6}$ (Mbar) , T = 293ºK, C_v = 718x10^{-8} cm^2/μs^{2}ºK and $\rho_0 = 1.204\, x\, 10^{-3}$ (g/cm^3), For these initial values eq. (4.42) gives $P_0 = 1.013$ (bar).

The EOS for air is then filled in with the following data:

Table 4. 4 – Properties used in the *EOS_ LINEAR_POLYNOMIAL card for air

EOS for Air	C_1	C_2	C_3	C_4	C_5	C_6	C_7	E_0	V_0
Data	0	0	0	0.4	0.4	0	0	2.533e-6	1

V_0 in the table above, means the initial relative volume. Relative volume is the ratio of current volume and the volume at the instant $t = 0$, so the initial relative volume is the ratio between the density at the reference state and the density at $t = 0$. Normally the reference density is equal to the density of the material at the initial instant and $V_0 = 1$.

The JWL and Linear Polynomial have been extensively used throughout this dissertation. They are well established, widely used and are already implemented in most hydrocodes, namely the LS-DYNA.

The most published value for the initial internal energy of air is 2.5x10^{-6} Mbar and the initial density is 1.293x10^{-3} g/cm^3. This results from considering the initial conditions of the air at 0º degrees Celsius. However, in general, the final results were not affected by different choices of initial conditions for the air.

4.7. HE material definition (*MAT_HIGH_EXPLOSIVE_BURN card)

4.7.1. Burning model

The wave front moves at a speed called the CJ speed (detonation speed) and will "detonate" all elements as it reaches them. This can be achieved in two ways: either by means of the volumetric compression of the element or controlling its detonation by means of an ignition time for each element. Pressure inside the element is then calculated by JWL, the material expands and transport of material occurs to adjacent elements. Once all explosive has been burnt the process continues through the ambient air mesh, with burnt products being transported across elements as the wave blast propagates.

The ignition time for every element of the explosive mesh is the ratio of its distance to the ignition point and CJ speed D:

$$t_L = t_d + \frac{L_d}{D} \tag{4.40}$$

where t_d is the instant of detonation (usually zero) and D is the detonation velocity.

The blast wave can be formed in several time intervals, a procedure that uses the burnt fraction F, intended to control the chemical energy release of the explosive (Aquelet, 2008) in a tri-dimensional domain. The pressure in each element varies as the value of the parameter F is incremented. The procedure takes several time steps until F reaches unity, therefore spreading the burnt front over several elements. LS-DYNA allows the user to select either a BETA burn, F_2, (based on volumetric compression and selected by setting the parameter BETA=1 in the input) or a programmed burn function of time, F_1, (setting BETA=2). A combination of the two has been set (BETA=0) such that the largest of the two calculated burn fraction ($F = max(F_1, F_2)$ have been used in the simulation. This was shown to yield a smooth propagation of the shock wave and is

recommended by the LS-DYNA user's community. The other BETA options were abandoned as the explosive would not ignite.

The procedure calculates F_1 and F_2 as follows:

$$F_1(3D) = \begin{cases} \frac{2(t-t_d)DA_{e\,max}}{3v_e} & if\ t > t_d \\ 0 & if\ t \le t_d \end{cases} \quad (4.41)$$

$$F_2 = \beta = \frac{1-V}{1-V_{CJ}} \quad (4.42)$$

where $V = \rho_0/\rho$ is the relative volume or the relation of the initial density of the explosive to its actual density. V_{CJ} is the relative volume at CJ condition. LS-DYNA adjust the pressure by multiplying F by the EOS,

$$P = FP^{HE} \quad (4.43)$$

where P^{HE} is the pressure obtained from the EOS (equation 4.29).

The modeling of the explosive in LS-DYNA becomes complete with the input of the parameters of the equation of state (*EOS_JWL), properties of the HE (*MAT_HIGH_EXPLOSIVE_BURN) and the coordinates and time of the detonation point (*INITIAL_DETONATION). Pressure inside the explosive increases as we move away from the detonation point and its maximum value will be P_{CJ}.

4.7.2. Properties of explosive materials

Since it is easier to obtain and a significant number of published work has been based on the detonation of TNT it was also chosen and used in some of the numerical simulations. Table 4.4 shows the material properties for TNT and Table 4.5 shows those of C4.

Table 4.5- Properties of TNT for input in *MAT_HIGH_EXPLOSIVE_BURN card

Properties of TNT	ρ_0 g/cm3	D cm/μs	P_{CJ} Mbar	BETA
Ref A	1.590	0.693	0.21	0
AUTODYN Manual	1.630	0.693	0.21	0

Ref A: (Adamik, et al., 2004)

Table 4. 6- Properties of plastic explosive for input in *MAT_HIGH_EXPLOSIVE_BURN card

Properties of C4 and PE4	ρ_0 g/cm3	D cm/μs	P_{CJ} Mbar	BETA
C4-Ref B	1.601	0.804	0.281	0
PE4-Ref.C	1.601	0.819	0.280	0

Ref B: (Alia, et al., 2006)
Ref.C: (Rigby, et al., 2014)

In Table 4.6, D is the detonation velocity and P_{CJ} is the Chapman-Jouget pressure. BETA is the burning parameter explained above, normally set to zero (programmed burn plus beta burn). The other three parameters are omitted (unless Beta is chosen to be the option for a programmed burn only, BETA = 2), being the bulk modulus, the shear modulus and the yield stress of the explosive, respectively. If a Beta burn option is used, BETA = 1, any volumetric compression will cause detonation, F_1 is not computed (Hallquist, 2006) and $F = F_2$ as in equation (4.42).

If BETA = 2 then we have a programmed burn and the explosive will behave as an elastic perfectly plastic material, as long as the bulk modulus, shear modulus and yield stress are defined. With this option the explosive can be compressed without detonation.

The burning properties of PG2 could not be found but since it has 88% RDX in its composition it may be assumed very close to C4 or PE4 for simulation purposes.

4.7.3. Properties of the Air (*MAT_NULL)

The air (or any other fluid) is modeled by the *MAT_NULL card. Only one parameter is necessary to form a valid input, such as the mass density, RO. The NULL material considers no shear stiffness, no yield strength and behaves in a fluid-like manner. It requires an EOS, even if the deviatoric stresses are not computed. Due to the absence of shear strength it is necessary to use hourglass control with caution as the default values may lead to significant energy losses. The hourglass coefficient has been chosen to be less than 0.0001, as suggested in the LS-DYNA manual. Hourglassing is a nonphysical phenomenon that will be explained below.

Table 4.7– Properties of the Air in the *NULL_MATERIAL card

Properties	RO	PC	MU	TEROD	CEROD	YM	PR
Air	1.204×10^{-3}	0	0	0	0	0	0

PC is a pressure cut-off, normally negative. The cut-off pressure allows cavitation to occur below a very small negative value. In this thesis the value of this parameter has always been zero.

MU is the dynamic viscosity coefficient μ. If it is defined it allows the deviatoric viscous stress tensor to be derived as $\sigma'_{ij} = 2\mu\dot{\varepsilon}'_{ij}$, where $\dot{\varepsilon}'_{ij}$ is the deviatoric strain rate.

TEROD and CEROD are the relative volumes (V/V_0) for erosion in tension and compression, respectively. When they are zero the options remain inactive.

YM and PR are the young modulus and the Poisson's ratio. These values only apply to null beams and shells which may be used in the definition of areas of contact within nodal rigid bodies.

4.8. Hourglass

It is also worth to remember that internal forces in each element will not be integrated exactly[12] but computed at the centre of the element and multiplied by the element volume, instead, when using single integration point elements (under-integrated elements make the solution faster). Although this is computationally efficient it leads to hourglassing.

Hourglass is characterized by the occurrence of zero energy modes particularly when a FEM is made of under-integrated elements. In explicit analysis under-integrated elements are more attractive as they save computing time but this type of elements do not have sufficient internal strength to resist shape changes. These elements are unstable and nonphysical spurious shapes may appear in the mesh without energies being spent to deform them. The single integration point 8 – node hexahedral solid element which has been used in all numerical models is prone to these undesirable deformations associated with zero energy modes and will no longer describe correctly a constant stress field. These modes may be avoided by using viscous control (anti-hourglass viscosity) or elastic control (anti-hourglass stiffness) (Flanagan, et al., 1981) such that their effect on the stable global modes is negligible. The hourglass modes are orthogonal to the main strains and the work done by the hourglass resistance is neglected in energy calculations although a slight loss of energy will happen. For high velocity/high strain rate problems the viscous forms of hourglass control are better suited than stiffness forms. This results from the tendency of stiffener formulations to stiffen the response, which is aggravated in cases of high velocity. The three viscous forms of hourglass control appear as options 1 to 3 in LS-DYNA input. Method 1 is the less demanding in terms of processing but options 2 and 3 were also used (respectively Flanagan-Belytschko and Flanagan-Belytschko with exact volume integration). For fluids, which do not show shear strength the standard hourglass control method (IHQ = 1) combined with a low hourglass coefficient is often recommended and in fact no differences were found in the results obtained from simulations run with hourglass control methods 1, 2 or 3.

[12] This integral is $\boldsymbol{f}_i^e = \int \boldsymbol{B}^T \bar{\boldsymbol{\sigma}}\, dV$ and is rather complex to integrate where B contains the derivatives of the shape functions and $\bar{\boldsymbol{\sigma}}$ is a vector with six components

A more detailed explanation of how hourglass resistance methods are implemented is available in the LS-DYNA theory manual (Hallquist, 2006). A good post-processing indication has been to ensure that hourglass energy is kept less than 10% of internal energy

The hourglass phenomena have been prevented by using the following input in the *HOURGLASS card:

Table 4. 8– Hourglassing parameters for input in ALE mesh

IHQ	QM	IBQ	Q1	Q2	QB	QW
1,2,or 3	1e-6	1	1.5	0.06	1e-6	1e-6

IHQ selects the hourglass control type;
QM is an hourglass coefficients. For fluids low values are recommended;
IBQ is the bulk viscosity type. Defaults to 1;
Q1 is a quadratic bulk viscosity coefficient. The default value has been used;
Q2 is a linear bulk viscosity coefficient. The default value has been used;
QB is an hourglass coefficient for shell bending. The default value is QB = QM;
QM is an hourglass coefficient for shell warping. The default is QB = QW

4.9. Structural material model

4.9.1. Lagrangian or MM-ALE approach

The two techniques have been described above and both have been used in the numerical simulations. The simpler empirical approach basically applies a Friedlander type pressure curve at each point of the exposed area of the structure. The structure is modelled with Lagrangian meshes. Minimal input is required but no specific modelling of the explosive is used as it is defined as an equivalent weight of TNT. The technique has inherent limitations for near field explosions as the real data from where the empirical model was constructed also suffers from inconsistencies in close range

explosions. Also the reduction of all types of HE to a simple TNT equivalent ignores the different characteristics of each of them such as detonation speed, temperature, brisance, etc.. These parameters may have a significant effect that is totally ignored in this approach. However it has the important advantage of being much faster than other more sophisticated methods.

The other method used was ALE. Its foundation has been described above and will not be repeated but it provides a more realistic description of the system under investigation. The domain where the mixture of reaction gases and air moves is fixed in space (An Eulerian approach has been used in all simulations as a particular case of the ALE method) and the progression of the blast wave is defined by the advection of the accelerated gases through the fixed cells of the mesh until they impinge a structure surface. Structures are also modelled as Lagrangian meshes overlapping the ALE mesh. There is no requirement of node coincidence between the two meshes but a penetration detection algorithm, such as those defined to simulate contact between Lagrangian parts, is needed to model the transfer of energy from the blast wave to the deformable structure. This coupling is generally known as Fluid Structure Interaction (FSI) and it is achieved by a special command card named "CONTRAINED LAGRANGE IN SOLID.

It allows the simulation of the transfer of momentum from the expanding gases to the surrounding structures that will be hit by them. It has been explained above that in problems where a high distortion of the mesh is expected an ALE, or an Eulerian approach, which is a particular case of ALE methodology, is required. In the Eulerian analysis the reference mesh does not deform which avoids the computational problemas related with very distorted meshes. Thus an Euler-Lagrange coupling will provide the contact mechanism between the unmerged fluid and structure meshes. The methodology consists of searching for the existence of a fluid-structure interference (such as penetration) and to apply coupling forces to the penetrating nodes in the interface which will be added to the nodal forces. This is equivalent to a contact penalty-based approach. It relies on force equilibrium and energy conservation. A basic explanation of the notion of a contact-penalty approach is given below.

In an explicit finite element method the contact algorithm calculates interface forces due the impact between the structure and the fluid. It is important to note that most literature on contact technology apply to static or slow speed problems. High

speed dynamic problems involving high mesh distortion still pose a difficult problem to solve as even ALE models with re-meshing algorithms will not be capable of maintaining a regular mesh for the computation to proceed. The Eulerian description adopted in the present work is a suitable particular case of an ALE problem to circumvent this difficulty. As in contact algorithms one surface will be designated as a master surface while the other will be the slave surface.

Two coupling algorithms are available in LS-DYNA. One approach consists of computing the velocity of the slave node from the velocities of the four nodes of the master segment constraining the slave node to be maintained outside the master segment this way avoiding penetration. Total momentum is preserved but not total energy. Other approach consists in a contact-stiffness algorithm that calculates the restoring forces that shall be applied to both the master and the slave nodes, proportional to the penetration.

The default contact stiffness for a solid element is given by

$$k = \frac{\alpha K A^2}{V} \tag{4.44}$$

where K is the material bulk modulus, α is the penalty scale factor, A is the segment area and V is the segment volume. For a shell element,

$$k = \frac{\alpha K A}{max\ sheldiagonal} \tag{4.45}$$

Although the penalty based method does not accurately satisfy the contact boundary conditions as the kinematic constraint method does, it is simpler, suffers less from numerical noise, it is less affected by hourglassing and arbitrary intersections of slave-slave and master-master surfaces are possible. The major difficulty is the determination of the penalty factor α: if too high as when leakage (flow through the contact surface) needs to be prevented then the stable time-step will decrease in an explicit analysis. At each time step the algorithm searches for the fluid-structure interface and the penalty interface forces are computed and added to nodal forces. The forces are applied to both the slave, F_s and master nodes, F^i_m in opposite directions to

satisfy equilibrium. The forces applied to the master segment are scaled to the element shape functions (Aquelet, et al., 2005),

$$F_s = -kd \tag{4.46}$$

$$F_m^i = N_i kd \tag{4.47}$$

where N_i is the shape function at node i (i=1, 4 in three dimensions) of the master segment taken at the slave node location and d is the penetration distance and k has been defined above as the equivalent spring stiffness of the materials at the penetration. The main difficulty in the coupling problem consists of determining the spring stiffness, This parameter is problem dependent and if incorrectly set two consequences may arise: either its value is too high and energy will be dissipated in the contact mechanism, and total energy will not be preserved, or if it is too low penetration will not be prevented and leakage through the structure will occur. The mass of the fluid particle will be determinant in the stiffness calculation which requires that the volume fractions in the ALE multi-material mesh cells must be as accurate as possible which requires a good initialization of the detonation process.

4.9.2. *CONSTRAINED LAGRANGE IN SOLID card

With this command the two interacting parts, the multi-material ALE and the Lagrangian meshes will be identified and the method of detecting their interference is defined together with a number of other input dedicated to ensure that all penetrating nodes of a part defined as master (the ALE fluid) will be detected and opposed by a numerically determined force by the slave part (the structure). The main core of the logic of the method resides in solving the three main balance equations describing the conservation of mass, momentum and energy. As it has been described above these

conservation equations are solved in a spatial finite element discretization but using a central difference time integration scheme for the time discretization (explicit solving).

A penalty based method has been chosen which has the advantage of conserving energy. After the impact, both momentum and kinetic energy are conserved. The penalty method tracks the relative displacement between the fluid and the structure and applies forces to the overlapping nodes that are proportional to the magnitude of such relative displacement, forcing the structure and the fluid to follow each other. Normally an extra input effort appears when leakage occurs (fluid going through the Lagrangian mesh). A finer coupling grid or the activation of suitable controls in the input deck will generally solve the problem but introduces energy in the system which will cause a non-physical pressure rise which will have to be compensated in turn. The alternative is to define a higher number of coupling points (parameter NQUAD) which must be distributed over each Lagrangian slave segment. If penetration at a coupling point is found a coupling force is applied to the penetrating node to counteract that penetration thus if the grid of coupling points is defined too dense and the coupling forces may become excessive and the coupling may become very stiff and unstable. The author has also been observed that stiff coupling reduces the time-step size, sometimes up to the point of having to abort the simulation.

Thus the correct modelling of fluid structure interaction is not straightforward requiring a persistent but tedious simulation work.

In the present simulations NQUAD was set to either 2 or 3. However the NQUAD is not the only parameter that can be changed. The penalty forces can also be directly set by the user. A pressure factor together with a coefficient of friction were also set (Pressure was set to 0.1 and Friction to zero). Alternatively a penalty curve was also set and adjusted by trial and error until unrealistic leakage was eliminated. A simpler way to prevent leakage uses a parameter called PLEAK and a flag, ILEAK, which calls a leakage control routine. As it can be seen four parameters have been manipulated, ILEAK ,PLEAK, NQUAD and the penalty factor α (with an alternative description as a curve instead of a single value). Some effort was necessary to adjust the leakage parameters of the model and it was observed that leakage control became too severe after some manipulation of the constitutive model simulation parameters. This was not entirely clear and it was necessary to alleviate some of the penalty parameters to allow

the flow of the explosive gases through the cracks that appeared in the blasted plate of the apparatus described in Chapter 7.

4.10. Johnson-Cook constitutive model

A reliable prediction of damage and failure of the components of a structure exposed to blast loading is a major challenge. Relevant effects to the description of the phenomenon have been presented in Chapter 3 in which the main physically based or phenomenological constitutive models have been presented together with a review of some of the results achieved, but despite the large number of models available the technology of simulating failure is still not fully understood (Du Bois, et al., 2007). It became clear that most methods are only valid within the range of values present in the sample of experimental results used to derive the model or the values of the coefficients used in their equations. Physically based methods, although recommended for their more solid foundations are, sometimes, difficult to calibrate due to the number and nature of the parameters that must be input. Some parameters relate to the microstructure of the metal which makes it difficult to obtain suitable and validated data. In the other group of models, the phenomenological constitutive equations seem to be simpler with less parameter to be used.

The Johnson-Cook (JC) has the advantage of only needing a few parameters to be obtained which, in many instances, can be found in the available literature. It can be combined with a failure model that works reasonably well as it is based on physical results and includes stress triaxiality effects. Alternatively an erosion criterion could be combined with the constitutive model. The definition of values for such criteria is not straightforward. Despite this advantage the JC failure criteria results are mesh dependent. This mesh dependency may be minimized by the use of a function of LS-DYNA that regularizes the failure model (*MAT_NONLOCAL) but in most simulations a mesh dependency of results arise. This function averages failure values of neighbouring elements to minimize that mesh dependency of results.

Other difficulties were present in the modelling process: Validation is difficult as hardening data beyond necking can only be obtained through reverse engineering (Du

Bois, et al., 2007) and mesh refinement must be enough to capture strain localization prior to failure. It has also been explained in Chapter 3 that there is no general form of JC model that covers the whole range of the space of interest of triaxiality and lode angle parameters. The function approximates zones of that space by exponential curves and therefore there is no single set of parameters for the JC model but a few of them, each one having been derived for a range of triaxiality (the JC model do not consider the Lode angle parameter dependency). There are a number of JC sets of parameters available in the literature for AA508 but most of them were used in the context of ballistics were failure occurs by plugging and shear strain is the main deformation mechanism. Some shear was expected in the present work but also in-plane tension and this meant that the use of available published models may still need some adjustment.

The need for calibration of a JC model would require Hopkinson Pressure bar tests together with traction and shearing testing of coupons in a traction machine. Unfortunately it was not possible to perform such tests and published data has been the followed option to calibrate the JC equation.

LS-DYNA has a few implementations of the JC material. It calculates the equivalent stress as a function of plastic hardening, strain rate sensitivity and temperature softening has been presented and described in Chapter 3. It has been implemented in LS-DYNA in a simplified form without considering the effect of temperature, as material 098. In this model only the hardening law and the strain rate are considered, as shown in eq. (4.48), where the parameters were described in Chapter 3.

$$\sigma_{eq} = (A + B\varepsilon_p^n)\left[1 + C\,ln\left(\frac{\dot{\varepsilon}_p}{\dot{\varepsilon}_{p0}}\right)\right] \tag{4.48}$$

Failure can be set by defining a limiting value for the effective plastic strain. Once this value is reached the corresponding element is deleted from the mesh. The model is rather un-expensive to use but it is a considerable simplification of the failure phenomenon. This implementation was used in Chapter 6 to simulate the deformation of square AA5083-H111 aluminium alloy plates subject to blast loading.

The other implementation of the JC constitutive model is material 015 which uses the full model including the failure equation developed by the same authors

(Johnson & Cook, 1985). In *MAT_JOHNSON_COOK_015 temperature softening effect is included, as shown in eq. (4.49).

$$\sigma_{eq} = (A + B\varepsilon_p^n)\left[1 + C\,ln\left(\frac{\dot{\varepsilon}_p}{\dot{\varepsilon}_0}\right)\right]\left[1 - \left(\frac{T - T_0}{T_{melt} - T_0}\right)^M\right] \tag{4.49}$$

where T_{melt} is the melting temperature of the material, T is current material temperature and T_0 is the reference temperature taken when determining the parameters *A, B, C, n* and *M*. $\dot{\varepsilon}_p$ is the effective plastic strain rate, and $\dot{\varepsilon}_{p0}$ is a reference plastic strain rate. This parameter is used as a strain-rate normalizing parameter but in reality it refers to the strain rate used in the experiments to determine the parameters ***A,*** *B* and *n* (Schwer, 2007). The value of $\dot{\varepsilon}_{p0}$, must be consistent with the yield and hardening parameters *A* and *B* whose values should normally be determined from the quasi-static effective stresses versus the effective plastic strain data. Thus $\dot{\varepsilon}_{p0}$ should be set to the value of the effective strain-rate used in the quasi-static tests, typically $\dot{\varepsilon}_{p0} = 10^{-4}$ sec^{-1}. Thus the parameters *A* and *B* should be adequately modified if a different value is set. However most published data do not refer the value of this reference plastic strain rate, $\dot{\varepsilon}_{p0}$ and it is common practice to use $\dot{\varepsilon}_{p0} = 1$ (in the present work since the time unit is the micro-second it has been set to $\dot{\varepsilon}_{p0} = 10^{-6}$).

The first term in the equation represents the quasi-static stress-strain relation at room temperature and the second term is the strain-rate hardening while the third has already been described as a temperature softening term that introduces a temperature dependency in the model. Temperature increments are determined by the values of the specific heat C_p and mass density ρ, in equation (4.50)

$$\Delta T = \frac{1}{\rho C_p}\int \sigma d\varepsilon_p \tag{4.50}$$

The material card input requires that the user also defines the shear modulus and an Equation-of-State (if solid elements are used) that will be used to define the pressure in terms of the volumetric strain (for low pressures the EOS is assumed to be

defined by the bulk modulus). For shell elements the EOS is not necessary but the Young's modulus and the Poisson's ratio.

It was not possible to find the EOS for AA5083-H111 although an expression derived from the Hugoniot of AA5083 (Hauver, et al., 1973) has been attempted but with poor results. The best results were found with a modified linear polynomial equation of state derived for AA6061 aluminium (Schwer, 2009).

JC material card also includes the failure model later developed by Johnson and Cook (Johnson & Cook, 1985). It is based on cumulative-damage and is expressed as,

$$\varepsilon_p = \left(D_1 + D_2 \exp\left[D_3 \frac{P}{\sigma_{eff}} \right] \right) \left(1 + D_4 \ln \dot{\varepsilon}\right) \left(1 + D_5 \frac{T - T_0}{T_{melt} - T_0} \right) \tag{4.51}$$

P is the hydrostatic stress and σ_{eff} is the Von Mises equivalent stress. The ratio of P on Von Mises stress is designated by triaxiality and its effect on failure of ductile materials has been discussed in Chapter 3.

The input card also allows the choice of alternate rate forms such as those of Huh-Kang, Allen-Rule-Jones and Cowper-Symonds rate forms, that replaces the linear form used in the standard JC model, respectively shown by the two parameter eq. (4.52) the exponential form of eq. (4.53), and the two parameter exponential rate form of eq. (4.54):

$$1 + C_1 \ln \dot{\varepsilon} + C_2 \left(\ln \dot{\varepsilon} \right)^2 \tag{4.52}$$

$$\dot{\varepsilon}^C \tag{4.53}$$

$$1 + \left(\frac{\dot{\varepsilon}_{eff}^p}{C} \right)^{1/P} \tag{4.54}$$

where C_1, C_2, C and p are constants to be input, and $\dot{\varepsilon}_{eff}^p$ is the effective plastic strain.

Failure may be simulated in two ways: either by deleting from the computation in accordance with the observance of a certain failure criterion (which is a simple and

fast method) or by detaching elements and creating new nodes as a "crack" propagates along the mesh. The two major underlying theories consider either that failure occurs when a failure variable reaches a critical value (Gurson) or that the material strength and/or stiffness are reduced progressively in function of a damage variable (Lemaitre). LS-DYNA accepts principal strain ε_1, thinning ε_3, equivalent plastic strain ε_p and the Johnson-Cook criterion as failure criteria. As referred above the JC failure model is cumulative and is based on the equivalent plastic strain ε_p. Failure occurs when the damage parameter D, defined in eq. (4.55), reaches one:

$$D = \sum \frac{\Delta \varepsilon_{eff}^{p}}{\varepsilon_{p}} \tag{4.55}$$

The model also considers a shell element deletion criterion based on time step size. Generally the time step diminishes as the elements became increasingly distorted. Since the global solving time-step is taken as the minimum of the time steps computed for each element (to ensure that the Courant's condition is not violated anywhere) this procedure avoids crashing or excessively time consuming simulations although its results must be judged with care.

The calibration of the JC equation for high-strain rate regimes requires high-speed loading dynamic tests of the type of a Split-Hopkinson Pressure Bar which was not in reach of the resources available for this work. This meant that suitable coefficients had to be found in the published literature where nowhere could be found data for the H111 temper although the alloy 5083 is often cited in technical publications. However different authors published different sets of coefficients for the same material which involved a large array of data to test and adjust. The major starting point has been the work of Clausen on AA5083-H116 (Clausen, et al., 2004) but good results were obtained with the parameters published by Winzer (Winzer, et al., 2011) which have been adopted in the present work and are shown in Table 4.9.

Table 4. 9– Parameters used for the Johnson-Cook visco-plastic deformation model

JC parameters	A (MPa)	B (MPa)	n	C
AA5083-H111	147.0	349.2	0.396	0.104

5. The behaviour of blast waves in a confined space

A parametric analysis is conducted to understand the pattern behaviour of wave reflexions unside an enclosed space after the detonation of an high explosive. An attempt has been made to predict the maximum pressure resulting from the combination of space geometry and position of the charge.

5.1 Introduction

Confined explosions have been studied in the last three decades, thought not to the same extent as free air explosions. Although extensive work has been published on the effect of stand-off free-air explosions, mainly on civil infrastructures (Kingery, et al., 1983) (Gibson, 1994) (Remennikov, 2003) (Luccioni, et al., 2004) (Remennikov, et al., 2005) (Sherkar, et al., 2010), significantly fewer publications are available on explosions inside closed spaces such as tunnels, buildings, aircraft structures and vessels. The main reason for this resides on the added complexity of the analysis, making the blast environment very difficult to describe. Nonetheless, understanding confined explosions is highly relevant as the energy concentration in these cases is typically much higher than on a free air blast (Silvestrini, et al., 2009). Analytical and numerical tools will help in the evaluation of the threat of blast in buildings and vehicles.

In confined explosions, depending on the degree of venting, the early time-blast phenomena will be similar to a free air spherical or hemispherical burst. Gaseous products will remain trapped in the closed space and the shock wave will be reflected from the boundaries of the compartment until the energy of the explosion is dissipated into heat. Reflected waves will propagate and interact with other surfaces generating more reflected waves. After a peak overpressure the high pressure and temperature gases will expand throughout the space in a more lengthy process. This is known as the gas pressure phase, where pressure will decay to ambient pressure as the gases cool down or leakages occur (Krauthammer, 2008). The initial pressure peak will be

followed by a series of lower pressure reflections and the average pressure curve will decay towards the initial ambient pressure.

The equivalent TNT charge mass, the volume of the room *Vi*, the internal exposed area *Aw*, the ambient pressure *Pa* and the vented area *Ai*, if it exists, are the main parameters that affect the resulting internal pressure. The volume plays an important role as the confinement will cause an increase in pressure which in turn will increase the rate of the combustion causing an increase in temperature and again an increase in pressure, and so on until the peak overpressure for internal blast is reached. However, other parameters are the geometry of the compartment and the location of the explosive. This makes empirical predictions very difficult due to the lack of suitable empirical models contemplating so many combinations of different parameters. Excluding experiments, which are unpractical for design purposes, numerical methods are the most appropriate tool for solving these problems as long as validation of the methods and models can be ensured. Lagrangian methods that use empirical blast curves based on experimental data (Randers-Pehrson, et al., 1997) are not appropriate in confined spaces as these methods cannot model reflections. To allow for a complete modelling of incident and reflected waves travelling along the full length of the compartment the Arbitrary Lagrangian-Eulerian (ALE) method is more adequate. This study shows that this can be a useful approach to the analysis of the effects of the detonation of high explosives (HE) inside closed structures.

5.2. Confined explosions

A review of previous work has been presented in Chapter 2 but some references are also relevant for the present Chapter and some material may be revised here.

Structures exposed to a blast from the detonation of the same mass of explosive at the same stand-off distance will experience different loads depending on the degree of the confinement of the surrounding space. The degree of venting of the compartment ranges from fully vented to unvented as shown in Fig. 5.1, reproduced from the US Armed Forces jointly edited manual (DoD, 2008) which presents abacuses and curves for engineering calculations on blast loadings on confined structures.

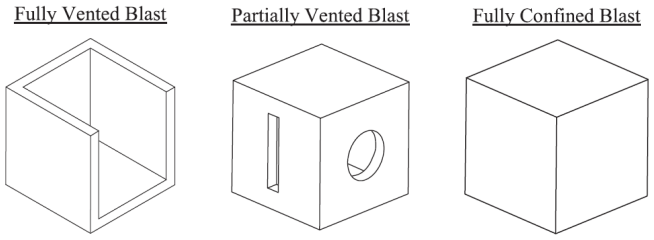

Figure 5.1 - Schematic representation of the degree of venting of the blast for an explosion inside a compartment: (a) fully vented; (b) partially vented; (c) fully confined (DoD, 2008)

The pressure-time curve at a point near an explosion follows a Friedlander type curve, as shown in Fig. 2.13. The positive duration of the curve will be longer in a confined explosion. In a fully confined blast the curve will tend asymptotically to a final equilibrium pressure higher than P_0. Consequently, the resulting impulse i_s, which is the area under the pressure-time curve, that is,

$$i_s = \int_{t_a}^{t_a+t_d} P(t)dt \tag{5.1}$$

may be higher than that of a free-air burst, therefore imparting a more severe loading to the structure. It follows that the resulting damage may be potentially higher in confined explosions. However, Kinney et al. (Kinney, et al., 1979) reported that the damaging effect of a confined explosion may be less than expected due to the longer duration of the pulse, which may be larger than the critical response time of the structure. These authors also reported that peak overpressure is lower in confined unvented spaces and even lower if certain constituents are present, such as aluminium powder, which will be oxidised by the ambient air therefore diminishing the amount of oxygen available.

Relevant published work on confined explosions was published mostly in the 1970s (Baker, et al., 1983) (Esparza, et al., 1975) (Baker, et al., 1975a) (Baker, et al., 1975b) (Kingery, et al., 1978) although research on the subject started earlier.

Most contemporary studies consider the influence of the venting area on the value of peak pressures, with most publications producing a number of empirical equations meant to facilitate the design of safe suppressive structures (Kinney, et al., 1979) (Baker, et al., 1975a) (Baker, et al., 1975b). Such empirical relations between

overpressure and energy release are derived from experimental data, making it possible to calculate peak pressures and pressure decays for confined explosions as a function of an effective vented area. Design applications such as frangible covers (Keenan, et al., 1982) or exit tunnels in underground ammunition storage facilities (Kingery, 1989) benefitted from this early work. A comprehensive collection of empirical calculation methods for venting can be found in the works of Razus (Razus, et al., 2001) and Tamanini (Tamanini, 2001) for gaseous deflagrations. The design of venting covers has been widely addressed as well. Molkov and co-workers (Molkov, et al., 2005) (Molkov, et al., 2003) (Molkov, et al., 2004) published a comprehensive study on venting considering various types of movable covers acted by the blast pressure. In a recent work, Feldgun (Edri, et al., 2011) used experimental, analytical and numerical models to compare results for a cover or a free opening in a closed chamber. In both cases the pressure relief was observed to be similar. In the first instants, however, the chamber behaves as a fully confined room, before the cover moves sufficiently for the overpressure to drop to zero.

The use of computer codes has proved to be effective in these studies. Proctor (Proctor, et al., 1972) was one of the first to use them to study energetic reactions in closed structures, leading to the development of new codes such as INBLAST or BLASTINW in the early 1980s (Montanaro, et al., 1990). Numerical analysis and hydrocodes (Tancreto, et al., 1998) were later used to calibrate the empirical equations and new semi-empirical methods were developed and incorporated into the US Tri-services manual (DoD, 2008). Other authors (Pritchard, et al., 1996) (Ferrara, et al., 2006) (Rigas, et al., 2005) also used CFD codes to study venting effects on relief pipes. The location of the ignition point was found to have a strong effect on the measured peak pressures inside the chamber. Other aspect in favour of the use of numerical models is their ability to handle large scale and complex problems where experimentation is impossible, such as the assessment of blast damage in buildings (He, et al., 2011).

More recent studies on confined blast confirm the growing interest in the field. Geretto (Geretto, et al., 2014) presented a comparison of the maximum plate deflection resulting from various degrees of confinement in an enclosed explosion, showing that the structural deflection increases with the degree of confinement, contradicting the observations of Kinney (Kinney, et al., 1979) in 1979. Dragos (Dragos, et al., 2013)

derived an equivalent idealised load from experimental pressure curves inside a closed space subjected to a confined explosion. This author proposed a simplified load curve that can be incorporated into structural response analysis tools, such as pressure-impulse diagrams. Benselama et al. (Benselama, et al., 2009) did three-dimensional simulations of rigid and closed box configurations inside which an explosive charge detonates, and the simulation of the propagation of a blast wave inside a tunnel with bifurcation. It was found that, in confined domains, the flow remains supersonic a long distance from the blast charge. The bifurcation led to a reduction in the overpressure inside the main pipe while the overpressure inside the secondary pipe was weaker and the flow transonic. As expected, the results for the closed chamber showed an increase both in the peak pressure and in the reflexions from the compartment walls.

This brief reviewcomplementar to the one presented in Chapter 2, shows the added complexity of a confined explosion, which involves reflexion and interaction of blast waves. The published information on internal blast simulation is still scarce although some parametric analyses are available (Hu, et al., 2011) and recent publications show a growing interest in the field.

5.3. Numerical model

Setting-up experimental tests for confined explosions is more complex than for free-air explosions. Numerical simulations, however, can be used to rapidly accommodate different geometries, HE (mass, material, etc.), stand-off distances, that otherwise would require building different test devices. Hydrocodes are widely used for the purpose of analysing high-pressure, high-velocity, dynamic, transient phenomena (Zukas, 2004) and one of such commercially available codes is LS-DYNA, from the Livermore Software Technology Corporation (LSTC). LS-DYNA is a numerical analysis code that incorporates different methods to study explosive blast phenomena. Amongst these, the Arbitrary Lagrangian-Eulerian (ALE) approach is reported to have been successfully used in numerical simulation of high-explosive detonations and blast waves. ALE mathematical foundations are well documented (Hughes, et al., 1981) (Benson, 1995) (Belytschko, 2006) (Benson, 1990) and the method has been further developed to overcome the difficulties that arise from large mesh distortions. It is based

on an arbitrary movement of a reference computational domain (the initial mesh position) in relation to both a material domain (the initial material configuration) and a spatial domain (the current configuration). This relative movement of the computational mesh reduces element distortion of an otherwise Lagrangian mesh. In a fully Eulerian approach, which is a particular case of the ALE formulation, the computational domain will remain fixed and coincident with the spatial domain, completely eliminating element distortion. A multi-material formulation can be used to simulate the propagation of the reaction products of the detonation and the fluid-structure interaction problem where the fluid can be defined by more than one material. In an explosion problem an element may contain air and gas produced from the detonation of the explosive (Alia, et al., 2006) and state variables will be obtained by adequate weighing of the respective values for each of the two materials present in the element.

In a numerical simulation using LS-DYNA the Navier-Stokes equations need to be integrated in time, together with boundary conditions, if the solution for the flow of the products of the explosion is to be found. A major simplification can be done by considering the reference mesh fixed in space, which corresponds to an Eulerian approach. This removes the need for a re-meshing and smoothing process albeit maintaining the complexity of the time integration procedure. A split approach (Benson, 1990) has been implemented in LS-DYNA to simplify the problem. In this split approach each time-step is divided in two: a Lagrangian step and an advection step.

Revising the contents of section 4.3.2:

The Navier-Stokes equations are

$$\frac{\partial \rho}{\partial t} + \nabla \cdot (\rho \boldsymbol{v}) = 0 \tag{5.2}$$

$$\frac{\partial \rho \boldsymbol{v}}{\partial t} + \nabla \cdot (\rho \boldsymbol{v} \otimes \boldsymbol{v}) = \nabla \cdot \boldsymbol{\sigma} + \boldsymbol{f} \tag{5.3}$$

$$\frac{\partial \rho E}{\partial t} + \nabla \cdot (E \boldsymbol{v}) = \boldsymbol{\sigma} : \nabla \boldsymbol{v} \tag{5.4}$$

where ρ is the density, v is the flow velocity, f is the vector of externally applied forces, E is the total (internal plus kinetic) energy and $\boldsymbol{\sigma}$ is the total Cauchy stress which is given by:

$$\boldsymbol{\sigma} = -pI + \mu\nabla\boldsymbol{v} + \nabla\boldsymbol{v} \tag{5.5}$$

In the above equation, p is the pressure, I is the identity tensor and μ is the dynamic viscosity. Equations (5.2 to 5.4) can be rewritten generically as

$$\frac{\partial\phi}{\partial t} + \nabla\cdot\Phi = S \tag{5.6}$$

where

$$\phi = \begin{bmatrix} \rho \\ \rho\boldsymbol{v} \\ \rho E \end{bmatrix}, \quad \Phi = \begin{bmatrix} \rho\boldsymbol{v} \\ \rho\boldsymbol{v}\otimes\boldsymbol{v} \\ E\boldsymbol{v} \end{bmatrix}, \text{ and } \quad S = \begin{bmatrix} 0 \\ \nabla\cdot\boldsymbol{\sigma} + \boldsymbol{f} \\ \boldsymbol{\sigma} : \nabla\boldsymbol{v} \end{bmatrix} \tag{5.7}$$

Mass conservation is used in its integral form

$$\rho J = \rho_0 \tag{5.8}$$

rather than the equation of continuity (Belytschko, 2006) because of its simplicity and better accuracy to compute the current density ρ. ρ_0 is the initial density and J is the volumetric strain given by the Jacobian

$$J = det\left(\frac{\partial X_j}{\partial X_j}\right) \tag{5.9}$$

The splitting approach consists of separating the Eulerian conservation Equation (5.7) into two terms: a source and a convective term, that are, respectively

$$\frac{\partial\phi}{\partial t} = S \tag{5.10}$$

$$\frac{\partial \phi}{\partial t} + \nabla \cdot \boldsymbol{\Phi} = 0 \tag{5.11}$$

The source equations (5.10) are the Lagrangian conservation equations, corresponding to the Lagrangian step. The convective equations (5.11) describe the transport phenomena and can be referred to as the Eulerian step. In the split approach the two steps are solved separately and sequentially to calculate velocity and internal energy. In the Lagrangian step the stresses are calculated at the integration points and nodal accelerations, velocities and displacements are then obtained with an explicit time integration scheme. The mass is assumed to be lumped at the nodes, which leads to a diagonal matrix which simplifies the calculation of the accelerations.

In the second step the resulting distorted mesh is remapped onto an arbitrary position in the case of an ALE mesh, or to its previous position for an Eulerian description. The advection problem will then be solved using a finite volume procedure. State variables can thus be mapped onto the rezoned mesh. An advection scheme is necessary to calculate the material fluxes. This can be done using one of three methods: the first order accurate Donor Cell (which is a first order Godunov method) (Godunov, 1959), the second-order van Leer (Leer, 1977) and a first order accurate Donor Cell modified to conserve total energy over each advection step instead of conserving only internal energy. LS-DYNA also combines these algorithms with the Half-Index Shift method (Benson, 1992) to find the advection of node-centred variables.

By using a Multi-Material ALE (MM-ALE) element formulation, the gaseous products of the explosion and the ambient air that initially fills the mesh can occupy the same elements. It is possible, using a suitable interface tracking algorithm, to follow the flow of both materials through the Eulerian mesh. This is a computationally demanding task and under-integrated elements will be used in this type of simulation. This calls for hourglass control as under-integrated elements do not account for the internal forces necessary to counter zero energy deformation modes, which tend to appear in these cases.

An additional set of equations has to be considered when solving these problems because, when pressures are significant, volumetric deformations will be large as well, and the hydrostatic component of the stress tensor becomes larger than the deviatoric

stresses. As a consequence, a relation between pressure, volumetric deformation and energy is necessary, an equation of state (EOS). In a simulation of an explosion at least two EOS are needed, one for the explosive and another for the air. To simulate the high explosive detonation process the following Jones-Wilkins Lee EOS is normally used (Lee, et al., 1968)

$$P = A\left(1 - \frac{\omega}{R_1 V}\right)e^{-R_1 V} + B\left(1 - \frac{\omega}{R_2 V}\right)e^{-R_2 V} + \omega\frac{E}{V} \qquad (5.12)$$

This is an empirical equation obtained from the expansion of the internal energy equation near the isentrope of the detonation products (Grys, et al., 2010). More details on its derivation can be found in the work of Alia and Souli (Alia, et al., 2006).

For air a gamma law modelled by a linear polynomial equation (linear relative to the internal energy E) has been used:

$$P = C_0 + C_1\mu + C_2\mu^2 + C_3\mu^3 + E(C_4 + C_5\mu + C_6\mu^2) \qquad (5.13)$$

where $\mu = (\rho/\rho_0) - 1$ and ρ/ρ_0 is the ratio of current to initial (reference) densities. Coefficients C_2 and C_6 are set to zero if $\mu < 0$. For an ideal gas the expression is reduced to

$$P = (\gamma - 1)\frac{\rho}{\rho_0}E_0 \qquad (5.14)$$

as all coefficients will be made equal to zero except $C_4 = C_5 = (\gamma - 1)$ and $\gamma = c_p/c_v$ is the ratio of specific heats.

When refinement or a problem scale is expected to make computations very lengthy, another available technique is mapping. For full scale domains were meshes will easily have millions of elements, the domain can be scaled using 1D to 3D or 2D to 3D mapping techniques (Aquelet, 2008). Mapping is implemented in most commercial hydrocodes, including LS-DYNA, which allows analyses to be split into two phases. In the first phase a 1D or 2D mesh is used to initialise the detonation and the expansion of the reaction gases. This mesh has to be very refined to allow the development of a

smooth wave front and a good set of energy results. Afterwards, the 3D problem is initialised with the input data calculated from the previous analysis. The 3D mesh can be significantly coarser, which is the real advantage of the technique.

To ensure good overall results it is necessary that the 1D or 2D results are as good as possible. Some authors (Larcher, 2007) compared results obtained with spherical and prismatic meshes. The first allow a much better definition of the blast wave. However, further away from the detonation point, the element aspect ratio increases and for aspect ratios in excess of ten pressures will tend to be overestimated. This imposes a practical limit in the mesh extent. Prismatic meshes may also suffer from some anomalies. Larcher (Larcher, 2007) reported that peak pressure values are smaller along the diagonals of prismatic meshes. In the present study a regular square mesh of 200×200 [cm^2] with 250000 elements was used and some differences were initially found for the peak pressure values at tracer points equally distant from the detonation point but at different azimuths. However, the higher peak pressure values were found along the diagonals, contradicting Larcher's findings (Larcher, 2007). These anomalies were minimised by using a delayed mesh relaxation technique and coincident readings of peak pressure were obtained both at the diagonal and at a point near one of the edges of the box-shaped mesh.

5.4. Validation examples

The optimal choice of modelling techniques and parameters to replicate the physical response of the system is known to be a complex task (Zukas, et al., 2000). A thorough validation method was defined to ensure the proposed models were reliable. Three examples where experimental results are available in the literature were thus used for validation purposes. These examples are described in the following sections. The high explosive used is C4, which is a mixture of Hexogen (RDX) with a plasticiser compound, often used in military applications. Air and explosive properties were adopted from Alia and Souli (Alia, et al., 2006). Data for the Equations of State of both materials are listed in Tables 4.3 and 4.4, where D is the detonation velocity and P_{CJ} is the Chapman-Jouguet pressure. E_0 and V_0 are the initial internal energy and the relative

volume, respectively. The C_i coefficients are all set to zero except $C_4 = C_5 = \gamma - 1$ where γ is the ratio of specific heats $\gamma = C_p/C_v$. The material properties are shown in Table 4.6 and 4-7.

5.4.1. Free air explosion – Validation example 1

Alia and Souli (Alia, et al., 2006) and Kamal and Aquelet (Mahmadi, et al., 2014) reported an experiment where a spherical charge of plastic explosive C4 was detonated in a mass of air at room temperature. These authors also used LS-DYNA to simulate the

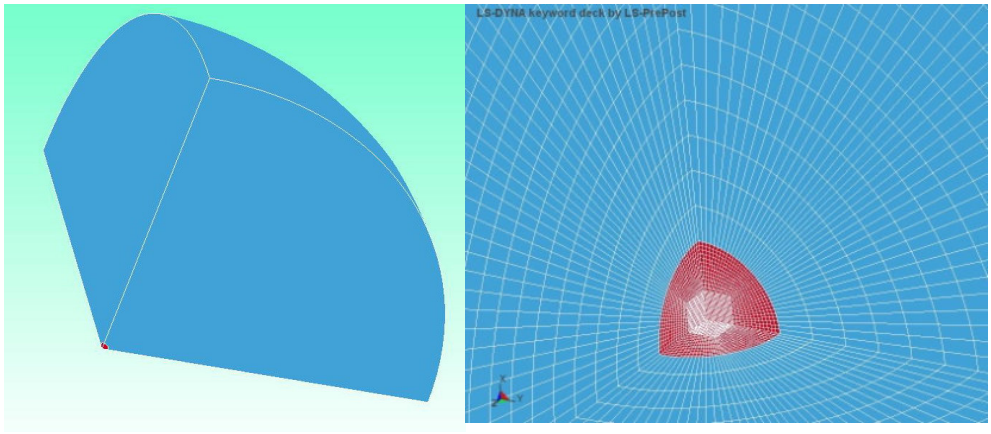

Figure 5. 2 - A meshed model of an Air domain (blue) where a spherical explosive charge (red) at his centre will be detonated. Only one-eighth of the domain has been modelled. (Mesh size 147649 elements)

phenomenon. In the experiment the pressure peak was measured by a sensor placed 5 ft (152.4 cm) from the point of detonation. In LS-DYNA these pressure sensors can be simulated by means of tracer points defined at the sensor positions. The mass of the charge was 1 lb (454 g), corresponding to a sphere with radius 4.07 cm. Both papers (Alia, et al., 2006) (Mahmadi, et al., 2014) present a comparison of numerical and experimental results and report a very good agreement in the time of arrival and only slightly different peak pressure values. These results are listed in Table 5.1 and were used for comparison and validation purposes in the present paper. It is important to note that the two experimental results reported by the authors are not the same as shown in Table 5.1. This has probably to do with the fact that the explosive composition

can vary slightly if obtained from different batches or ambient conditions (pressure, humidity and temperature) may also vary.

All simulations were run with LS-DYNA R711 and using the same machine. Different degrees of mesh refinement were used, namely 71199, 104329 and 147649 elements. Symmetry boundary conditions were also adopted. Numerical parameters that were varied include the advection logic and the advection method. A mesh delaying relaxation option was also used to increase accuracy, as suggested by Kamal (Mahmadi, et al., 2014). This contracts the mesh locally at the shock wave front. The geometry of the model – one-eighth of the domain modelled with a spherical mesh – is shown in Fig. 5.2. The region where the explosive is has been greatly refined in comparison to the remaining mesh (see Fig. 5.2) to allow for a better representation of the detonation process and development of a well-defined wave front.

Results are listed in Fig. 5.3 and can be compared with the reference experimental and numerical results in Table 5.1. Fig. 5.3 shows the pressure-time readings at the same tracer point for all the three considered meshes and two advection logics available in LSDYNA. For each mesh the advection method was also varied. It is immediately apparent that using the alternative advection logic (see Fig. 5.3a) the pressure peaks are much lower than when using the default logic (see Fig. 5.3b) and significantly different from the experimental result obtained by Alia and Souli (Alia, et al., 2006). The alternative method was then abandoned. From the results in Fig. 5.3b it can be seen that there is good agreement between the proposed numerical model and Alia and Mahmadi's experimental results. From Fig. 5.3b) it can be concluded that the best pressure results were obtained when combining the Van Leer advection method and the most refined mesh or with the modified Donor Cell method and the intermediately refined mesh (peak pressure results were 2.9 and 3.0 bar, respectively). An even more refined mesh (255949 elements) was also used but, as mentioned above, results diverged excessively, unrealistic pressure curve shapes and values were found and thus this refined mesh was discarded. Consequently, in subsequent runs only advection methods 2 and 3 were applied as it was found that method 1 (Donor Cell method) was not entirely satisfactory. An extensive research through technical and scientific papers and LS-DYNA user groups did not reveal other reported anomalies with very refined meshes. Although this is not entirely clear it is believed that since advection methods accumulate errors due to the material boundaries tracking

difficulties, above a certain number of elements the accumulated errors may tend to become noticeable.

Table 5.1 - Peak pressure and time of arrival (experimental and numerical) as reported by Alia and Souli and Kamal and Aquelet: (a) with a mesh of 27972 elements (b) With a mesh of 56916 elements.

Experimental pressure peak at sensor point [bar]		Experimental value of time of arrival [milliseconds]	Numerical pressure peak at sensor point [bar]	Numerical value of time of arrival [milliseconds]
(Alia, et al., 2006)	2.96	1.50	2.70 (a)	1.44
			2.90 (b)	1.50
(Mahmadi, et al., 2014)	3.406	Not mentioned	3.405	Not mentioned

Table 5.2 - Free air explosion: results obtained with 2D meshes and different advection logics and advection methods

Nº elements in 2D Mesh (quarter of a circle)	Advection logic DCT	Advection method METH	Delayed mesh relaxation parameter PREF	Pressure peak at sensor (bar)	Time of arrival of shock wave (milliseconds)
14375 elements	alternative	Van Leer	Not used	4.90	1.25
	alternative	Van Leer	0.01	6.00	1.13
	alternative	M. Donor Cell	Not used	4.25	1.55
	alternative	M. Donor Cell	0.01	5.20	1.25
	default	Van Leer	Not used	2.64	1.52
	default	Van Leer	0.01	2.93	1.46
	default	M. Donor Cell	Not used	2.81	1.47
	alternative	Donor Cell	0.01	2.92	1.44
250000 elements (squared)	default	M. Donor Cell	0.01	2.63	1.54
	default	Van Leer	0.01	2.88	1.42
	alternative	M. Donor Cell	Not used	4.69	1.30
	alternative	Van Leer	Not used	5.52	1.23

A second set of simulations of the same validation problem, albeit in two dimensions (2D), was run leading to good results for both advection logics. The optimal combinations of advection method and advection logic results are highlighted in Table 5.2 and it can be concluded that for this particular problem the default advection logic should only be combined with the first order Donor Cell advection method, whilst the

alternative advection logic yielded good results combined with a second order accurate (van Leer) advection method. Delayed relaxation (Mahmadi, et al., 2014) was found to be necessary in all 2D simulations in order to better match the numerical results to the experimental observations.

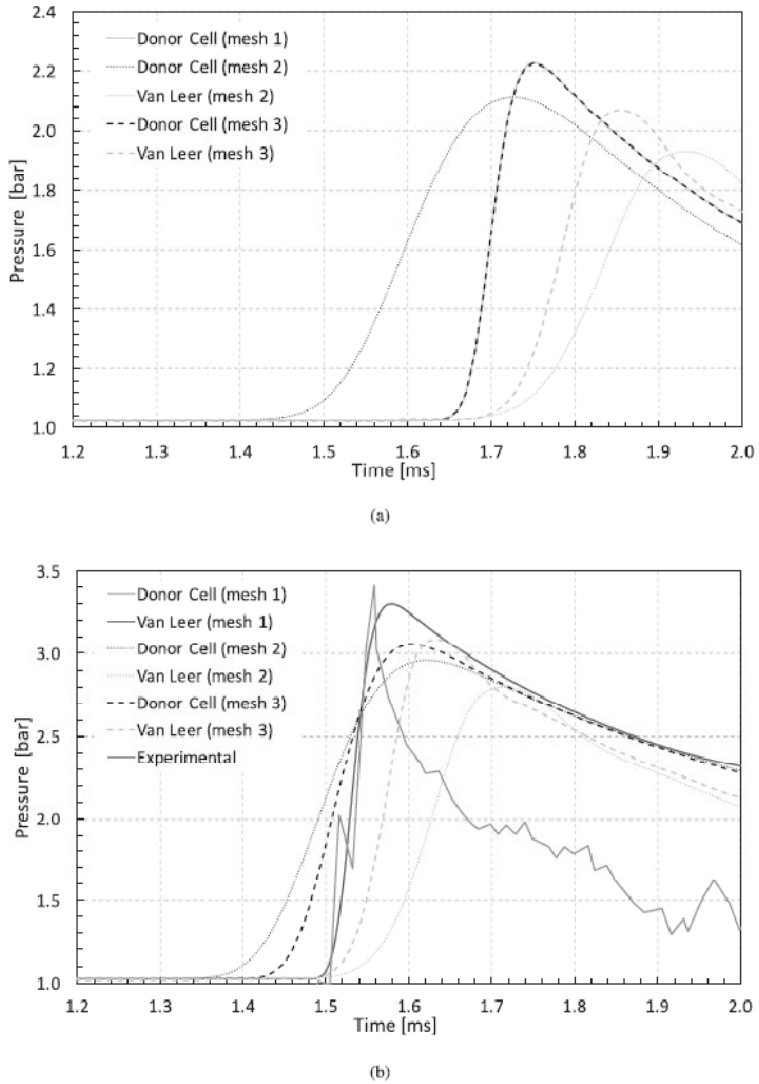

Figure 5. 3 - Numerical and experimental pressure curves read at the same tracer point: a) Using the alternative advection logic ; b) Using the default advection logic (Parameters used in each curve are presented in Table 5.2)

5.4.2. Confined explosion – Validation example 2

The second example was used to validate the ALE methodology in the analysis of a confined explosion. Chan (Chan, et al., 1994). published experimental data on a confined blast inside a rectangular steel bunker measuring 10×8×8 [ft^3]. The authors used 1 lb of C4 at the centre of the compartment and pressures were measured on three gages (front, left and corner). The location of the gages is shown in Fig. 5.4. Mesh refinement is known to be a very important factor in ALE simulations but this may become unpractical for full scale domains such those described by Chan (Chan, et al., 1994). Consequently, a mapping technique was used to speed up the simulation whilst maintaining accuracy. A 2D radial mesh of 6776 elements (only one fourth of a circle was modelled) with a radius of 200 cm was used. Simulation time was stopped at 500 microsec and the resulting map file used to initialize the 3D mesh. The total running time was set to 7500 microseconds. No mesh relaxation was used in the 2D run.

The obtained numerical results are shown in Fig. 5.5 along with the experimental observations. The initial peak overpressures recorded at the front, left and corner gages were 600, 420 and 200 kPa, respectively (see Fig. 5.5a, 5.5b and 5.5c). The equivalent numerical results are 667, 300 and 210 kPa. With the exception of the left gauge, there is good agreement between numerical and experimental values for both pressure and time of arrival. The overall pattern of the series of incident and reflected waves are in reasonable agreement with the numerical results, although a shorter time lag is observed. This may be due to the fact that in confined explosions the ambient air heats up and this affects the shock wave speed. Additionally, a ± 20 % error in the gauges was reported by Chan (Chan, et al., 1994). which will certainly add to the observed discrepancies.

A mesh convergence analysis was done, using 2.26, 1.4 and 0.8 million brick elements. This 1.4 million element mesh has been chosen, as it gave good results corresponding to elements of approximately 2.4 cm in length, and all simulations were run on an Intel i7-2700K CPU at 3.5 GHz in about 1 hour. ALE settings included the alternate advection logic and the Donor-Cell combined with the Half-Shift Index, advection method. Hourglass control default values were used without any indication of the presence of instabilities.

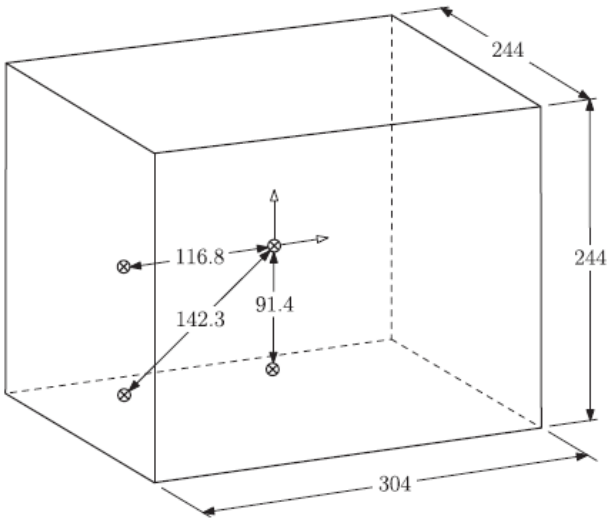

Figure 5.4 - The dimensions (mm) of the steel bunker and the positions of the pressure sensors in the experiment of Chan (Chan, et al., 1994)

5.4.3. Confined explosion – Validation example 3

The last validation example is based on the experiments reported by Zykowski (Zykowski, et al., 2004) who measured blast wave pressures from the detonation of a mixture of oxygen and hydrogen in a small box (dimensions 50×40×30 [cm^3]). Hu (Hu, et al., 2011) used the ALE method to simulate the same experiment using AUTODYN relying on a single mesh of hexahedral elements and assuming rigid compartment walls. A diagram of the Hu's test device is shown in Fig. 5.6. The present study replicated Hu's analysis in LS-DYNA albeit using the mapping technique. Under-integrated solid elements were used with the mesh sizes (Hu, et al., 2011) listed in Table 5.3. The geometry of the box and the location of the tracer point are included in this table as well. The explosive mixture was modelled considering 0.315g as its TNT equivalent mass, as reported by Hu (Hu, et al., 2011) , with the properties listed in Table 4.5.

The same calibration parameters were used as in the previous example, to confirm its validation. Different combinations between advection method and advection logic confirming that alternative logic gave better results.

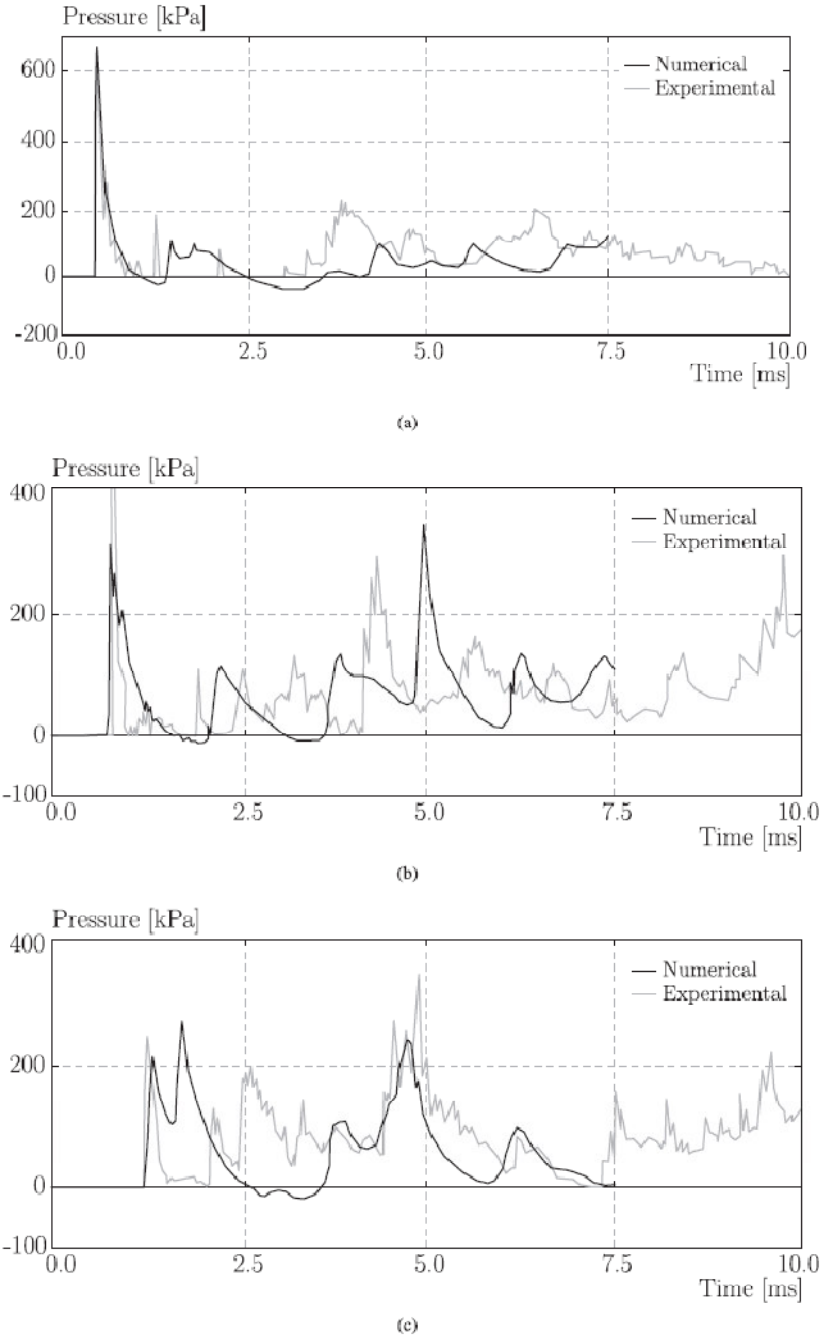

Figure 5. 5 - Measured and calculated peak blast overpressures from a confined explosion inside in a closed steel bunker, (a) Front sensor (b) Lateral sensor (c) Corner sensor. Pressures in KPa and time in milli-seconds. Ref: (Chan, et al., 1994) for experimental results only. Numerical results were added in the present work

Table 5. 3 - Finite element mesh parameters for the simulation of a confined explosion of a mixture of oxygen and hydrogen in a closed rigid compartment.

Simulation	Meshes			
	2D		3D	
	Size (x, y) [cm]	Element size [cm]	Size (x, y, z) [cm]	Element size [cm]
1	(25, 30)	0,02	(50, 30, 40)	0,625
2		0,04		1,25
3		0,08		2,5

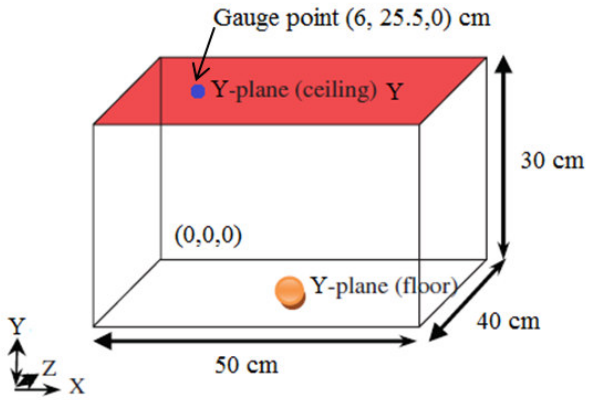

Figure 5. 6 - Diagram of Hu's experiment for a confined space measuring x, y, z = 50, 30, 40 cm, where the explosive is on the centre of the floor and a pressure sensor is placed at coordinates (6,25.5,0)cm. (Hu, et al., 2011)

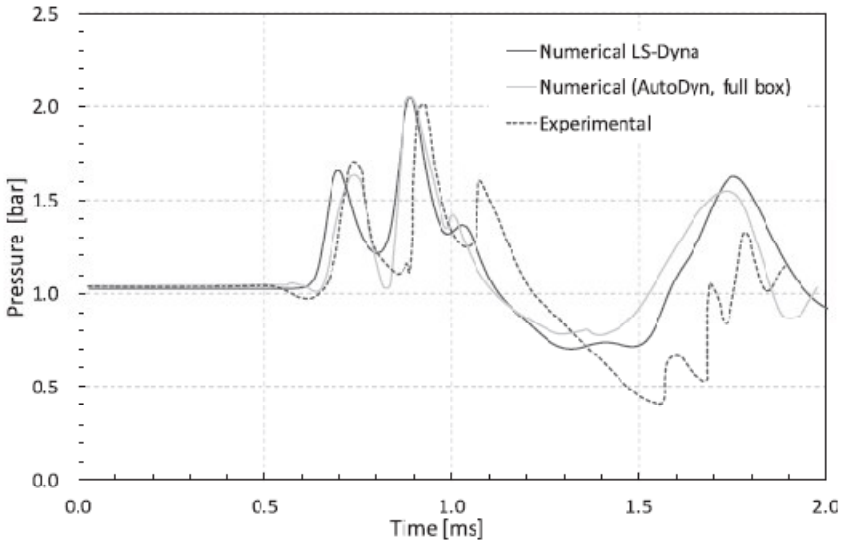

Figure 5. 7 - Comparison between numerical and experimental results. The alternative advection logic defined in LS-DYNA input has been used in the numerical curve. The Autodyn and experiments curves were reproduced from Hu (Hu, et al., 2011)

Other modelling parameters where: Hourglass coefficient QM = 10^{-6}, alternate advection logic and Donnor Cell method of advection combined with the Half-Shift Index method were used. The obtained peak pressure and time of arrival results are plotted in Fig. 5.7 showing that the 1.7 bar peak pressure and the shape of the pressure history plot agrees well with both the experimental and numerical results reported by Hu (Hu, et al., 2011).

The best results were found for a mesh with 245760 elements (case 1 for the 3D mesh in Table 5.3). The mapping file was obtained running a 2D rectangular mesh with 1875000 elements (25 x 30 cm with elements 0.4 mm wide) for a model time of 30 microseconds. The charge was placed in the middle of the lower border representing only half charge. Fig. 5.7 shows the numerical pressure curve using the alternate advection logic. Both advection logic methods were tested and the solution showed to be strongly influenced by the advection logic as it can be seen in Fig. 5.8. The two solutions shown follow similar trends but differ in the peak pressures values. The same was not true for the advection methods which gave similar peak pressures.

As stated above, the compartment walls were defined as rigid in all simulations. This agreed with the original experiment performed inside a bunker and in which the small charge and low peak pressures involved are consistent with a rigid wall assumption. However, a real system would surely deform elastically and eventually plastically, affecting the observed peak pressure values. As such, the structure was subsequently modelled considering a suitable fluid structure interaction (FSI) technique (Chafi, et al., 2009). With this added feature, the obtained pressure histories retain the generic shape but the peak pressure values are reduced by approximately 20%, as can be seen in Fig. 5.9. As the material has been modelled as rigid this apparent discrepancy may be explained by the dissipation of energy in the FSI algorithm, as explained before. As a remark it was concluded that further calibration should be necessary to correct the discrepancy. Apart from this, the FSI results are qualitatively consistent and did not vary significantly when changing advection methods and logics.

The above findings showed that in the free air explosion validation procedure the default advection logic was yielding too low pressures while in the case of internal explosions the opposite was observed. A recommendation advising the alternate logic for simulations with explosives was found on LS-DYNA User Group but it is not possible to quote it as a reliable source. Therefore no recommendations have been published so

far on robust guidance on the numerical calibration of an ALE model for the simulation of explosions. As it was shown above some advection methods work better with more refined meshes than others and deriving conclusions may be misleading as the proper choice of parameters requires some experience and a validation process as it is being described above.

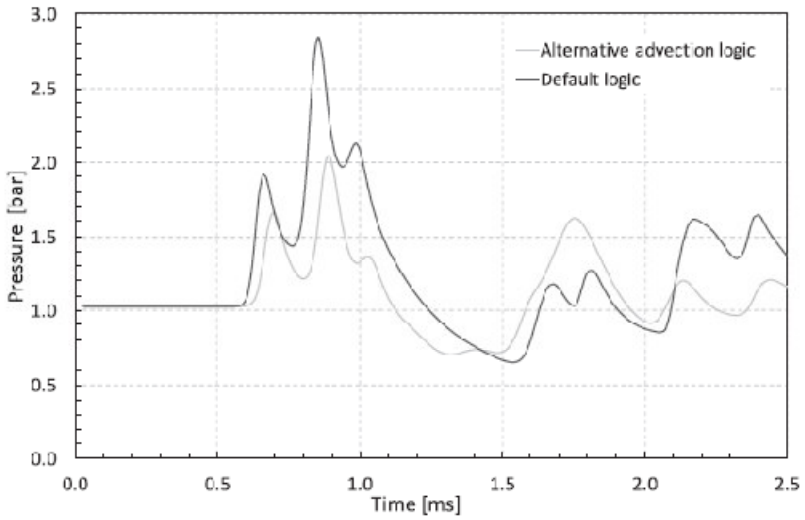

Figure 5. 8 - Comparison between two solutions for the confined TNT explosion described by Hu (Hu, et al., 2011). The blue solution used an alternative advection logic and the red solution used the default logic.

5.5. Parametric studies

5.5.1. Description of the simulations

In this section a parametric study is described where numerical simulations are used to identify how the variation in the relative dimensions of a confined space can influence the maximum pressures impinging on the interior walls. The numerical models described in the preceding sections, assessed by published experimental data, allowed the tune-up of the major modelling parameters that are now used.

A family of five closed rigid boxes where one of the dimensions was kept constant and the others varied in such proportions that volume remained constant was subjected to the internal detonation of a fixed mass of TNT. The volume was set equal to 216000 cm^3 and the mass of explosive, TNT (trinitrotoluene), was set to 1.25 g. Table 5.4 shows the dimensions of each box, along with the number of elements used in each

3D simulation. The origin of coordinates is always located at the centre of each box and *Lx*, *Ly* and *Lz* are half the box sizes along each axis.

For all 5 cases, the mapping file was obtained running a 2D initial simulation on a rectangular mesh with 468750 elements (25×30 cm rectangular domain, with 0.04 cm edge length elements).

For each one of the five boxes eight numerical simulations were performed, each one corresponding to a defined position of the explosive relatively to the three main axes. The complete description of the eight positions considered for each box is presented in Table 5.5, where *cx*, *cy* and *cz* are the coordinates of the charge along each axis. This way a comprehensive coverage of the effect of eccentric detonations inside a closed box is made available for analysis.

Table 5.4 - Box dimensions and characteristics of the meshes used in the simulations

Simulation	Box dimensions (2*Lx*, 2*Ly*, 2*Lz*) [cm]	Number of elements along x, y, z
1	60 ; 60 ; 60	120 ; 120 ; 120
2	75 ; 60 ; 48	150 ; 120 ; 96
3	90 ; 60 ; 40	180 ; 120 ; 80
4	100 ; 60 ; 36	200 ; 120 ; 72
5	120 ; 60 ; 30	240 ; 120 ; 60

Table 5. 5 - Position of the explosive charges in each box relative to box dimensions

Position	*cx*/*Lx*	*cy*/*Ly*	*cz*/
0	0.0	0.0	0.0
1	0.5	0.0	0.0
2	0.0	0.5	0.0
3	0.0	0.0	0.5
4	0.5	0.5	0.0
5	0.5	0.0	0.5
6	0.0	0.5	0.5
7	0.5	0.5	0.5

To describe the pressure distributions in the interior of the boxes nineteen sensors were used. They were always placed 5 mm apart from the walls of the box and the sensor arrangement is the same for all simulations and is shown in Fig. 5.10. As an example a tabular description of their positions for box no. 1 is presented in Table 5.6. Only one eight of the box was monitored assuming that the major effects should be observed in the close proximity of the explosive.

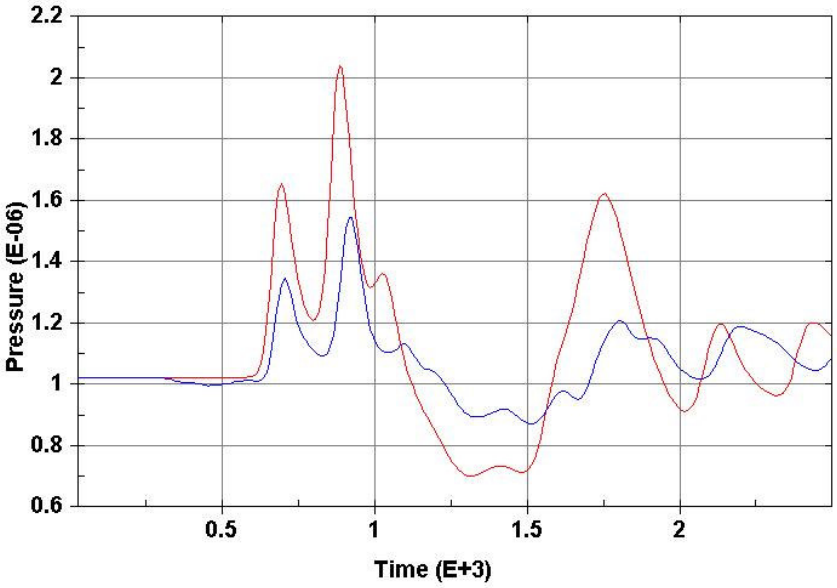

Figure 5.9 - Comparison between the pressure curve at sensor point xyz (6,25.5,0), in the confined box described by Hu (Hu, et al., 2011) not using FSI (Curve in red) and using FSI (curve in blue).

As mentioned, 5 boxes were considered and for each of them 8 explosive positions were simulated and the resulting pressure curves were registered at 19 tracer points defined for each box. This analysis yielded 760 curves, each one with several pressure peaks producing thousands of peak values to consider. As this forest of information could hide the more important phenomena that might be present in the simulations it was decided that in each curve only the first incident peak and reflection peaks which value was higher than the incident peak value, should be considered in the analysis. All other reflexion pressure peaks were ignored. It was also decided to look for the pressure peaks at the centre of each internal wall, at the more exposed mid points of the edges and finally at the corner where such edges intersect. This approach reduced the universe under analysis to a more tractable number.

Varying the input parameters revealed that the advection options had little influence on the results. The input parameters were kept constant throughout the

simulations and replicated those used in the small box validation examples described in the preceding section. Element size has been set to 5 mm which was considered adequate. Smaller values did not yield significantly better results and the computation times jumped to dozens of hours. The UFC manual (DoD, 2008) was also used as another checking tool. The average peak reflected pressure obtained from the UFC tables was 6.2 bar which compares reasonably well with the numerical result of 7.7 bar at the plate centre. However the UFC manual assumes a uniform pressure loading on the internal surface being considered, do not considers wave blast reflections and only allows calculations on the closest faces to the explosive.

Table 5. 6- Position of all sensors for box nº 1

Sensor	Box nº 1 sensor coordinates [cm]		
	x	*y*	*z*
1	0.0	29.5	0.0
2	0.0	29.5	29.5
3	29.5	29.5	29.5
4	29.5	29,5	0.0
5	0.0	0.0	29.5
6	29.5	0.0	29.5
7	29.5	0.0	0.0
8	14.75	29.5	14.75
9	0.0	29.5	14.75
10	14.75	29.5	0.0
11	14.75	29.5	29.5
12	29.5	29.5	14.75
13	0.0	14.75	29.5
14	14.75	14.75	29.5
15	29.5	14.75	29.5
16	14.75	0.0	29.5
17	29.5	14.75	14.75
18	29.5	0.0	14.75
19	29.5	14.75	0.0

Finally, it results from the above that, as a guidance, it is possible to say that the alternate advection method works better for confined explosions, combined with the Donnor Cell plus Half-Shift Index advection method. These parameters must be checked against different degrees of mesh refinement.

5.5.2. Discussion of results - Data

A plot of the maximum pressure reached along vertical and horizontal lines passing thought the walls midpoint is illustrated in Fig. 5.11, for a centred explosion (position 0) and box no 1 (cubic shape). It is important to note that the figure shows the peak incident and reflected[13] pressure values at selected positions in the wall and not an instantaneous pressure distribution at a certain instant in time. It has been assumed that, for engineering purposes, the peak values should be the driving criteria in design or engineering analysis. The general trend observed in all faces show a peak value at the centre of each face reducing towards the edges and increasing again as they get closer to those edges. Along the edge the same is observed such that the highest pressure values are observed at the corners. It is important to note that when mention is made to reflected blast waves or peak reflexions it refers to the bouncing waves generated by

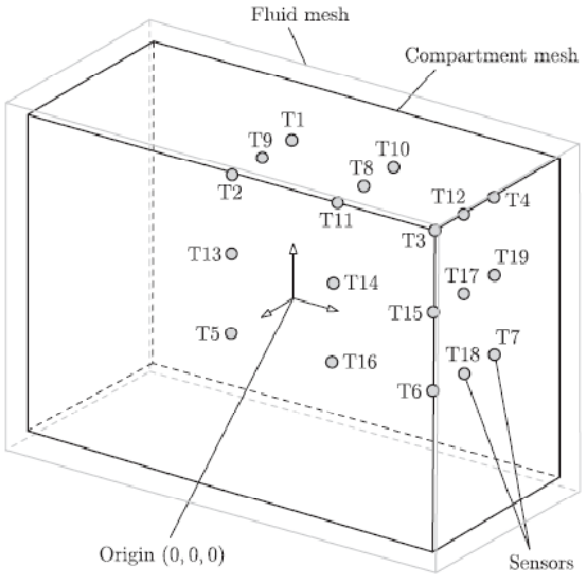

Figure 5.10 - Positions of the sensors used to record the pressure-time curves resulting from the simulated confined explosion in each compartment.

reflexions on the inside walls of the confinement and not to the concept of reflected pressure that is due to the fluid particle deceleration where conversion of

[13] In this context the reflected wave means a wave that bounced in a wall and is passing through the sensor point after that.

kinetic energy into static pressure will occur greatly enhancing the pressure exerted by the fluid on the solid surface.

Varying input parameters revealed that the solution is insensitive to the order of accuracy of the advection method selected, however the LS-DYNA advection logic parameter had a strong effect. The input parameters were all the same throughout the simulations and replicated those used in the small box validation examples described in the preceding section.

Analysing the time-pressure curves obtained it becomes clear that the maximum incident peak pressures show a great dependency on the *Z* scaled distance. Some analysis were performed to investigate the possible correlations between the maximum pressures and the geometric ratios of the boxes as they are defined in the empirical charts of the UFC manual (DoD, 2008). However, low correlations were obtained with other than the *Z* scaled parameter.

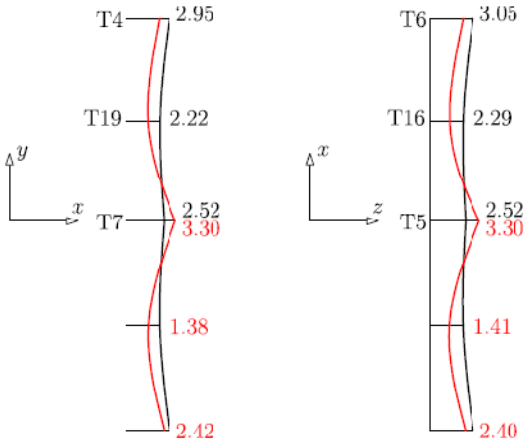

Figure 5.11 - Profiles of incident pressure waves arriving at the walls of the closed Box nº 1 (60x60x60cm) (a) in the vertical middle plane of face normal to X (b) in the horizontal middle plane of face normal to Z. (The incident wave is shown in blue and the first reflected wave is in red)

For centred and non-centred explosions, the highest pressures in the walls were always observed at the points closer to the explosive. Nevertheless, it was verified that the confinement caused a pressure enhancement effect at corners and edges together with the presence of complex patterns of internal blast reflexions, which in certain cases resulted in peak pressure values higher than in the initial blast wave. This makes

pressure distribution predictions within confined spaces subjected to internal blast rather difficult.

Semi-empirical expressions such as those from Henrych (Henrych, 1979) for instance, have been widely used for engineering purposes but were not derived to be applied to a confined explosion. However a monotonic relation between the *Z* scaled distance and the incident pressure peak was observed in all the simulations. A modification of the Henrych expression was found to give a good engineering approximation for the peak pressure results measured at the centre of all faces in the 5 boxes. Such equation is,

$$P_{walls} = \frac{5.924}{Z} + \frac{2.941}{Z^2} + \frac{3.259}{Z^3} + \frac{0.210}{Z^4} + \frac{0.037}{Z^5} \text{ [bar]} \qquad (5.15)$$

$$Z = \frac{R}{\sqrt[3]{W}} \qquad (5.16)$$

where *R* is the stand-off distance in m and *W* is the equivalent TNT weight of explosive in kg. Fig. 5.12 shows how the new equation fits relatively well the numerical data obtained from the simulations. The original Henrych equation is also plotted, always giving lower peak pressures than those obtained in the numerical simulations. Since the Henrych curve was derived for a free air explosion this observation agrees well with previous remarks (DoD, 2008) (Hu, et al., 2011) (Remennikov, et al., 2005) stating that the confinement enhances the internal pressures.

Eq. (5.15) approximates the peak pressure at the centre of the walls. However, in several cases larger pressures were recorded in some sensors due to blast reflections. In the case of box no 1 and position 0 (centred explosive), a peak pressure value of 10.3 bar was obtained at the vertex, much larger than the direct overpressure of 2.52 bar, measured at the internal surfaces of the box. This was due to the orthogonal symmetry of the cubic shape that makes reflected waves to arrive at the same time at the opposing vertex, reinforcing each other.

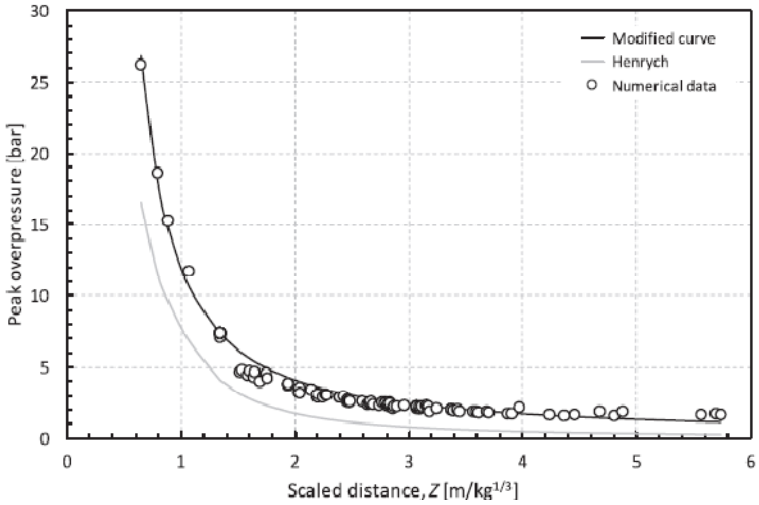

Figure 5.12 - First arriving wave at the centres of faces – Values of maximum pressures: Comparison between experimental data and numerical results

In many references it has been assumed that the pressures of reflected blast waves will show a decay for any subsequent wave (Dragos, et al., 2013) and this result shows how this assumption may deviate from reality. It was observed that the pressure enhancement observed at corners and edges could not be predicted in terms of single parameter only, such as the *Z* scaled distance. Reflected peak-pressures at corners are also influenced by other factors such as the angles at which the wave front arrives in relation to the adjacent faces to the corner. The maximum, minimum and average angles as well as the angular deviation from octahedral angle, assumed to be the optimum in terms of the induction blast wave mutual reinforcement, were all investigated and it was found that the maximum angle between each of the three concurrent walls at a corner and the radial stand-off direction, between explosive and sensor gave the best correlation (about 0.615 by assuming a two degree polynomial fit). This can be seen in Fig. 5.13 which shows how the corner peak-pressure varied with that maximum angle. At angles near one radian the pressures showed the highest values. However, as referred above, the stand-off distances play the important role in this phenomenon and thus the two variables were combined to give a rough predictor of the maximum pressures at corners. The results, which can be seen in Fig. 5.14 show that the new predictor gave better results than the modified curve used in eq. (5.15), of a single parameter, which under-predicted most of the results for corners. The new equation has a coefficient of correlation of 0.766 and a standard deviation of 1.487, which is

reasonably acceptable for engineering work. The equation, which is obtained from a multiple variable regression analysis, is as follows:

$$P_{corners} = 26.228 - 11.475 \cdot \theta_{\max} - 1.4785 \cdot Z \text{ [bar]} \qquad (5.17)$$

where $\theta_{\max}$ is the maximum angle between the radial stand-off direction and the planes that contain the intersecting walls at the corner being considered. However the equation under-predicts the results for the highest values of pressure. A further correction has been thought such as multiplying the values of P_{corners} obtained through eq. (5.17) by a suitable multiplier but this would not add to the physical meaning of the predictions. Table 5.7 shows results for pressures at corner sensor no. 3 obtained both numerically and using the estimation eq. (5.17)). In this table only the highest pressure values in the simulations were listed. In all other cases the pressure at corners was neglected as there were pressures much higher acting in other points of the box.

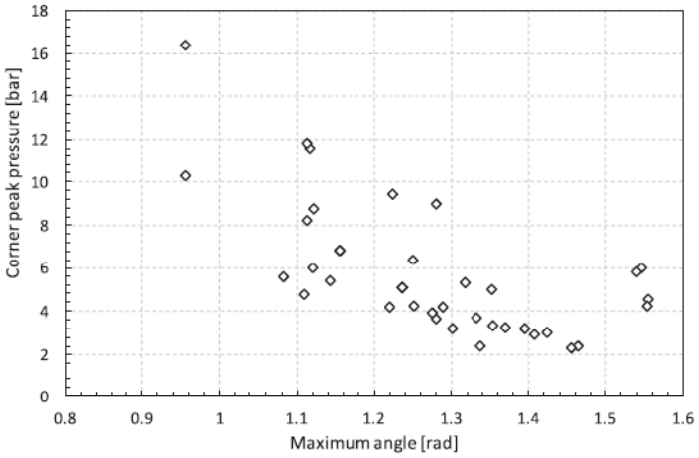

Figure 5.13 - Variation of peak pressure at corner with the maximum angle between the stand-off direction and any of the three planes crossing at the corner

Eq. (5.15) fits well the results for maximum pressures occurring at the centre of the confinement walls. For the corners a closer fit is proposed using equations (5.17). In all other situations, either edges or off-centred face points, eq. (5.15) will under-predict the maximum peak-pressures. All these data points were aggregated as the edges only contributed with about 15% of the maximum peak-pressure values. To avoid this

systematic under-prediction a new fit was derived and the results can be seen in Fig. 5.15. The data correlation found was reasonably high (R2 = 0.8369) and the fit is reasonable as shown in Table 5.8. This new equation is:

$$P_{edges} = 13.685 \cdot Z^{-0.974} \text{ [bar]} \tag{5.18}$$

Table 5. 7 - Comparison between the peak pressures obtained numerically and from equation (17) at corner sensor no. 3

Box	Position of Explosive	Pressure (Numerical) [bar]	Pressure (Eq. 15 and 17) [bar]	Error %
1	0	10.3	8.25	-20
1	7	16.4	11.82	-28
2	0	4.76	6.24	31
2	1	6.0	7.62	27
2	4	11.6	8.86	-24
2	7	11.8	9.9	-16
3	1	5.57	8.09	45
3	4	8.24	8.96	9
3	7	9.43	8.33	-12
4	4	8.75	8.77	0
4	7	8.98	8.70	-3
5	7	5.82	6.34	9

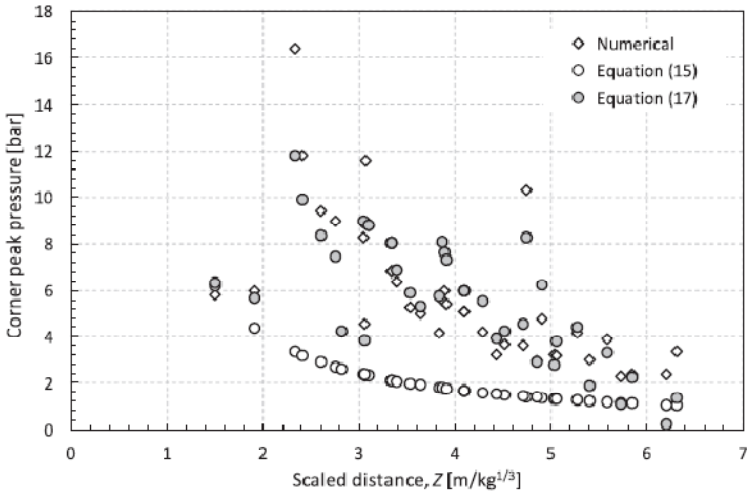

Figure 5.14 - Comparison between the numerical values and two different fits (Eq. 15) and (Eq. 17), for peak-pressures at corners

where the independent parameter is again the Z scaled distance. With eq. (5.15), (5.17) and (5.18) it is possible to cover most of the pressure distribution inside a closed unvented prismatic box.

Table 5.8 - Comparison between the peak pressures obtained numerically from equations (18)

Box	Position of Explosive	Z scaled distance [m/kg^3]	Sensor point	Pressure (Numerical) [bar]	Pressure (Eq. 18) [bar]	Error %
1	4	1.90	4	8.78	7.31	16.7
2	2	1.73	9	4.64	8.01	72.6
2	4	1.07	16	11.7	12.84	9.7
2	6	1.72	2	9.06	8.08	10.8
3	0	4.96	4	4.28	2.88	32.7
3	2	2.26	2	6.12	6.20	1.3
3	5	0.88	16	15.3	15.47	1.11
3	6	0.88	13	15.3	15.47	1.11
3	7	0.88	14	15.3	15.47	1.11
4	1	1.53	16	5.24	9.02	72.1
4	2	2.11	2	6.81	6.61	2.9
4	5	0.70	16	19.2	19.3	0.5
4	6	0.70	13	19.2	19.3	0.5
4	7	0.70	14	19.2	19.3	0.5
5	1	1.35	16	7.41	10.24	38.2
5	2	1.90	2	7.88	7.31	7.2
5	4	1.90	11	7.88	7.31	7.2
5	5	0.65	16	26.2	20.82	20.5
5	6	0.65	13	26.2	20.82	20.5
5	7	0.65	14	26.2	20.82	20.5

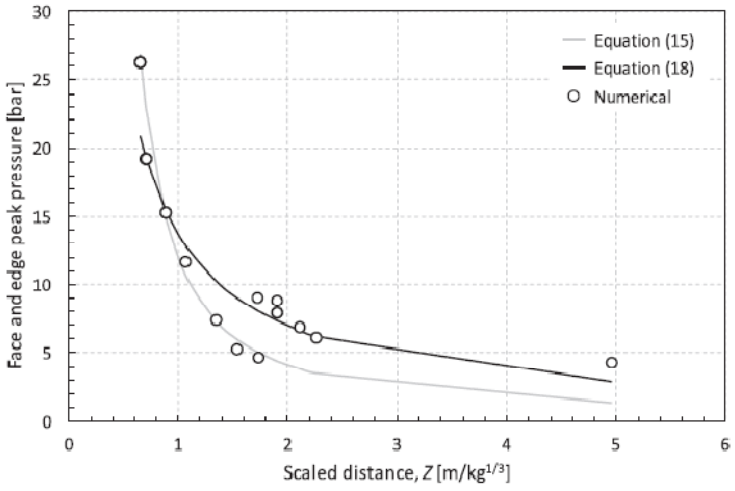

Figure 5. 15 - Comparison between the numerical values and two different fits (15) and (18), for peak-pressures at edges and face off-centred points

5.5.3. Description of results – Qualitative description

The cubic box pressure-time curve at the wall centre is shown in Fig. 5.16. Due to symmetry the results are the same for all faces and only one curve is represented. In this configuration the peak-pressure of the blast reflexion is higher than the direct shock wave reflected pressure. As the box shape is changed into a more slender shape (longer and narrower)) it is observed that the first blast reflexion gradually increases its strength, as shown in the pressure-time curve at the face normal to X axis for Box nº 5, and at the same time the first direct peak becomes lower, due to the increased stand-off distance. The increasing slenderness ratio also favours reflexions in the longer direction. Stronger reflected blasts are observed in the centre of the face normal to X and sometimes also in the adjacent sensors T18 and T19 for those cases where the explosive was moved to a position in front of those points (respectively positions 5 and 6). In the other directions the gradually shorter stand-off distance in the Z direction explains the rapid increase of the peak-pressure in the faces normal to Z while the peak values do not change significantly in the Y direction, whose width has been kept constant. At the vertex a strong reflexion was observed due to the simultaneously arrival of reflexions from all the three orthogonal directions. Even for non-cubic boxes the wave reinforcement is evident as shown in Fig. 5.17 showing the pressure distribution pattern at a certain time of the simulation, where the corners of the box nearer to the explosive are experiencing the largest pressures.

As the explosive is moved from its central position the phenomena becomes more difficult to understand but the shortest stand-off will generally dictate the highest peak-pressure. At corners a better correlation was obtained by also considering the influence of the angles between the line of sight from the explosive to the sensor and the main coordinate axis. The highest peaks were found for maximum angles around one radian. It is interesting to note that as the distance to the face normal to *Z* diminished, the peak moved from the centre point of the face to the edge (T2) which has a stand-off distance larger than the face centre point.

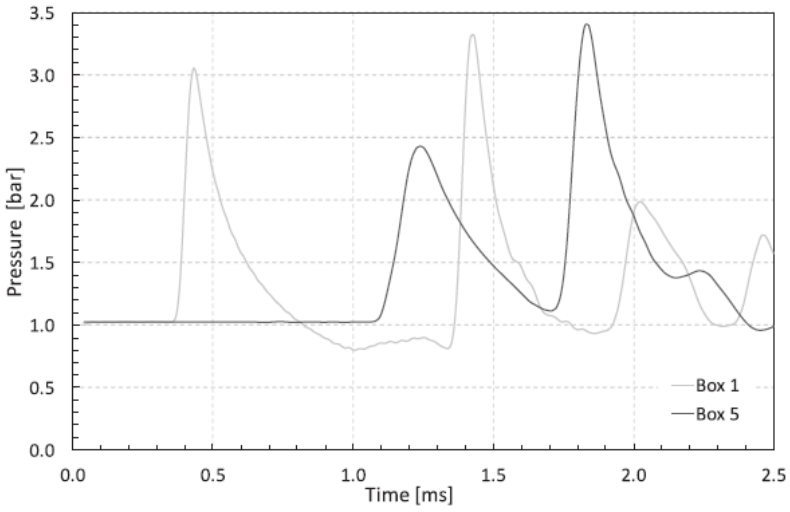

Figure 5. 16 – Pressure time history at the centre of the faces normal to x for boxes 1 and 5

From the above, three major observations emerged from the simulations: as a box becomes more slender the blast reflexions in the longer direction becomes more significant than the direct blasts; as the transverse dimension diminishes the edges will experience higher pressures than the faces perpendicular to that transverse direction; symmetry makes pressure at corners to be increased. In the remaining positions pressure will be mainly depend on stand-off distance.

Table 5.9 shows the positions and values of the maximum pressures for all boxes and explosive positions. In the right column the values of the maximum blast reflexion pressure has also been added as well as the sensor where it occurred in all cases when the peak-pressure of the blast reflexion was higher than the first peak. As it can be noticed in most cases the reflexions yielded pressures lower than the first direct peaks.

Table 5. 9 - Listing of the highest peak pressures recorded at each case analysed (Note that due to symmetry, only cases 1, 4 and 7 were considered for the cubic box nº 1)

Position Explosive	Box no	Z	Direct Blast	Reflected Blast
			P_{max} (Sensor)	P_{max} (Sensor)
1	0	4.74	4.80(3)	10.3(3)
1	1	1.35	7.47(7)	3.39(11)
1	4	1.90	8.78(4)	2.55(14)
1	7	2.33	16.4(3)	
2	0	4.90	4.76(3)	3.72(4)
2	1	3.89	6.00(3)	
2	2	1.35	8.00(1)	2.37(19)
2	3	1.07	11.7(5)	4.17(3)
2	4	2.16	11.6(3)	
2	5	1.07	11.7(16)	
2	6	1.72	9.06(2)	
2	7	1.72	11.8(3)	
3	0	1.81	5.24(5)	3.58(6)
3	1	3.87	5.57(3)	
3	2	2.26	6.12(2)	2.30(7)
3	3	0.88	15.3(5)	2.58(18)
3	4	3.04	8.24(3)	
3	5	0.88	15.30(16)	3.35(18)
3	6	0.88	15.3(13)	1.87(19)
3	7	0.88	15.3(14)	
4	0	1.62	6.61(5)	3.24(1)
4	1	3.91	5.40(3)	2.26(1)
4	2	2.11	6.81(2)	2.1(19)
4	3	0.79	19.2(5)	2.46(18)
4	4	3.10	8.75(3)	3.36(7)
4	5	0.70	19.2(16)	2.85(18)
4	6	0.70	19.2(13)	
4	7	0.70	19.2(14)	
5	0	1.35	8.14(5)	3.4(7)
5	1	1.35	7.41(16)	4.22(7)
5	2	1.90	7.88(2)	1.95(6)
5	3	0.65	26.2(5)	2.8(6)
5	4	1.90	7.88(11)	3.75(19)
5	5	0.65	26.2(16)	
5	6	0.65	26.2(13)	
5	7	0.65	26.2(14)	

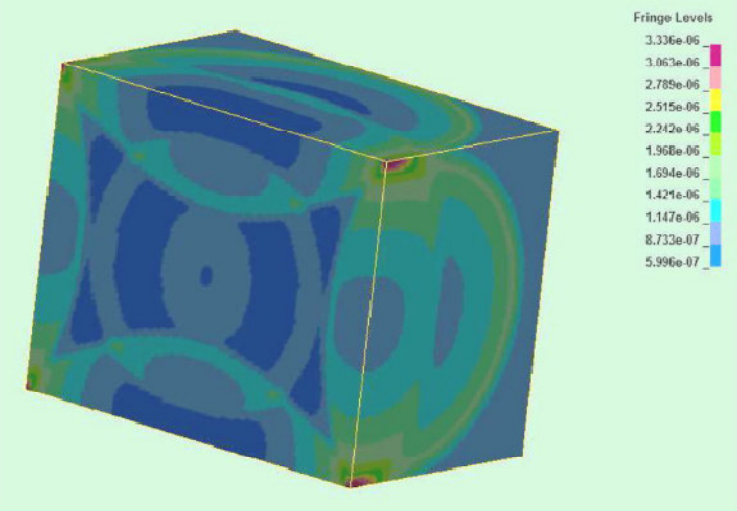

Figure 5.17 - Reflected wave pressure peak at corner (Tracer point 3) for Box nº 2 and explosive at mid-point of distance between the centroid of the box and face normal to Z(m.kg-1/3)

5.6. Conclusions

The validation studies showed that it is possible, in engineering problems, to obtain reasonably accurate numerical solutions for confined explosions by using the ALE methodology. However certain input choices will work better in certain problems and not in others. It remains difficult to define recommendations regarding the input parameters for ALE simulation of an arbitrary confined explosion. The present numerical calculations were performed with LS-DYNA and some of the parameters mentioned are specific for this hydrocode. However it is believed that some remarks may be useful even for the users of different hydrocodes. Users will have to carefully judge the choice of the simulation parameters available as guidance on this choice only comes from experience or available experimental data to compare with.

It has been seen that the direct shock wave reflected peak-pressures at the centre of walls of an unvented prismatic confinement subject to an internal explosion can be reasonably well predicted in terms of the stand-off distance by means of a modified equation (5.15) based on the work of Henrych (Henrych, 1979). The subsequent reflexions are more difficult to understand but in general their pressure intensity is lower than the first blast. However traditional empirical assumptions

regarding the decay of reflected peaks inside the enclosure (Dragos, et al., 2013) may not correspond to reality in some cases of interest, particularly in the case of slender boxes where some reflected peaks tend to be more intense. For corners, the angle between the stand-off direction and the main planes of the internal faces of the box correlates reasonably with the peak-pressures obtained. It is believed that these angles will contribute to the pressure enhancement effect observed in certain cases, which could not be explained by the stand-off or Z scaled distance only. Eq. (5.17) provided a fit for the maximum pressure at corners. For all other positions it was found that a better description of the peak-pressures could be obtained from a third fitting equation, such as eq. (5.18).

It has been observed that in terms of a pressure only analysis the contributions of blast reflexions are relatively unimportant although results show that in many cases reflexions may show higher pressure peaks than the first arriving waves.

As a closing remark it is important to remember that the present work has only addressed one family of boxes. Conclusions about the generality of the equations found still require the consideration of different box volumes for the same slenderness ratios.

Chapter 5

6. Blast loading of AA5083-H111 aluminium plates: Experimental and numerical analysis

Experimental work on blast loading of AA5083-H111 aluminium plates subjected to free air explosions is presented and discussed

6.1. Introduction

Investigations on the vulnerability of ships are unpractical to be carried out experimentally due to the destructive nature of blast load testing. A real structure has stiffeners, imperfections, weld defects, residual stresses and micro-structural changes in the weld heat affected zone. All these combined effects are extremely complex to model. The characterisation of these variables is outside the scope of this work and only unstiffened plates have been considered in the experimental setup. The good resistance-to-weight ratio and corrosion characteristics of AA5083 and AA5086 aluminium alloys makes them widely used materials in the shipbuilding industry, which favours the choice for one of these alloys. In the present Chapter square plates of AA5083-H111 aluminium alloy were exposed to the free air detonation of PG2, a military grade plastic explosive, where charge weight and stand-off distances were varied and resulting deflections compared with numerical predictions. The numerical simulations were obtained by using the commercial hydrocode LS-DYNA (Hallquist, 2006), a code specially dedicated to the analysis of high speed and very short duration transient dynamic phenomena. The simulation of highly dynamic problems is very demanding computationally and it was decided to use models as simple as possible since lengthy and complex calculations are unpractical for engineering purposes, particularly at design stages. From the wide range of available material constitutive models, the Johnson-Cook equation was preferred due to its simplicity and computational efficiency

in the high-strain rate loading regimes. For the finite element simulation of the detonation and resulting blast waves both a semi-empirical Lagrangian approach and an Arbitrary Lagrangian-Eulerian method were used and their results compared.

The aim of the work was to provide design engineers, particularly in the naval field, with a numerical tool that contributes for the analysis of the effect of blast loads on common naval grade aluminium alloy structures.

6.2. Previous work on the strength of plates under blast loading

The modes of failure of beams subjected to blast loads have been reviewed and described in Chapter 3, Section 3.3. Table 3.1 summarizes the relevant failure modes.

Although most of the above review refers to plates made of steel the effect of blast loads on aluminium structures have also been widely analysed. However published work on naval grade aluminium alloys such as AA5083-H111 is scarce and only a few can be found (Abdulhamid, et al., 2013) (Winzer, et al., 2011) . The preference of the investigators have been focused on high-strength aluminium alloys due to their suitability for ballistic protection (Borvik, et al., 2004) (Borvik, et al., 2004). This will be discussed in the next section.

6.3. The strength of aluminium alloy plates subject to blast loads

Research on aluminium plate response to blast loading is scarce. The few exceptions have considered the ballistic aptitudes of aluminium plating due to its very interesting strength-to-weight ratio, as explained in Chapter 3, Section 3.4.

One the most widely used constitutive models for aluminium alloys has been the Johnson-Cook model, already presented above but that is being reviewed here for the sake of clarity.

The JC constitutive equation can be written as

$$\sigma_{eq} = \left[A + B\varepsilon_p^n\right]\left[1 + C\,ln\left(\frac{\dot{\varepsilon}^*_p}{\dot{\varepsilon}_0}\right)\right]\left[1 - \left(\frac{T - T_0}{T_{melt} - T_0}\right)^q\right] \quad (6.1)$$

where σ_{eq} is the von Mises equivalent flow stress. The first term on the right side represents the quasi-static stress-strain relation at room temperature; the second term is the strain-hardening function and the third term introduces the temperature dependence in the stress-strain relation. The dependence on strain rate is expressed by the term $\dot{\varepsilon}_p^*$ which can be set to mean the effective total strain rate or the effective plastic strain rate, and is normalized to the quasi-static threshold strain rate $\dot{\varepsilon}_0$. T_0 and T_{melt} are respectively the room temperature and the material melting temperature. A, is the yield stress at a reference temperature, B is a strain-hardening coefficient and n is the strain-hardening exponent. C and q are material constants that represent the coefficients of strain-rate hardening and thermal softening, respectively. The equivalent flow stress is then the product of three factors taken independently without concern about strain-rate and temperature history effects: strain hardening, strain rate and the softening effect of temperature.

Table 6. 1– Definition of observed failure modes according to Jacob et al. (Jacob, et al., 2004)

Some modes of failure	Modes of failure Details
Mode I	Large inelastic deformation
Mode Ib	Large inelastic response with thinning at the boundary
Mode II-1	Tensile tearing at one of the borders
Mode Itc	Large inelastic response with thinning in the central area
Mode II*c	Partial tearing in the central area
Mode IIc	Complete tearing at the central area (capping)

In Chapter 3 some discussion on the effects of anisotropy were presented and was shown that the JC model worked well with moderately anisotropic materials (Borvik, et al., 2005). AA5083-H111 plates are delivered with very little temper which means that it will be treated to remove the strain-hardening due to the rolling manufacture process. It is this work processing that would give the material the

different behaviours along the rolling direction and the other two perpendicular directions. It may assumed that the simplifying assumption of isotropy behaviour will not affect results significantly.

6.4. Experimental set-up

A set of experiments were performed to investigate and understand the response of AA5083-H111 aluminium alloy plates under blast loading. The chemical composition of the allow is (in percentage) shown in Table 6.2.

Table 6. 2- Chemical composition of the AA5083-H111 aluminium alloy

Element	Al	Mg	Si	Ti	Cr	Mn	Fe	Cu	Zn
Composition [%]	96.9	2.7	0.3	0.01	0.07	0.4	0.4	0.05	0.07

The tests consisted of subjecting square plates of 400 x 400 [mm^2] with a thickness of 3.1 mm to a free air burst. The explosive used is PG2, which is a mixture of a polymeric plastic and RDX (Hexogen)[14]. The aluminium plates were mounted on a steel framed stand (shown in Fig. 6.1) made of 18 mm mild steel plates (see Fig. 6.1 and 6.2) and secured with 24 x M12 steel bolts. The bolts were all tightened with a torque of 100 Nm. As shown in Fig. 6.1 the explosive charges were of spherical shape and placed on stands made of polyurethane foam cut to four stand-off distances adjusted to give the following distances from the plate to the centre of the charge: 150, 130, 100 and 80 mm. The energy imparted on the plates was determined with the help of strain gages located on the steel frame. The detonations occurred at open air to avoid wave reflexions caused by space confinement. The soil was sandy which again absorbed shock waves and contributed to avoid unwanted reflexions.

A total of 15 experiments were performed, all under dry weather conditions and an ambient temperature of approximately 28º C. Table 6.3 lists the main parameters

[14] Unconfirmed information stated that the composition is 88% of RDX, 11% of plasticizer and 1% of lubricant and smelling agent.

defining the experimental program. All experiments took place in one of the Portuguese Navy explosives and demolition training sites.

Figure 6. 1- Test bench for the experiments showing an aluminium plate bolted to the steel frame. A polyurethane stand supports a PG2 charge (photograph taken before adding the detonator).

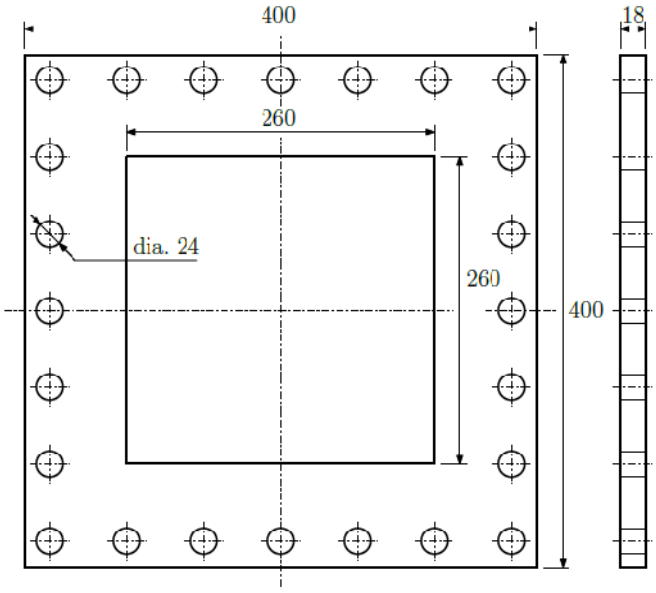

Figure 6. 2 - Dimensions of the steel frames used in the experiments. Thickness of the frames is 18 mm.

The technical description of the explosive refers a density $\rho = 1500$ kg/m^3 value that was adopted although weighing of a sample of the explosive yielded values slightly lower. The charges were shaped with a set of spherical moulds specially cut in a 3D printer and prepared to produce three sets of charges, of 40, 60 and 90 g. The electrical detonators used (L2A2) had an output charge of PETN (pentaerythritol tetranitrate) initiated by a primary charge of aluminium/lead styphnate/lead azide, and had a maximum charge mass of 1.49 g. The effect of this charge was not considered in the simulations but future work should analyse the effect of the detonator charge on the impulse imparted to the target. However this effect was found to be negligible when testing the detonator alone.

The effect of the bolts was modelled in a very simple way by modelling only the holes and fixing the outer circumferential nodes of the plate hole. This effect was shown to reproduce the constraint caused by the holes and the local numerical deformations were found to be similar to those observed experimentally as it can be seen in Fig. 14.

A straightforward relation can be derived between explosive impulse and maximum plate deflection (Hargather, et al., 2009) and it was attempted to measure the impulse imparted by the blast wave produced in each detonation by using strain gauges. These were glued on the vertical supports of the frame. Mathematically impulse is defined as,

$$I = \int F dt \tag{6.2}$$

and the force F was evaluated with the help of four HBM strain gauges fitted in a full bridge arrangement that allowed the recording of strains during each experiment. The set-up used to record the strains was composed of a signal capture chart NI PCI-6259, 16-bit, 1 MS/s (Multichannel) connected to the strain gauges by a signal processor SCXI 1000 and a SCXI 1520 universal strain gage input module connected to a PC through a SCXI 1314 block of connections. The position of the two strain gages can be seen in Fig. 6.3. Good results were obtained although special care was needed to handle the very large data files produced by the high sampling rate used. No pressure data was collected due to the absence of pressure sensors and so empirical relations involving explosive parameters such as the incident or reflected overpressures could not be derived.

However, the integral values shown in Fig. 6.4 were computed from the collected data files and a relation between the impulse and plate deflection was obtained. Table 6.3 presents the main parameters of the experiments and the corresponding results.

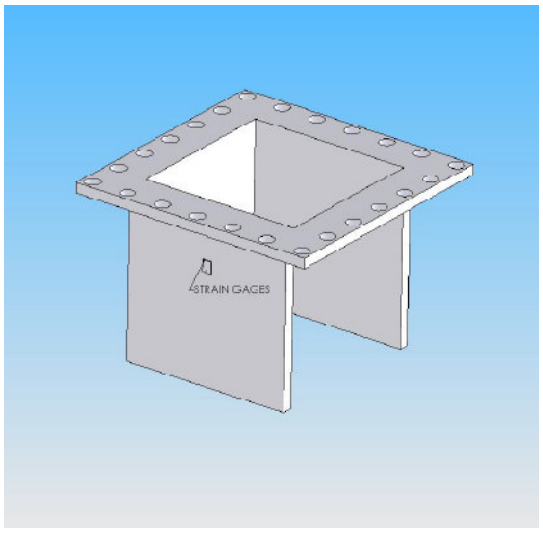

Figure 6. 3 – Set-up for the strain gages. Two sets were mounted one each side of the stand in a full Wheatstone bridge

Table 6 .3 – Free air blast midpoint deflection results

Test No	Mass of Explosive(g)	Stand-off Distance (mm)	Total impulse	Deflection (mm)
1	43	150	21.0	25.3
2	62	150	-	32.9
3	89	150	-	38.0
4	40	130	21.6	29.4
5	59	130	26.5	46.9
6	87	130	-	51.3
7	42	125	22.9	28.7
8	61	130	-	35.4
9	85	135	(c)	45.9
10	41	100	(c)	44.0
11	80	100	(b)	72.3
12	60	100	28.3	54.9
13	90	80	62.3	(a)
14	60	81	42.5	63.7
15	75	85	49.9	(a)

(a) Total rupture of the plate was observed (petalling and tearing off from the frame)
(b) Initial tearing type rupture
(c) Impulse results were meaningless

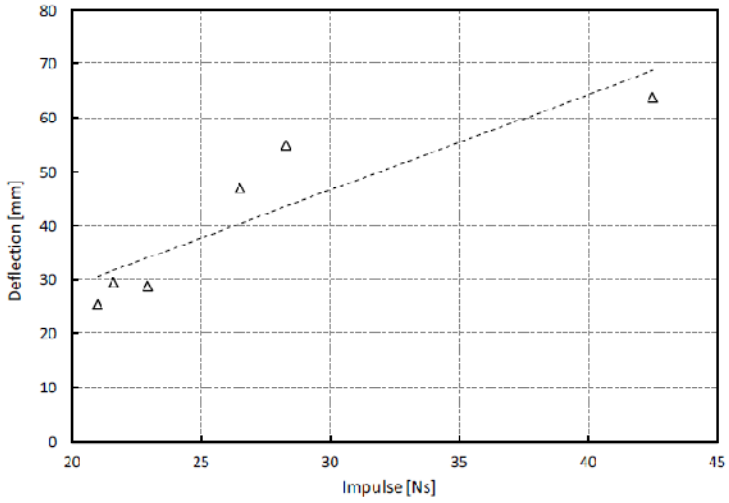

Figure 6. 4 - Relation between measured values of impulse and deflections at the mid-point of the plate specimens.

6.5. Analysis of experimental results

When a shock wave impinges upon the plate, a portion of its momentum is transferred to the plate, resulting in plate motion and deformation. The impulse may be obtained from a detailed characterisation of the energy characteristics of the explosive detonation or using a ballistic pendulum. In this experiment, however, the determination of the exact momentum imparted to the plate was not possible since part of the impulse was absorbed by the steel frame. The specimen carried only a part of the total impulse imparted to the ensemble. The amounts of the impulse received by plate and frame were not proportional to the relative exposed areas (Spranghers, et al., 2014) due to the proximity between the explosive and the plate. As such, the pressure distribution on the test rig cannot be assumed constant. Another source of error may be due to the fact that although the test rig had three plates supporting the frame only two of them were instrumented. The laboratory calibration accounted for this structural arrangement but it is possible that the *in situ* support conditions may have influenced some of the readings. The impulse readings versus the mid-point plate deflections are shown in Fig. 6.4, where deviations from a data fitting straight line confirms the possibility of set-up errors in some of the tests. Small differences were also registered when weighing the charges presumably because the warm ambient temperature made

the explosive material to become very sticky and difficult to handle which also may have distorted their spherical shape as they had to be placed on the foam stands by hand.

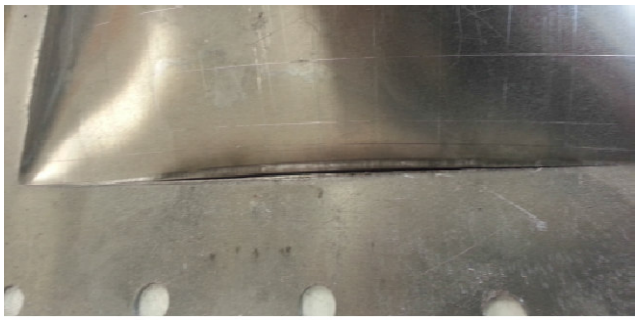

Figure 6. 5 - Mode II tearing at plate experiment 11.

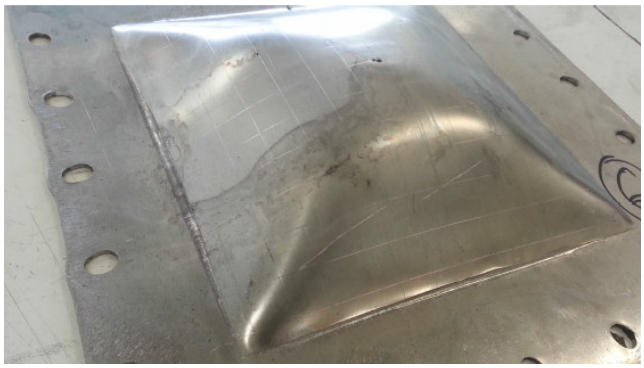

Figure 6. 6 – Thinning and stretching at the plate boundaries in experiment 6

Finally, it is important to mention that although the polyurethane stands were small, they may have slightly affected the blast parameters. However its effect in plate deformation, although not fully understood, was considered unimportant for the purposes of the project where this work is included. It was also observed that for measured impulses approaching 50 Ns and above, tearing off and rupture of the plate specimens occurred, as is shown in Fig. 6.5. The Z scaled-distance, which is defined below, showed a limiting value before rupture close to 0.195 and rupture happened in two tests both for Z values lower than this value. Tearing rupture at the edges of the

plate was observed for Z values lower or equal to 0.219. In other cases there was no tearing but a considerable thinning and stretching at the plate boundaries, as can be seen in Fig. 6.6. These modes of failure, as quoted by Jacob et al. (Jacob, et al., 2004), are listed in Table 6.1.

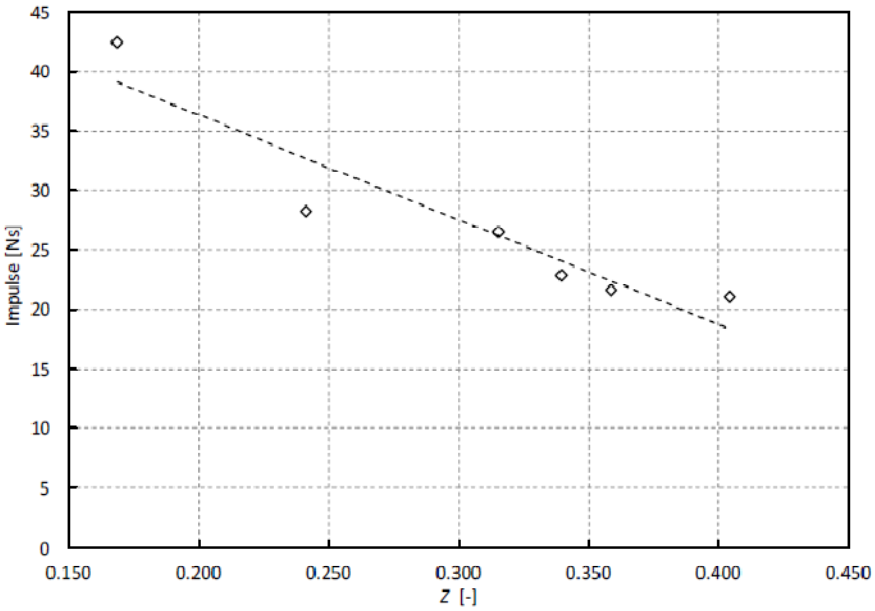

Figure 6. 7- Dependence of the measured scaled distance $Z = R/\sqrt[3]{W}$, where R is the stand-off distance and W is the mass of explosive (normally its TNT equivalent).

A very good correlation was found by plotting the scaled distance Z and the measured impulse, as can be seen in Fig. 6.7, which seems to confirm that the strain measurement device behaved well. Comparing Fig. 6.4 and 6.7 it can be concluded that the impulse showed a better correlation with the scaled distances than the measured deflections. This may be explained by the fact that, for most of the range of experiments (particularly the last four) the test conditions were close to near field range, where small deviations to the spherical shape of the explosive or the exact position of the detonation point may have induced differences in the results. In accordance with the US services manual (DoD, 2008) the present range of peak pressures may be considered low, which means that the structure's response will depend on both pressure and impulse, changing from pressure to impulse as the stand-off distance is reduced and the peak pressure increases.

The Z scaled has been defined in Chapter 2 and is given by,

$$Z = \frac{R}{W^{1/3}} \tag{6.3}$$

where R is the stand-off distance and W is the TNT equivalent mass of explosive. This scaled-distance concept states that two explosions using different explosive masses W_1 and W_2 at different stand-off distances R_1 and R_2, will yield similar overpressure curves at the targets when their Z parameter is the same. Use of empirical equations requires the use of equivalence TNT factors as most of them are based on TNT explosive data. At the time the simulations were performed there was no data available on PG2 but a similarity with the plastic explosive PE4 (or C4) has been assumed since both explosives are blends of RDX and a plasticizer. The equivalence factors for C4 are as shown in Table 6.4 and the calculated values of Z are listed in Table 6.5.

Table 6. 4- TNT equivalence factors for plastic explosive C4.

Explosive	TNT Equivalence	
	Peak pressure	Impulse
C4	1.37	1.19

More recently a report has been published including a TNT equivalence factor for PG2 of about 1.48 (Rubio, 2017). This could improve some of the results of the Lagrangian analysis but since the major objective of the analysis was to test and calibrate de ALE/FSI/Constitutive model this finding does not affect the major conclusions of the thesis and quality of the obtained numerical model.

Calculated values for deflections were obtained by using the dimensionless damage number of Nurick and Martin (Nurick, et al., 1989a) (Nurick, et al., 1989b). From the plot of measured impulses versus scaled distances, shown in Fig. 6.8, a linear fit for impulse was obtained allowing the full range of damaged numbers to be predicted from the experimentally obtained impulse data. Calculations were based on Eqs. (6.3) and (6.4) with the correction for localised loading as proposed by Jacob et al. (Jacob, et

al., 2004) based on a similar correction suggested by Nurick and Martin (Nurick, et al., 1989b) for circular plates.

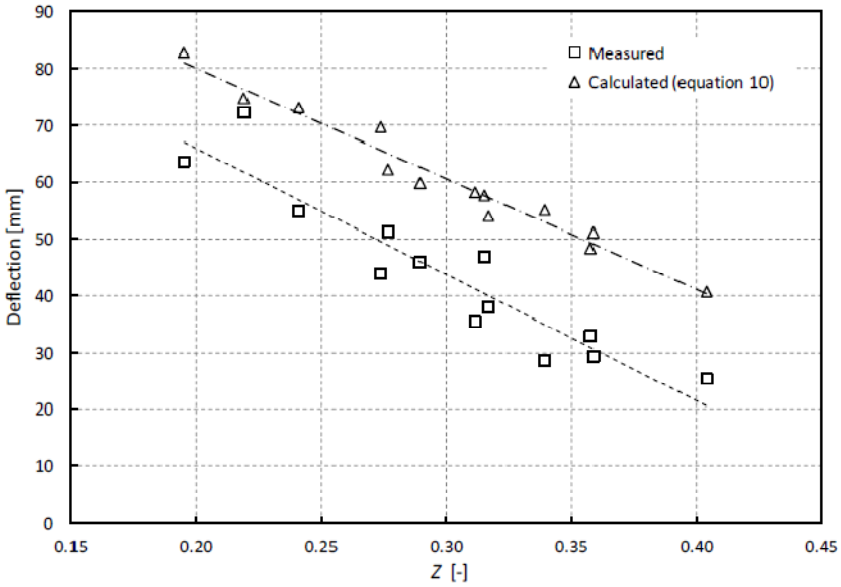

Figure 6. 8 - Relation between the mid-point deflections and the *Z* scaled distances.

The localized loading parameter ξ_{ql} (Jacob, et al., 2004) is

$$\xi_{ql} = 1 + ln\left(\frac{LB}{\pi R_0^{\,2}}\right) \tag{6.4}$$

which introduced into eq. (6.9) results in

$$\frac{\delta}{t} = 0.48\phi_q\xi_{ql} + 0.277 \tag{6.5}$$

where L and B are the length and width of the plate and R_0 is the charge radius. It was verified that eq. (6.10) overestimates the results when comparing with experimental data. However, the slopes of the two sets of data follow similar trends.

Table 6. 5 – Scaled distance *Z* parameter values for the explosive tests assuming a 1.19 impulse equivalence factor for TNT.

Test No	Mass of Explosive PG2 (g)	Stand-off Distance (mm)	Total impulse (N·s)	*Z*	Mode of failure
1	43	150	21.0	0.4040	Mode I
2	62	150		0.3576	Mode I
3	89	150		0.3170	Mode I
4	40	130	21.6	0.3587	Mode I
5	59	130	26.5	0.3151	Mode I
6	87	130		0.2769	Mode Ib
7	42	125	22.9	0.3393	Mode I
8	61	130		0.3116	Mode I
9	85	135		0.2897	Mode Ib
10	41	100		0.2737	Mode Ib
11	80	100		0.2190	Mode II
12	60	100	28.3	0.2410	Mode Itc
13	90	80	62.3	0.1685	Total rupture
14	60	81	42.5	0.1952	Mode Itc
15	75	85	49.9	0.1902	Total rupture

The maximum deflections (measured at the mid-point of the target plates) are plotted in Fig. 6.8 against the scaled distance, for both the measured and calculated values. However, since only one plate thickness was used in the experiments this data is insufficient to obtain a more general empirical deflection estimator expression. It can be noticed in Fig. 6.8 that there is an offset between the two sets of data. This has also been reported by other authors (Jacob, et al., 2007) which used successfully a correction for the stand-off distance. However, the same correction did not work with the present set of data , perhaps because that corrector was constructed for circular plates. It should be noted that the strain gages measured the total forces imparted on the apparatus but the plate deformation was only due to the fraction of the impulse being transmitted to the plate. It should nonetheless be noted that both sets of data show a similar trend.

Due to the small stand-off distances employed, the pressure on the plate was not uniformly distributed and in the centre, where the reflected pressure – and hence the impulse – was higher, the deformation showed sometimes a circular cap (see Fig. 6.9), corresponding to a thinning of the material indicating proximity to the onset of failure.

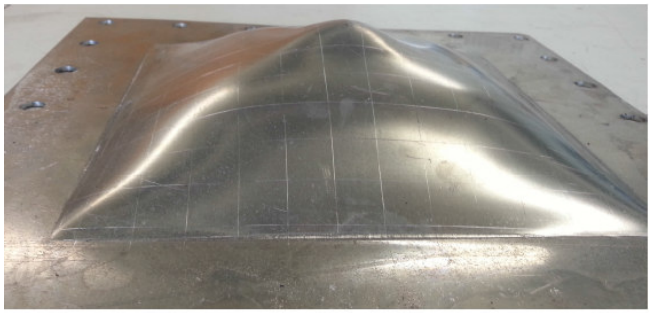

Figure 6. 9 - Illustration of the presence of a cap in plate specimens subjected to larger loading and closer stand-off distances.

6.6. Numerical results

Formulae for calculating the pressure resulting from a certain weight of explosive and its stand-off distance are available in the literature (Larcher, 2008). Kingery regression equations (Kingery, et al., 1984) are well reputed and are often used by researchers and they form the basis of the US Convention Weapons Effects Program (CONWEP) software. His report presented a curve fitting result from test data, ranging from less than 1 kg to over 40,000 kg of TNT. The data was fit by polynomial equations that represent the air blast parameters versus stand-off distance, in metres, for a spherical air-burst from 1 kg of TNT. Such parameters are the incident pressure, incident impulse, reflected pressure and reflected impulse ((UNODA), 2013). The implementation of this methodology in hydrocodes consists of applying a Friedlander type curve (such as the one shown in Fig. 2.13) derived from the data calculated using Kingery's polynomials, at each point of a target. Even though these equations were not intended to be an absolute standard but rather a comparison tool, many researchers often use them as a validation tool for numerical modelling. Their implementation in LS-DYNA (Randers-Pehrson, et al., 1997) was used in the present work through the function *LOAD BLASDT ENHANCED (LBE). Other solution methodologies are also available in the code such as the ALE (Arbitrary Lagrangian-Eulerian) (Souli, et al., 2000) (Mahmadi, et al., 2014) approach in combination with a coupled FSI (Fluid-Structure Interaction) technique, the Smooth Particle Hydrodynamics (SPH) method or even the Particle Blast (PB) techniques (Schwer, et al., 2015). In the present work only

the ALE approach was used to compare with the pure semi-empirical Lagrangian LBE analysis.

In the present ALE analysis the particular case of an Eulerian approach has been followed where the computational mesh, representing the ambient air, is fixed in space and the flow of the gaseous products of the explosion is obtained by solving the main balances equations of mass, momentum and energy. The integration of these equations is computationally demanding and a split approach has been implemented in LS-DYNA where each time-step is computed in two stages: a Lagrangian step and an advection step. In the Lagrangian step the stresses are calculated at the integration points and nodal accelerations, velocities and displacements are then obtained with an explicit time integration scheme. The mass is assumed to be lumped at the nodes, which leads to a diagonal matrix which simplifies the calculation of the accelerations.

In the second step the resulting distorted fluid mesh is remapped onto its previous position. An advection problem is then solved using a finite volume procedure. The state variables are mapped onto the fixed mesh. The impact of the mass of fluid on the the aluminium plate is simulated by a contact penalty algorithm between the fluid nodes and the plate nodes. It is important to note that no matching of nodes is required between the ALE and the Lagrangian parts to set-up this momentum transfer

An additional set of equations had to be considered to allow for the fact that when pressures are significant, volumetric deformations will be large and the hydrostatic component of the stress tensor becomes larger than the deviatoric stresses. As a consequence, an Equation of State (EOS), which is a relation between pressure, volumetric deformation and energy is necessary. To simulate the high explosive detonation process the Jones-Wilkins Lee EOS is normally used, where *A, B, R_1, R_2, E* and ω are empirical coefficients to be input.

$$P = A\left(1-\frac{\omega}{R_1 V}\right)e^{-R_1 V} + B\left(1-\frac{\omega}{R_2 V}\right)e^{-R_2 V} + \omega\frac{E}{V} \qquad (6.6)$$

For air a gamma law modelled by a linear polynomial equation (linear relative to the internal energy *E*) has been used:

$$P = C_0 + C_1\mu + C_2\mu^2 + C_3\mu^3 + E(C_4 + C_5\mu + C_6\mu^2) \qquad (6.7)$$

where $\mu = (\rho / \rho_0) - 1$ and ρ / ρ_0 is the ratio of current to initial (reference) densities. Coefficients C_2 and C_6 are set to zero if $\mu < 0$. For an ideal gas the expression is reduced to

$$P = (\gamma - 1)\frac{\rho}{\rho_0} E_0 \qquad (6.8)$$

as all coefficients will be made equal to zero except $C_4 = C_5 = (\gamma - 1)$ and $\gamma = c_p / c_v$ is the ratio of specific heats.

To complete the simulation the properties of both materials (the air and the explosive) need also to be input. Data was taken from Tables 4.3 and 4.4 for the EOS of air and C4 and 4.6 and 4.7 for the air and explosive material properties used in the simulations. The material properties of air are just its density. A value of 1.204 x 10^{-3} g/cm3 was adopted in the simulations The EOS of air is defined by setting in eq. (13) the coefficients C_4 and C_5 equal to 0.4 and all the others as zero and the specific energy E = 2.533 bar.

The finite element model developed is shown in Fig. 6.10 where only one quarter of the plate and frame that constitutes the test bench have been represented. Two sets of simulations were used: with shell and with solid elements. The shells were modelled with 1 mm elements and the solid elements used 2 mm elements and 5 layers through the thickness.

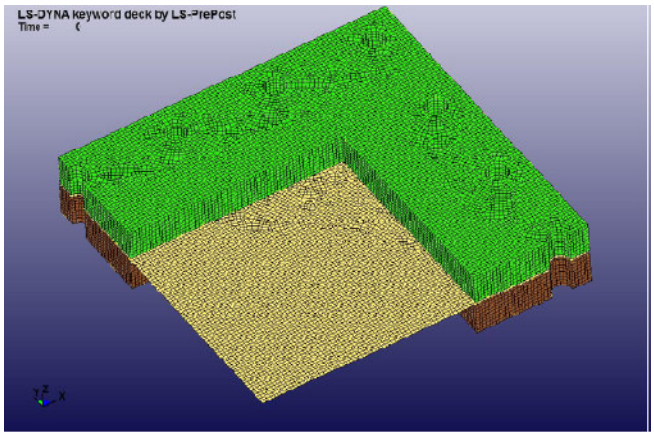

Figure 6. 10 - Finite Element Model of one-quarter of a plate bolted to a steel frame exposed to the detonation of a high-explosive charge of PG2.

Symmetry boundary conditions were applied at the cut edges of the plate to ensure the similarity of the displacement field between the one-quarter model and the full representation of the test bench. The explosive is located on the *z*-axis and the origin of coordinates was placed at the vertex of the quarter-plate model, as shown in Fig. 6.10. Deflections were measured and compared with the numerical results along the *x*-axis of symmetry in discrete points at 20 mm intervals. The outer nodes of the plate holes have been constrained to simulate the effect of the presence of the bolts, which were also assumed as rigid. A penalty contact has been defined between the frames and the plate to function in conjunction with the blast loading of the frame. The steel frame was initially modelled as an elastic material but it was found that a considerable simplification could be adopted without changing the plate deformation results by assuming the frame as rigid. This speeded-up the solution considerably without affecting the results. Two sets of simulations were used: with shell and with solid elements. The use of solid elements yielded small differences in the results, mostly closer to the experimental data. In both cases the JC material model was used, albeit without temperature effects (Johnson, et al., 1983) Calibration parameters were taken from published data on this alloy (Winzer, et al., 2011) and are reproduced in Table 6.6. The selected shell element was the Belytschko-Lin-Tsai which is based on the Reissner-Mindlin kinematic assumption and uses one point integration for efficiency.

Table 6. 6– Johnson-Cook model parameters for AA5083-H111 (Winzer, et al., 2011)

JC parameters	*A* (MPa)	*B* (MPa)	*n*	*C*
AA5083-H111	147.0	349.2	0.396	0.104

.

Friction has been defined between the frames and the plate but it was found that it had no effect for high z scaled distances and underestimated the response for low z scaled distances. The same happened when preloading the apparatus (applying to the frames a normal load equivalent to the effect of the applied torque in all bolts). As the applied torque to the bolts was low, the friction force was much less significant than the bolts in restraining the plates. As explained before the main constrain has been defined as the plate restriction at the holes due to the presence of the bolts which were assumed

to b rigid. This assumption was shown to work well when compared with the observations in the field as shown in Fig. 6.14.

It was decided to use 5 mm element for the ALE mesh after a convergence check where meshes of 2.5, 5 and 7.5mm were considered. Table 6.7 shows the effect of this comparison on the plate deflexion of experiment no 1. Taking in consideration the variation in results and the CPU time the option for the 5 mm mesh was the more rational.

Table 6. 7– Comparison between different element sizes of ALE mesh in the calculation of plate deflexion from experiment no 1 and CPU time in a i7-2700K CPU @ 3.50 GHz machine

	2.5mm	5mm	7.5mm	Experiment
Δ (mm)	21.1	21.4	20.7	25.3
CPU hr	>12 hr	2.5 hr	1.5 hr	

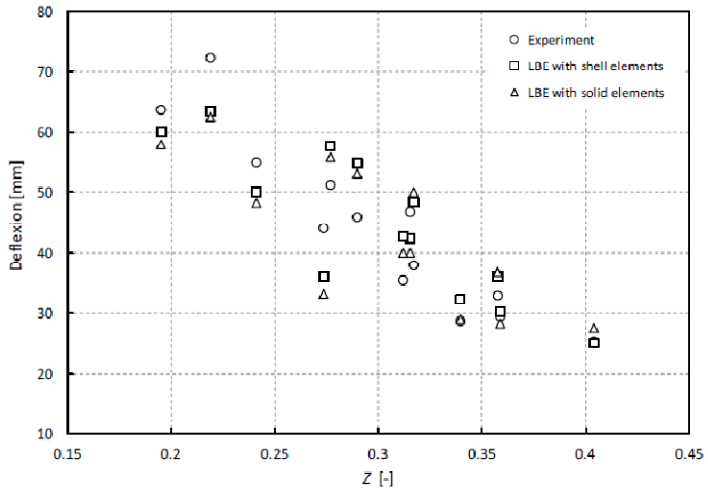

Figure 6.11 - Results of Lagrangian FEA using the LOAD BLAST ENHANCED function of LS-DYNA.

A 2D to 3D mapping technique (Aquelet, 2008) has been used where the first phase of the simulation has been performed with a highly refined mesh of 0.5 mm. In this mapping technique, in a first phase a 2D simulation is run where the detonation phenomena and the pressure wave formation is modelled using a highly refined mesh.

The results from this run are then used as the input for the subsequent phase, where the nodal velocities, accelerations and masses and element properties are mapped on a coarser 3D mesh and the simulation will continue from that point. This speeds up the overall simulation time since the most refined mesh is used only in the first 2D phase. The explosive spherical portion has been modelled in 2D phase by using the command "VOLUME FRACTION GEOMETRY which consists of parametrically defining the volume to be occupied by the explosive within the air mesh. For both air and gaseous products of detonation it was necessary to input the appropriate material parameters and to define the respective equations of state.

In the three planes of symmetry nodal velocities normal to the planes were prevented. In the outer boundaries no constraints were introduced to avoid unwanted reflections. Ideally these should have been placed as far away possible but this would turn the simulation computationally untractable. Results of the Lagrangian LBE analysis are presented in Table 6.8.

Table 6. 8 – Results for maximum mid-plate deflexions obtained from FEA (LBE).

Test No	Mass of Explosive PG2 (g)	Stand-off Distance (mm)	Mid-plate deflexion (measured (mm)	Mid-plate deflexion (LBE-shell) (mm)	Error for LBE-shell (%)	Mid-plate deflexion (LBE-solid) (mm)	Error for LBE-solid (%)
1	43	150	25.3	25.0	-1.2	26.9	8.3
2	62	150	32.9	36.6	11.2	37.0	12.4
3	89	150	38.0	48.5	27.6	49.7	30.8
4	40	130	29.4	30.2	2.7	28.2	-4.1
5	59	130	46.9	42.3	-9.8	39.5	-15.8
6	87	130	51.3	57.2	11.5	55.4	8.0
7	42	125	28.7	32.4	12.9	28.4	-1.0
8	61	130	35.4	41.7	17.8	40.7	15.0
9	85	135	45.9	53.5	16.6	53.2	15.9
10	41	100	44.0	36.0	-18.2	33.2	-24.3
11	80	100	72.3	63.6	-12.0	62.6	-13.4
12	60	100	54.9	49.7	-9.5	47.8	-12.9
13	90	80	-	-		-	
14	60	81	63.7	59.6	-6.4	63.9	0.3
15	75	85	-	-		-	

It can be noticed that some results are very close to the experiments but others show large variations. As mentioned above the LBE method suffers from uncertainties in near field conditions, probably because, in such conditions, the expanding reaction gaseous products will also hit the plate and this is not accounted by the empirical LOAD BLAST methodologies. However, all the simulations were within the limits of the method that states that the stand-off distance shall not be less than three times the radius of the explosive charge. The LBE method under-predicted about half of the results and a significant change in the error distribution was observed between shell and solid elements. Overall the errors were reasonable bearing in mind the extreme complexity of the explosive phenomena and the fact that the explosives were handled in real field conditions rather than laboratory conditions. The C4 plastic explosive has two TNT equivalence weight factors: 1.19 for impulse and 1.37 for pressure (Dusenberry, 2010), which have been both used or averaged in the literature, depending of the author. CONWEP for instance averages both factors (Borenstein, et al., 2013) . In the present work, the 1.37 factor gave the best results and was used in all Lagrangian LBE simulations. Examples of LBE results for shell and solid plate elements are shown in Fig. 6.11.

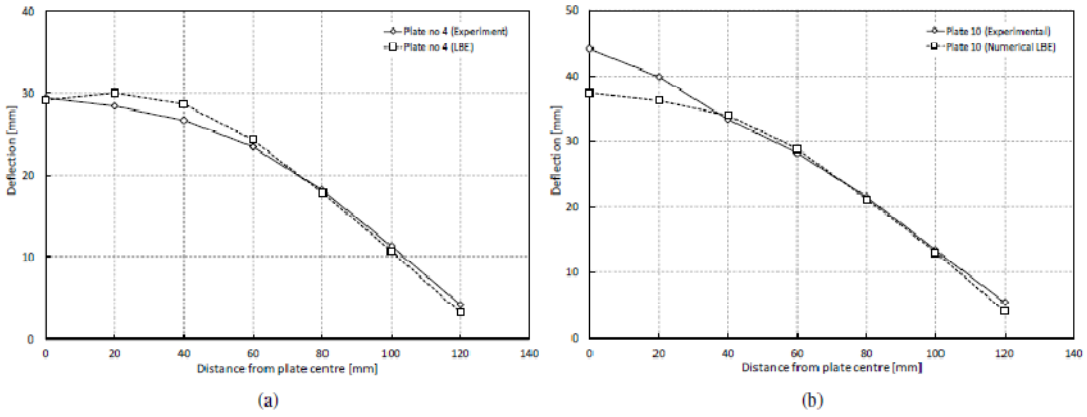

Figure 6. 12 – Comparison between the deformed shape amd the numerical LBE prediction: (a) plate 4 and (b) plate 10

Fig. 6.12 shows results for plate 4, where a good agreement is observed between the experimental and the numerical deflexions. However, a worse agreement can be seen for the deflexions of plate 10, where the numerical model could not reproduce the existing cap at the centre of the experimental plate. A possible way to consider the

effects of near field explosions is to use ALE techniques where a physical model of the gaseous products of the explosion being advected through the mesh elements and impinging on the target plate may provide a more detailed description of the blast phenomena. However, the ALE procedure has many more parameters to define and the running times of the simulations are often one order of magnitude longer for the same degree of mesh refinement (an LBE simulation took less than 10 min whilst an equivalent ALE analysis took about 90 min to run, using the same machine Intel® Core™ i7-2700K CPU @ 3.50 GHz).

Comparing the three numerical models: LBE with shell or solid elements and ALE with shell elements (see Fig. 6.13), it can be seen that both the Lagrangian LBE and ALE methods using shell elements provided reasonably close results. For higher scaled distances, the solid elements overestimated the deflections while shell elements underestimated these. As the scaled distance is reduced the opposite trend is observed. For smaller scaled distances a better proximity is observed between the three FEA methods and the measured values except when there exists a pronounced cap at the centre of the plate. The degree of approximation varies along the range of experiments but the best approximation was observed in the intermediate range of scaled values. For instance plates 4, 5, 12 and 14 show a very good agreement between the experimentally measured and the numerically obtained result with shell elements. Globally, it may be concluded that all results may be considered qualitatively good. ALE results agreed well with the empirical blast load procedure and it may also be concluded that the extra effort of modelling with solid elements did not pay off in terms of accuracy. None of the simulations was capable of reproducing the cap deformation which depends on the constitutive equation and this has been kept unaltered in all simulations.

The use of solid elements yielded small differences in the results, mostly closer to the experimental data. In both cases the JC material model was used, albeit without temperature effects (Johnson, et al., 1983). Calibration parameters and the true stress-strain curves at various strain.-rate regimes were taken from published data on this alloy (Winzer, et al., 2011) and are reproduced in Table 6.6. The selected shell element was the Belytschko-Lin-Tsai which is based on the Reissner-Mindlin kinematic assumption and uses one point integration for efficiency.

For close-range explosions ($Z < 0.4$ m/kg$^{1/3}$) the target may be inside the fire-ball of the explosion which raises doubts about the adequacy of methods based on the Kingery and

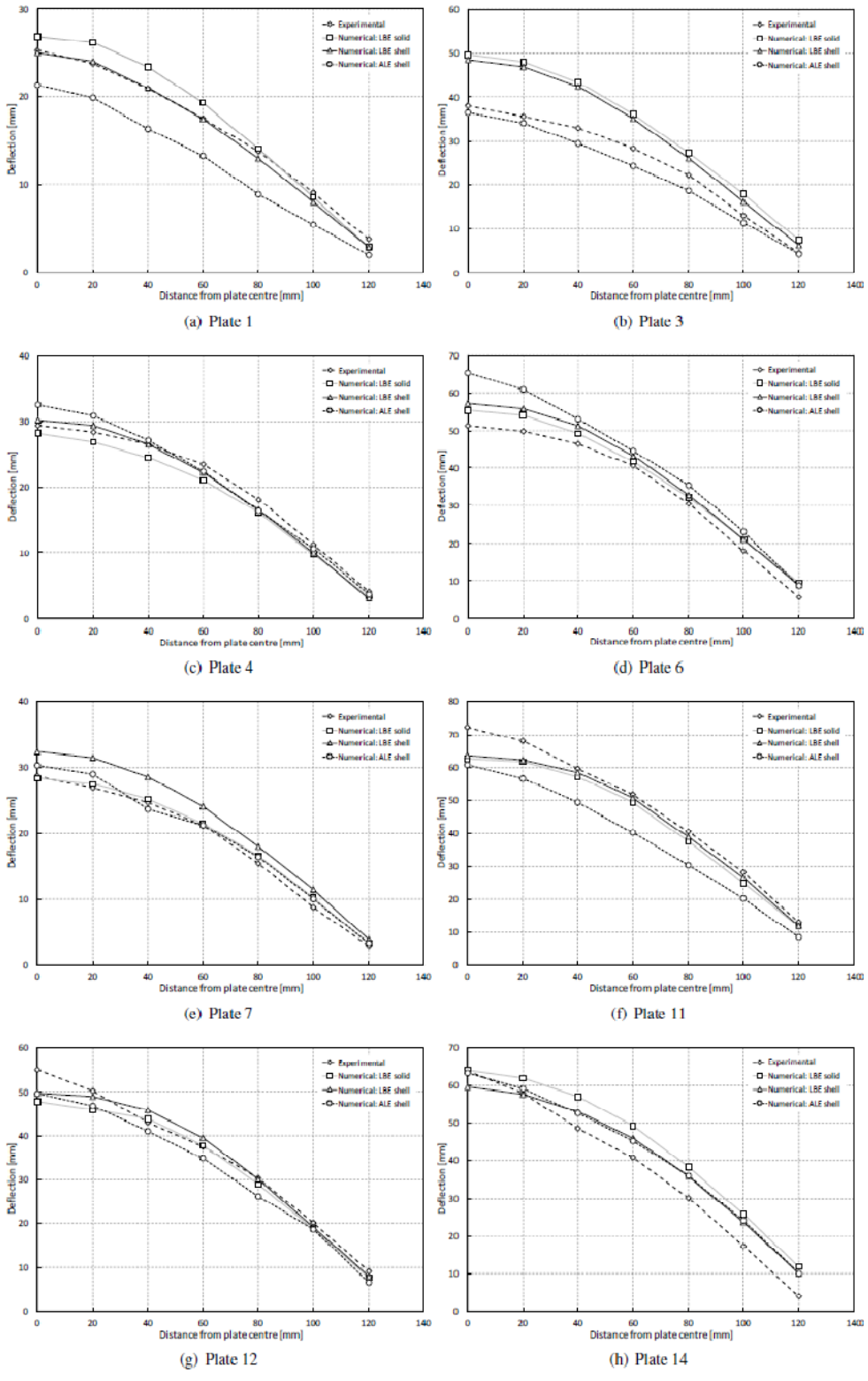

Figure 6. 13 – Comparison between the three FEA approaches and the measured deflexions.

Bulmash semi-empirical predictions, like the LBE approach existant in LS-DYNA, which do not cover this range. However, Rigby (Rigby, et al., 2014) conducted near-field tests and concluded that CONWEP gave accurate predictions at very short Z scaled distances.

To consider the effects of near field explosions ALE techniques have been used since the underlying physical model is much closer to reality than the empirical load-blast approach. Some examples of the use of ALE to simulate near-field explosions can be found in the literature (Rigby, et al., 2014) (Cheng, et al., 2013) (Shin, et al., 2015) (Shin, et al., 2014).

For the ALE mesh the results obtained were generally underpredicted and no significant differences were obtained by using a more refined mesh except for the shortest stand-off distance, case 14, where a 2.5 mm mesh gave a plate deflection of 63.2 mm which is a much better result than that produced by the 5 mm mesh. This is an aspect to be investigated further.

Some other features could be captured by the FEA such as the thinning at the plate boundaries as shown in Fig. 6.14, where the FEA results compared well with observations. High shear stresses will develop at the edges of the plate due to the large lateral deflection caused by the applied blast on the plate. This will lead to large strains at the edges, that may initiate tearing, while at the bolt holes tensile stresses resulting from the plate in-plane stresses cause plastic strains that are visible both in the photograph and in the simulated results. The red coloration indicates the areas of high shear stress in the plate (output indicated a shear stress of approximately 70 MPa).

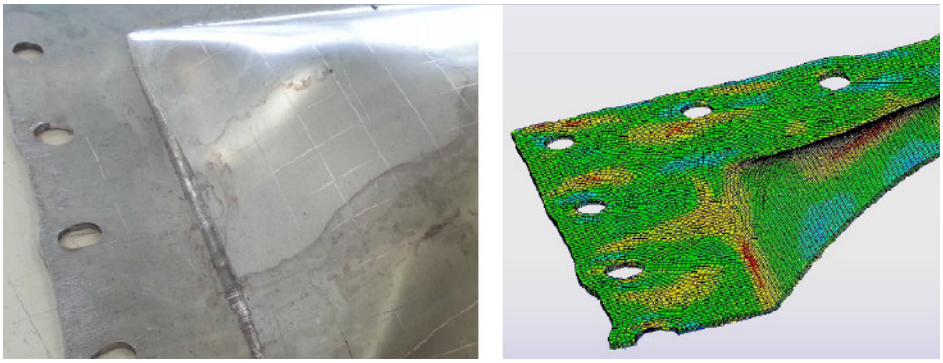

Figure 6. 14 - High localized strains at the edges and holes of the plate samples both observed and simulated, for plate 6.

Table 6. 9 –ALE shell results for plate maximum deflection.

Test No	Mid-plate deflexion (measured(mm)	Mid-plate deflexion (ALE-shell)	Error for ALE-shell (%)
1	25.3	21.1	-16.6
2	32.9	28.3	-13.9
3	38.0	37.1	-2.4
4	29.4	3.4	10.2
5	46.9	43.2	-7.9
6	51.3	53.9	2.6
7	28.7	25.6.	-10.8
8	35.4		
9	45.9	43.0	-6.3
10	44.0	36.0	-18.2
11	72.3	58.5	-19.1
12	54.9	51.3	-3.6
13	-	-	
14	63.7	56.2	-11.8
15	-	-	

6.7. Concluding remarks

Experiments were performed by subjecting square plates of AA5083-H111 aluminium alloy to blast loads resulting from close detonations of spherical charges of PG2 plastic explosive to obtain data that could be used to calibrate a constitutive model for that alloy. An extensive set of simulations using the two more commonly used approaches (empirical and physically based) was performed in order to obtain a suitable constitutive model that could be used in the next stages of an ongoing study requiring simple, fast but accurate solutions. The Johnson Cook model was selected due to its simplicity and because calibration data is available in the literature for a large number of engineering materials.

It was observed that very similar results were obtained within a reasonable approximation for engineering purposes by using both a Lagrangian approach based on a CONWEP type routine implemented in LS-DYNA and an Arbitrary Lagrangian-Eulerian technique combined with shell elements. Solid elements required significantly longer

computation times and the results were not found to be better than those obtained with shell elements. The differences between measured and numerical values were mainly observed on the plates that were exposed to the lower scaled distances, i.e., that were tested closer to near range conditions. In these plates the deformations showed a spherical cap at the centre of the plate that was not predicted by the constitutive model. This suggests that a more complex constitutive model should have been used if a precise prediction of the deformed shape had to be obtained. Also the handling and shaping of the explosive charges must be improved as this may also have contributed for some scatter obtained in the results.

It can be concluded that the ALE technique combined with a Fluid Structure Interaction mechanism provides reliable and reasonably accurate engineering results for the response of structures to blast loading. The use of shell elements proved to provide reasonable results with the advantage of being much faster than by using solid plate elements. Alternatively, the use of a Lagrangian LBE analysis also proved to be very efficient in terms of computational effort and accuracy of results. The techniques could be used in the design stages of structures exposed to the risk of blast loads with a minimum input effort.

Chapter 6

7. Blast wave transmission between two adjacent confined compartments

The more complex subject of a confined explosion rupturing a boundary and transferring some of its blast energy to the adjacent compartment is addressed both experimentally and numerically. Results and predictions are presented and discussed.

7.1. Experimental set-up

An explosion in a confined space may cause the rupture of one or more of its causing damage to the adjacent compartments. The aim of this work shall be to model the phenomena in order to be able to assess this damage and thus to be able to understand the risk of damage and injury in compartments adjacent to the hit compartment. Generalizing for all adjacent compartments, the lethal or destructive radius can be established for defined types of weapons assisting designers in setting risk mitigation measures or establishing vulnerability predictions. This is of a decisive importance in naval vessels and leading navies have been studying the subject since WWII. Unfortunately, such work has been mostly classified and thus not been made available to the public. The present contribution intends to show how modern hydrocodes can be used to make studies of a similar nature but on smaller patrol vessels involved in law enforcement or force and harbor protection missions, where the possibility of facing enemy fire has been increasing in recent times.

The simulation of the internal blast pressure fields that results from a detonation inside an adjacent closed compartment is the subject of this Chapter and one of the

objectives of the present thesis. As far as the author knows there has been no published analysis as such until the publication of this thesis.

A set of field tests comprising explosions of spherical PG2 charges, a plastic explosive compound presented in Chapter 6, has been performed using the apparatus shown in Fig. 7-1. It consisted of two boxes of mild steel built from 16 mm steel plate, separated by a 3 mm AA5083-H111 plate firmly framed between the two boxes by 14 bolts of 13 mm diameter. This plate will be from now on referred as Plate 1.

Spherical charges of PG2 were placed inside the first box, standing on polyurethane blocks cut to pre-defined stand-off distances. The box was then tightly closed and the explosive detonated. A small groove was cut on the cover of the topmost flange of the apparatus to allow the passage of the detonator's electric wire. This small groove also allowed the venting of the chamber after the explosion to permit its safe opening.

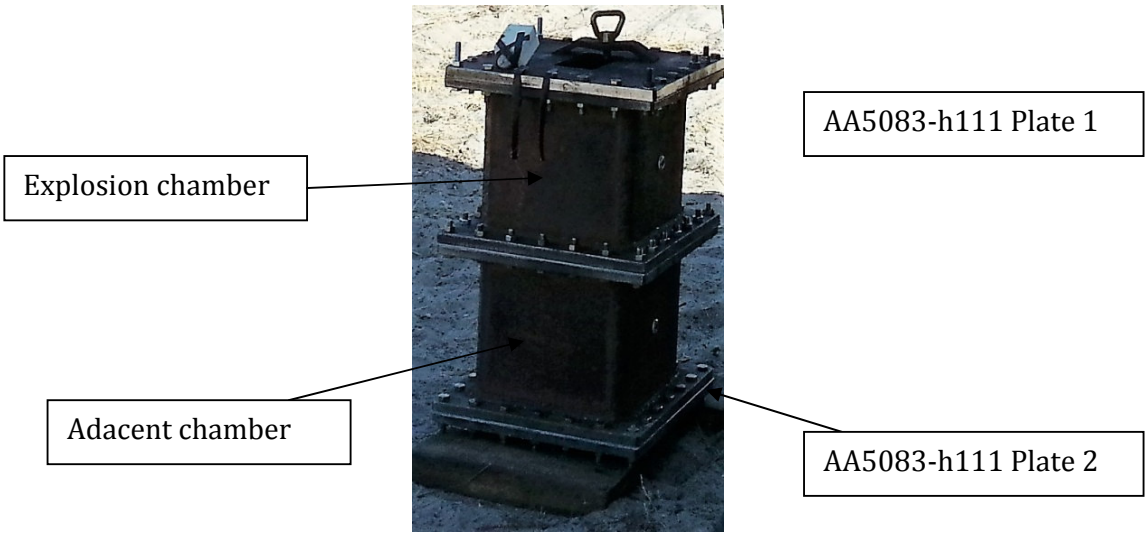

Figure 7. 1 – Testing device with two closed chambers separated by an aluminium plate to be deliberately ruptured. In the bottom a second aluminium plate acts as witness plate. On the top the cover plate has a movable opening that can be tightly closed and secured.

The charges were set to cause rupture of the dividing aluminium alloy plate, Plate 1, allowing some blast energy to pass to the second box. The bottommost plate, which will be designated by Plate 2, was made of the same material and had the characteristics of Plate 1 and has also been bolted to the outer frame of the second box to act as a witness plate. Its deformation was expected to give an indication of the

energy of the blast that passes through the ruptured plate. The main aim of the experiment is to understand the amount of damage that can be imparted to the compartments adjacent to one where a confined detonation takes place. The plates have been cut from the same AA5083-H111 aluminium alloy plate that was used in the experiments described in Chapter 6.

Two Piezo-Electronics type113B03 pressure sensors were fitted, one in each of the two boxes, both placed along the same side of the apparatus. The sensor range goes up to 103420 kPa, with an output of about 0.06 pC/kPa. A KISTLER 5070 Multichannel Charge Amplifier converted the charge output from the sensor into a voltage that was read by a National Instruments BNC 2110 data logger. The output was registered and later analyzed in a computer. However, a software issue prevented the use of the data acquisition system in the first two days and finally when the problem was solved an hardware malfunction of one of the sensor connections limited the readings to one channel instead of the two that were planned. The problem was circumvented by alternating the reading connection between the two sensors in repeated experiments. This allowed the collection of the pressure data in both chambers for a similar charge detonation but the time relation between both curves was impossible to capture. However, this procedure did not allow a comparison in time of the pressure curves in both chambers not allowing a measure of the elapsed time between the explosive blasts within the first and the second chambers. This time interval would provide an indication of the response of the first plate and the importance of afterburning in the failure of plate 1. The recognition of the importance of this information led to a third session of experiments which took place six months after the second session. This time good readings were obtained from the two sensors simultaneously.

7.2 Experimental results

A total of 26 tests were performed in the explosive test range of the Portuguese Navy. Due to the operational engagements of the military personnel involved and the demolition and mining training courses scheduled for the test area, there was a time constraint which limited the time available for the program of tests. From these, 22 tests

were performed on the second session of experiments on August 2016 and the remaining 4 about 6 months later in February 2017. Both sets of experiments were performed under good weather conditions although the ambient temperature was different (28ºC in August and 18ºC in February)

It was observed that the confinement had a strong enhancement effect in the damage imparted to the aluminum Plate 1. From the first phase of tests (Chapter 6) it was observed that tearing was initiated with a charge of 80 g at a stand-off of 10 cm and complete tearing at the four plate edges occurred for 90 g of explosive and a stand-off of 8 cm. However, within the confinement a complete tearing of the four edges occurred at the first experiment with a charge of only 40 g at a stand-off of 10 cm and even Plate 2 had three of its edges completely torn.

It was also observed that for stand-off distances above 4 cm Plate 1 would either tend to have two opposed edges completely torn out, or would remain deformed without rupture (Mode I damage) depending on very small variations on the weight of explosive. Slightly above 25 g complete tearing of two or three edges was observed but slightly below that value no rupture was observed. This showed that in a confinement the variation between the whole range of modes of failure happens in a very abrupt way with the weight of explosive. A compilation of the main parameters and results obtained in the series of tests is shown in Table 7.1 where the centre plate deflections of Plate 2 have been added. The third series of experiments have been added to the table under the order numbers 23 to 26.

The values indicated for stand-off distances correspond to the height of the polyurethane stands. Contrary to what has been adopted in the previous Chapter, where the indicated stand-off distances correspond to the sum of the height of the polyurethane stands plus the radius of the spherical charge, this time it was decided to cut the stands with integer values in cm. In this series of experiments a nearly constant mass of explosive was used together with a fixed stand-off distance. However, for simulation purposes the correct value of the charge radius is required to allow the definition of the point of detonation. This raised the need to confirm the specific mass of the explosive which varies accordingly to the source. From the manufacturer a value of 1.5 g/cm^3 was obtained and from measurement a value of about 1.37g/cm^3 was determined.

Table 7 .1 –Results of experiments of confined explosions in a double chamber divided by an aluminium plate diaphragm. The experiments considered successful are highlighted in yellow

Exp. no.	Mass of explosive (g)	Stand-off dist (cm)	Pressure peak of chamber 1 (MPa)	Pressure peak of chamber 2 (MPa)	δ Plate 2 (mm)	Damage of Plate 1
1	40	10				Complete tearing of four edges
2	20.2	10				Incomplete burn. Test disregarded.
3	20	9				No detonation
4	30.6	8			55.3	Complete tearing of four edges
5	31	11				Complete tearing of four edges
6	30.3	9			54.2	Complete tearing of four edges
7	25.1	8				No rupture
8	25.1	6				No rupture
9	25.1	4			46.7	Complete tearing of two edges
10	**22.0**	**4**			**38.5**	**Rupture of centre cap**
11	20.0	4		4.2		No rupture
12	**23**	**4**		**2.0**	**46.4**	**Petalling**
13	23	5	7.9			No rupture
14	25	5	5.6			No rupture
15	22	4	7.7			No rupture
16	**22.5**	**4**	**8.3**		**39.5**	**Rupture of central cap**
17	25	4	6.5		47.7	Complete tearing of two edges
18	**22.5**	**4**			**39.2**	**Rupture of centre cap**
19	21.5	4		0.24		Tearing of one edge
20	**23**	**4**		**1.6**	**40.2**	**Rupture of centre cap**
21	**23.5**	**4**		**3.3**	**50.8**	**Petalling**
22	**23.5**	**4**	**10.3**		**42.8**	**Petalling**
23	22.94	4	8.7			No rupture
24	23.95	4	4.5			No rupture
25	**25.04**	**4**	**4.9**	**2.6**		**Petalling**
26	24.12	4	7.4	2.6		Tearing in one edge

But when assuming that the material is similar to PE4 or C4 then the typical value that is available from the literature is 1.6 g/cm^3 (Alia, et al., 2006). In the simulations it has been decided to use the value of 1.5 recommended by the manufacturer.

Table 7.1 shows the peak overpressures of all experiments where it was possible to obtain a pressure record. The pressure-time curves collected were all similar in shape: a very sharp peak followed by a quick decrease and a slight pressure increase which may be due to the gas pressure increase resulting from afterburning. Then the pressure decreases again due to the release through the small orifice for the detonator wires. The pressure recording for experiment 22 is shown in Fig. 7.2 where these three effects can be observed.

The effects of the detonation in Plate 1 varied significantly, nearly following the whole range of modes of failure, depending on the selected combinations of stand-off distance and charge mass. A description has been included in Table 7.1 but the results can also be observed in Fig. 7.3, which shows pictures of Plate1 after the experiments.

Experiments 1, 4, 5, 6 caused the complete tearing of the four edges of Plate 1, as shown in Fig. 7.3 (a). For this reason, these experiments were considered inconclusive. Experiments 9 and 17, which are shown in pictures (b) and (f) of Fig. 7.3, show total tearing of two edges, and experiment 19 exhibited tearing at one edge, which was unexpected and is difficult to explain. This may be the result of a slight deviation of the explosive charge from the spherical shape. The charges were shaped on site and due to the warm ambient conditions (ambient temperature was around 28° C) the explosive compound became sticky and difficult to handle. Experiments 2 and 3 were affected by a defective batch of the explosive which caused a misfire in experiment 2 and a deflagration instead of a detonation in experiment 3. In experiments 7, 8, 11, 13 and 15 no rupture of Plate1 was observed. This left only experiments 10, 12, 16, 18 and 20-22 to be analysed.

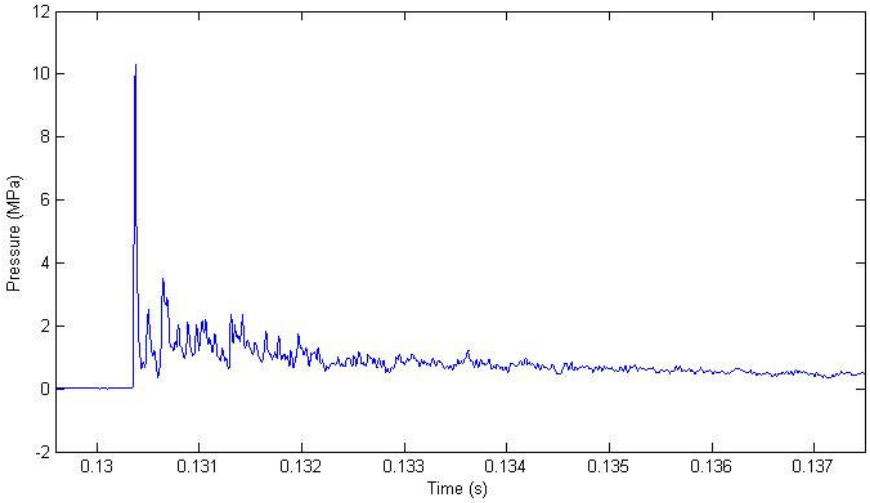

Figure 7. 2 – Pressure-time curve recorded in chamber 1 of experiment 22

The results were organized in accordance with the respective *Z* scaled distance as shown in Table 7.2. From the results it may be concluded that localized rupture occurred at a very definite range of *Z*, between 0.195 and 0.197. For smaller values of *Z* a progressive increase of the degree of damage occurs as the value of Z decreases: at a *Z* value of 0.194 the localized rupture evolved to petalling of the plate and for an even lower *Z* such as 0.191 complete tearing of two edges was observed. It is expected that for an even lower *Z* complete tearing of all four edges would be observed. For values of *Z* above 0.197 at first no ruptures were observed but as *Z* increased complete tearing of the plate four edges started to be observed. Within that narrow range of *Z* the pressure distribution had a very localized pattern. As the plate was plastically bent, a local cap was formed due to thinning of the material and that cap ended by tearing in a circular fashion. Outside that narrow range the pattern of pressure changed and this localized thinning ceased to occur. For larger *Z* values the pressure tends to be more uniform over the plate favouring Mode III type failure or no failure at all. And for very small *Z* the cap tearing evolved to a petalling type rupture where for the lower *Z* values the rupture was characterized by the plate being divided in two halves (two petals).

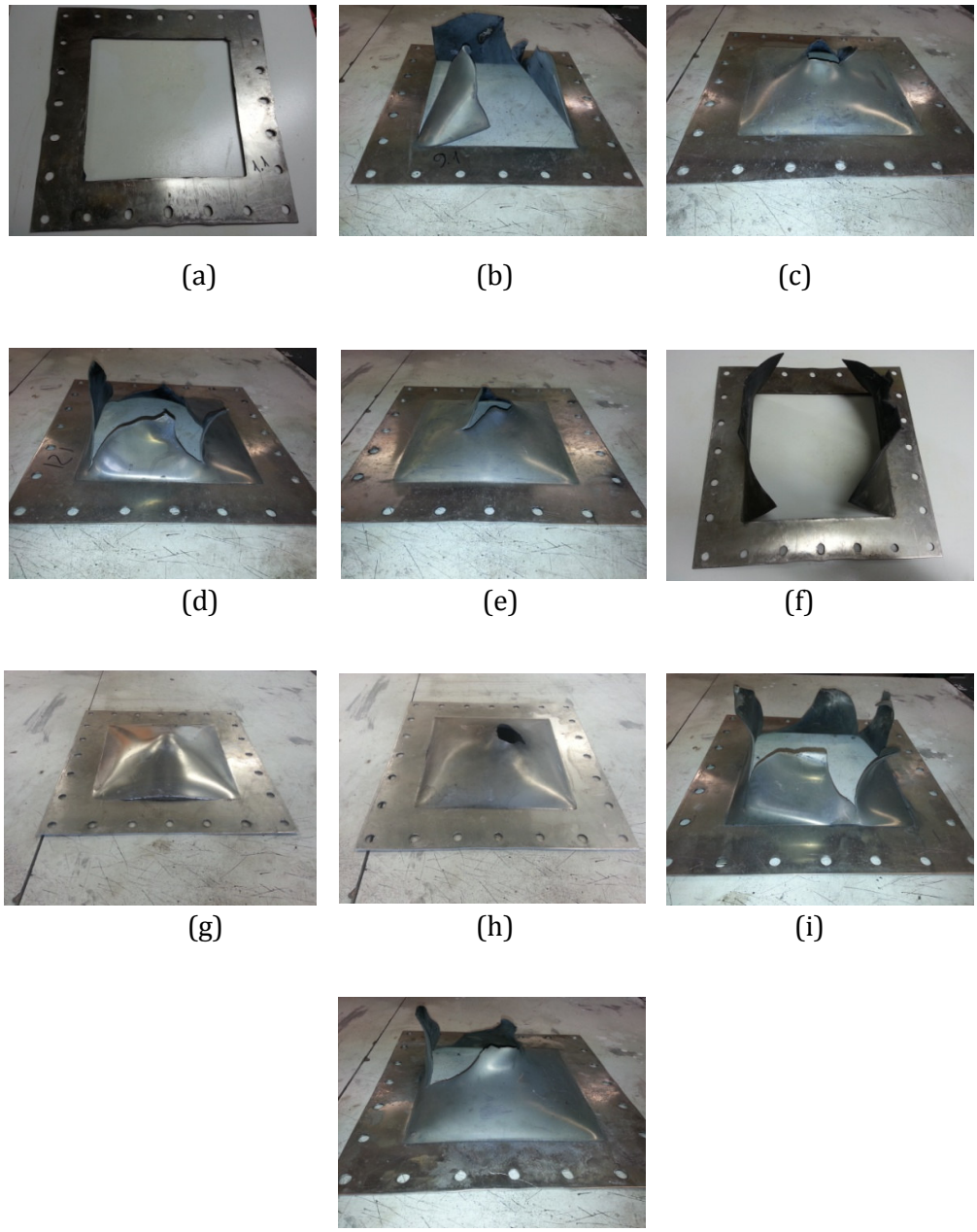

(a) (b) (c)

(d) (e) (f)

(g) (h) (i)

(j)

Figure 7. 3 – Images of the effect of the detonations on Plate 1, placed between the two closed chambers: (a) Exp.1 (b) Exp.9 (c) Exp.10 (d) Exp.12 (e) Exp.16 (f) Exp.17 (g) Exp.19 (h) Exp.20 (i) Exp.21 (j) Exp. 22

Table 7. 2 – Experimental results of the second phase placed by the order of increasing Z scaled distance

Exp. no	Z (m.kg$^{-1/3}$)	Type of failure of Plate 1	δ plate 2 (mm)
9	0.191	Complete tearing of two edges	46.7
17	0.191	Complete tearing of two edges	47.7
21	0.194	**Petalling**	50.8
22	0.194	**Petalling**	42.8
12	0.195	**Petalling**	46.4
20	0.195	**Rupture of centre cap**	40.2
16	0.196	**Rupture of centre cap**	39.5
18	0.196	**Rupture of centre cap**	39.2
10	0.197	**Rupture of centre cap**	38.5
15	0.197	No rupture	
19	0.198	Tearing of one edge	
11	0.202	No rupture	
14	0.225	No rupture	
13	0.230	No rupture	
8	0.259	No rupture	
4	0.310	Complete tearing of four edges	55.3
7	0.327	No rupture	
6	0.343	Complete tearing of four edges	54.2
1	0.347	Complete tearing of four edges	
3	0.386	No detonation	
5	0.404	Complete tearing of four edges	
2	0.421	Incomplete burn. Test disregarded	

Table 7 .3 - Experimental results of the third phase placed by the order of increasing Z scaled distance

Exp. no	Z (m.kg$^{-1/3}$)	Type of failure of Plate 1	δ plate 2 (mm)
25	0.191	**Petalling**	
26	0.193	Tearing at one edge	
24	0.193	No rupture	
23	0.195	No rupture	

The reader will notice that the last four experiments performed in the third session were not included in Table 7.2. In relation to the second session these four experiments show a small off-set in terms of the mass of explosive (or the *Z* scaled distance) required to produce similar effects. In these experiments the onset of rupture appeared at *Z* values of 0.193 and the petalling effect was achieved with a *Z* value as low as 0.191 whilst in the preceding session the phenomena was observed for *Z* values of 0.194 and 0.195. Table 7.3 shows the results of the third session of experiments. This offset corresponds roughly to the addition of 2 g of explosive.

7.3 Analysis of experimental results

There is no obvious relation between the *Z* scaled distance in chamber 1 and the deflection of Plate 2. The analysis of results showed that the deflection of Plate 2, being dependent on the blast transmitted to the second chamber, was directly influenced by the damage of Plate 1. The wider the aperture of the ruptured area of Plate 1, the larger the mass of reaction products moving from chamber 1 to chamber 2 and impinging on Plate 2. However, no obvious relation between the *Z* scaled distance of the explosive charge in relation to the dividing plate and the resulting damage was observed. As mentioned above, it was observed that the smaller apertures and the occurrence of no rupture events occurred for a short range of values of *Z*. Above and below that range the resulting ruptured areas tend to be wider. For a *Z* scaled value of around 0.195 a centre cap with a localized rupture was observed. For lower *Z* values, that is to say for a stronger blast, Plate 1 was completely torn and total detachment occurred. However, the same has been observed for higher *Z* values for combinations of higher masses of explosive with larger stand-off distances. The same trend was observed in experiments 23 to 26 albeit for a different range of *Z* scaled distances.

Some features of the experimental set-up may have influenced the behaviour of the variables involved in the phenomena. It is relevant to identify some of these features:

- The explosive chamber has 5 rigid sides and a frangible one;

- The volume of the explosive chamber was shown to produce stoichimetric conditions for the explosive reactions in the range that caused the central cap rupture of Plate 1;
- There was an unintended venting hole in the chamber due to the need of allowing the passage of the detonator wires to the inside of the chamber.

The frangible wall favoured the occurrence of pressure wave reflexions and interactions that may have enhanced the reflected and incident pressures of the blast impinging Plate 1. This has been investigated in Chapter 4 but the present experimental results seem to indicate that the inside pressure increased sharply, resulting in a nearly constant pressure distribution, which in many instances caused a complete tearing of the plate edges. Localized thinning and rupture only occurred within a very discrete range of scaled distances when the effect of the direct blast was largely preponderant.

The stoichimetric condition provided by the inside volume of the explosive chamber led to the need of considering the effect of afterburning since this condition means that enough air exists in the confinement to support the combustion of the non reacted products of the detonation. The plot of the inside pressures as recorded by the sensors placed in both chambers indicated that the time interval between the two peaks is very small, showing that the rupture of Plate 1 occurred very quickly after the detonation of the explosive. Fig. 7.4 shows the two plots from which it may be observed that the pressure in the second chamber starts to rise 25 μs after the initiation of the detonation. The build-up of pressure in the second chamber took about 1.2 ms until the peak. But the phenomenon of afterburning normally lasts for milliseconds and may start at about 1 ms after the detonation time (Feldgun, et al., 2016). The detection of a pressure rise 25 μs after the start of the detonation reaction reveals that at this time the plate has already been ruptured and leakage of combustion gases from the first to the second chamber has started. It is thus possible that afterburning did not contribute to the rupture of Plate 1.

At the time the pressure is peaking at the second chamber, conditions exist for the occurrence of afterburning. The 2 mm wide hole in way of the detonator wires may, however, have acted as a venting nullifying the effect of the afterburning. In fact, during the experiments a jet-stream of gases and flames was observed coming out through this

hole. It is then difficult to reach a definite conclusion about the effect of afterburning given the venting hole but it is certain that it did not contribute to the rupture of the first plate but rather to the deformation of the second plate.

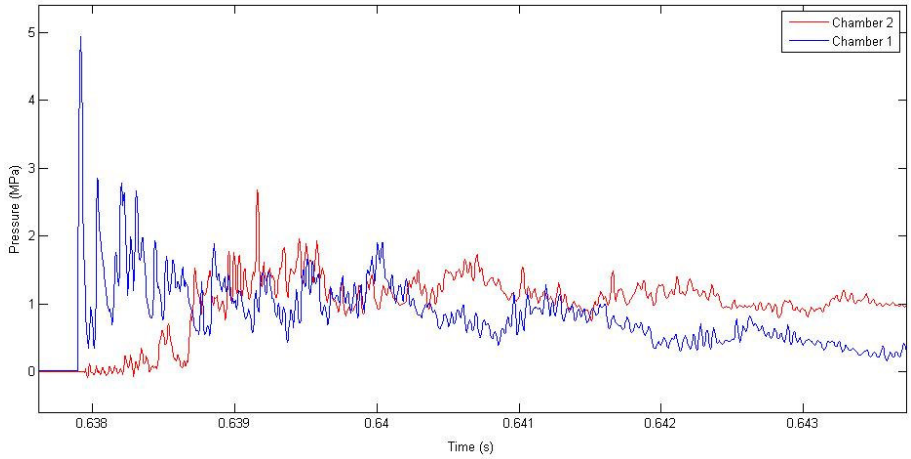

Figure 7. 4 – Pressure time curves at the two adjacent confined chambers for experiment 25

For a better understanding of the phenomena, Fig. 7.4 above is shown below, in Fig. 7.5, with a different scale.

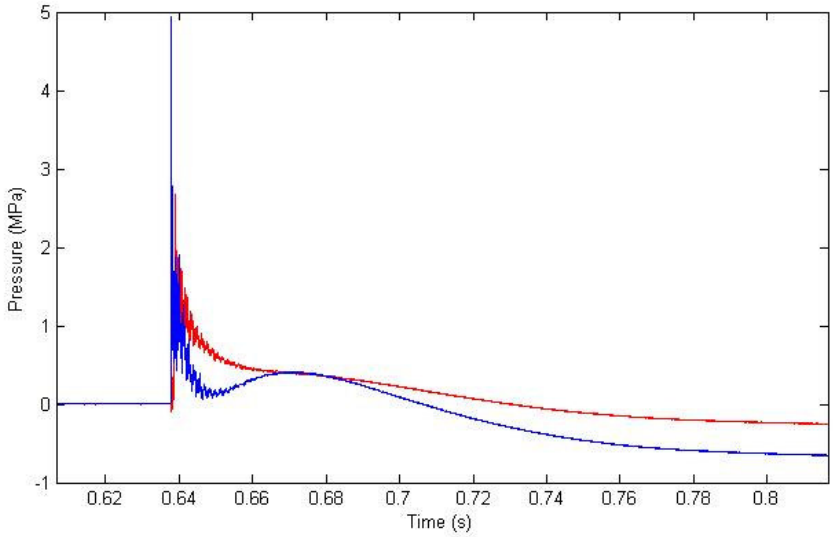

Figure 7 . 5 - Pressure time curves at the two adjacent chambers at a larger scale, for experiment 25

It is now possible to notice that the pressure in the second chamber decreases smoothly after peaking, showing no increase due to afterburning. However, in the first chamber a considerable pressure build-up of about 35 ms was noticed after the first peak. This seems to indicate the occurrence of afterburning but at a time much later than the occurrence of the detonation, rupture and the impact on Plate 2. This pressure increase dissipates quickly due to venting and a rarefaction may be seen on Fig. 7.5, probably due to the cooling of the reminiscent gaseous products and the transfer of part of the generated volume of gases to the adjacent chamber.

7.4 Afterburning analysis

Although it was observed from the pressure measurements that afterburning did not have a decisive role in straining and failure of Plates 1 and 2 it did occur at a later time. Its effect ended up not being relevant for the mechanical response of the plates under observation but even so it was decided to leave a note on the relative amounts of energy involved in both the detonation and the afterburning phenomena.

7.4.1 Energy of afterburning

Afterburning was introduced in Chapters 2 and 5. It is a complex chemical process that results from the reaction of combustible products of a detonation. These products will form in case of an incomplete reaction of the explosive if it has insufficient oxygen in its composition. In this situation, if there exists oxygen from the ambient atmosphere and the temperature is high enough, those products may react and release more energy. It is likely that the temperature of the hot gaseous products of a detonation in a confined space will be high enough to ignite the burning of those products. However, the extent of the reaction will depend on how much oxygen is available or, which is the same, the free volume of the confinement. The length of both phases of the explosion, detonation and afterburning, will be of the order of microseconds and milliseconds, respectively which means that although the

afterburning gas pressure is lower than the pressure peaks that result from the detonation, the structure will be exposed to a significant impulse in the afterburning phase, which may result in more damage. The phenomena will however, not be relevant for oxygen balanced explosives or even for a small oxygen balance (OB) . A measure of this oxygen balance for RDX is given by the expression

$$\mathrm{OB}[\%] = 100\frac{\mathrm{AW(O)}}{\mathrm{MW(RDX)}}\left(\mathrm{z} - 2\mathrm{x} - \frac{\mathrm{y}}{2}\right) \tag{7.1}$$

where *AW(O)* is the atomic weight of oxygen (g/mole) and MW(RDX) is the molecular weight (g/mole) and *x, y* and *z* are the numbers of atoms of carbon, hydrogen and oxygen in the explosive chemical formula $C_xH_yN_wO_z$. In an explosion reaction nitrogen dioxide, water and carbon monoxide will form. The carbon monoxide will then react with available oxygen to produce carbon dioxide.

The Cyclotrimethylene Trinitramine (RDX) high-explosive has the chemical composition $C_3H_6N_6O_6$ whose products of reaction are,

$$\begin{aligned} &6\mathrm{N} \rightarrow 3\mathrm{N}_2 \\ &6\mathrm{H} + 3\mathrm{O} \rightarrow 3\mathrm{H}_2\mathrm{O} \\ &3\mathrm{C} + 3\mathrm{O} \rightarrow 3\mathrm{CO} \end{aligned} \tag{7.2}$$

it can be seen that the available oxygen is not sufficient to react with the carbon monoxide to give carbon dioxide. RDX is stoichimetrically balanced to H_2O and CO but the latter is still reactive and may burn. This will require an extra 1.5 moles of oxygen molecules to convert the three carbon monoxide moles of molecules into three moles of molecules of carbon dioxide,

$$3\mathrm{CO} + 1.5\mathrm{O}_2 \rightarrow 3\mathrm{CO}_2 \tag{7.3}$$

This can be also seen from the term $z - 2x - y/2$ from eq. (7.1). If this term is lower than zero then the explosive is under oxidized. For RDX this term gives 6 – 6 – 3 = -3 showing that there is a lack of oxygen in the explosive. The molecular weight of RDX (MW(RDX)) is:

12.01(3)+ 1.008 (6) + 14.008 (6) + 16.0 (6) = 222.126 g/mole

which introduced in eq. (7.1) gives an oxygen balance of -21.61% (Cooper, 1996). Assuming that air constituents, oxygen and nitrogen, will behave like an ideal gas and will follow the equation of state shown (7.4) it is possible to calculate the minimum volume of air required for the complete reaction of one mole of RDX explosive, which is 168 lts. The molar mass of RDX is 222.13 g/mole so the stoichimetric value of *W/V* (DoD, 2008) , the ratio of the mass of explosive (*W*) to the free volume of the structure (*V*), for one mole of RDX, is 1.33 kg/m^3. The volume of the combustion chamber 1 is (0.260 m)^3 =0.0176 m^3 which results that the maximum mass of explosive that will burn completely is 23.4 g. Since PG2 has 88% of RDX, this corresponds to approximately a mass of explosive of 26.6 g. In all experiments the mass of the explosive charge was lower than this value, which means that in all situations a complete afterburning was, at least, theoretically admissible.

The law of an ideal gas is

$$P = \frac{nR\gamma T_p}{V} \tag{7.4}$$

where *P* is the pressure of the gas (Pa), *V* the volume of the gas (m^3), *n = m/M* is the number of moles of the gas (kg/kg/kmol), and *m* is the mass of the gas (kg) and *M* is the molecular mass (kg/kmol). Finally, T_p is the absolute temperature (K) at constant pressure and γ is the heat capacity ratio. *R* is universal ideal gas constant which is *R* = 8.3145 kJ/(kmole.K).

The reaction formula that describes the RDX combustion is (Cooper, 1996):

$$\mathrm{C_3H_6N_6O_6} \rightarrow 3\mathrm{N_2} + 3\mathrm{H_2O} + 3\mathrm{CO} \tag{7.5}$$

However, CO is a fuel and it will react with available atmospheric oxygen to form CO_2. Thus the complete reaction is:

$$C_3H_6N_6O_6 + 1.5O_2 \rightarrow 3N_2 + 3H_2O + 3CO_2 \tag{7.6}$$

Equation (7.5) represents the detonation of one mole of RDX and equation (7.6) represents the full combustion of the explosive including the burning of the carbon monoxide formed in the detonation process (Feldgun, et al., 2016) (Cooper, 1996).

The afterburning energy is provided by the formation enthalpy of carbon dioxide molecules minus the formation enthalpy of carbon monoxide in eq. (7.7)[15]:

$$\Delta H_{ab} = \Delta H_f\left(CO_2\right) - \Delta H_f\left(CO\right) \tag{7.7}$$

$$= (3)(-393.78) - (3)(-110.60)$$

$$= -849.55 \text{ kJ/mole RDX}$$

The detonation energy needs not to be derived because it is included in the material model which has been used in all simulations, e.g. in Chapter 5, regarding PE4 or C4, which have been assumed to have the same properties of PG2. However, it may be interesting to note that the experimental value for the heat of detonation is -1404 kJ/mole (Cooper, 1996), which means that the energy of afterburning is only 37.7% of the total explosion energy. It may be said that RDX is not significantly under-oxidized when compared with TNT (Chapter 5), where the afterburning energy is about two thirds of the total explosion energy. In this explanation, explosion energy is the total energy released by the burning of the explosive, which is equal to the detonation energy added to the afterburning.

Numerical modeling of afterburning requires that energy is input per unit of volume. From the molar weight of RDX and assuming that the density is as stated by the manufacturer, 1500 kg/m3, the afterburning energy is then calculated as:

$$\frac{849.55\frac{\text{kJ}}{\text{mole}}}{22.126\frac{\text{g}}{\text{mole}}}1.5\frac{\text{g}}{\text{cm}^3} = \tag{7.8}$$

$$5.737\frac{\text{kJ}}{\text{cm}^3} = 0.0576 MBar$$

[15] 1 kcal = 4.1868 kJ

This is an approximated figure as the correct density has been a difficult choice between the many values available in literature such as the published values for PE4 or C4, the density quoted in the data sheet of PG2 and the value obtained by measurement.

Hydrocodes simulate afterburning by considering the release of the respective energy amount, which has to be input by the user together with the choice of an option for the way the energy is released. Start and end times for the release of the afterburning energy and the rate of release, which may be linear or follow an empirical function. The inclusion of afterburning in a numerical analysis is reported to take much longer than a normal analysis, which also adds to the complexity of such analysis and in the present case, in which experimental evidence seems to indicate a release time of more than 35 ms, the time necessary to run one simulation would exceed three and a half months as a simulation considering just one ms took more than two days.

7.2 Numerical analysis

The numerical analysis of the phenomena described above consisted in modelling an ALE domain representing the two adjacent chambers. Two lagrangian deformable planar parts were added to represent Plates 1 and 2 of the test apparatus. The plates were held in place by two frames each, modelled as rigid materials.

Plate 1 was modelled with solid elements to capture the shear effects in failure. For Plate 2, which was only subjected to large inelastic deformation, shell elements were used. All remaining parts used also solid elements, such as the rigid frames and the air domain, which elements have ALE multi-material capability. LS-DYNA has a wide range of solid elements which are called by a suitable selection of a parameter of the *SECTION_SOLID card. For the present analysis an under-integrated constant stress element was selected for computational efficiency. This element has, however a drawback, as it needs hourglass stabilization for which the choice of an effective formulation remains a difficulty. A fully integrated element could have been used but they are more unstable for large deformations. More details on the modelling technologies utilized throughout the dissertation were presented in Chapter 4.

Although the validation of such a complex model would be rather tedious, given the enormous number of parameters to tune, a continuous validation process was adopted. In Chapter 3 a comprehensive review of candidate constitutive models suitable for blast problems was discussed and the Johnson-Cook equation was chosen and explained (Salvado, et al., 2017b). In Chapter 5 the ALE technique was tested and its results evaluated for different input parameters and compared with published results. The range of results and the various comparisons with experimental data that were reported in Chapter 5 gave the support for the choice of the suitable parameters to set an ALE analysis of a blast in a confined space. The verification of the Johnson-Cook viscous-plastic material model for aluminium AA5083-H111 was discussed on Chapter 6, based on published material and comparing with experimental results of explosive blast. With the experimental data gathered and the subsequent numerical analysis it was possible to set the constitutive model for this specific aluminium alloy. It is necessary to consider the five parameters of the Johnson-Cook failure model, the hourglassing formulation, the setting of the boundary conditions and the fluid-structure interaction parameters, to cite only the most important.

One particular feature of the experimental setup was referred to be the small hole that was necessary to pass the detonator electrical wires. An investigation has been done to decide on the numerical effect of such orifice and a small hole of approximate dimensions was modelled. It was found that the outflow was noticeable only after the rupture of Plate 1 and most of the deformation of Plate 2 occurred and no pressure drop was detected within the time interval of the interest for the analysis. Therefore, the hole was not included in the finite element model of the closed chambers.

Fig. 7.6 shows the global model used. The red part is the ALE domain which boundaries were defined as rigid (normal nodal velocities set to zero) and the yellow parts correspond to the rigid flanges that connect the two closed chambers and hold Plates 1 and 2 in place, respectively. The explosions occur at the topmost chamber and the lower one is the empty chamber which will be blasted after Plate 1 is ruptured

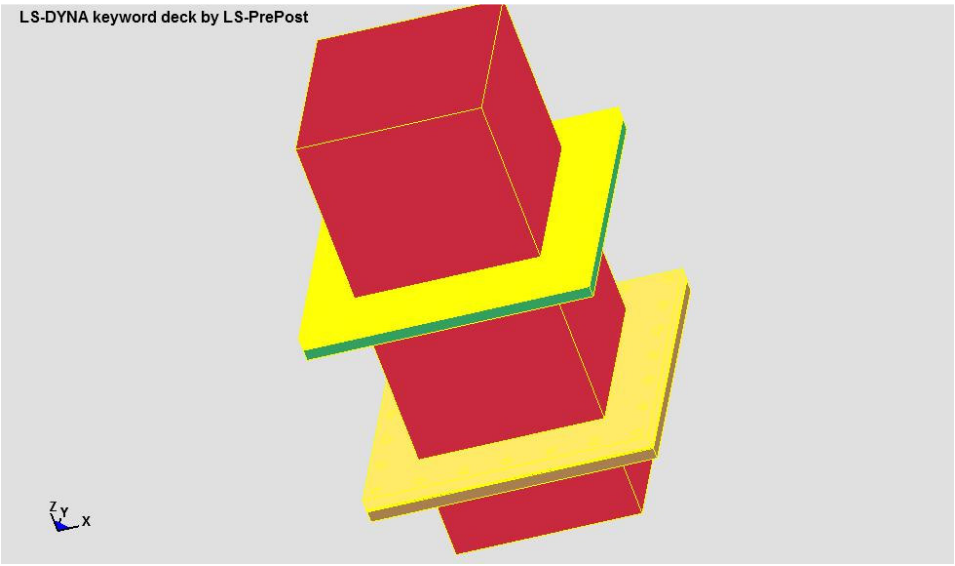

Figure 7. 6 – LS-DYNA finite element model of the experimental apparatus

.

It can be seen that he ALE domain extends below the lower flange. This is required to provide an ALE volume where the gaseous reaction products coming from the first chamber can expand and deform Plate 2. The boundary conditions in this region will allow all degrees of freedom since there are no physical barriers there.

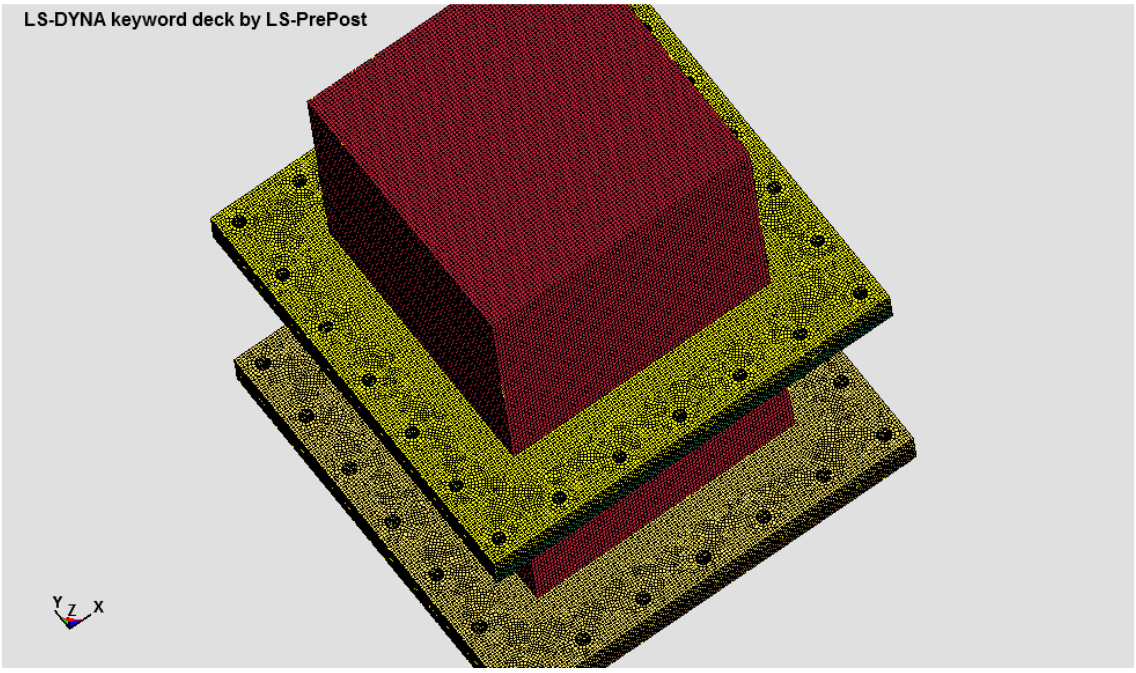

Figure 7. 7 – More detailed view of the finite-element model of the two chambers.

Fig. 7.7 shows more clearly some details of the model such as the holes of the connecting bolts. The flanges have 24M13 mm bolts. This restraint has been modelled by fixing the nodes of the outer half circular perimeter of the plate holes. This assumes that the holes are rigid and that the plate nodes that are in contact with them will not penetrate the space occupied by the bolts. This assumption is sufficiently realistic as elastic deformation of the bolts is much smaller that the plastic deformation of the aluminium alloy in the vicinity of the holes. It was verified that none of the bolts suffered plastic deformation.

The tightening of the bolts will press the flanges against the aluminium alloy plate in between. During the field experiments one of the bolts suffered damage in its thread during tightening and it was decided to limit the torque applied to the bolts to a value of 75 Nm. In the smaller Z scaled values considerable plastic deformation was observed in the aluminium alloy plates around the holes, which indicate that most of the restraint was ensured by the bolts rather than by friction between the plate and the frames. In light of this, a simpler model was preferred rather than a full representation of bolts and nuts and the pre-loading due to the torque applied. An equivalent force was applied to the plate instead by means of a contact algorithm. This worked reasonably well in the open air blasts (Chapter 6) and so it was also assumed to be adequate for the closed chamber. The need for a fine tuning of this parameter may have been critical for the success of the simulation since a too strong restraint of plate slip would have led to more bending stresses and shear effects along the edges of the plate. A lighter restraint would allow some axial slip, enhancing the effect of planar stresses. As will be discussed below, the occurrence of unwanted tearing along the edges of the plate has been an issue during all the model validation process.

The fluid-structure interaction involved a considerable effort until leakage was eliminated. To avoid it a user supplied penalty curve had to be considered.

The explosion was simulated with the help of a mapping technique. A two dimensional problem with the required mass of explosive was run with a highly refined mesh of a quarter of a million 0.5 mm elements. The results were then mapped in the 3D model which has elements of approximately 3 mm. The simulation time was set to 1 ms. The explosive used was C4, which presents small differences to PE4 being arguable which should be considered closer to PG2 from which no written indication of

composition was provided. The choice of parameters has been presented and discussed in Chapter 4 and will thus not be discussed again here.

In the setup of the hourglassing formulation, two formulations were attempted: (i) the Flanagan-Belytschko viscous form and (ii) the same formulation with exact volume integration for solid elements. The default values for the bulk viscosity worked well most of the times but given the difficulties experienced in the deformation and failure of Plate 1 it was also attempted to use a larger value, which is recommended for the propagation of shock waves in solid elements. Unfortunately, this did not resolve the problem of the rupture at the plate edges.

The effect of afterburning was commented above and it was concluded from the observation of the recorded pressure-time curves that the occurrence of the phenomena would not affect the early stages of the process. Therefore not interfering with Plate 1 rupture and Plate 2 deformations. Also, the venting effect would neutralize its effect of afterburning. However, its inclusion in the model was considered. Since the function was not initially available in commercially available versions of the LS-DYNA code, a developer's license was requested to the supplier. However, this version behaved in an unexpected way aborting for unknown reasons even with input files that were run without errors in the commercial license.

Two tracer points to record pressure were defined at the same positions where the pressure sensors were located during the experiments. Running the models was in general a very lengthy process whenever it involved rupture. Depending on the combinations of parameters of the JC failure model in a number of runs only Mode I damage (large inelastic deformation) was observed and the time of the simulation was close to the running time estimated by the solver (about 12 hours). However when rupture was observed some of the runs had to be aborted as the time step kept dropping until the run became virtually stopped. In all such cases the inception of the ruptures at the edges of the plate was nevertheless observed.

Another interesting finding was an apparent interaction between the failure model and the fluid-structure interaction mechanism. As explained above the elimination of leakage was an issue and the only way to have it minimized was by means of a penalty curve. However, it was found later that the model was too impermeable and the combustion gases were not passing through the fractured zones of the plate. Thus the penalty parameters were alleviated. This resulted in a reasonable FSI

behaviour. However, it was not clear why using such parameters yielded a strong leakage in some of the initial simulations. Since the constitutive parameters were the only part of the model that were systematically changed a relation seems to exist between material behaviour and the mechanism of imposing restoring forces to ALE nodes impinging on the material surface, though not well understood. Although this phenomena is a possible explanation for the tearing along Plate 1 edges (if no gases were passing through the initial plate fracture in the middle a pressure build-up would occur ending up by tearing the plate borders) the correction of the penalty factors, though improving the FSI behaviour, did not eliminate the final tearing of Plate 1 along its edges.

Throughout the analysis it has been assumed that the point of detonation was in the geometric centre of the spherical charge. This was in agreement with the experimental work, where the detonator had to be inserted nearly up to the centre of the charge, in order to hold itself in position. However, it was decided to consider a different point of detonation in the simulation, near the point where the detonator was inserted (at the top of the charge), in an attempt to obtain a focal effect that might impart more energy to the centre of Plate 1, in order to break it. This did not change the results of the simulation.

In the discussion of the experimental results it was observed that the range of Z scaled values where the intended petalling effect was observed is rather small. This may constitute one of the main difficulties experienced in the numerical analysis, meaning that only a very precise and definite setting of the model will yield the intended results. This becomes even more difficult as a numerical model always implies some simplifying assumptions making it more difficult to simulate a very sharply defined phenomenon.
It is possible to simulate other situations where a complete tearing of Plate 1 edges was observed but these are difficult to validate since they occurred at a wider range of Z. This became a deadlock, since to validate the model the experimental phenomenon must be uniquely defined but at the same time the effort to obtain such accuracy of settings has revealed itself to be enormous. It is believed that mechanical testing at high strain rates (by using a Hopkinson Pressure bar for instance) of samples of the aluminium alloy under investigation would narrow the range of values of the parameters needed to calibrate the JC model. This was not done before due to funding constraints and remains as an identified limitation on the present numerical analysis.

Another line of action that was pursuit was to attempt an improvement of the results by using a mesh regularization technique. LS-DYNA has a material model, called via the keyword *MAT_NONLOCAL (Schwer, 2011), that can be associated to the model. It is well known that the modelling of damage is mesh-dependent and strain and damage tends to localize in the smallest elements of the mesh. This means that for a given mesh the smallest elements will erode before the larger elements. Traditionally this would require a change in the mesh, eventually with a different topology, leading to different results. This non local treatment attempts to provide a means to regularize meshes by averaging their values of damage and failure on neighbouring elements to minimize the mesh dependency of the results avoiding the need for a new mesh.

The method uses a three parameter weighting factor which is then used to average the damage ratio parameter within a certain number of integration points, defined by a user defined length parameter (Pijaudier-Cabot, et al., 1987). However the use of this regularization technique was not successful in reproducing the fracture behaviour expected for the plate and caused a considerable delay in the time to run the simulations. However the theory behind the technology points to the fact that failure localize where the mesh has smaller elements then the compression of Plate 1 along the supported edges, affecting element size, may induce the localization of failure along the edges.

The simulation is then facing numerical and modelling problems, which have been impairing a solution in a long and persisting manner.

At this point it was decided to abort the numerical investigation due to the time constraint, after persisting attempts during about five months of intense simulation.

Numerical analysis shall be object of a revaluation since without validation the envisaged numerical tool for the analysis of confined explosions cannot be fully validated. It is believed that we may also be facing a discretization problem as fracture is very sensitive to the mesh. This could not be improved because the ALE mesh was refined to the possible extent, bearing in mind the CPU time of the simulation. As one of the main purposes of the envisaged tool is its use for engineering and design work, CPU time and the complexity of the model must be compatible with the use of a standard workstation, rather than being only usable on a network with parallel computing. Otherwise it would lose is purpose and turn into a research tool rather than a design tool, which is the objective of the present work.

Chapter 7

It is considered that the most suitable numerical techniques and technologies have been investigated and many of them were adopted to create a model, which is believed to reproduce the physical phenomenon with engineering accuracy.

It is believed that it remains to find a suitable calibration and combination of the several technologies involved in the simulation, to obtain realistic results. And this shall be more a matter of persistent and systematic work than of developing new technologies.

Thought some limitations of the model where pointed out above it is considered that the objective of identifying the modelling tools and technologies necessary to understand and simulate the phenomena of a confined explosion and its effect on adjacent compartments has been fulfilled.

8. Conclusions

A wrap-up of the work done is presented together with a summary review of the relevant findings, together with conclusions and recommendations for future work

8.1 Summary of the work performed

The objective of the thesis was to study the behaviour of two adjacent confined compartments, one of them being subject to an internal explosion. The work presented in this thesis aimed to relate the first explosion and rupture and the effect in neighbouring structures of the sequential wave blast. This required a numerical tool that could simulate the rupture of a blast loaded plate inside a confinement and the propagation of the blast to an adjacent chamber where the effect of such blast load on the chamber structure could be reproduced and analysed for a number of geometries, explosive charges and stand-off distances. Such a simulation requires the accurate modelling of, at least, three phenomena: (i) the explosion and the propagation of the blast wave and the flow of the detonation products in a closed space where wave bouncing may occur between the internal walls; (ii) the fluid structure mechanism where the blast wave momentum is transmitted to the plate; (iii) and the plate material behaviour in the visco-plastic high strain rate regime, with failure and without failure.

The explosion and blast wave propagation, particularly in a confined space was analysed in a parametric way in Chapter 5, where a considerable effort was devoted to the understanding of the effect of the various parameters involved in the model. The work was peer-reviewed and published (Salvado, et al., 2017a).

The mechanism of mechanical response of the plate under a blast wave was analysed both in terms of an empirical blast loading and the fluid-structure interaction mechanism, by using the ALE approach described in Chapter 4. The simulated results

were validated with experimental data and the data and conclusions were presented in Chapter 6. An article describing the work performed and derived conclusions was submitted for publication and is currently being reviewed after having been object of a first set of comments from the peer-reviewers.

The material model was selected after a careful review of many of the available constitutive models, bearing in mind its limitations, availability of data to calibrate the models and expected accuracy. This review, presented in Chapter 3, was later published in the "Progress in Materials Science" international journal (Salvado, et al., 2017b).

These different works were synthesized in a final model that should solve the full problem of blast across a ruptured wall between two adjacent confined compartments and was described in Chapter 7. The main reasons for the present limitation of the model were presented and discussed in this Chapter.

8.2 Present limitations of the full simulation model

As referred in Chapter 6, Plate 1, the plate exposed to the direct explosive wave blast always breaks along the supported edges, no matter where the fracture first initiates (at the centre or at the middle of the edges). This was observed in some of the experimental work, meaning that the model reproduces the real phenomena observed in the field, but for validation of the model it was important to reproduce a very definite case where the rupture was only local and not generalized since when the plate breaks along all the edges there is no unique solution for the problem and a range of possible Z scaled distances exist that can cause the same damage.

Validation of the model was not succeeded for all damaged cases since, as confirmed by the experimental data, the set of conditions necessary to cause the central rupture of Plate 1, without breakage along its edges, is very precisely defined and difficult to reproduce bearing in mind the wide range of parameters to calibrate, both in the material model and the fluid-structure interaction phenomenon.

The model simulates the fracture appearing at the centre of the plate, its propagation and the resulting pettaling effect. The flow of the high-pressure explosive reaction gases through the fracture is also reproduced by the model, although it is felt

that some delay in the initiation of this flow shall may be contributing to a pressure build-up in the explosive chamber that may contribute for the tearing at the edges of Plate 1.

It was also observed, in the experiments, that prior to rupture a localized dome form at the centre of Plate 1, but the material model failed to reproduce this dome.

However, the collection of experimental observations is a novel contribution to the understanding of the phenomenon under analysis and so far, no related published material exists, to the knowledge of the author.

8.3 Final conclusions

The present work has made several contributions to the actual state of knowledge of the phenomena of the interaction of blast waves and structures, particularly in confined spaces. The major aspects that shall be pointed follow below:

- A review of the state of art on the relevant work on the constitutive behaviour of aluminium alloys was compiled and published, providing guidance and support to the understanding of the physics behind the phenomena of material response to large pulse pressures at very high strain rate regimes;
- Numerical simulations were proven to be an effective and reliable analysis tool for the analysis of explosions and an equation was derived to predict the direct shock wave reflected peak pressure at the centre of prismatic unvented confinement walls exposed to an internal explosion. The equation was a modification of an existing one (Henrych, 1979) and the model predicted relatively well the increasing effect of the confinement on the peak pressure values, and the effect of varying the proportions of the compartment.
- The numerical tool provided further insight on the phenomena of the wave bouncing between the internal walls of the confinement revealing some situations were two or more waves reinforced mutually yielding pressure peak values much higher than previously published works suggested;

- It was shown that the stand-off distance cannot explain alone such increased peak pressures and a relation also appears to exist between those peak pressures and the angles between the charge and the points where those peaks occurred;
- However the equations derived have a limited range of validity due to the fact that the large number of cases to be analysed prevented the use of different volumes and masses of explosive in the parametric analysis;
- It was shown that a simple and reliable numerical model is able to reproduce the real behaviour of aluminium alloy plates subjected to the free air explosion of explosive charges. However the experimental set-up may be criticized for their limitation in terms of instrumentation particularly for not allowing the measurement of blast pressures and for considering only one plate thickness;
- A small adjustment in an existing set of input parameters for the Johnson-Cook constitutive model provided an effective material model for the alloy under investigation (AA5083-H111), within engineering accuracy and yielding results with a very reasonable computation effort;
- Although the tool was capable of computing impulse, its validation has to be looked cautiously as the method used to measure the impulse imparted to the plates has limitations. This is discussed in a scientific paper currently under review which has been submitted for publication;
- It is believed that this part of the work provided a contribution to science bearing in mind that as far as the author is aware there are no published works on the blast loading response of aluminium alloy AA5083-H111;
- The collection of experimental evidence on the response of AA5083-H111 to confined blast loading revealed a very sharp border between different modes of failure, as described above;
- A numerical tool, appropriate to the description of material failure under a confined blast, was presented and discussed although it was not possible to present a validated set of results. However both the experimental set-up and the results obtained are novel, in the sense that there is no published work on this approach;

- A more accurate material model might have detected the deformed cap identified in some of the experiments and thus would allow a more accurate numerical representation of the material response, hence improving the validation effort. It would, however, require testing in a Hopkinson Pressure Bar (HPB) to determine the material properties under high strain rate regimes.

8.4 Recommendations and future work

The experimental set-up used in the present work had limitation of which some have been presented above. Unfortunately, budgetary constraints prevented the acquisition of most required sensors, external services such as the testing in a facility that has a HPB device, more testing material with different thicknesses which would have allowed the collection of more experimental data. Time was also a constraint due to the fact that the handling of explosives was only allowed to be performed by certified people, in the present work, the navy divers instructors, which had only limited periods of time available in between their training and operational engagements.

It is believed that this work is of interest for the navy and it should be continued in order to fulfil the initial objective of providing a tool for the vulnerability analysis of small patrol and combatant vessels. A further effort may allow the numerical model to be validated and this would complete the objectives set for this work. However, it is possible to go further in the potentialities of the numerical model in full scale analysis of real structures. Some lines of action for improvement are thus recommended. The most important recommendation has to do with the material model parameters for input in the JC equation. Some suggestions for future work follow:

The experimental testing of AA5083-H111 samples by means of a HPB equipment at the strain rates appropriate for the simulation of a blast impact;

The eventual attempt of setting a user material model in LS-DYNA, specially designed to reproduce the AA5083-H111 material behaviour under blast loading;

To further investigate the parametric model explained in Chapter 5 with different volumes and charges, to better understand the wave bouncing phenomenon in a confinement;

To repeat the free-field and confined experiments considering different plate thicknesses and installing blast-wave pressure sensors in the free-field experiments for a more accurate representation of the phenomenon;

To experiment the effect of blast loading on stiffened plates;

To eventually measure the real impulse on the exposed area of the plate, for instance by using a ballistic pendulum;

Finally, in a more advanced state, to use a real explosive ammunition instead of plastic explosive charges in order to compare with the effect of fragmentation and the projection of fragments on the target plates.

For future work it is recommended that the effect of aluminized explosives (thermobaric) is investigated and compared with the present results in order to be included in the numerical models for vulnerability analysis under this type of threat.

Bibliography

(UNODA) United Nations Office for Disarmament Affairs, International Ammunition Technical guideline 01.80, 2013

Abdulhamid H, Kolopp A, Bouvet C and Rivallant S, Experimental and numerical study of AA5086-H111 aluminum plates subjected to impact, International Journal of Impact Engineering, Vol. 51, pp: 1-12, 2013

Abed F H and Voyiadjis G Z, A consistent modified Zerilli-Armstrong flow stress model for BCC and FCC metals for elevated temperatures, Acta Mechanica, Vol. 175, pp: 1-18, 2005

Adamik V, Vágenknecht J and Vávra P, Effect of TNT charges orientation of general air blast waves, ANSYS User's Meeting, Hrubé Skále, Czech Republic, 2004

Alia A and Souli M, High explosive simulation using multi-material formulations, Applied Thermal Engineering, Vol. 26, pp: 1032-1042, 2006

Andrade U, Meyers M A, Vecchio K S and Chokshi K S, Dynamic recrystallization in high-strain, high-strain-rate plastic deformation of copper, Acta Metallurgica et Materialia, Vol. 42, pp: 3183-3195, 1994

Andrade U E, Meyers M A and Chokshi A H, Constitutive description of work-and-shock-hardened copper, Scripta Metallurgica et Materialia, Vol. 30, pp: 933-938, 1994

Aquelet N, Souli M, Gabrys J and Olovson L, A new ALE formulation for sloshing analysis, Structural Engineering and Mechanics, Vol. 16, Nº 4, 2003

Aquelet N, Seddon C, Souli M and Moatamedi M, Initialization of volume fraction in fluid-structure interaction problem, Intenational Journal of Crashworthiness, Vol. 10, pp: 237-247, 2005

Aquelet N, ALE Modeling of surfece waves, 6th European LS-DYNA User's Conference, Gothemburgh, 2007

Aquelet N and Souli M, 2D to 3D ALE mapping, 10th International LS-DYNA Users Conference, Detroit, pp. 15-34, 2008

Armero F and Love E, An arbitrary Lagrangian-Eulerian finite element method for finite strain plasticity, International Journal for Numerical Methods in Engineering, Vol. 57, pp: 471-508., 2003

Armstrong R W and Walley S M, High strain rate properties of metals and alloys, Internatiional Materials Review, Vols. 53, No.3, pp: 105-127, 2008

Armstrong R W, Arnold W and Zerilli F J, Dislocation mechanics of copper and iron in high rate deformation tests, Journal of Applied Physics, Vol. 105, pp: 23511-1: 23511-7, 2009

Armstrong R W, Arnold W and Zerilli F J, Dislocation mechanics of shock-induced plasticity, Metallurgical and Materials Transactions A, Vol. 38A, pp: 2605-2610, 2007

Department of the Army, U.S.A, Technical Manual TM 5-855-1, Fundamentals for protective design for conventional weapons, 1986

Arnold W and Rottenkolber E, Fragment mass distribution of metal cased explosive charges, International Journal of Impact Engineering, Vol. 35, pp: 1393-1398, 2008

Aune V, Fagerholt E, Hauge K O, Langseth M and Børvik T, Experimental study on the response of the thin aluminum and steel plates subjected to airblast loading, International Journal of Impact Engineering, Vol. 90, pp:106-121, 2016

Auslender F and Combescure A, Spherical elastic-plastic structures under internal explosion. Approximate analytical solutions and applications, Engineering structures, Vol. 22, pp: 984-992, 2000

Austin R A and McDowell D L, A dislocation-based constitutive model for viscoplastic deformation of FCC metals at very high strain rates, International Journal of Plasticity, Vol. 27, pp: 1-24, 2011

Austin R A and McDowell D L, Parametrization of a rate-dependent model of shock-induced plasticity for copper, nickel, and aluminum, International Journal of Plasticity, Vol. 32-33, pp: 134-154, 2012

Bai Y and Dodd B, Adiabatic shear localization - Occurrence, theories and applications, Oxford, Pergamon Press, 2002

Bai Y and Wierzbicki T, A new model of metal plasticity and fracture with pressure and Lode dependence, International Journal of Plasticity, Vol. 24, pp: 1071-1096, 2008

Bai Y, Effect of loading history on necking and fracture, PhD Thesis, Massachussetts Institute of Technology, 2008

Baker E L, Balas W, Capellos C, Pincay J and Stiel L, Combined effects of aluminized explosives, Technical Report ARMET-TR-10007, US Army Armament Research, Development and Engineering Center, 2010

Baker E L, Capellos C and Pincay J, Accuracy and calibration of high explosive thermodynamic equations of state, Technical Report ARMET-TR-100005, US ARMY Armament Research, Development and Engineering Center, 2010

Baker W E and Oldham G A, Estimate of blowdown of quasi-static pressures in vented chambers, San Antonio, Texas, Southwest Research Institute, 1975b

Baker W E and Westine P S, Methods of predicting blast loads inside and blast fields outside supressive structures, San Antonio, Texas, Southwest Research Institute, 1975a.

Balden V and Nurick G, Numerical simulation of the post-failure motion of steel plates subjected to blast loading, International Journal of Impact Engineering, Vol. 32, pp: 14-34, 2005

Banerjee B, The mechanical threshold stress model for various tempers of AISI 4340 steell, International Journal of Solids and Structures, Vol. 44, pp: 834-859, 2007

Bao Y and Wierzbicki T, On fracture locus in the equivalent equivalent strain and stress triaxiality space, International Journal of Mechanical Sciences, pp. 81-98, 2004

Bao Y, Prediction of ductile crack formation in uncracked bodies, PhD Thesis, Massachussets Institute of Technology, 2003

Barlat F and Lian J, Plastic behaviour and stretchability of sheet metals. Part I: A yield function for orthotropic sheets under plane stress conditions, International Journal of Plasticity, Vol. 5, pp: 51-66, 1989

Baudin G and Serradeill R, Review of Jones-Wilkins-Lee equation of state, EPJ Web of Conferences, Vol. 10, pp: 21-1:21-4, 2010

Bayoumi H N and Gadala M S, A complete finite element treatment for the fully coupled implicit ALE formulation, Computational Mechanics, Vol. 33, pp: 435-452, 2004

Belytschko T, Liu W K and Moran B, Nonlinear finite element for continua and structures, Wiley, 2006

Benallal A, Berstad T, Børvik T, Hopperstad O S, Koutiri I and Nogueira de Codes R, An experimental and numerical investigation of the behaviour of AA5083

aluminium alloy in presence of the Portevin-Le Chatelier effect, International Journal of Plasticity, Vol. 24, pp: 1916-1945, 2008

Benallal A, Berstad T, Børvik T, Clausen A H and Hopperstad O S, Dynamic strain aging and related instabilitoes: experimental, theoretical and numerical aspects, European Journal of Mechanics A/Solids, Vol. 25, pp: 397-424, 2006

Benselama A del M, William-Louis Mame J-P and Monnoyer F, A 1D-3D mixed method for the numerical simulation of blast waves in confined geometries, Journal of Computational Physics, Vol. 228, pp: 6796-6810, 2009

Benson D, Computational methods in Lagrangian and Eulerian hydrocodes, Dept. of AMES, University of California, San Diego, 1990.

Benson D J, A mixture theory for contact in multi-material Eulerian formulations, Computer Methods in Applied Mechanics and Engineering., Vol. 140, pp: 59-86, 1997

Benson D J, A multi-material Eulerian formulation for the efficient solution of impact and penetration problems, Computational Mechanics., Vol. 15, pp: 558-571, 1995

Benson D J, Momentum advection on a staggered mesh, Journal of Computational Physics, Vol. 100, no. 1, 1992

Bethe H A, Fuchs K, Hirxhfelder J O, Magee J L, Peierls R and von Neuman J, Blast Wave, Los Alamos Scientific Laboratory, Los Alamos, New Mexico, 1947(Distributed 1958)

Bishop J and James D J, The effect of light casings on the blast parameters from a spherical charge of RDX/TNT 60/40, United Kingdom Atomic Energy Authority, Aldermaston, 1968

Biss M, Characterization of blasts from laboratory-scale composite explosive charges, PhD Thesis in Mechanical Enginnering, Pennsylvannia State University, 2009

Bodner S R and Partom Y, Constitutive equations for elastic viscoplastic strain-hardening materials, Journal of Applied Mechanics, 1975, pp: 385-389, 1975

Bonora N, A nonlinear CDM model for ductile failure, Engineering Fracture Mechanics, Vol. 58, pp: 11-28, 1997

Bonorchis D and Nurick G N, The analysis and simulation of welded stiffener plates subjected to localised blast loading, International Journal of Impact Engineering, Vol. 37, pp: 260-273, 2010

Bonorchis D and Nurick GN, The influence of boundary conditions on the loading of rectangular plates subjected to localised blast loading - Importance in numerical simulations, International Journal of Impact Engineering, Vol. 36, pp: 40-52, 2009

Borenstein E and Benaroya H, Loading and structural response models of circular plates subjected to near field explosions, Journal of Sound and Vibration, Vol. 332, pp: 1725-1753, 2013

Børvik T, Hopperstad O S, Berstad T and Langseth M, A computational model of viscoplasticity and ductile damage for impact and penetration, European Journal of Mechanics A/Solids, Vol. 20, pp: 685-712, 2001

Børvik T, Langseth M, Hopperstad O S, and Malo K A, Ballistic penetration of steel plates, International Journal of Impact Engineering, Vol. 22, pp: 855-886, 1999

Børvik T , Clausen A H, Eriksson M, Berstad T, Hopperstad O S and Langseth M, Experimental and numerical study on the perforation of AA6005-T6 panels, International Journal of Impact Engineering, Vol. 32, pp: 35-64, 2005

Børvik T, Olovsson L, Dey S and Langseth M, Normal and oblique impact of small arms bullets on AA6082-T4 aluminum protective plates, International Journal of Impact Engineering, Vol. 38, pp: 577-589, 2011

Børvik T, Hopperstad O S, Berstad T and Langseth M, Numerical simulation of plugging failure in ballistic penetration, International Journal of Solids and Structures, Vol. 38, pp: 6241-6264, 2001

Børvik T, Hopperstad O S, Berstad T and Langseth M, Perforation of 12 mm thick steel plates by 20 mm diameter projectiles with flat, hemispherical and conical noses. Part II: numerical simulations, International Journal of Impact Engineering, Vol. 27, pp: 37-64, 2002

Børvik T, Clausen A H, Hopperstad O S and Langseth M, Perforation of AA5083-H116 aluminium plates with conical-nose steel projectiles - experimental study, International Journal of Impact Engineering, Vol. 30, pp: 367-384, 2004

Børvik T, Forrestal M J, Hopperstad O S, TWarren T L and Langseth M, Perforation of AA5083-H116 aluminium plates with conical-nose steel projectiles - calculations, International Journal of Impact Engineering, Vol. 36, pp: 426-437, 2009

Børvik T, Hanssena A G, Deya S, Langbergb H and Langseth M, On the ballistic and blastload response of a 20 ft ISO container protected with aluminium panels filled

with a local mass - Phase I: Design of protective system, Engineering Structures, Vol. 30, pp: 1605-1620, 2008

Børvik T, Hopperstad O and Berstad T, On the influence of stress strain triaxiality and strain rate on the behaviour of a structural steel. Part II. Numerical study, European Journal of Mechanics A/Solids, Vol. 22, pp: 15-32, 2002

Bosrisov A A, Sulimov A A, Sukoyan M K, Komissarov P V, Shamshin I O, Ibragimov R Kh, and Mikhailov Y M, Blast waves generated in an unconfined space by a nonideal detonation of high-density aluminium-enriched formulations, Russian Journal of Physical Chemistry B, Vol. 3, pp: 936-944, 2009

Bowen I G, Albright R W, Fletcher R and White C S, A model designed to predict the motion of objects translated by classical blast waves, CEX-58.9, U.S.Atomic Energy Commission, Civile Effects Test Operations, 1961

Brode H L, A calculation of the blast wave from a spherical charge of TNT, The RAND Corporation, Santa Mónica, California, 1958

Brode H L, Numerical solutions of spherical blast waves, Journal of Applied Physics, Vol. 26, pp: 766-775., 1955

Browne S, Ziegler J and Shepherd J, Numerical solution methods for shock and detonation jump conditions, Report FM2006.006, Aeronautics and Mechanical Engineering, California Institute of Technology, Pasadena, 2004

Buyuk M, Development of a tabulated thermo-viscoplastic material model with regularized failure for dynamic ductile prediction of structures under impact loading, PhD Thesis, George Washington University, National Crash Analysis Center, 2013.

Cerik B C, Damage assessment of marine grade aluminium alloy-plated structures due to air blast and explosive loads, Thin-Walled Structures, Vol. 110, pp: 123-132, 2017

Chaboche J, A review of some plasticity and viscoplasticity constitutive theories, International Journal of Plasticity, Vol. 24, pp: 1642-1693, 2008

Chafi M S, Karami G and Ziejewski M, Numerical analysis of blast-induced wave propagation using FSI and ALE multi-material formulations, International Journal of Impact Engineering, Vol. 36, pp: 1269-1275, 2009

Chan P C and Klein H H, A study of blast effects inside an enclosure, Journal of Fluids Engineering, Vol. 116, pp: 450-455, 1994

Chang T S, Reflection of strong blast waves, The Physics of Fluids, Vol. 7, pp. 1225-1232, 1964

Chen S, Huang C, Wang C and Duan Z, Mechanical properties and constitutive relationships of 30CrMnSiA steel heated at high rate, Materials Science and Engineering A, Vol. 483-484, pp: 105-108, 2008

Cheng D, Hung C and Pi S, Numerical simulations of near-field explosion, Journal of Applied Science, Engineering and Technology, Vol. 16, pp: 61-67, 2013

Cheng Y Q, Zhang H, Chen Z H and Xian K F, Flow stress equation of AZ31 magnesium alloy sheet during warm tensile deformation, Journal of Processing Technology, Vol. 208, pp: 29-34, 2008

Chow S K, Cleaver R P, Fairweather M and Walker D G, An experimental study of vented explosions in a 3:1 aspect ratio cylindrical vessel, Transactions of the Institute of Chemical Engineers, Vol. 78-B, 2000

Clausen A H, Børvik T, Hopperstad O S and Benallal A, Flow and fracture characteristics of aluminium alloy AA5083-H116 as function of strain rate, temperature and triaxiality, Materials Science and Engineering A, Vol. 364, pp: 260-272, 2004

Cloete T J, Nurick G N and Palmer R N, The deformation and shear failure of peripherally clamped centrally supported blast loaded circular plates, International Journal of Impact Engineering, Vol. 32, pp: 92-117, 2005

Conrad H, The cryogenic properties of metals, in High Strength Materials, John Wiley, New York, 1964

Cooper P W, Explosives engineering, Wiley-VCH, 1996

Corbett G, Reid S and Johnson W, Impact loading of plates and shells by free-flying projectiles: a review, International Journal of Impact Engineering, Vol. 18, pp: 141-230, 1996

Department of the Navy, OPNAVINST 9070.1, 1988

Dobratz B M and Crawford P C, LLNL Explosives Handbook, Lawrence Livermore National Laboratory, University of California, San Diego, 1985

DoD USA, Unified Facilities Criteria (UFC 3-340-02) Structures to resist the effect of accidental explosions, 2008

Dolinski M, Rittel D and Dorogoy A, Modeling adiabatic shear failure from energy considerations, Journal of Mechanics of Physics and Solids, Vol. 58, pp: 1759-1775, 2010

Donea J, Huerta A, Ponthot J-Ph and Rodríguez-Ferran A , Arbitrary Lagrangean-Eulerean methods, Encyclopedia of Computational Mechanics, Edited by Erwin, Borst René and Hughes J R, John Wiley & Sons, 2004

Dorward R C and Hasse K R, Strain rate effects on tensile deformation of 2024-0 and 7075-0 aluminum alloy sheet, Journal of Materials Engineering and Performance, Vol. 4, pp: 216-220, 1995

Dragos J, Wu C and Oehlers D J, Simplification of fully confined blasts for structural response analysis, Engineering Structures, Vol. 56, pp: 312-326, 2013

Du Bois P A, Kolling S, Feucht M and Haufe A, A comparative review of damage and failure models and tabulated generalization, 6th Europeam LS-DYNA User's Conference, Gottemburgh, pp: 75-86, 2007

Duffey T A and Romero C, Strain growth in spherical explosive chambers subjected to internal blast loading, International Journal of Impact Engineering, Vol. 28, pp: 967-983, 2000

Durrenberger L, Molinari A and Rusinek A, Internal variable modeling of the high strain-rate behavior of metals with applications to multiphase steels, Materials Science and Engineering A, Vol. 478, pp: 297-304, 2008

Dusenberry D O, Handbook for blast-resistant design of buildings, John-Wiley & Sons, 2010

Edri I, Savir Z, Feldgun V R, Karinski Y S and Yankelevsky D Z, On blast pressure analysis due to a partially confined explosion:I. Experimental studies, International Journal of Protective Structures,Vols. 2-1, 2011

Esparza E D, Baker W E and Oldham G A, Blast pressures inside and outside supressive structures, Edgewood Arsenal Contractor Report EM-CR-76042, San Antonio, Texas, 1975

Esparza E D, Spherical equivalency of cylindrical charges in free-air, 25th Department of Defense Explosives Safety Seminar, Vol. I, 1992

Etse G and Carosio A, Constitutive equations and numerical approaches in rate dependent material formulations, MECOM99, 1999

Farrokh B and Khan AS, Grain size, strain rate, and temperature dependence of flow stress in ultra-fine grained and nanocrystalline Cu and Al: Synthesis, experiment, and constitutive modeling, International Journal of Plasticity, Vol. 25, pp: 715-732, 2009

Feldgun V R, Karinski Y S and Yankelevsky D Z, Prediction of the quasi-static pressure in confined and partially confined explosions and its applications to blast response, International Journal of Impact Engineering, Vol. 90, pp: 46-60, 2016

Feldgun V R, Karinski Y S and Yankelevsky D Z, A simplified model with lumped parameters for explosion venting simulation, International Journal of Impact Engineering, Vol. 38, pp: 964-975, 2011

Ferrara G, Di Benedetto A, Salzano E and Russo G, CFD analysis of gas explosions vented through relief pipes, Journal of Hazardous Materials., Vol. A137, pp: 654-665, 2006

Ferrara G, Willacy S K, Phylaktou H N, Andrews G E, Di Benedetto A, Salzano E and Russo G, Venting of gas explosion through relief ducts: Interaction between internal and external explosions, Journal of Hazardous Materials, Vol. 155, pp: 358-368, 2008

Fisher E M, The effect of the steel case on the air blast from high explosives, White Oak, Maryland, US Naval Ordnance Laboratory, 1953

Flanagan D P and Belytschko T, A uniform strain hexahedron and quadrilateral with orthogonal hourglass control, International Journal for Numerical Methods in Engineering, Vol. 17, pp: 679-706, 1981

Follansbee P S and Kocks U F, A constitutive description of the deformation of copper based on the use of the mechanical threshold stress as an internal state variable, Acta Metallurgica, Vol. 36,pp: 81-93, 1988

Forde L C, Walley S M, Peyton-Jones M, Proud W G, Cullis L G and Church P D, The use of symetric Taylor impact to validadte constitutive models for an FCC metal (copper) and a BCC alloy (RHA steel), DYMAT / ed. Sciences EDP, pp: 1245-1250, 2009

Forde L C, Proud W G and Walley S M, Symmetrical Taylor Impact studies on copper, Proceedings of the Royal Society, Vol. 465, pp: 769-790, 2009

Forrestal M and Piekutowski A, Penetration experiments with 6061-T6511 aluminium targets and spherical-nose steel projectiles at striking velocities

between 0,5 and 3.0 Km/s, International Journal of Impact Engineering., Vol. 24, pp: 57-67, 2000

Fressmann D and Wriggers P, Advection approaches for single - and multi - material arbitrary Lagrangian - Eulerian finite element procedures, Computational Mechanics, Vol. 39, pp: 153-190, 2007

Freund L B, Dynamic Fracture Mechanics, Cambridge University Press, New York ,1990

Fried L E and Souers P C, Cheetah 2.0: User's Manual, Lawrence Livermore National Laboratory, Livermore CA, 1998

Gao C Y and Zhang L C, A constitutive model for dynamic plasticity of FCC metals, Materials Science and Engineering A, Vol. 527, pp. 3138-3143, 2010

Gao C Y and Zhang L C, Constitutive modelling of plasticity of FCC metals under extremely high strain rates, International Journal of Plasticity, Vols. 32-33, pp: 121-133, 2012

Gao X , Zhang T, Hayden M and Roe C, Effects of the stress state on plasticity and ductile failure of an aluminium 5083 alloy, International Journal of Plasticity, Vol. 25, pp: 2366-2382, 2009

Geretto C, Yuen S C Kim and Nurick G N, An experimental study of the effects of degrees of confinement on the response of square mild steel plates subjected to blast loading, International Journal of Impact Engineering, http://dx.doi.org/10.1016/ j.ijimpeng.2014.08.002, 2014

Gibson P W, Blast overpressure and survivability calculations, Technical Report NATICK/TR-95/003 / U.S. Army Natich Research, Development and Engineering Center, NATICH, Massachussets, 1994

Godunov S K, Finite difference methods for numerical computation of discontinuous solutions of the equation of fluid dynamics, Matemtichskii Sbornik, Vols. 47, no. 3, pp: 271-306, 1959

Goel M D, Matsagar V A and Gupta A K, Dynamic response of stiffened plates under air blast, International Journal of protective Structures, Vol. 2, pp: 139-155, 2011

Gould P J and Goldthorpe B D, A path-dependent constitutive model for gilding copper, Journal of Physics IV France, Vol. 10, pp: 39-45, 2000

Grady D E, Fragment size distributions from the dynamic fragmentation of brittle solids, International Journal of Impact Engineering, Vol. 35, pp: 1557-1562, 2008

Gronostajski Z, The constitutive equations for FEM analysis, Journal of Materials Processing Technology, Vol. 106, pp: 40-44, 2000

Grys S and Trzcinski W A, Calculation of combustion, explosion and detonation characteristics of energetica materials, Central European Journal of Energetic Materials, Vol. 7, pp: 97-113, 2010

Grytten F Borvik T, Hopperstad O S and Langseth M, Low velocity perforation of AA5083-H116 aluminium plates, International Journal of Impact Engineering, Vol. 4, pp: 597-610, 2009a

Grytten F, Borvik T, Hopperstad O S and Langseth M, Quasi-static perforation of thin aluminium plates, International Journal of Impact Engineering, Vol. 36, pp: 486-497, 2009b

Grytten F, Low-Velocity penetration of aluminium plates, PhD Thesis, Department of Structural Engineering, Norwegin University of Science and Tecchnology, Trondheim, 2008.

Guo W G, Zhang X Q, Su J, Su Y, Zeng Z Y and Shao X J, The characteristics of plastic flow and a physically-based model for 3003 Al-Mn alloy upon a wide range of strain rates and temperatures, European Journal of Mechanics A/Solids, Vol. 30, pp: 54-62, 2011

Gupta N, Iqbal M A and Sekhon G S, Efect of projectile nose shape, impact velocity and target thickness on deformation behaviour of aluminum plates, International Journal of Impact Engineering., Vol. 44, pp.: 3411-3429, 2007

Gupta N, Iqbal M A and Sekhon G S, Experimental and numerical studies on the behaviour of thin aluminum plates subjected to impact by blunt-and hemispherical-nosed projectiles, International Journal of Impact Engineering, Vol. 32, pp: 1921-1944, 2006

Gupta N K, Iqbal M A and Sekhon G S, Experimental and numerical studies on the behavior of thin auminum plates subjected to impact by blunt-and-hemispherical-nosed projectiles, International Journal of Impact Engineering, Vol. 32, pp: 1921-1944, 2006

Gurson A, Continuum theory of ductile rupture by void nucleation and growth: Part 1 - Yield criteria and flow rules for porous ductile media, Journal of Engineering Materials and Technology, No. 2, pp. 1-15, 1977

Hallquist J O, LS-DYNA Theory Manual, Livermore Software Technlogy Corporation, 2006.

Hargather M J and Settles G S, Laboratory-scale techniques for the measurement of a material response to an explosive blast, International Journal of Impact Engineering, Vol. 36, pp: 940-947, 2009

Hauver G and Melani A, BRL MR 2345 - The Hugoniot of 5983 aluminum, USA Ballistic Research Laboratory, Aberdeen Proving Ground, Maryland, 1973

Hawreliak J, Butterfield M, Davies H, El-Dasher B, Higginbotham A, Kalantar D, Kimminau G, McNaney J, Milathianaki D, Murphy W, Nagler B, Lorenzana H, Park N, Remington B, Thorton L, Whitcher T, Wark J and Lorenzana H, In-situ probing of lattice response in shock compressed materials using X-ray diffraction, UCRL-PROC-233046, Lawrence Livermore Laboratory, 2007

He W, Chen J and Guo J, Dynamic analysis of subway station subjected to internal blast loading, Journal of Cent. South University Technol, Vol. 18, pp. 917-924, 2011

Henderson L, General Laws for Propagation of Shock Waves through Matter, Handbook of Shock Waves, book auth. Ben-Dor G, Igra O and Elperin T, Academic Press, Vol. 1, 2001

Henrych J, The dynamicas of explosion and its use, Elsevier Scientific Publishing Company, Osford, 1979

High W D, High explosives: the interaction between chemistry and explosives, The Alamos Science, 1982.

Hoge K G and Mukherjee A K, The temperature and strain rate dependence of the flow stress of tantalum, Journal of Materials Science, Vol. 12, pp: 1888-1672, 1977

Holmedal B, On the formulation of the mechanical threshold stress model, Acta Materiallia, Vol. 55, pp: 2739-2746, 2007

Hou Q Y and Wang J T, A modified Johnson-Cook constitutive model for Mg-Gd-Y alloy extended to a wide range of temperatures, Computational Materials Science, Vol. 50, pp: 147-152, 2010

Hu Y Q, Application of response number for dynamic plastic response of plates subjected to impulsive loading, International Journal of pressure Vessels and Piping, Vol. 77, pp: 711-714, 2000

Hu Y, Wu C, Lukaszewicz M, Dragos J, Ren J and Haskett M, Characteristics of confined blast loading in unvented structure, International Journal of Protective Structures, Vols. 2 - 1, 2011

Hughes T J R, Liu W K and Zimmermann T K, Lagrangian-Eulerian finite element formulations for incompressible viscous flows, Computer Methods in Applied Mechanics and Engineering, Vol. 29, pp: 329-349, 1981

Hutchinson M D, Width-fracture Gurney model to estimate both fragment and blast impulses, Central European Journal of Energetic Materials, Vol. 7, pp: 175-186, 2010

Iqbal M A, Khan S A, Ansari R and Gupta N K, Experimental and numerical studies of double-nosed projectile impact on aluminum plates, International Journal of Impact Engineering, Vol. 54, pp: 232-245, 2013

Jacinto A C, Ambrosini R D and Danesi R F, Experimental and computational analysis of plates under air blast loading, International Journal of Impact Engineering, Vol. 25, pp: 927-947, 2001

Jacob N, Yuen C K, Nurick G N, Bonorchid D, Desai S A and Tait D, Scalling aspects of quadrangular plates subjected to localised blast loads - experiments and predictions, International Journal of Impact Engineering, Vol. 30, pp:1179-1208, 2004

Jacob N, Nurick G N and Langdon G S, The effect of stand-off distance on the failure of fully clamped circular mild steel plates subjected to blast loads, Engineering Structures, Vol. 29, pp: 2723-2736, 2007

Janovsky B, Podstawka T, Makovicka D, Horkel J and Vejs L, Pressure wave generated in vented confined gas explosions: experiment and simulation, Transactions of the 17th International Conference Structural Mechanics in Reactor Technology (SMIRT 17), Prague, Vols. Paper J04-6, 2003

Jeunechamps P-P, Simulation numérique, à l'aide d'algorithmes thermomécaniques implicites, de matériaux endommageables pouvant subir de grande vitesses de déformation, PhD Thesis, Faculté des Sciences Appliqués, Université de Liège, 2008

Johnson G R and Cook W H, Fracture characteristics of three metals subjected to various strains, strain rates , temperatures and pressures, Engineering Fracture mechanics, Vol. 21, No. 1, pp: 31-48, 1985

Johnson G R and Cook W H, A constitutive model and data for metals subjected to large strains, high strain rates and high temperatures, Proceedings of the Seventh International Symposium on Ballistics, The Hague, Netherlands, 19-21 April, pp: 541-548, 1983

Jones N and Paik J, Impact perforation of aluminium alloy plates, International Journal of Impact Engineering, Vol. 48, pp: 46-53, 2012

Jones N, Recent studies on the response of structures subjected to large impact loads, Ship Structures Symposium '93.,Arlington, Virginia, 1993

Jones N, Structural Impact, Cambridge University Press, 1989

Jones N, Uran T O and Tekin S A, The dynamic plastic behaviour of fully clamped rectangular plates, International Journal of Solids Structures, Vol. 6, pp: 1499-1512, 1970

Kapoor R and Nemat-Nasser S, Comparison between high strain-rate and low strain-rate deformation of tantalum, Metall. Mater. Trans. A, Vol. 31, pp: 815-823, 2000

Karnesky J, Chatterjee P, Tamanini F and Dorofeev F, An application of 2D gasdynamic modeling for the prediction of overpressures in vented enclosures, Journal of Loss prevention in the Process Industries, Vol. 20, pp: 447-454, 2007

Kazemahvazi S, Radford, D, Deshpande, V and Fleck, N, Dynamic failure of clamped circular plates subjected to an underwater shock, Journal of Mechanics of Materials and Structures, Vol. 2, pp: 2007-2013, 2007

Keenan W A and Tancreto J E, Design criteria for frangible covers in ordnance facilities, Naval Civil Engineering Laboratory, Port Hueneme, California, 1982.

Khan AS, Su Y S, Chen X, Takacs L and Zhang H, Nanocrystalline aluminium and iron: Mechanical behaviour at quasi-static and high strain rates, and constitutive modeling, International Journal of Plasticity, Vol. 22, pp: 195-209, 2006

Khan A S and Huang S, Experimental and theoretical study of mechanical behaviour of 1100 aluminum in the strain rate range 10^{-5} - 10^{4} s^{-1}, International Journal of Plasticity, Vol. 8, pp: 397-424, 1992

Khan A S and Liang R, Behaviours of three BCC metal over a wide range of strain rates and temperatures: experiments and modeling, International Journal of Plasticity, Vol. 15, pp: 1089-1109, 1999

Khan A S and Liang R, Behaviours of three BCC metals during non.proportional multi-axial loadings: experiments and modeling, International Journal of Plasticit, Vol. 16, pp: 1443-1458, 2000

Khan A S and Zhang H, Mechanically alloyed nanocrystalline iron and copper mixture: behaviour and constitutive modeling over a wide range of strain rates, International Journal of Plasticity, Vol. 16, pp: 1477-1492, 2000a

Khan A S, Suh Y S and Kazmi R, Quasi-static and dynamic loading responses and constitutive modeling of titanium alloys, International Journal of Plasticity, Vol. 20, pp: 2233-2248, 2004

Khan A S, Zhang H and Takacs L, Mechanical response and modeling of fully compacted nanocrystallin iron and copper, International Journal of Plasticity, Vol. 16, pp: 1459-1476, 2000b

Kim J B and Shin H, Comparison of plasticity models for tantalum and a modification of the PTW model for wide ranges of strain, strain rate, and tyemperature, International Journal of Impact Engineering, Vol. 36, pp: 746-753, 2009

Kingery C N and Bulmash G B, Airblast parameters from TNT spherical air burst and hemispheral surface burst, Technical Report TR-02555, Ballistic Research Laboratory, Aberdeen Proving Ground, Maryland, 1984

Kingery C N, Schumaker R and Ewing Jr W, Internal pressure from explosions in supressive structures, Ballistic Research Laboratory, Aberdeen Proving Ground, Maryland, 1978

Kingery C N and Coulter G, Reflected Overpressure Impulse on a Finite Structure, Technical Report ARBRL-TR-02537, Ballistic Research Laboratory, Aberdeen Proving Ground, Maryland, 1983

Kingery C N, Survey of airblast data related to underground munition store sites, Ballistic Research Laboratory, Aberdeen Proving Ground, Maryland, 1989

Kingery C N, Air blast parameters versus scaled distance for hemispherical TNT surface burst, BRL Report 1344, Ballistic Research Laboratories, Aberdeen Proving Ground, Maryland, 1966

Kinney G F and Graham K K, Explosive shocks in air, Springer Science, New York, 1985

Kinney G F, Sewell R G and Graham K J, Peak Overpressures for Internal Blast, NWC Technical Publication, Naval Weapons Center, China Lake, California, 1979

Klepaczko J, Thermally activated flow and strain rate history effects for some polycrystalline FCC metals, Division of Engineering, Brown University, Providence, 1974

Kocks U F and Mecking H, Physics and phenomenology of strain hardening: the FCC case, Progress in Material Science, Vol. 48, pp: 171-273, 2003

Kocks U F, Laws for work-hardening and low temperature creep, Journal of Engineering Materials and Technology, Vol. January, pp: 76-85, 1976

Kocks U F, Realistic constitutive relations for metal plasticity, Material Sciences and Engineering A, Vol. 317, pp: 181-187, 2001

Koko T S and Olson M D, Non-linear analysis of stiffened plates using super elements, International Journal for Numerical Methods in Engineering, Vol. 31, pp: 319-343, 1991

Krauthammer T, Modern Ptotective Structures, CRC Press, 2008

Kuhl E, Hulshoff S and de Borst R, An arbitrary Lagrangian Eulerian finite-element approach for fluid-structure interaction phenomena, International Journal for Numerical Methods in Engineering, Vol. 57, pp: 117-142, 2003

Langdon G S and Schleyer G K, Inelastic deformation and failure of profiled stainless steel blast wall panels. Part I: experimental investigations, International Journal of Impact Engineering, Vol. 31, pp: 341-369, 2005c.

Langdon G S, Ozinsky A and Yuen C K, The response of partially confined right circular stainless steel cylinders to internal air-blast loading, International Journal of Impact Engineering, Vol. 73, pp. 1-14, 2014

Langdon G S and Schleyer G K, Deformation and failure of profiled stainless steel blast wall panels. part III: finite element simulations and overall summary, International Journal of Impact Engineering, Vol. 32, pp: 988-1012, 2006

Langdon G S and Schleyer G K, Inelastic deformation and failure of profiled stainless steel blast wall panels. part I: analytical modelling considerations, International Journal of Impact Engineering, Vol. 31, pp: 371-399, 2005b

Langdon G S, Yuen C K and Nurick G N, Experimental and numerical studies on the response of quadrangular stiffened plates. Part II: localised blast loading, International Journal of Impact Engineering, pp: 85-111, 2005a

Larcher M, Pressure-time functions for the description of air blast waves, JRC European Communities, 2008

Larcher M, Simulation of the effects of an air blast wave, JRC, European Commission, 2007

Lee B J, Ahzi S and Asaro R J, On the plasticity of low symmetry crystals lacking five independent slip systems, Mechanics of Materials, Vol. 20, pp: 1-8, 1995

Lee E L, Finger M and Collins W, JWL equation of state coefficients for high explosives, Lawrence Livermore Laborator, University of California, San Diego, California, 1973

Lee E L, Hornig H C and Kury J W, Adiabatic expansion of high explosive detonation products, Lawrence Livermore Laboratory, Livermore, California, 1968

Lee W S and Liu C Y, The effects of temperature and strain rate on the dynamic flow behaviour of different steels, Materials Science and Engineering A, Vol. 426, pp: 101-113, 2006

Lee Y-W and Wierzbicki T, Fracture prediction of thin plates under localized impulsive loading. Part I: dishing, International Journal of Impact Engineering, Vol. 31, pp: 1253-1276, 2005a

Lee Y-W and Wierzbicki T Fracture prediction of thin plates under localized impulsive loading. Part II: discing and petalling, International Journal of Impact Engineering, Vol. 31, pp: 1277-1308, 2005b

Lee Y-W, Fracture prediction in metal sheets, PhD Thesis, Massachusetts Institute of Technology, 2005

Van Leer, Towards de ultimate conservative difference scheme. IV. A new approach to numerical convection, Journal of Computational Physics, Vol. 167, pp. 276-299, 1977

Lemaitre J, A course on damage mechanics, Springer-Verlag, 1992

Lemaitre J and Chaboche J L, Mechanics of Solid Materials, Cambridge University Press, 1990

Lesuer D R, Kay G J and LeBlanc M M, Modeling large-strain, high rate deformation in metals, Third Biennal Tri-Laboratory Engineering Conference Modeling and Simulation, Pleasanton, 2001

Lesuer D R, Kay G J and LeBlanc M M, Modeling large-strain, high rate deformation in metals, UCRL-JC-134118, Lawrence Livermore National Laboratory, 2001

Li Q M and Jones N, On dimensionless numbers for dynamic plastic response of structural members, Archive of Applied Mechanics, Vol. 70, pp: 245-254, 2000

Li Q M and Jones N, Formation of a shear localization in structural elements under transverse dynamic loads, International Journal of Solids and Structures, Vol. 37, pp: 6683-6704, 2000

Li Q M and Jones N, Shear and adiabatic shear failures in an impulsivey loaded fully clamped beam, International Journal of Impact Engineering, Vol. 22, pp: 589-607, 2000

Liang R and Khan A S, A critical review of experimental results and constitutive models for BCC and FCC metals over a wide range of strain rates and temperatures, International Journal of Plasticity, Vol. 15, pp: 963-980, 1999

Lin Y C, Li Q F, Xia Y C and Li L T, A phenomenological constitutive model for high temperature flow stress precistion of Al-Cu-Mg alloy, Materials Science and Engineering A, Vol. 534, pp: 654-662, 2012

Lin Y C, Xia Y C, Chen X M and Chem M S, Constitutive descriptions for hot compressed 2124-T851 aluminum alloy over a wide range of temperature and strain rate, Computational Materials Science, Vol. 50, pp: 227-233, 2010

Lin Y C and Chen X M, A combined Johnson-Cook and Zerilli-Armstrong model for hot compressed typical high-strength alloy steel, Computational Materials Science, Vol. 49, pp: 628-633, 2010

Lin Y C and Chen X M, A critical review of experimental results and constitutive descriptions for metals and alloys in hot working, Materials and design, Vol. 32, pp: 1733-1759, 2011

Lin Y C and Liu G, A new mathematical model for predicting flow stress of typical high-strength alloy steel at elevated high temperature, Computational Materials Science, Vol. 48, pp: 54-58, 2010

Lin Y C, Chen M S and Zhong J, Constitutive modeling for elevated temperature flow behaviour of 42CrMo steel, Computational Materials Science, Vol. 42, pp: 470-477, 2008

Lin Y C, Chen X M and Liu G, A modified Johnson-Cook model for tensile behaviors of typical high-strength alloy steel, Materials Science and Engineering A, Vol. 527, pp: 6980-6986, 2010

Linder C, An Arbitrary Lagrangian-Eulerian finite element formulation for dynamics and finite strain plasticity models, Universuty Stuttgart, 2003

Liu J, Yan Q and Wu J, Analysis of blast wave propagation inside tunnel, Transactions Tianjin University, DOI.10.1007/s12209-008-0061-3, 2008

Longère P, Dragon A, Trumel H and Deprince X, Adiabatic shear banding-induced degradation in a thermo-elastic viscoplastic material under dynamic loading, International Journal of Impact Engineering, Vol. 32, pp: 285-320, 2005

Louar M A, Belkassem B, Ousji H, Spranghers K, Kakogiannis D, Pyl I and Vantomme J, Explosive driven shock tube loading of aluminium plates; experimental study, International Journal of Impact Engineering, Vol. 86, pp: 111-123, 2015

Louca L A, Pan Y G and Harding J E, Response of stiffened and unstiffened plates subjected to blast loading, Engineerinmg Structures, Vol. 20, pp: 1079-1086, 1998

Lu Y and Wang Z, Characterization of structural effects from above-ground explosion using coupled numerical simulation, Computers and Structures, Vol. 84, pp: 1729-1742, 2006

Luccioni B M, Ambrosini R D and Danesi R F, Analysis of building collapse under blast loads, Engineering Structures, Vol. 26, pp: 63-71, 2004

Lutzky M, The flow field behind a spherical detonation of TNT using Landau-Stanyukovitch equations of state for detonation products, NOL - United States Naval Ordnance Laboratory, White Oak, Maryland, 1965

Ma L, Xin J, Hu Y and Zheng J, Ductile and brittle fracture assessment of containment vessels subjected to internal blast loading, International Journal of Impact Engineering, Vol. 52, pp: 28-36, 2013

Mahmadi K and Aquelet N, Delayed mesh relaxation for multi-material ALE formulation, International Journal of Heat and Flow, Vol. 46, pp: 102-111, 2014.

Mc Clintock F A, A criterion for ductile failure by the growth of holes, Journal of Applied Mechanics, Vol. 35, pp: 163-171, 1968

Mecking H and Kocks U F, Kinetics of flow and strain-hardening, Acta Metallurgica, Vol. 29, pp: 1865-1875, 1981

Menkes S B and Opat H J, Tearing and Shear Failures in Explosively Loaded Clamped Beams, Experimental Mechanics, Vol.13, pp: 480-486, 1973

Mespoulet J, Plassard F, Hereil P and Lefrançois A, Influence of HE shape on blast profile, 8th European LS-DYNA Users Conference, Strasburg, 2011.

Meyer Jr, H W, A modified Zerilli-Armstrong constitutive model describing the strength and localizing behaviour of Ti-6Al-4V, Technical Report ARL-CR-0578, Army Research Laboratory, Aberdeen Proving Ground, 2006

Meyer R, Kohler J and Homburg A, Explosives, WILEY-VCH, 2007

Meyers M A, Nesterenko V F, LaSalvia J C, Xu Y B and Xue Q, Observation and modelling of dynamic recrystallization in high-strain, high-strain rate deformation of metals, Journal of Physics IV, France, Vol. 10, pp: 51-56, 2000

Meyers M A, Benson D J, Vohringer O, Kad B K, Xue Q and Fu H-H, Constitutive description of dynamic deformation: physically-based mechanisms, Materials Science and Engineering A, Vol. 322, pp:194-216, 2002

Meyers M A, Dynamic behaviour of materials, John Wiley & Sons, 1994

Molinari A and Ravichandran G, Constitutive modeling of high-strain-rate deformation in metals based on the evolution of an effective microstructural length, Mechanics of Materials, Vol. 37, pp: 737-752, 2005

Molkov V V, Grigorash A V, Eber R M and Makatov D V, Vented gaseous deflagrations: modeling of hinged inertial vent covers, Journal of Hazardous Materials, Vol. A116, pp: 1-10, 2004

Molkov V V, Eber R M, Grigorash A V, Tamanini F and Dobashi R, Vented gaseous deflagrations: modeling of translating inertial vent covers, Journal of Loss Prevention in the Process Industries, Vol. 16, pp: 395-402, 2003

Molkov V V, Grigorash A V and Eber R M, Vented gaseous deflagrations: modelling of spring-loaded inertial vent covers, Fire Safety Journal, Vol. 40, pp: 307-319, 2005

Montanaro P E and Swisdak Jr M M, INBLAST - A new and revised computer code for the prediction of blast inside closed or vented structures, Naval Surface Warfare Center, Silver Spring, 1990

Murr L E, Meyers M A, Niou C-S, Chen Y J, Pappu S and Kennedy C, Shock-induced deformation twinning in tantalum, Acta Materialia, Vol. 45, pp: 145-175, 1997

Naderi M, Durrenberger L, Molinari A and Bleck W, Constitutive relationships for 22MnB5 boron steel deformed isothermally at high temperatures, Materials Science and Engineering A, Vol. 478, pp: 130-139, 2008

Nebuda D and Oswald C J, Single-degree-of-freedom blast effects design spreadsheets (SBEDS), Protective Design Center Technical Report, US Army Corps of Engineers, 2005

Needham C, Blast Waves, Springer-Verlag, 2010

Needham C, Blast propagation through windows and doors, ISSW26, July, 2007

Nemat-Nasser S and Isaacs J B, Direct measurement of isothermal flow stress of metals at elevated temperatures and high strain rates with application to Ta and Ta-W alloys, Acta Materialia, Vol. 45, pp: 907-919, 1997

Nemat-Nasser S and Li Y, Flow stress of FCC polycrystals with application to OFHC Cu, Acta Materiallia, Vol. 46, pp: 565-577, 1998b

Nemat-Nasser S and Okinaka T, A new computational approach to crystal plasticity: FCCsingle crystal, Mechanics of Materials, Vol. 24, pp: 43-57, 1996

Nemat-Nasser S, Guo W and Liu M, Experimentally-based micromechanical modelling of dynamic response of molybdenum, Scripta Materialia, Vol. 40, pp: 859-872, 1999

Nemat-Nasser S, Guo W G and Cheng J Y, Mechanical properties and deformation mechanisms of a commercially pure titanium, Acta Materialia, Vol. 47, pp: 3705-3720, 1999

Nemat-Nasser S, Guo WG and Cheng JY, Mechanical properties and deformation mechanisms of a commercially pure titanium, Acta Materialia, Vol. 47, pp: 3705-3720, 1999b

Nemat-Nasser S, Guo W G and Kihl D P, Thermomechanical response of AL-6XN stainless steel over a wide range of strain rates, Journal of the Mechanics and Physics of Solids, Vol. 49, pp: 1823-1846, 2001

Nemat-Nasser S, Ni L and Okinawa T, A constitutive model for FCC crystals with application to polycrystalline OFHC copper, Mechanics of Materials, Vol. 30, pp: 325-341, 1998a

Nemat-Nasser S, Okinawa T and Ni L, A physically-based constitutive model for BCC crystals with application to polycristalline tantalum, Journal of Mechanics and Physics of Solids, Vol. 46, pp: 1009-1038, 1998c

Nes E, Modelling of work hardening and stress saturation in FCC metals, Progress in Materials Sciences, Vol. 41, pp: 129-193, 1998

Neuberger A, Peles S and Rittel D, Scaling the response of circular plates subjected to large and close-range spherical explosions. Part I: Air-blast loading, International Journal of Impact Engineering, Vol. 34, pp: 859-873, 2007

Neukamm F, Feucht M and Haufe A, Consistent damage modelling in the process chain of forming to crashworthiness simulations, LS-DYNA Anwenderforum, Bamberg, 2008

Ngo T , Mendis P, Gupta A and Ramsay J, Blast loading and blast effects on structures - An overview, EJSE Special Issue, pp: 76-91, 2007

Nurick G, Olson M D, Fagnan J R and Levin A, Deformation and tearing of blast-loaded stiffened square plates, International Journal of Impact Engineering, Vol. 16, pp: 273-291, 1995

Nurick G and Martin J, Deformation of thin plates subjected to impulsive loading - A review Part I: Theoretical considerations, International Journal of Impact Engineering, Vol. 8, pp: 159-170, 1989a

Nurick G and Martin J, Deformation of thin plates subjected to impulsive loading - A review Part II: Experimental studies, International Journal of Impact Engineering, Vol. 8, pp: 171-186, 1989b

Nurick G and Shave G, The deformation and tearing of thin square plates subjected to impulse loads - an experimental study, Internatiional Journal of Impact Engineering, Vol. 18, pp: 99-116, 1996

Nurick G, Gelman M and Marshall N, Tearing of blast loaded plates with clamped boundary conditions, International Journal of Impact Engineering, Vol. 18, pp: 803-827, 1996a

Nystrom U and Gylltoft K, Numerical studies of the combined effect of blast and fragment loading, International Journal of Impact Engineering, Vol. 36, pp. 995-1005, 2009

Olson M, Nurick G and Fagnan J, Deformation and rupture of blast loaded square plates - predictions and experiments, International Journal of Impact Engineering, Vol. 13, pp: 279-292, 1993

Ornellas D L, Calorimetric determinations of the heat and products of detonation for explosives: October 1961 to April 1982, Report UCRL-52821, Lawrence Livermore National Laboratory, Livermore CA, 1982

Pan Y and Louca LA, Experimental and numerical studies on the response of stiffened plates subjected to gas explosions, Journal of Constructional Steel Research, Vol. 52, pp: 171-193, 1999

Panov V, Modelling of behaviour of metals at high strain rates, PhD Thesis, Cranfield University, 2006

Park D J, Lee Y S and Green A R, Experiments on the effect of multiple obstacles in vented explosion chambers, Journal of Hazardous Materials, Vol. 153, pp: 340-350, 2008

Park D J, Lee Y S and Green A R, Prediction for vented explosions in chambers with multiple obstacles, Journal of Hazardous Materials, Vol. 155, pp: 183-192, 2008

Piekutowski A, Forrestal M J, Poormon K L and Warren T L, Perforation of aluminium plates with ogive-nose steel rods at normal and oblique impacts, International Journal of Impact Engineering, Vol. 18, pp: 877-887, 1996

Piekutowski A, Holes produced in thin aluminium sheets by the hypervelocity impact of aluminium spheres, International Journal of Impact Engineering, Vol. 23, pp: 711-722, 1999

Peng W, Modelling and simulation of interaction between blast waves and structures for blast wave mitigation, PhD Thesis, University of Nebraska, Lincoln, Nebraska, 2009

Pérez-Bergquist S J, Gray III J T, Cerreta E T, Trujillo C P and Pérez-Bergquist A, The dynamic and quasi-static mechanical response of three aluminum armor alloys: 5059, 5083 and 7039, Materials Scence and Engineering A, Vol. 528, pp: 8733-8741, 2011

Perzyna P, Temperature and rate dependent theory of plasticity of crystalline solids, Revue de Physique Appliquée, Vol. 23, pp: 445-459, 1988

Pijaudier-Cabot G and Bazant Z P, Nonlocal damage theory, Journal of Engineering Mechanics, ASCE, Vol. 113, pp: 1512-1533, 1987

Preston D L, Tonks D L and Wallace D C, Model of plastic deformation for extreme loading conditions, Journal of Applied Physics, Vol. 93, pp: 211-220, 2003

Price C, Sherburn J A, Nelson D, Slawson T and Boone R N, Evaluation of predictive methods for airblast propagation through an enclosed structure, International Journal of Protective Structures, Vol. 2, pp: 71-82, 2010

Pritchard D K, Freeman D J and Guilbert P W, Prediction of explosion pressures in confined spaces, Journal of Loss Prevention in the Process Industries, Vol. 9, pp: 205-215, 1996

Proctor J F and Filler W S, A computerized technique for blast loads from confined techniques, 14th Annual Explosives Safety Seminar, New Orleans, Louisiana, 1972

Rajendran R and Lee L M, Blast loading plates, Marine Structures, Vol. 22, pp: 99-127, 2009

Ramajeyathilagam K and Vendhan C P, Deformation and rupture of thin rectangular plates subjected to underwater shock, International Journal of Impact Engineering, Vol. 30, pp: 699-719, 2004

Ramajeyathilagam K, Vendham C P and Bhujanga R V, Non-linear transient dynamic response of rectangular plates under shock loading, International Journal of Impact Engineering, Vol. 24, pp: 999-1015, 2000

Randers-Pehrson G and Bannister K A, Airblast loading model for DYNA2D and DYNA3D, ARL-TR-1310, Army Research Laboratory, 1997

Razus D M and Krause U, Comparison of empirical and semi-empirical calculation methods for venting of gas explosions, Fire Safety Journal, Vol. 36, pp: 1-23, 2001

Read H, Triplett J and Cecil R, Dislocation dynamics and the formulation of constitutive equations for rate-dependent plastic flow in metals, 01-70-C-0055, Defense Atomic Support Agency, 1970

Remennikov A M, A review of methods for predicting bomb blast effects on buildings, Journal of Battlefield Technology, Vol. 6, pp: 5-10, 2003

Remennikov A M and Rose T A, Modelling blast loads on complex city geometries, Computers and Structures, Vol. 83, pp: 2197-2205, 2005

Remington B A, Allen P, Bring E M, Hawreliak J, Ho D, Lorenz K T, Lorenzana H, McNaney J M, Meyers M A, Pollaine S W, Rosolankova K, Sadik B, Schneider M S, Swift D, Wark J and Yaakobi B, Material dynamics under extreme conditions of pressure and strain rate, Materials Science and Technology, Vol. 4, pp: 474-488, 2006

Rice J R and Tracey D M, On the ductile enlargement of voids in triaxial stress fields, Mechanics of Physics and Solids, Vol. 17, pp: 201-217, 1969

Rice J R, Inelastic constitutive relations for solids: an internal-variable theory and its application ro metal plasticity, Journal of Mechanics and Physics of Solids, Vol. 19, pp: 433-455, 1971

Rigas F and Sklavounos S, Experimentally validated 3-D simulation of shock waves generated by dense explosives in confined complex geometries, Journal of Hazardous Materials., Vol. A121, pp: 23-30, 2005

Rigby S E and Sielicki P W, An investigation of TNT equivalence of hemispherical PE4 charges, Engineering Transactions, Polish Academy of Sciences, pp: 423-435, 2014

Rittel D, A different viewpoint on adiabatic shear localization, Journal of Physics D: Applied Physics, Vol. 42, pp: 1-6, 2009

Rittel D and Osovski S, Dynamic failure by adiabatic shear banding, International Journal of Fracture, DOI 10.1007/s10704-010-9475-8, 2010

Rodriguez-Martinez J A, Rusinek A and Arias A, Thermo-viscoplastic behaviour of 2024-T3 aluminium sheets subjected to low velocity perforation at different tempratures, Thin-Walled structures, Vol. 49, pp: 819-832, 2011

Roeder B and Sun C, Dynamic penetration of alumina/aluminum laminates: experiments and modeling, International Journal of Impact Engineering, Vol. 25, pp: 169-185, 2001

Rose T A, An approach to the evaluation of blast loads on finite and semi-infinite structures, PhD Thesis, Engineering Systems Department, Cranfield University, 2001

Rubio I, Equivalente TNT de diversos explosivos basado en la velocidad de la onda de choque, Final course dissertation, Departamento de Ingenieria Geológica y Minera, Escuela Técnica Superior de Ingenieros de Minas y Energía, 2017

Rudrapatna N S, Vaziri R and Olson M D, Deformation and failure of blast-loaded stiffened plates, International Journal of Impact Engineering, Vol. 24, pp: 457-474, 2000

Rudrapatna N S, Vaziri R and Olson M D, Deformation and failure of blast-loaded square plates, International Journal of Impact Engineering, Vol. 22, pp: 449-467, 1999

Rule W K and Jones S E, A revised form for the Johnson-Cook strength model, International Journal of Impact Engineering., Vol. 21, pp: 609-624, 1998

Rusinek A and Klepaczko J R, Shear testing of a sheet steel at wide range of strain rates and a constitutive relation with strain-rates and temperature dependence of the flow stress, International Journal of Plasticity, Vol. 17, pp: 87-115, 2001

Rusinek A and Rodriguez-Martinez J A, Thermo-viscoplastic constitutive relation for aluminium alloys, modeling of negative strain rate sensitivity and viscous drag effects, Materials and Design, Vol. 30, pp: 4377-4390, 2009

Rusinek A, Rodriguez-Martinez J A and Arias A, A thermo-viscoplastic constitutive model for FCC metals with application to OFHC copper, International Journal of Mechanical Sciences, Vol. 52, pp: 120-135, 2010

Salvado F, Teixeira-Dias F, Walley S M, Lea L J and Cardoso J B, A review on the strain rate dependency of the dynamic viscoplastic response of FCC metals, Progress in Materials Science, Vol. 88, pp: 136-231, 2017

Salvado F S, Arikson J T, Teixeira-Dias F and Cardoso J B, Confined explosions: The effect of compartment geometry, Journal of Loss Prevention in the Process Industries, Vol. 48, pp: 126-144, 2017

Salzano E and Basco A, Comparison of the explosion thermodynamics of TNT and black powder using Le Chatelier diagrams, Propellants, Explosives, Pyrothecnics, Vol. 37, pp: 724-731, 2012

Samantaray D, Mandal S, Borah U, Bhaduri A K and Sivaprasad P V, A thermo-viscoplastic constitutive model to predict elevated-temperature flow behaviour in a titanium-modified austenitic stainless steel, Materials Science and Engineering A, Vol. 526, pp: 1-6, 2009

Sauvan P E, Sochet I and Trélat S, Analysis of reflected blast wave pressure profiles in a confined room, Shock Waves, Vol. 22, pp: 253-264, 2012

Schleyer G K, Hsu S S, White M D and Birch R S, Pulse pressure loading of clamped mild steel plates, International Journal of Impact Engineering, Vol. 28, pp: 223-247, 2003

Schubak R B, Olson M D and Anderson D L, Rigid-plastic modelling of blast-loaded stiffened plates - part I: One way stiffened plates, International Journal of Mechanical Sciences, Vol. 35, pp: 289-306, 1993a

Schubak R B, Olson M D and Anderson D L, Rigid-plastic modelling of blast-loaded stiffened plates - part II: Partial end fixity, rate effects and two-way stiffened plates, International Journal of Mechanical Sciences, Vol. 35, pp: 307-324, 1993b

Schwer L E, A brief look at *MAT_NONLOCAL: a possible cure for erosion illness?, 11th International LS-DYNA Users Conference, Detroit, 2011

Schwer L E, Aluminum plate perforation: a comparative case study using Lagrange with erosion, Multi-Material ALE, and Smooth Particle Hydrodynamics, 7th European LS-DYNA Conference, Salzburg, 2009

Schwer L E, Jones-Wilkens-Lee (JWL) Equatoon of State with afterburning, 14th International LS-DYNA Users Conference, 2016

Schwer L E, Teng H and Souli M, LS-DYNA Air blast techniques: Comparison with experiments for close-in charges, 10th European LS-DYNA Conference, 2015

Schwer L E, A Brief Introduction to Coupling Load-Blast Enhanced with Multi-Material ALE: The Best of Both Worlds for Air-Blast Simulation, LS-DYNA Forum, Bamberg, 2010

Sewell R and Kinney G F, Response of structures to blast: a new criterion, Naval Weapons Center, China Lake, California, 1968

Sherkar P, Whittaker A S and Aref A J, Modeling the effects of detonations of higjh explosives to inform blast-resistant design, Technical Report MCEER -10-0009, 2010

Shin H and Kim J B, A phenomenological constitutive equation to describe various flow stress behaviors of materials in wide strain rate and temperature regimes, Journal of Engineering Materials and Technology, Vol. 132: 021009, 2010

Shin J, Whittaker A, Cormie D and Wilkinson W, Numerical modeling of close-in detonations of high explosives, Engineering Structures, Vol. 81, pp: 88-97, 2014

Shin J, Whittaker A S and Cormie D, TNT equivalence for overpressure and impulse for detonations of spherical charges of high explosives, International Journal of Protective Structures, Vol. 6, pp: 567-580, 2015

Showalter D, Placzankis B and Burkins M, Ballistic performance testing of aluminum alloy 5059-H131 and 5039-H136 for armor applications, Technical Report ARL-TR-4427, Army Research Laboratory, Aberdeen Proving Ground, Maryland, 2008

Silvestrini M, Genova B and Trujillo F J L, Energy concentration factor. A simple concept for the prediction of blast propagation in partially confined geometries, Journal of Loss Prevention in the Process Industries, Vol. 22, pp: 449-454, 2009

Sklavounos S and Rigas F, Computer simulation of shock waves transmission in obstructed terrains, Journal of Loss Prevention in the Process Industries, Vol. 17, pp: 407-417, 2004

Slavik T P, A coupling of empirical explosive blast loads to ALE air domains in LS-DYNA, 7th European LS-DYNA Conference, Salzburgo,, 2009

Song S C, Duan Z P and Tan D W, The application of B-P constitutive equations in finite element analysis of high velocity impact, International Journal of Solids and Structures, Vol. 38, pp: 5215-5222, 2001

Sorensen B, Kimsey K and Love B, High-velocity impact of low-density projectiles on structural aluminum armor, International Journal of Impact Engineering, Vol. 35, pp: 1808-1815, 2008

Sorensen B R, Kimsey K D and Love B M, High-velocity impact of low-density projectiles on structural aluminum armor, International Journal of Impact Engineering, Vol. 35, pp: 1808-1815, 2008

Souli M, Ouashine A and Lewin L, ALE formulation for fluid-structure interaction problems, Computer methods in Apllied Mechanicas and Engineering, Vol. 190, pp: 659-675, 2000

Spranghers K, Vasilakos L, Lecompte D, Sol H and Vantomme J, Identification of the plastic behaviour of aluminum plates under fre air explosions using inverse methods and full-field measurements, International Journal of Solids and Structures, Vol. 51, pp: 210-226, 2014

Spranghers K, Vasilakos L, Lecompte D and Vantomme J, Numerical simulation and experimental validation of the dynamic response of aluminum plates under free air explosions, International Journal of Impact Engineering, Vol. 54, pp: 83-95, 2013

Steinberg D J and Lund C M, A constitutive model for strain rates from 10^{-4} to 10^{6} s^{-1}, Journal of Applied Physics, Vol. 65, pp: 1528-1533, 1989

Steinberg D J, Cochran S G and Guinan M W, A constitutive model for metals applicable at highstrain rate, Journal of Applied Physics, Vol. 51, pp: 1498-1504, 1980

Stoker C, Developments of the Arbitrary Lagrangian-Eulerian method in non-linear solid mechanics, PhD Thesis, University of Twente, Enschede, 1999.

Strømsøe E, Calculation of pressure and temperature from explosions in confined spaces, Technical Report, Norwegian Defence Research Establishment, Kjeller, 1978

Sung J H, Kim J H and Wagoner R H, A plastic constitutive equation incorporating strain, strain-rate, and temperature, International Journal of Plasticity, Vol. 26, pp: 1746-1771, 2010

Swisdak M M, Simplified Kingery airblast calculations, 26th DoD Explosives Safety Seminar, Miami, 1994

Tamanini F, Scaling parameters for vented gas and dust explosions, Journal of Loss Prevention in the Process Industries, Vol. 14, pp: 455-461, 2001

Tancreto J E and Zehrt W H, Design for internal quasi-static pressures from partially confined explosions, 28th DDESB Seminar, Orlando, FLorida, 1998

Tang E K, Numerical simulation of a long span bridge response to blast loading, MSc Thesis, University of Western Australia, 2009

Taylor G I, Plastic Strain in metals, Journal of the Institute of Metals, Vol. 62, pp: 308-324, 1938

Taylor G I, The mechanism of plastic deformation of crystals. Part I. Theoretical, Proceedings of the Royal Society of London A, Vol. 145, pp: 362-387, 1934

Teeling-Smith R and Nurick G, The deformation and tearing of thin circular plates subjected to impulsive loads, International Journal of Impact Engineering, Vol. 11, pp: 77-91, 1991

Tvergaard and Needleman, Analysis of the cup-conefracture in a round tensile bar, Acta Metallurgica, Vol. 32, pp: 157-169, 1984

Vadhe P P, Pawar R B, Sinha R K, Astana S N and Rao A S, Cast aluminized explosives, Combustion, Explosion and Shock Waves, Vol. 44, pp: 461-477, 2008

van Thiel M, Lee EL and Cochran S, Effects of overdriven shock states on the equation of state of 9404 explosive, Journal of Applied Physics, Vol. 54, pp: 6760-6763, 1983

Vitalli E, An extended finite element formulation for contact in multi-material arbitrary Lagrangian - Eulerian calculations, PhD Thesis, University of California, S.Diego, 2007

Voce E, The relationship between stress and strain for homogeneous deformation, Journal of the Institute of Metals, Vol. 74, pp: 537-556, 1948

Von Newmann J and Richtmeyer R D, A method for numerical calculation of hydrodynamic shocks, Journal of Applied Physics, Vol. 21, 1950

Voyiadjis G Z and Abed F H, Microstructural based models for BCC and FCC metals with tempearature and strain rate dependency, Mechanics of Materials, Vol. 37, pp: 355-378, 2005

Voyiadjis G Z and Almasri A H, A physically based constitutive model for FCC metals with applications to dynamic hardness, Mechanics of materials, Vol. 40, pp: 549-563, 2008

Vural M and Cairo J, Experimental analysis and constitutive modeling for the newly developed 2139-T8 alloy, Materials Science and Engineering A, Vol. 520, pp: 56-65, 2009

Wagenhofer M, Erickson-Natishan M A, Armstrong R W and Zerilli F, Influences of strain rate and grain size on yield and serrated flow in commercial Al-Mg Alloy 5086, Scripta Materialia, Vol. 41, pp: 1177-1184, 1999

Walley S M, Church P D, Townsley R and Field J E, Validation of a path-depemdent constitutive model for FCC and BCC metals using "symmetric" Taylor impact, Journal Pfysics IV France, EDP Sciences, Vol. 10, pp: 69-73, 2000

Wang Y, Zhou Y and Xia Y, A constitutive description of tensile behaviour for brass over a wide range of strain rates, Materials Science and Engineering A, Vol. 372, pp: 186-190, 2004

Warren T and Poormon K, Penetration of 6061-T6511 aluminum targets by ogive-nosed VAR 4340 steel projectiles at oblique angles: experiments and simulations, International Journal of Impact Engineering, Vol. 25, pp: 993-1022, 2001

Webster K G, Investigation of close proximity underwater explosion effects on a ship-like structure using the multi-material Arbitrary Lagrangian Eulerian finite element method , MSc Thesis, Virginia Polytechnic Institute, 2007

Wehrenberg C, Comley A J, Rudd R E, Terry M, Hawreliak J, Maddox B R, Prisbrey S T, Park H-S and Remington B A, Strain anisotropy and shear strength of shock compressed tantalum from in-situ Laue diffraction, Journal of Physics, Conference Series 500, 18th APS-SCCM and 24th AIRAPT, 2014

Whenhui Z, Honglu X, Guangkuan Z and Schleyer G J, Dynamic response of cylindrical explosive chambers to internal blast loading produced by a concentrated charge, International Journal of Impact Engineering, Vol. 19, pp: 831-845, 1997

Wierzbicki T and Nurick G N, Large deformation of thin plates under localized impulsive loading, International Journal of Impact Engineering, Vol. 18, pp: 899-918, 1996

Wierzbicki T, Petalling of plates under explosive and impact loading, International Journal of Impact Engineering, Vol. 22, pp: 935-954, 1999

Wilkins M L and Guinan M W, Impact of cylinders on a rigid boundary, Journal of Applied Physics, Vol. 44, pp: 1200-1206, 1973

Wilkinson C R and Anderson J G, An introduction to detonation and blast for the non-specialist, DSTO-TN-0526, Weapons Systems Division, Department of Defence, Australian Government, 2003

Williams C and Love B, Dynamic failure of materials: A review, ARL-TR-5275, Army Research Laboratory, Aberdeen Proving Ground, Maryland, 2010.

Winzer R and Glinika, **A** The static and dynamic compressive behaviour of selected aluminium alloys, Engineering Transactions, pp: 85-100, 2011

Woodward R and Cimpoeru S, A study of the perforation of aluminium laminate target, International Journal of Impact Engineering, Vol. 3, pp: 117-131, 1998

Wright T, The physics and mathematics of adiabatic shear bands, Cambridge University Press, 2002

Wu C, Fattori G, Whittaker A and Oehlers D J, Investigation of air-blast effects from spherical and cylindrical-shapped charges, International Journal of Protective Structures, Vol. 1, pp: 345-362, 2010

Wu C, Lukaszewicz M, Schebella K and Antanovskii L, Experimental and numerical investigation of confined explosion in a blast chamber, Journal of Loss Prevention in the Process Industries, Vol. 26, pp: 737-750, 2013

Xue L, Damage accumulation and fracture in uncracked ductile solids subject to triaxial loading, International Journal of Solids and Structures, Vol. 44, pp: 5163-5181, 2007

Xue L, Ductile fracture modelling - Theory, experimental investigation and numerical verification, PhD Thesis , Department of Mechanical Engineering, Massachusetts Institute of Technology, 2007

Young D L, An interface tracking method for a 3D Eulerian Hydrodynamics code, AWRE/44/92/35, AWRE Design Mathematics Division, 1987

Young D L, Time-dependent multi-material flow with large fluid distortion, Numerical methods for fluid dynamics, book auth. Morton K W and Baines M J, Academic Press, New York ,1982

Yu H, Guo Y, Zhang K and Lai X, Constitutive model on the description of plastic behaviour of DP600 steel at strain rate from 10^{-4} to 10^{3} s^{-1}, Computational Materials Science, Vol. 46, pp: 36-41, 2009

Yu J and Jones N, Numerical simulation of a clamped beam under impact loading, Computers and Structures, Vol. 32, pp: 281-293, 1989

Yu T X and Chen F L, The large deflection dynamic plastic response of rectangular plates, International Journal of Impact Engineering, Vol. 12, pp: 603-616, 1992

Yuan Y and Tan P J, Deformation and failure of rectangular plates subjected to impulsive loadings, International Journal of Impact Engineering, Vol. 59, pp: 46-59, 2013

Yuen S and Nurick G, Experimental and numerical studies on the response of quadrangular stiffened plates. Part I: subjected to uniform blast load, International Journal of Impact Engineering, Vol. 31, pp: 55-83, 2005

Yuen S C K, Nurick G N, Verster W, Jacob N, Vara A R, Balden V H, Bwalya D, Govender R A and Pittermann M, Deformation of mild steel plates subjected to large-scale explosions, International Journal of Impact Engineering, Vol. 35, pp: 684-703, 2008

Zener C and Hollomon J H, Effect of strain rate upon plastic flow of steel, Journal of Applied Physics, Vol. 15, pp: 22-32, 1944

Zerilli F J and Armstrong R W, Dislocation mechanicas based constitutive relations for material dynamics calculations, Journal of Applied Physics, Vol. 61, pp:1816-1825, 1987

Zhang H, Wen W, Cui H and Xu W, A modified Zerilli-Armstrong model for alloy IC10 over a wide range of temperatures and strain rates, Materials Science and Engineering A, Vol. 527, pp: 328-393, 2009

Zhang H, Wen W and Cui H, Behaviours of IC10 alloy over a wide range of strain rates and temperatures: Experiments and modeling, Materials Science and Engineering A, Vol. 504, pp: 99-103, 2009

Zhang S, McCormick P and Estrin Y, The morphology of Portevin-Le Chatelier bands finite element simulation fo Al-Mg-Si, Acta Materialia, Vol. 49, pp: 1087-1094, 2001

Zhao H and Gary G, The testing and behaviour modelling of sheet metals at strain rates from 10^{-4} to 10^{4} s^{-1}, Materials Science and Engineering A, Vol. 207, pp: 46-50, 1995

Zhao Y P, Suggestion of a new dimensionless number for dynamic plastic response of beams and plates, Archive of Applied Mechanics, Vol. 68, pp: 524-538, 1998

Zhou X Q and Hao H, Prediction of airblast loads on structures behind a protective barrier, International Journal of Impact Engineering, Vol. 35, pp: 363-375, 2008

Zhu L, Transient deformation modes of square plates subjected to explosive loadings, International Journal of Solids and Structures, Vol. 33, pp: 301-314, 1996

Zukas A J, Introduction to Hydrocodes, Elsevier, Vol. Studies in Applied Mechanics 49, 2004

Zukas J A and Scheffler D R, Practical aspects of numerical simulations of dynamic events: effects of meshing, International Journal of Impact Engineering, Vol. 24, pp: 925-945, 2000

Zukas J A, Introduction to Hydrocodes, Elsevier, Baltimore, 2004

Zukas J A and Walters W P, Explosive effects and applications, Springer-Verlag, New York, 1998

Zykowski A, Sochet I, Mavrot G, Bailly P and Renard J Study of the explosion process in a small scale experiment - structural loading, Journal of Loss Prevention in the Process Industries, Vol. 17, pp: 291-299, 2004

Published Work

The author has shared some of his findings in a series of scientific papers as described below:

(Conference paper)

Salvado F C, The behaviour of 5083-H111 naval aluminium alloy square plates under blast loading: experimental and numerical approaches, MARTECH Conference 4-6 July, Instituto Superior Técnico, Lisbon, 2016

(Work published in Scientific journals)

Salvado F [et al.], A review on the strain rate dependency of the dynamic viscoplastic response of FCC metals, Progress in Materials Science, Vol. 88, pp: 136-231, 2017

Salvado F S [et al.], Confined explosions: The effect of compartment geometry, Journal of Loss Prevention in the Process Industries, Vol. 48, pp: 126-144, 2017

(Work submitted for publication)

Salvado F [et al.], Blast loading of AA5083-H111 aluminium plates: Experimental and numerical analysis.